SPATIAL VARIABILITY AND TERMINAL DENSITY

– IMPLICATIONS IN SOIL BEHAVIOR –

A Thesis
Presented to
The Academic Faculty

By

Guillermo Andres Narsilio

In Partial Fulfillment
of the Requirements for the Degree
Doctor of Philosophy in Civil and Environmental Engineering

Georgia Institute of Technology
May 2006

SPATIAL VARIABILITY AND TERMINAL DENSITY

– IMPLICATIONS IN SOIL BEHAVIOR –

Approved by:

Dr. J. Carlos Santamarina, Advisor
Professor, Goizueta Foundation Chair
School of Civil and Environmental
Engineering
Georgia Institute of Technology

Dr. J David Frost
Professor, School of Civil and
Environmental Engineering
Director, Regional Engineering Program
Georgia Institute of Technology

Dr. Guillermo H. Goldsztein
Professor, School of Mathematics
Georgia Institute of Technology

Dr. Paul W. Mayne
Professor, School of Civil and
Environmental Engineering
Georgia Institute of Technology

Dr. Glenn J. Rix
Professor, School of Civil and
Environmental Engineering
Georgia Institute of Technology

Date Approved: *February 13th, 2006*

To my wife, Gabriela, and
To my parents, Graciela and Hector

ACKNOWLEDGEMENTS

TABLE OF CONTENTS

LIST OF TABLES

LIST OF FIGURES

xi

SUMMARY

Geotechnical engineers often face important discrepancies between the observed and the predicted behavior of geosystems. Two conceptual frameworks are hypothesized as possible causes: the ubiquitous spatial variability in soil properties and process-dependent terminal densities inherent to granular materials.

The effects of spatial variability are explored within conduction and diffusion processes. Mixtures, layered systems, inclusions and random fields are considered, using numerical, experimental and analytical methods. Results include effective medium parameters and convenient design and analysis tools for various common engineering cases. In addition, the implications of spatial variability on inverse problems in diffusion are numerically explored for the common case of layered media.

The second hypothesis states that there exists a unique "terminal density" for every granular material and every process. Common geotechnical properties are readily cast in this framework, and new experimental data are presented to further explore its implications. Finally, an unprecedented field study of blast densification is documented. It involves comprehensive laboratory and site characterization programs and an extensive field monitoring component. This full scale test lasts one year and includes four blasting events.

CHAPTER I

INTRODUCTION

1.1 SPATIAL VARIABILITY

Geotechnical engineers often face important discrepancies between the observed and the predicted behavior of geosystems. It is herein hypothesized that this is often consequence of the ubiquitous spatial variability in soil properties.

The most common type of soil variability is layering. However, natural soil deposits can exhibit large variability in both vertical and horizontal dimensions as a result of deposition history, as well as post-depositional physical, chemical or biogenic effects (Lacasse and Nadim 1996; Phoon and Kulhawy 1999).

The effects of spatial variability of soil properties have been studied in the past in relation to geo-processes such as liquefaction (Popescu and Prevost 1996; Popescu et al. 1997; Kokusho 1999, 2002), vertical strain and settlement (Zeitoun and Baker 1992; Paice et al. 1996), flow of water through porous media (Dagan 1989; Griffiths and Fenton 1993; Fenton and Griffiths 1996; Nishimura et al. 2002), slope stability (Young et al. 1977; Tonon et al. 2000), and strength (Griffiths and Fenton 2001; Kim 2005).

The effects of spatial variability on conduction and diffusion phenomena are explored in the first half of this work (Chapters II and III).

1.2 TERMINAL DENSITY

It is herein hypothesized that there exists a unique "terminal density" for every granular material and every process. This conceptual framework permits analyzing a wide range of soil responses and complex systems. Blast densification and post-improvement soil response is the case in point. Blast densification is a soil improvement technique whereby explosives are used to rearrange the particles of a loose, saturated, coarse-grained soil into a more stable, denser configuration. If the blasting-induced porewater pressure equals the initial effective stress, the shear resistance is temporarily lost, the soil liquefies, and gradually regains strength as the excess pore pressure dissipates. Typically, the accompanying settlements are 2% to 10% of the treated thickness (Ivanov 1983; Charlie et al. 1985; Dowding and Hryciw 1986; Hryciw 1986; Minaev 1993; Narin van Court and Mitchell 1997; Narin van Court 2003). However, multiple densification cycles may be needed and, still, the post-densification volumetric strain may remain shear strain dependent.

The detailed analysis of the new concepts of terminal density, and an unprecedented field study of blast densification constitute the second half of this thesis (Chapters IV, V and VI).

1.3 ORGANIZATION

This work is organized into seven chapters. Chapter II explores the influence of spatially varying hydraulic conductivity fields on steady state seepage, and seeks an equivalent effective medium hydraulic conductivity. Mixtures, combinations, inclusions

and random hydraulic conductivity fields are considered using numerical, experimental and analytical methods.

Chapter III focuses on excess pore pressure diffusion, i.e., consolidation, in soils with a depth-varying coefficient of consolidation. Both forward and inverse problems are addressed with discrete mathematics. The forward problem results in convenient consolidation charts that can be used to compute the diffusion of excess pore pressure for various common engineering cases. In addition, it is shown that the spatially varying coefficient of consolidation can be found as the solution of an inverse problem when excess pore pressure profiles are measured.

Chapter IV introduces the concept of terminal density and reconsiders common geotechnical properties in this framework. Furthermore, new experimental data are presented to corroborate the underlying hypothesis.

Chapter V presents a comprehensive laboratory and field soil characterization study of a test site where blast densification is attempted. Then, Chapter VI documents the multi-instrumented case history of ground densification by blasting. This full-scale test lasts one and a half years and includes four blasting events. The extensive database collected during this study is analyzed in the context of lessons learned from previous chapters.

Finally, salient conclusions and recommendations for further research are summarized in Chapter VII.

CHAPTER II

SPATIAL VARIABILITY AND CONDUCTION PHENOMENA

2.1 INTRODUCTION

The presence of fluids affects all aspects of soil behavior, including chemical, mechanical, and biological processes. The understanding of fluid flow through porous media starts in the eighteenth century. Daniel Bernoulli (1700-1782) recognizes the importance of total-energy based analysis. Following the work by Pierre Laplace (1749-1827), Claude-Louis Navier (1785-1836) presents in 1823 the differential equations for pressure and velocity in unsteady three-dimensional viscous flow, which later becomes the Navier-Stokes equations. Jean Louis Poiseuille (1799-1869) and Gotthilf Hagen (1797-1884) study low-velocity flow in capillary tubes. Although they work independently from each other, they arrive at a similar semi-empirical equation of surprising accuracy (the Hagen-Poiseuille equation), later corroborated with the analytical solution based on Newton's viscosity law published by Wiedman in 1859 and by Neumann and E. Hagenbach in 1860 (Rouse and Ince 1957; Sutera 1993). These formulations form the basis for Darcy's findings (Brown 2002). In 1856, Henry Darcy (1803-1858) realizes that the rate of seepage q (volume/time) through a cross-sectional area A can be considered to be linearly proportional to the hydraulic gradient i; in other words, $v = q/A = k \cdot i$, where v is the effective flow velocity and k is the hydraulic

conductivity. Darcy's law applies in the laminar regime, which occurs for a Reynolds number $R<20$ (R is the relation between inertial and viscous forces; $R = v \cdot d_e / v$, where v is the velocity of the fluid, d_e is the effective diameter of the soil skeleton and v is the cinematic viscosity of water).

The general form of Laplace's equation is obtained by combining Darcy's law in the three directions x, y and z (with hydraulic conductivities k_x, k_y and k_z), Bernoulli's energy equation, and the change in volume in soils as functions of degree of saturation S and void ratio e (Richards 1931),

$$k_x \cdot \frac{\partial^2 h}{\partial x^2} + k_y \cdot \frac{\partial^2 h}{\partial y^2} + k_z \cdot \frac{\partial^2 h}{\partial z^2} = \frac{1}{1+e} \cdot \left(e \cdot \frac{\partial S}{\partial t} + S \cdot \frac{\partial e}{\partial t} \right) \qquad (2.1)$$

where h is the total head. The values of e and S determine the flow regimes and are summarized in Table 2.1.

The special case of Equation 2.1 for steady state flow (e and S constant) in isotropic media ($k_x = k_y = k_z$) leads to $\nabla^2 h = 0$, independently of the hydraulic conductivity k. In general, the ratio between the horizontal and vertical hydraulic conductivity ranges between 1 and 10 (Lambe and Whitman 1969; Al-Khafaji and Andersland 1992).

Flow conditions described by Equation 2.1 cover a wide range of engineering problems: 1) the determination of rate of flows q, particularly important in dams, in construction under the water table, environmental treatments and petroleum engineering;

Table 2.1. Special cases of the generalized Laplace's equation (based on Lambe and Whitman 1969).

e and S functions	Equation	Comments
both e and S constant.	$$k_x \cdot \frac{\partial^2 h}{\partial x^2} + k_y \cdot \frac{\partial^2 h}{\partial y^2} + k_z \cdot \frac{\partial^2 h}{\partial z^2} = 0$$	Steady state flow.
both e and S constant, and isotropic k	$$\frac{\partial^2 h}{\partial x^2} + \frac{\partial^2 h}{\partial y^2} + \frac{\partial^2 h}{\partial z^2} = 0$$	Steady state flow. Laplace's equation. The flow lines intersect at right angles with equipotential lines.
e varies and S constant.	$$k_x \cdot \frac{\partial^2 h}{\partial x^2} + k_y \cdot \frac{\partial^2 h}{\partial y^2} + k_z \cdot \frac{\partial^2 h}{\partial z^2} = \frac{1}{1+e} \cdot \left(S \cdot \frac{\partial e}{\partial t} \right)$$	Consolidation (e decreases) or expansion (e increases).
e constant and S varies	$$k_x \cdot \frac{\partial^2 h}{\partial x^2} + k_y \cdot \frac{\partial^2 h}{\partial y^2} + k_z \cdot \frac{\partial^2 h}{\partial z^2} = \frac{1}{1+e} \cdot \left(e \cdot \frac{\partial S}{\partial t} \right)$$	Constant volume drainage (S decreases) or imbibition (S increases).
both e and S vary.	$$k_x \cdot \frac{\partial^2 h}{\partial x^2} + k_y \cdot \frac{\partial^2 h}{\partial y^2} + k_z \cdot \frac{\partial^2 h}{\partial z^2} = \frac{1}{1+e} \cdot \left(e \cdot \frac{\partial S}{\partial t} + S \cdot \frac{\partial e}{\partial t} \right)$$	Complex compression and expansion problems.

2) the determination of total heads *h*, which implies assessment of pore pressures and subsequently, effective stress in soils, 3) the determination of the seepage forces and uplift pressures, which can produce failures.

The hydraulic conductivity *k* of a soil depends on the size of pores, their spatial distribution and connectivity which in turn is a function of the grain size distribution, particle shape, and soil fabric.

Fluid flow is also affected by the spatial variability of the hydraulic conductivity *k(x,y,z)*. This is the central theme of this chapter, where analytical, experimental and numerical techniques are used to explore the implications of spatial variability in seepage.

2.2 ANALYTICAL SOLUTIONS

The equivalent hydraulic conductivity is used to represent a non-homogeneous medium by means of a homogeneous medium that allows equal flow through (see for example, Cardwell and Parsons, 1945; Warren and Price, 1961). An alternative criterion is equal energy dissipated by the viscous forces in both the real non-homogeneous medium and the equivalent one. Bøe (1994) shows that both the equal flow and the equal dissipated energy criteria are equivalent for periodic boundary conditions.

Extensive reviews of upscaling theories, theoretical bounds, analytical solutions, and numerical techniques can be found in Wen and Gómez-Hernández (1996) and Renard and de Marsily (1997). Some of the most important solutions are summarized next.

2.2.1 Bounds

Given a medium with two phases of known hydraulic conductivity, k_0 and k_1, and known volume fractions of those phases, f_0 and f_1, it is possible to identify upper and lower hydraulic conductivity bounds for an equivalent homogeneous medium with equivalent hydraulic conductivity $k_{equivalent}$. Table 2.2 summarizes such bounds. Figure 2.1 shows a comparison of the equivalent hydraulic conductivity bounds for a binary medium with hydraulic conductivity three orders of magnitude different ($k_1/k_0 = 1000$). The ranges for $k_{equivalent}$ given by Matheron bounds are narrower that the ones given by other bounds.
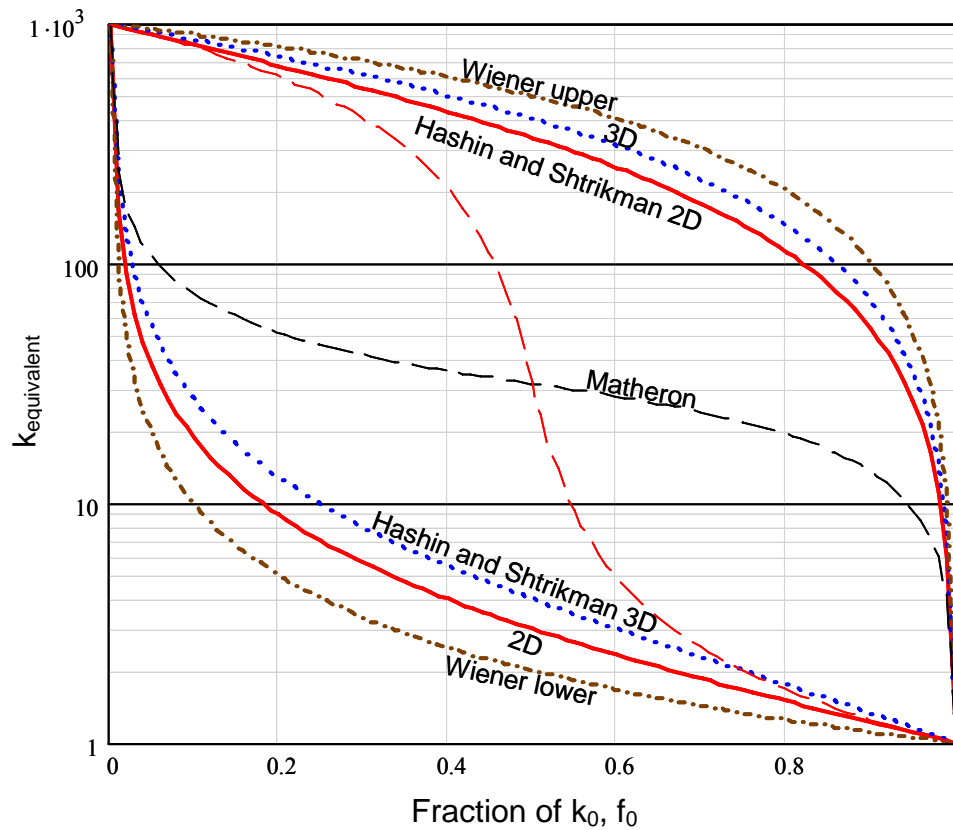
Figure 2.1. Equivalent hydraulic conductivity bounds. Comparison for a case where k_1/k_0 is 1000.

Table 2.2. Bounds for the equivalent hydraulic conductivity.

Inequality	Assumptions / Notes	Key reference
$\mu_h = \dfrac{1}{\dfrac{f_0}{k_0} + \dfrac{f_1}{k_1}} \le k_{eq} \le f_0 \cdot k_0 + f_1 \cdot k_1 = \mu_a$	Uniform flow. Exact analytical solutions for Ene bounds.	Wiener (1912)
$\mu_h^x(\mu_a^z(\mu_a^y)) \le k_{eq}^{xx} \le \mu_a^z(\mu_a^y(\mu_h^x))$	The upper bound is given by the harmonic mean of the arithmetic means of k, calculated over each slice of a cell perpendicular to the given direction x, y or z. Uniform flow.	(Cardwell and Parsons, 1945)
$\mu_a - \dfrac{f_1 f_0 (k_1 - k_0)^2}{k_0 (D - f_0) + k_1 f_0} \le k_{eq} \le \mu_a - \dfrac{f_1 f_0 (k_1 - k_0)^2}{k_1 (D - f_1)^2 + k_0 f_1}$	Based on a model constructed of composite spheres. Isotropic binary medium. Uniform flow	Hashin and Shtrikman (1962)
$if\ f_0 \ge 0.5 \Rightarrow k_{eq} \ge k_{ac}$ $if\ f_0 \le 0.5 \Rightarrow k_{eq} \le k_{ac}$ $if\ f_0 = 0.5 \Rightarrow k_{eq} = \sqrt{k_1 \cdot k_0}$ where $k_{ac} = \dfrac{1}{2}\left[(f_1 - f_0)(k_1 - k_0) + \sqrt{(f_1 - f_0)^2 (k_1 - k_0)^2 + 4 k_1 k_0} \right]$	Lower bound. Isotropic 2D random two phase mosaic medium. Uniform flow.	Matheron (1967)

Table 2.2 Continued. Bounds for equivalent hydraulic conductivity.

Inequality	Assumptions / Notes	Key reference
if $f_0 \geq 0.5 \Rightarrow k_{eq} \leq k_m$ $$k_m = \frac{f_1 k_0 k_1 + f_0 \mu_a \sqrt{k_0(2\mu_a - k_0)}}{f_1 m^* + f_0 \sqrt{k_0(2\mu_a - k_0)}}$$ if $f_0 \leq 0.5 \Rightarrow k_{eq} \geq k_m$ $$k_m = k_0 k_1 \frac{f_0 \mu_a + f_1 \sqrt{k_0(2m^* - k_0)}}{f_1 k_0 k_1 + f_1 m^* \sqrt{k_0(2m^* - k_0)}}$$	Upper bound. Isotropic 2D random two phase mosaic medium. Uniform flow.	Matheron (1967)
Method of homogenization is used.	Requires the numerical solution of a system of differential equations. Periodic medium and flow.	Ene Bounds

k_{eq} = equivalent hydraulic conductivity; μ_a =arithmetic mean; μ_h =harmonic mean; f_0 and f_1 are the fractions of the medium with hydraulic conductivity k_0 and k_1, where $k_1 > k_0$, D=space dimension (i.e., 1, 2 or 3); $\mu_h^x(g)$ =harmonic mean in the x direction of some function g; $m^* = f_1 \cdot k_0 + f_0 \cdot k_1$; and $\sigma^2 = f_1 \cdot f_0 \cdot (k_1 - k_0)^2$.

2.2.2 Closed form solutions and approximations

The most important closed form solutions are summarized in this section. Mathematical approximations are also included.

Stratified media. Typically, the hydraulic conductivity of sedimentary soils varies vertically. The upper and lower Wiener bounds constitute the exact values of the equivalent hydraulic conductivity in the case of a stratified medium with flow parallel or perpendicular to the strata respectively (Dagan 1989; Renard et al. 2000). Consider the horizontally layered system shown in Figure 2.2, the flow normal to the strata resembles a system in series, where, by continuity, the flow rate q through the area A remains constant across layers. Therefore, the head loss is:

$$\Delta h = \frac{q \cdot t_1}{A \cdot k_1} + \cdots + \frac{q \cdot t_i}{A \cdot k_i} + \cdots + \frac{q \cdot t_N}{A \cdot k_N} \tag{2.2}$$

and the equivalent hydraulic conductivity is the harmonic mean:

$$k_v = \frac{t_1 + \cdots + t_i + \cdots t_N}{\dfrac{t_1}{k_1} + \cdots + \dfrac{t_i}{k_i} + \cdots + \dfrac{t_N}{k_N}} = \frac{\displaystyle\sum_{i=1}^{N} t_i}{\displaystyle\sum_{i=1}^{N} \dfrac{t_i}{k_i}} = \mu_h \tag{2.3}$$

If the flow is parallel to the stratification, the head loss Δh over the same flow path length Δs is the same in each layer, $i_1 = i_i = i_N$. The flow rate through a layered block of soil of with B is:

$$q = B \cdot t_1 \cdot k_1 \cdot i_1 + \cdots + B \cdot t_i \cdot k_i \cdot i_i + \cdots + B \cdot t_N \cdot k_N \cdot i_N \tag{2.4}$$

and the equivalent hydraulic conductivity is the arithmetic mean:

11

$$k_h = \frac{t_1 \cdot k_1 + \cdots + t_i \cdot k_i + \cdots t_N \cdot k_N}{t_1 + \cdots + t_i + \cdots t_N} = \frac{\sum_{i=1}^{N} t_i \cdot k_i}{\sum_{i=1}^{N} t_i} = \mu_a \qquad (2.5)$$
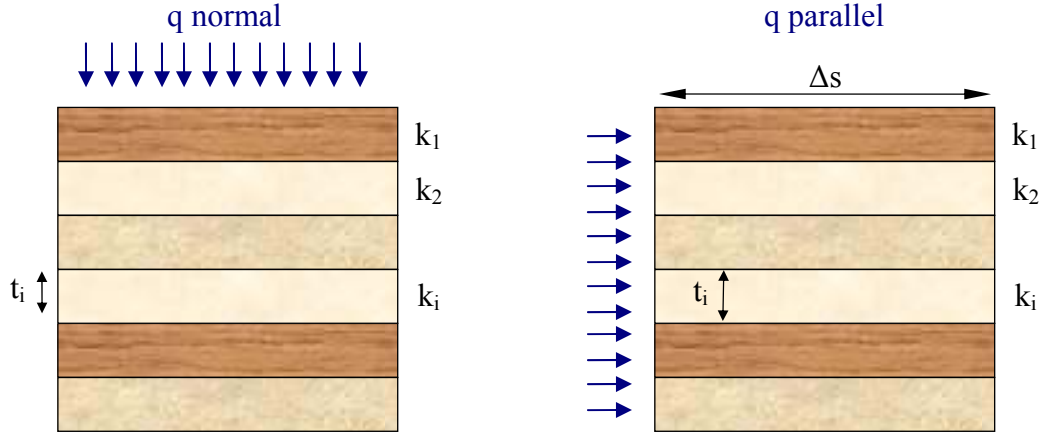
Figure 2.2. Stratified soils. Fluid flow normal and parallel to the stratification.

Percolation theory. Percolation theory refers to problems of connectivity across complex systems, and it has been frequently applied to binary materials, i.e., materials with two phases one of which is non-permeable. If f_1 is the volume fraction of the permeable medium, then, close to the percolation threshold f_c:

$$f_1 < f_c \rightarrow k_{equivalent} = 0$$
$$f_1 > f_c \rightarrow k_{equivalent} = A \cdot (f_1 - f_c)^{\mu} \qquad (2.6)$$

where μ depends on the space dimension (2D versus 3D) and A and f_c depend on the geometry of the network according to Table 2.3 (Berkowitz and Balberg 1993).

Table 2.3. Percolation theory coefficients (after Renard and de Marsily 1997).

Type of medium	A	f_c	M	Given by
2D isotropic		0.5	1.1	Sykes and Essam (1964)
2D	Depends on medium		1.1	de Gennes (1976)
3D	Depends on medium		1.6	de Gennes (1976)
	Depends on medium		1.8	Guyon et al. (1984)

Effective medium theory. The effective medium theory is also known as self-consistent approach, or the embedded matrix method. A heterogeneous medium constituted by contiguous homogeneous hydraulic conductivity blocks is first replaced by a homogeneous matrix with unknown hydraulic conductivity k_o and with only one single inclusion block of hydraulic conductivity k_1 embedded in it. Assuming the boundary conditions far enough, the hydraulic gradient and the flow are constant (Renard and de Marsily 1997). The analytical solution is found for this new medium. Then, other inclusions are gradually added at each step, under the hypothesis that the new inclusions do not interfere with the perturbations caused by other inclusions. Dagan (1989), found that for a binary medium with spherical inclusions the equivalent hydraulic conductivity is:

$$k_{equivalent} = \frac{1}{D}\left[\frac{f_0}{k_0 + (D-1)\cdot k_{equivalent}} + \frac{f_1}{k_1 + (D-1)\cdot k_{equivalent}} \right]^{-1} \qquad (2.7)$$

where f_0 and f_1 are the volume fractions of materials with hydraulic conductivity k_0 and k_1, where $k_1 > k_0$, and D represents the space dimension (i.e., 1, 2 or 3). This equation can be numerically solved. There exist more complex formulae for ellipsoidal and lens-shaped inclusions (Poley 1988; Dagan 1989; Fitts 1991; Dagan and Lessof 2001).

13

Renormalization. This recursive algorithm first proposed by King (1989), progressively converts a mesh of $2^{n.D}$ cells into $2^{[(n-1).D]}$ cells, until a mesh of only 1 cell is found (Figure 2.3). The equivalent hydraulic conductivity is calculated by successive aggregations on groups of four cells (in 2D, or eight in 3D) at each step using an electrical circuit analogy.

$$\text{Step 0,} \qquad \text{Step 1,} \qquad \text{Step 2,} \qquad \text{Step 3,}$$
$$2^{n\cdot D}=2^{3\cdot2}=64 \qquad 2^{2\cdot2}=16 \qquad 2^{1\cdot2}=4 \qquad 2^{0\cdot2}=1$$
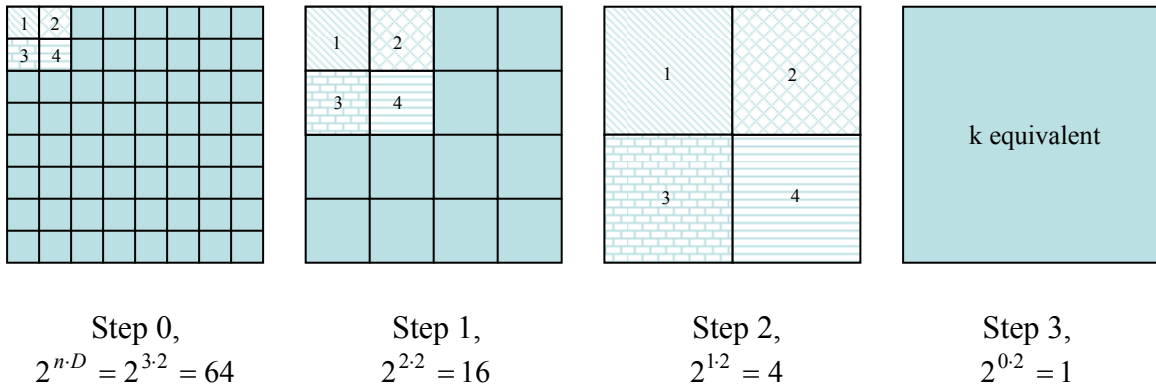
Figure 2.3. Renormalization example (with n=3 and D=2 , two dimensions).

This electrical analogy has constant head on two opposite faces and zero flow on the other faces which leads to harmonic means. Following this approach, the solution for a 2D problem in one direction consisting of four-cells is (Figure 2.4):

$$k^{xx}=\frac{4(k1+k3)(k2+k4)\left[k2\cdot k4(k1+k3)+k1\cdot k3(k2+k4)\right]}{\left[k2\cdot k4(k1+k3)+k1\cdot k3(k2+k4)\right]\cdot\left[k1+k2+k3+k4\right]+3(k1+k2)(k3+k4)(k1+k3)(k2+k4)}$$

$$(2.8)$$

Four-cell permeabilities   Direct analogue   Centered analogue
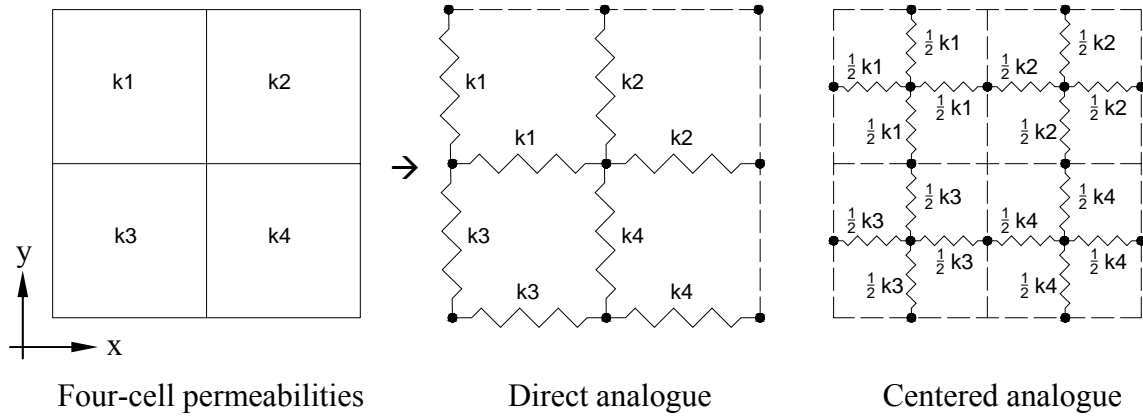
Figure 2.4. Electrical analogues to compute the equivalent hydraulic conductivity for an elementary cell in 2D.

A simplified renormalization technique groups cells alternatively in series and in parallel, and replaces them by single cells whose conductivity is the harmonic mean μ_h if the two original cells are in series, or by the arithmetic mean μ_a if the two original cells are in parallel (Le Loc'h 1987; Renard et al. 2000). Consider the case in Figure 2.5, for a 2D system, start grouping in series along the x direction, then group the new pairs in parallel along the y direction, and repeat this procedure until a single cell is obtained:

$$c_{\min}^{xx} = \mu_a^y (\ldots \mu_a^y (\mu_h^x) \ldots) \tag{2.9}$$

then, create groups starting in parallel along the y direction, and group the new pairs in series along the x direction, and repeat this process until the cell is obtained:

$$c_{\max}^{xx} = \mu_h^x (\ldots \mu_h^x (\mu_a^y) \ldots) \tag{2.10}$$

15

Finally, the equivalent hydraulic conductivity is computed with the technique of an exponent α varying between 0 and 1:

$$k_{equivalent}^{xx} \approx c^{xx} = \left(c_{max}^{xx}\right)^{\alpha} \left(c_{min}^{xx}\right)^{1-\alpha} \qquad \alpha \in [0,1] \qquad (2.11)$$
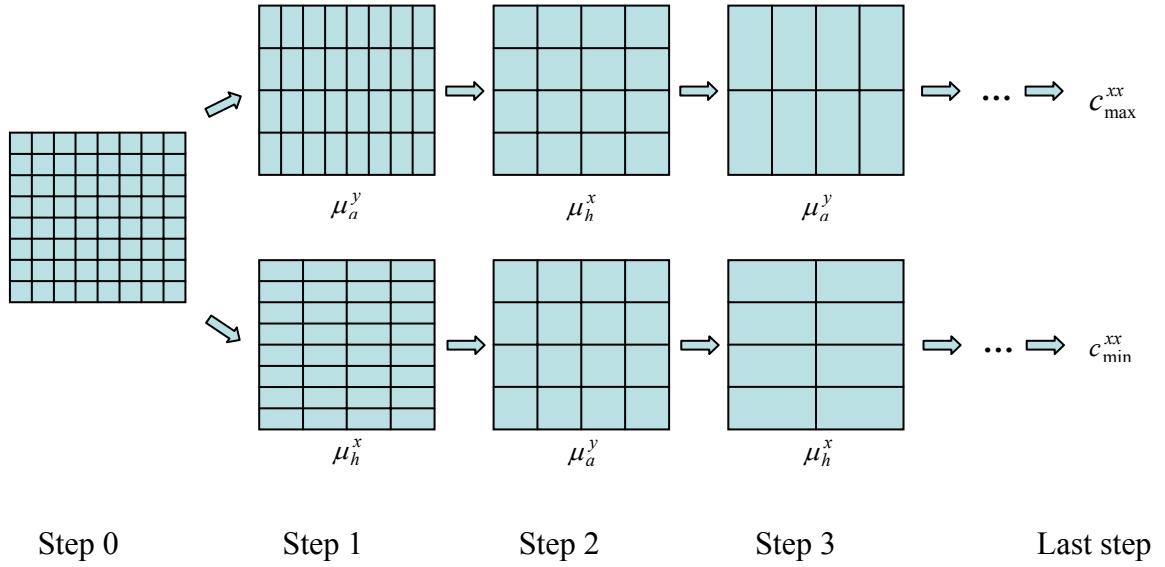
Figure 2.5. Simplified renormalization for computing the equivalent hydraulic conductivity in the x direction. Example.

Landau-Lifshitz-Matheron approximation and the geometric mean. Landau and Lifshitz (1960) and Matheron (1967) propose a first order approximation to the hydraulic conductivity for uniform flow in isotropic and stationary porous media:

$$k_{equivalent} = \mu_a^{\frac{(D-1)}{D}} \cdot \mu_h^{\frac{1}{D}} \qquad (2.12)$$

where μ_a and μ_h are the arithmetic and the harmonic mean, and D represents the space dimension (i.e., 1, 2 or 3). Numerical experiments show good agreement with this

16

solution for uncorrelated random media with lognormal distribution of k even for high variances.

The geometric mean $\mu_g = \left(\prod_{i=1}^{n} k_i\right)^{1/n}$ is the exact equivalent hydraulic conductivity in an infinite two-dimensional medium with a chessboard pattern of k, it is also the exact solution for a lognormal isotropic medium whenever the normalized local hydraulic conductivities $k/E(k)$ and their inverses $k^{-1}/E(k^{-1})$ have the same probability density function which is invariant by $\pi/2$ rotation, and the flow is uniform (Matheron, 1967; $E(x)$ is the expected value of x).

2.3 EXPERIMENTAL STUDY

An experimental study is implemented to study the equivalent hydraulic conductivity of mixtures and heterogeneous porous media. A rigid wall constant head permeameter is used. Details of these experimental studies follow.

2.3.1 Homogeneous mixtures

Two different uniform soils are selected to study the hydraulic conductivity of homogeneous mixtures using constant head permeametry (ASTM D 2434). The first one is Ottawa F-50 (US Silica Company named F-50; average hydraulic conductivity k=0.01 cm/sec, $D_{10} \cong 0.18$ mm, $C_u \cong 1.8$). The second one is Ottawa S-140, and it is obtained by sieving Ottawa F-110 between standard sieves #100 (150 μm) and #140 (106 μm, ASTM E11-95; average hydraulic conductivity k=0.00125 cm/s, $D_{10} \cong 0.11$ mm, $C_u \cong 1$). Figure 2.6 shows the grain size distribution of these soils as well as the grain size distributions for the mixtures used herein.
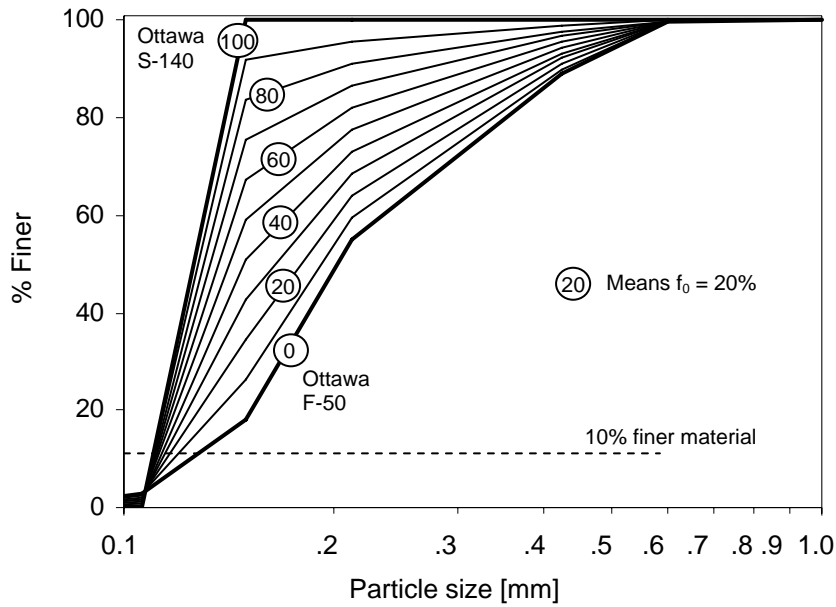
Figure 2.6. Grain size distributions – Soils used and mixtures.

The filter ratios $D_{15}^{F-50}/D_{85}^{S-140} = 2.8$ and $D_{15}^{F-50}/D_{15}^{S-140} = 1.6$, together with $D_{50}^{F-50}/D_{50}^{S-140} = 3$ indicate that mixtures are self filtering and no migration of fines should be expected (Terzaghi and Peck 1967; Valdes 2002)

Mixtures are prepared for different mass fractions and thoroughly mixed under dry conditions. The permeameter cell is 0.22 m height and 0.10 m in diameter. The permeameter diameter is large enough to minimize the influence of boundary flow along annulus packing of 3 to 5 particle diameters against the wall. Specimens are built in 0.5 cm layers, and compacted by rodding (60 times per layer). In order to avoid trend bias, the sequence of hydraulic conductivity tests is randomized (Table 2.4).

Table 2.4. Mixtures. Randomized sequence of tests.

Sequence of test	Material A [% in weight]	Material B [% in weight]
1	90	10
2	40	60
3	70	30
4	10	90
5	60	40
6	50	50
7	80	20
8	30	70
9	70	30
10	20	80

Figure 2.7 shows the mixture hydraulic conductivity against the mass fraction f_0 of the soil component with smaller hydraulic conductivity (i.e. F-50 sand). The evolution of void ratio of the different mixtures is also shown in Figure 2.7. A sensible drop in the equivalent hydraulic conductivity is observed when $f_0 > \sim 20\%$.
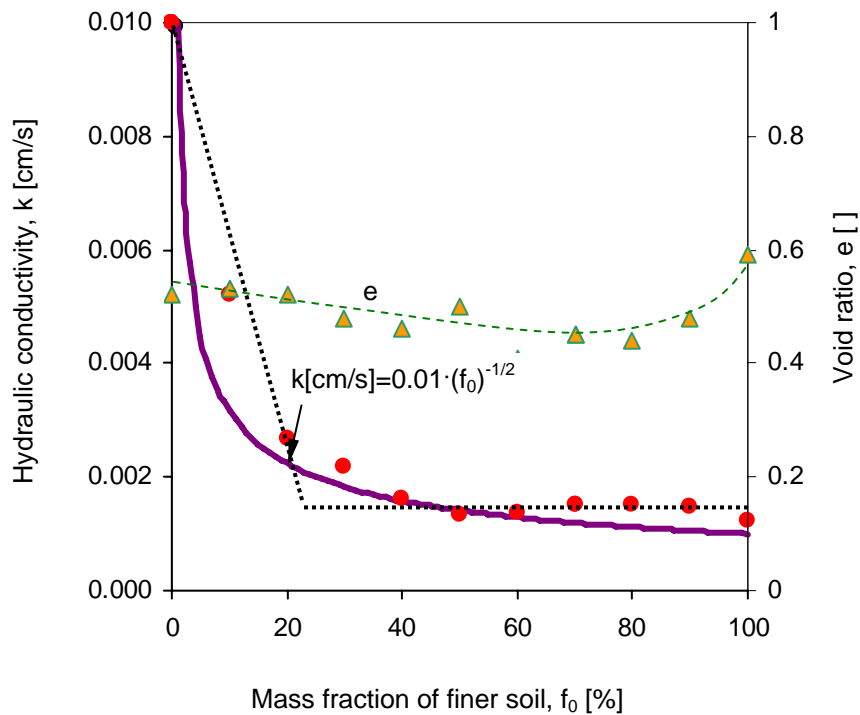
Figure 2.7. Equivalent hydraulic conductivity of mixtures. Experimental study and the two proposed models (data gathered in collaboration with J. Kammoe). The void ratio of each test is also shown.

19

2.3.2 Heterogeneous media

Two sets of heterogeneous systems are prepared and tested using the same permeameter cell and test procedure. The first set involves layered media. The second set corresponds to a homogeneous medium with a cylindrical inclusion. Each measurement is repeated twice with the same specimen. Table 2.5 shows the geometry and soil types for each test, measured results and simple estimates based on the expressions presented earlier.

Data and analytical predictions in Table 2.5(a) show that the hydraulic conductivity of stratified soils is adequately approximated by the harmonic mean which is the exact solution for layered media.

The effect of cylindrical inclusions is studied using various inclusion sizes and media. There exists a fixed relation between the radius and the length of the inclusion. The infinite hydraulic conductivity is modeled using a wire mesh covered by a textile filter.

Data in Table 2.5(b) show that while the hydraulic conductivity ratio between the host medium and the inclusion may be high, the measured equivalent hydraulic conductivity remains similar the the hydraulic conductivity of the host medium for the selected geometry. While there is no closed-form solution for this geometry, values predicted with (1) a simple series/parallel/series model, (2) a parallel/series/parallel model and (3) a Landau-Lifshitz-Matheron approximation, are of the same order of magnitude as measured values.

Table 2.5. Homogeneous specimens (data gathered in collaboration with J. Kammoe).

Specimen	Measured	Analytical model prediction
a) Layered systems — q normal, k_1 (7.5), k_2 (15.0)	0.00333cm/s	$\mu_h = k_v = \dfrac{7.5cm + 15.0cm}{\dfrac{7.5cm}{0.00125cm/s} + \dfrac{15.0cm}{0.01324cm/s}} = 0.00315cm/s$
k_2 (10.0), k_1 (12.5)	0.00302cm/s	$k_v = \dfrac{10.0cm + 12.5cm}{\dfrac{10cm}{0.01324cm/s} + \dfrac{12.5cm}{0.00125cm/s}} = 0.002092cm/s$
k_2 (5.0), k_1 (6.0), k_2 (6.5), k_1 (5.5)	0.00258cm/s	$k_v = \dfrac{5cm + 6cm + 6.5cm + 5.5cm}{\dfrac{5cm}{0.01324cm/s} + \dfrac{6cm}{0.00125cm/s} + \dfrac{6.5cm}{0.01324cm/s} + \dfrac{5.5cm}{0.00125cm/s}}$ $= 0.002284cm/s$ *Where k_1=0.0125cm/s and k_2=0.0134cm/s*

Dimensions in cm
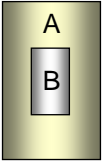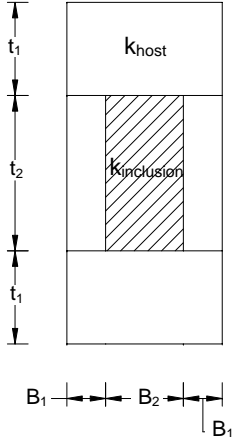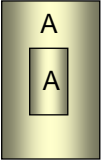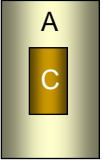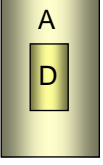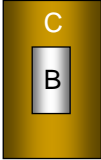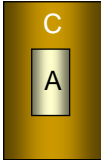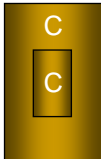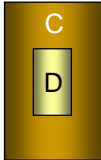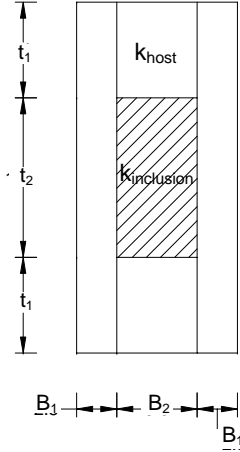
Table 2.5 Continued.

b) Cylindrical inclusion

Specimen	Measured k_{ef} [cm/s]	Analytical model prediction	
A B	0.00156 0.00156 0.00156 (average)	k_h=0.00449 k_a=0.00347 k_{Landau}=0.00378	(1)
A A	0.00241 0.00242 0.00255 0.00241 0.00245 (average)	$k_h=k_a=k_{Landau}$=0.00245	
A C	0.00347 (discarded) 0.00372 (discarded) 0.00256 0.00253 0.00255 (average)	k_h=0.00382 k_a=0.00327 k_{Landau}=0.00344	$$k_h = \dfrac{2t_1 + t_2}{\dfrac{2t_1}{k_{host}} + \dfrac{t_2 \cdot (2B_1 + B_2)}{2B_1 k_{host} + B_2 k_{inclusion}}}$$
A D	0.00241 0.00242 0.00255 0.00241 0.00245 (average)	k_h=0.00168 k_a→0.00122 k_{Landau}→0.00136	

Table 2.5 Continued

------------ b) Cylindrical inclusion ------------

Specimen	Measured	Analytical model prediction [cm/s]
C / B	0.01136 0.01149 0.01143(average)	k_h=0.038 k_a=0.029 k_{Landau}=0.032
C / A	0.01114 0.01106 0.01101 0.01108 0.01107 (average)	k_h=0.015 k_a=0.013 k_{Landau}=0.014
C / C	0.02084 0.02103 0.02047 0.02095 0.02082 (average)	k_h=k_a=k_{Landau}=0.02082
C / D	0.01914 0.01858 0.01886 (average)	k_h=0.014 k_a→0.01 k_{Landau}→0.012
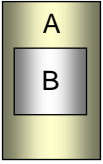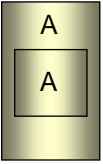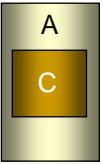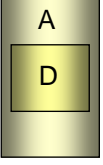
(2)

$$k_a = \frac{2B_1 k_{host} + \dfrac{B_2 \cdot (2t_1 + t_2)}{\dfrac{2t_1}{k_{host}} + \dfrac{t_2}{k_{inclusion}}}}{2B_1 + B_2}$$

Hydraulic conductivity of the media: A=0.00245cm/s; B→∞ ; C=0.02082cm/s; and D→0cm/s.

Table 2.5 Continued.
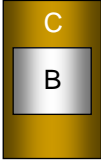
b) Cylindrical inclusion

Specimen	Measured k_{ef} [cm/s]	Analytical model prediction [cm/s]	
A / B	0.00145	k_h=0.00674 k_a=0.005433 k_{Landau}=0.00584	(3) $$k_{Landau} = k_a^{\frac{D-1}{D}} \cdot k_h^{\frac{1}{D}}$$ where *D=3* (3D space)
A / A	0.00245	k_h=k_a=k_{Landau}=0.0245	
A / C	0.00396	k_h=0.00526 k_a=0.00463 k_{Landau}=0.00483	
A / D	0.00535	k_h=0.000998 k_a→0.0007452 k_{Landau}→0.000821	

Table 2.5 Continued.

Specimen	Measured	Analytical model prediction	
C / B	0.00853	k_h=0.057 k_a=0.046 k_{Landau}=0.050	(3) $$k_{Landau} = k_a^{\frac{D-1}{D}} \cdot k_h^{\frac{1}{D}}$$ where $D=3$ (3D space)
C / A	0.00980	k_h=0.01 k_a=0.08843 k_{Landau}=0.009319	
C / C	0.02082	$k_h=k_a=k_{Landau}$=0.02082	
D	0.02693	k_h=0.00848 k_a→0.00633 k_{Landau}→0.00698	

b) Cylindrical inclusion

Hydraulic conductivity of the media: A=0.00245cm/s; B→∞ ; C=0.02082cm/s; and D→0cm/s.

2.4 NUMERICAL STUDY

Numerical simulations of spatial variability of hydraulic conductivity are performed using finite element modeling to extend the scope of the experimental study. Cases in 2D are solved using the Garlekin method to solve the Laplace equation with prescribed total head and flow boundary conditions (Dirichlet and Neumann boundary conditions; the MATLAB code can be found in Appendix A). In both cases, the codes are validated against closed-form solutions for simple geometries. Cases in 3D are solved with COMSOL Multiphysics 3.2. The influence of mesh size is investigated using the COMSOL code and the geometry and materials shown in Figure 2.8. Results in Figure 2.8 suggest a minimum number of ~6000 elements to attain a numerical error <0.1%. Salient results are presented next.
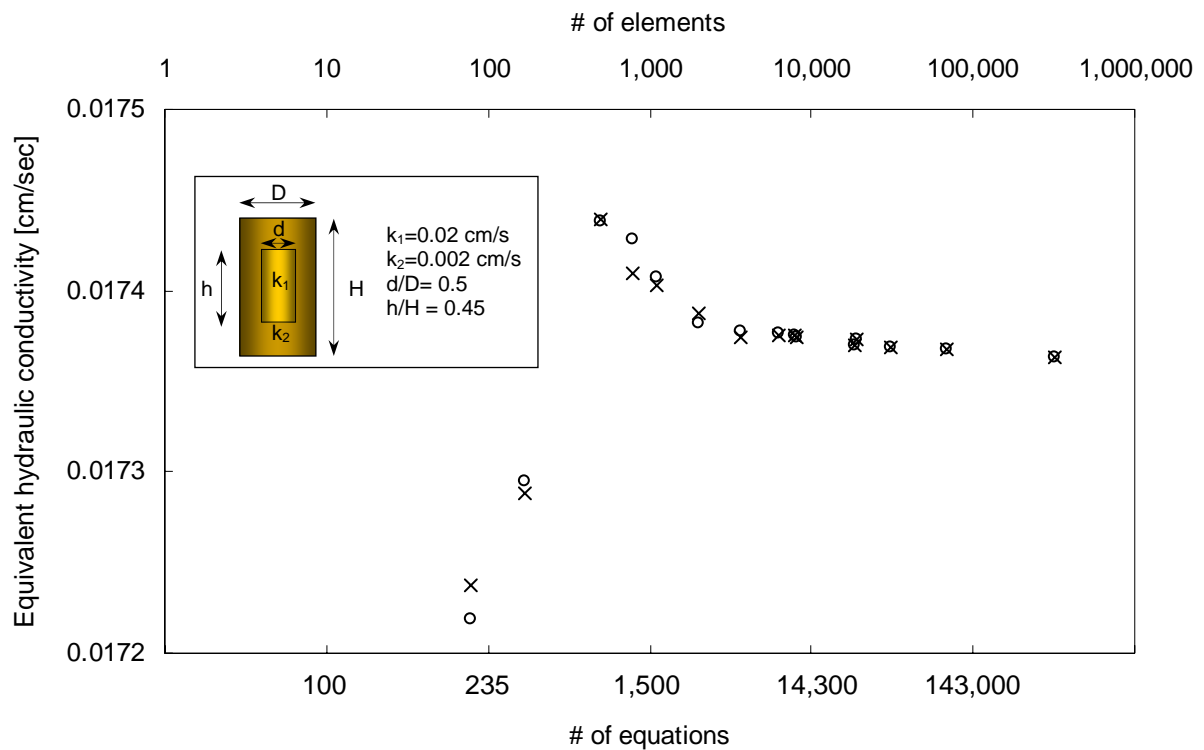
Figure 2.8. Study of mesh size effects.

26

2.4.1 Heterogeneous media

Once the Laplacian is solved using the finite element method, the equivalent hydraulic conductivity is computed by invoking Darcy's law. If q_{el} is the flow through each element on a given equipotential line (e.g. either inlet or outlet surfaces), A is the area of that surface and $\Delta h/L$ is the imposed hydraulic gradient, then the equivalent hydraulic conductivity $k_{equivalent}$ is:

$$k_{equivalent} = \frac{\int_A q_{el} \cdot dA}{\frac{\Delta h}{L} \cdot A} \qquad (2.13)$$

Figure 2.9 shows numerical results for 2D and 3D geometries, for different hydraulic conductivity ratios between inclusion and host medium. For this particular geometry, a 2D analysis gives a result sensibly different from the 3D case. Indeed, axial symmetry does not equate to plane conditions when spatial variability is involved. Therefore, experimental studies need to be properly simulated in their 3D geometries (e.g., Figure 2.10).

Figure 2.11 shows numerically computed equipotential and flow lines on a plane across the center of the modeled specimen (Figure 2.10) for different $k_{inclusion}/k_{host}$ ratios. Fluid flow focuses towards high hydraulic conductivity materials. Zones of relatively higher hydraulic conductivity lead to pressure accumulation upstream and force the flowlines to bend normal to the interfaces generating lateral flows that eventually affect the equivalent vertical hydraulic conductivity. Notice that no transverse flow develops in layered system. Regions of low hydraulic conductivity are subjected to high velocity flow at the interfaces, which may cause local internal erosion and short-circuit flow conditions.
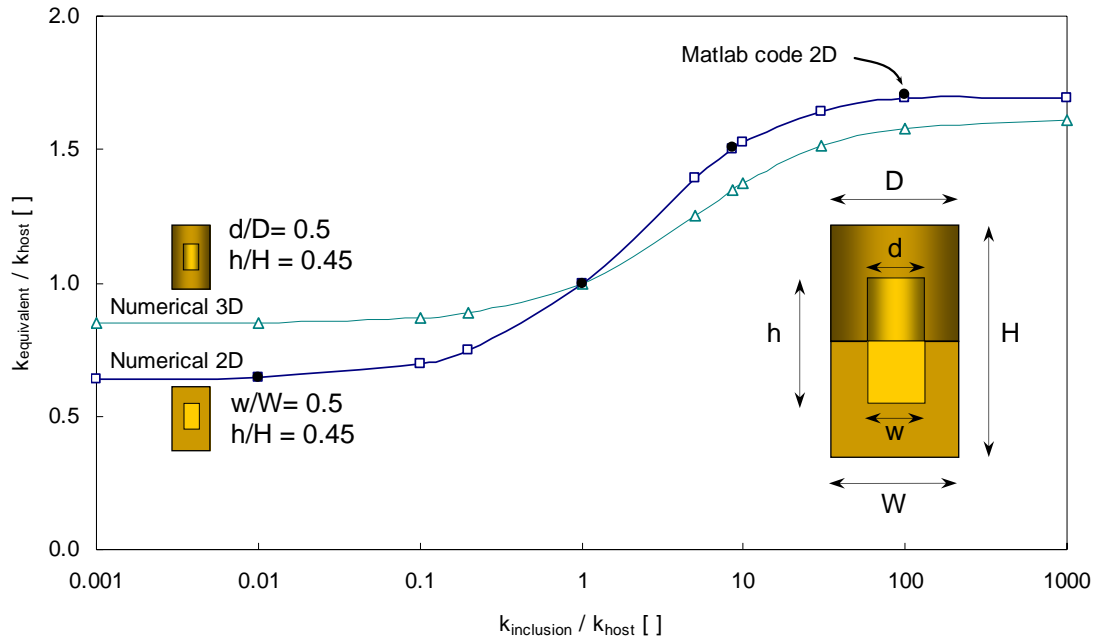
Figure 2.9. Two dimensional and three dimensional systems.
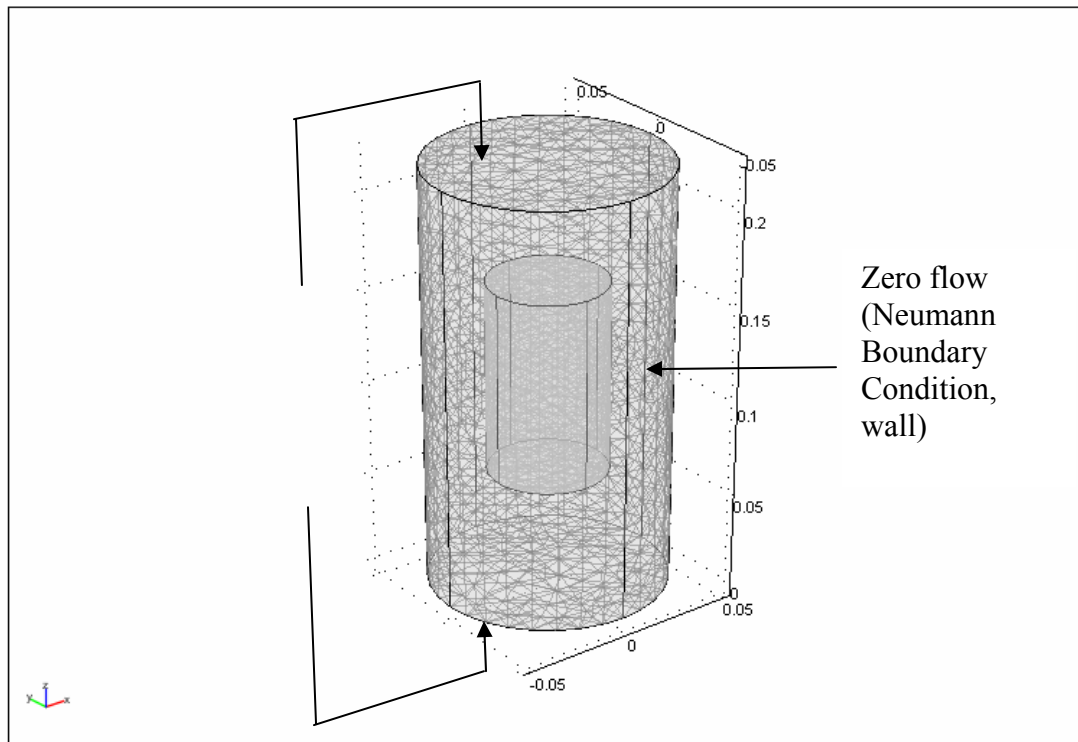
Figure 2.10. Numerical simulations. Specimen with a cylindrical inclusion, a 3-D COMSOL mesh and the boundary conditions. The total head is fixed on the top and bottom faces and no flow is allowed through the external walls.

28

$k_{inclusion} / k_{host} = 100$ 30   10

8   5   0.2

0.1   0.01   0
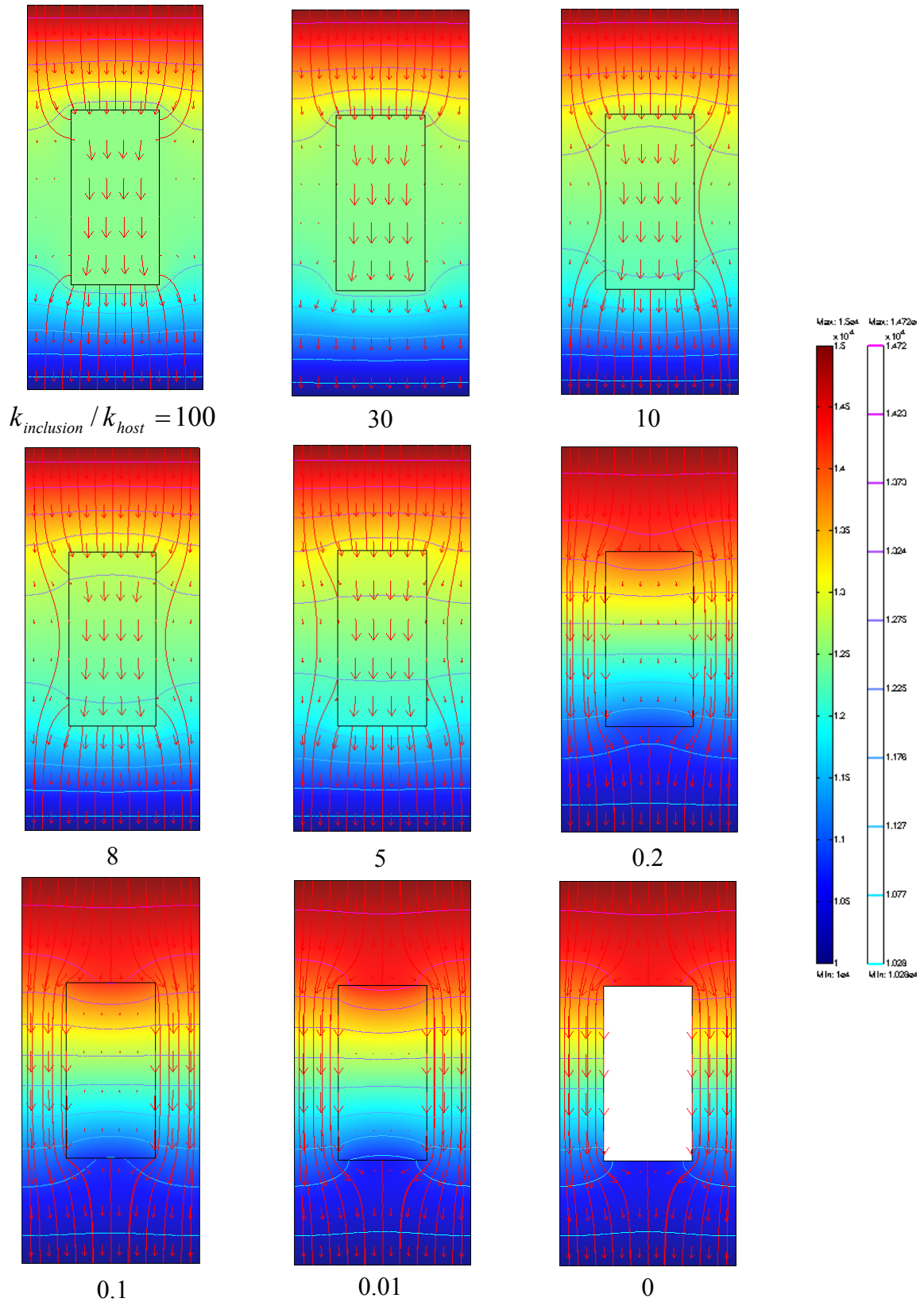
Figure 2.11. Diametral slices of 3D solution. Equipotential surfaces, flow lines, and velocity vectors.

Figure 2.12 shows the equivalent normalized hydraulic conductivity $k_{equivalent}/k_{host}$ for different relative inclusion sizes and various relative hydraulic conductivities $k_{inclusion}/k_{host}$. The relative size $\alpha = (r_{inclusion}/R_{host})^2$ is equal to the area ratio between the inclusion and the specimen. Experimental results with cylindrical inclusions and 3D numerical results are compared in Figure 2.13. Numerical results tend to overestimate the hydraulic conductivity.
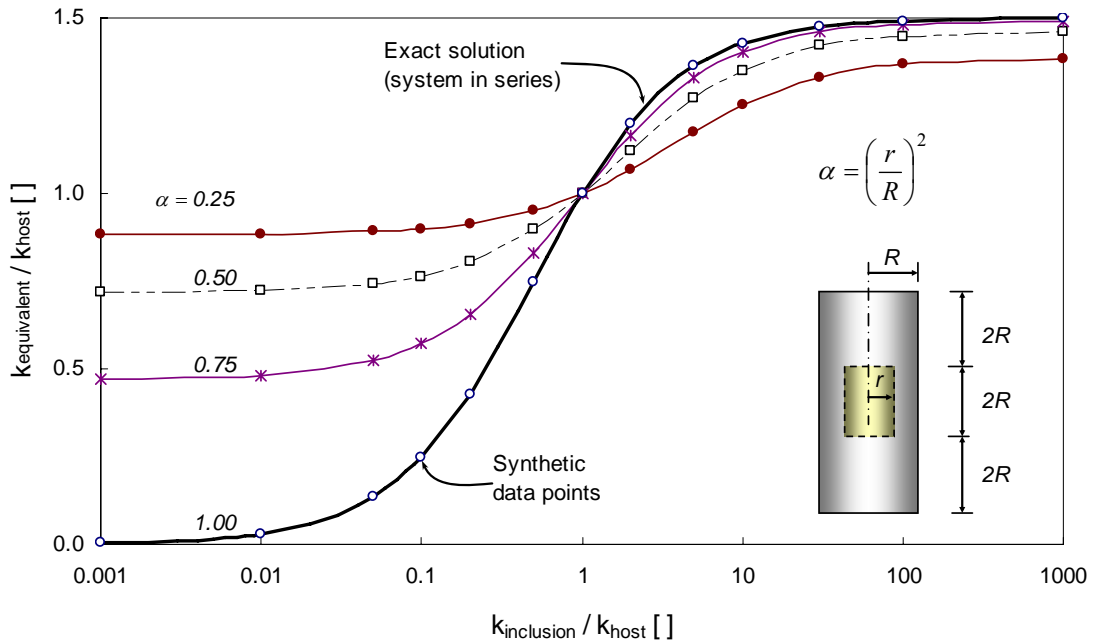
Figure 2.12. 3D Numerical study of equivalent hydraulic conductivity for specimen with cylindrical inclusions.
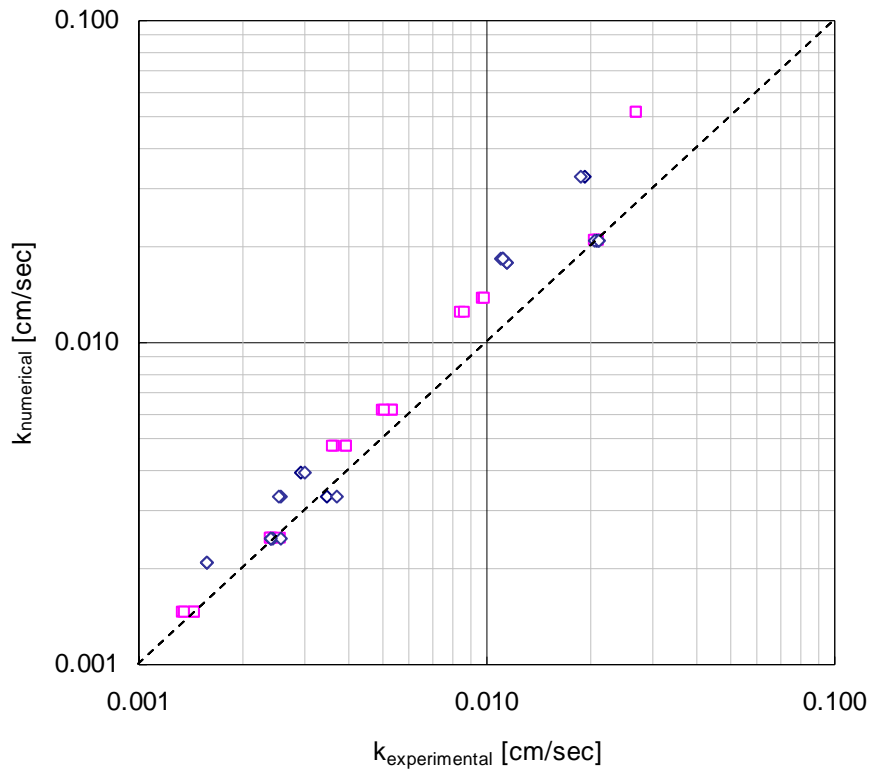
Figure 2.13. Comparison between 3D numerical results and experimental data gathered with cylindrical inclusions (data gathered in collaboration with J. Kammoe).

A possible hypothesis to explain this discrepancy is the potential compounded effect of anisotropy and spatial variability in real specimens. This is explored using the same 3D geometry and boundary conditions of the experiments, but this time imposing cross anisotropy k_h/k_v. Numerical results are summarized in Figure 2.14. Note that the effect of anisotropy on the equivalent hydraulic conductivity is small: even when $k_h/k_v=2$ the difference in $k_{equivalent}$ with respect to the isotropic case is less than 3%.
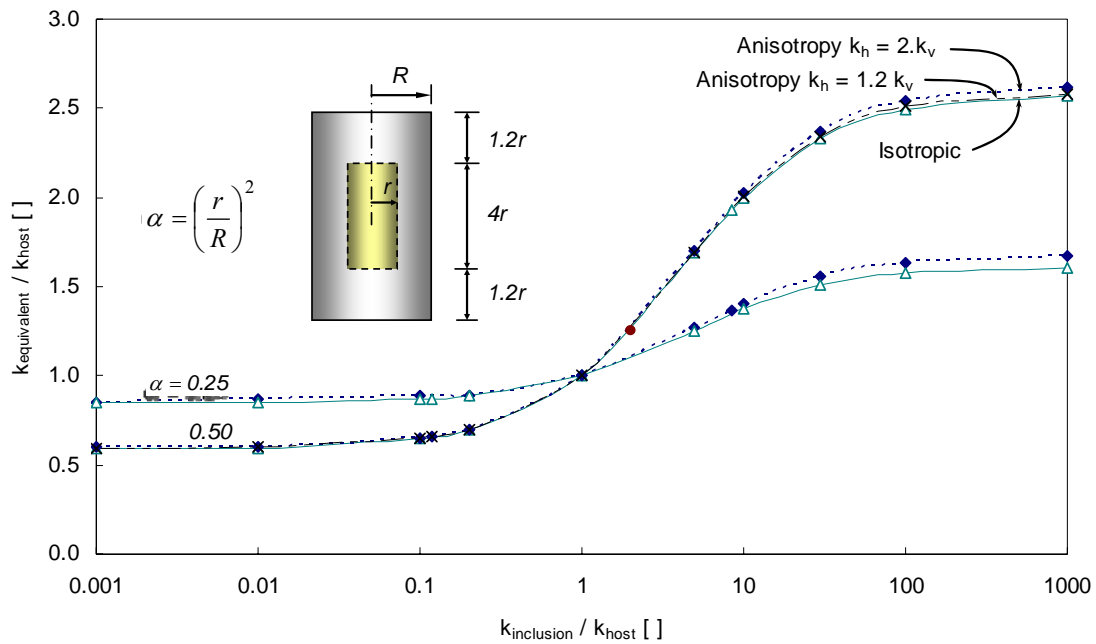
Figure 2.14. Coupling effect of anisotropy and spatial variability.

2.4.2 Correlated random fields

Statistical parameters can be used to capture the variability of hydraulic conductivity, including the central trend $\mu(k)$, standard deviation $\sigma(k)$, the coefficient of variation $COV(k) = \sigma(k)/\mu(k)$, the correlation length L, and anisotropy in variability distributions (Vanmarcke 1977; Kulhawy and Phoon 1996; Phoon and Kulhawy 1999; Kim 2005). Each of these parameters can be identified in each direction. Typical *COV* values for hydraulic conductivity range between *COV*=240 at 80% saturation and *COV*=90 at 100% saturation (Nielsen et al. 1973; Harr 1987).

The correlation length L or autocorrelation length is the distance where the spatial autocorrelation decays by *1/e≅0.368*. The autocorrelation distance for hydraulic conductivity varies from less than a meter to hundreds of meters, and tends to be higher in horizontal than in vertical direction. (Benson; 1991; Bjeng et al.; 1992; Ditmars et al. 1988; see DeGroot 1996 and Lacasse and Nadim, 1996 for detailed compilation).

Multiple realizations of correlated random hydraulic conductivity 2D fields are generated with correlation length $L=$ 20% of the total mesh size using the matrix decomposition technique (El-Kadi and Williams, 2000; see Kim, 2005 for detailed description and implementation). Figure 2.15 shows selected examples. Then, the Laplace equation is numerically solved. The spatial distribution of total head and flow lines are shown in Figure 2.15. Finally, the equivalent hydraulic conductivity is computed following the procedure indicated in Equation 2.13. The variation of the computed equivalent k versus *COV* for both correlated and uncorrelated random fields is shown in Figure 2.16-a. These results highlight the importance of *COV* and correlation on k. Moreover, there is a tendency to obtain higher hydraulic conductivity for uncorrelated fields than for the correlated ones (Figure 2.16-b).
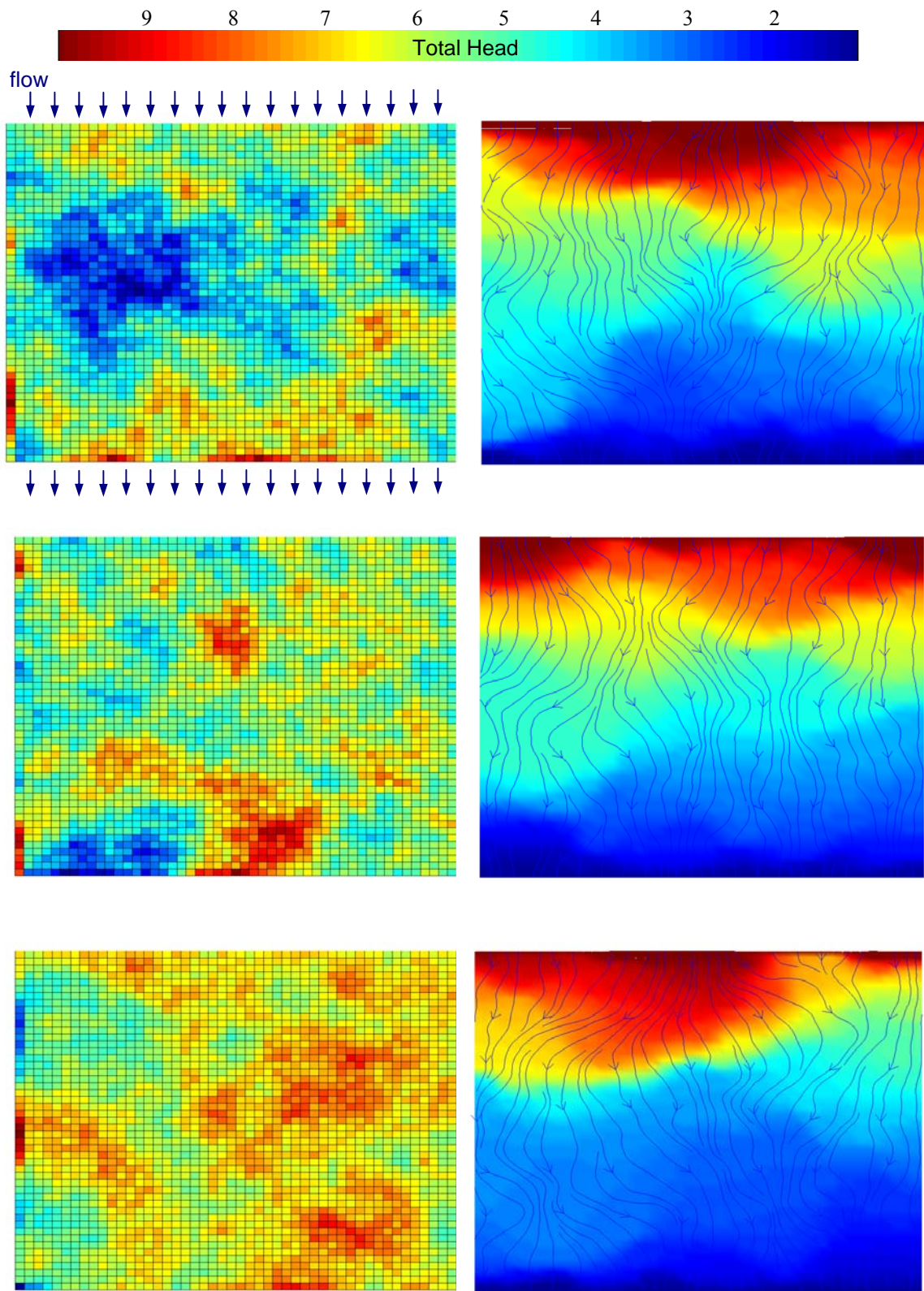
Figure 2.15. Correlated random fields (left) and associated flow (total head and flow lines, right).

34
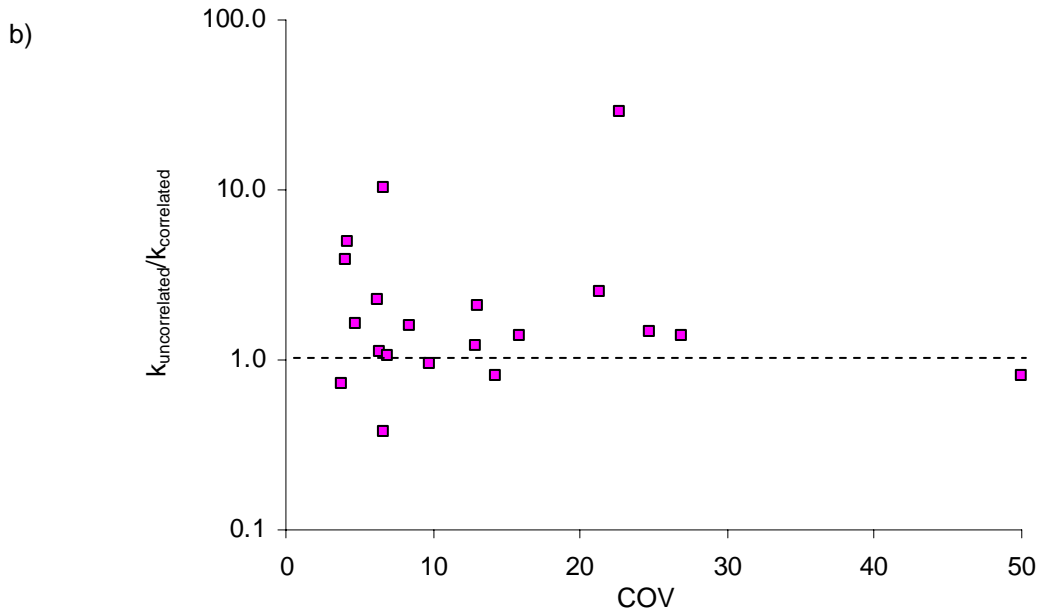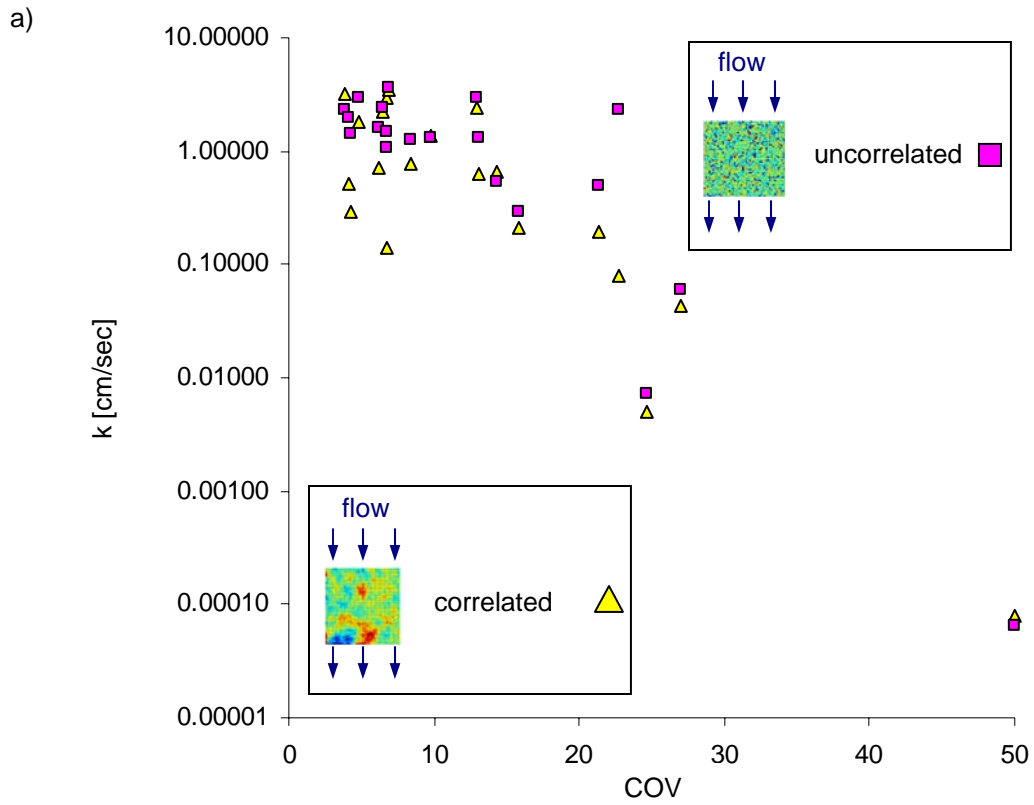
Figure 2.16. Uncorrelated and correlated random fields. a) Equivalent hydraulic conductivity (correlation length L=20% total domain). b) Ratio uncorrelated to correlated equivalent k.

35

2.5 DISCUSSION AND GEOTECHNICAL IMPLICATIONS

The homogeneous mixtures of sands in Section 2.2 cannot be assumed as ideal mixtures when the mass fraction of smaller components is not enough to fill voids. Predicting the hydraulic conductivity of these non-ideal mixtures requires knowledge of the pore-space variation with different mass fractions f_0 (Abichou et al. 2002; Zhang et al. 2005). Figure 2.7 shows that the equivalent hydraulic conductivity decreases one order of magnitude when the mass fraction of the less permeable component $f_0 \geq 18\%$. From that point on, the hydraulic conductivity finds a plateau that is coincident with the hydraulic conductivity the less permeable component (Ottawa S-140). Mixtures with $f_0 \geq 18\%$ have filled the primary void space of the base material (Ottawa F-50). From that point on, the particles of the coarser material (Ottawa F-50) can be considered as embedded within the percolating finer host material (Ottawa F-50). Increasing the finer material mass fraction f_0 causes a smaller or non-existent reduction in hydraulic conductivity because the smaller particles in the mixtures fill all of the primary void space between the bigger particles. This is accused in part by the reduction in void ratio also shown in Figure 2.7. The empirical Hazen's equation, $k = C_h \cdot D_{10}^2$ (where $20/cm.s \leq C_h \leq 1500/cm.s$ is a fitting dimensional value and D_{10} is expressed in cm), hinders this explanation. In fact, Figure 2.6 shows that the increment of D_{10} dramatically decreases for $f_0 \geq 20\%$. Mixtures of fine and coarse materials have been previously studied, with emphasis only in void ratio variation and correlations with meaningful fine soil index properties such as liquid limits (Kenney et al. 1992; Mollins et al. 1996; Sivapullaiah et al. 2000).

There is no analytical solution for the case of cylindrical inclusions. The renormalization method leads to the following equations for the case of cylindrical inclusions (recall Figure 2.12):

$$\frac{k_{eq}}{k_{host}} = \frac{3}{2} \cdot \left(\frac{1+\delta}{2+\delta}\right) \quad \text{for } \alpha=0.25 \qquad\qquad \frac{k_{eq}}{k_{host}} = \frac{3}{2} \cdot \left(\frac{3+\delta}{5+\delta}\right) \quad \text{for } \alpha=0.56$$

$$(2.14)$$

$$\frac{k_{eq}}{k_{host}} = \frac{3}{2} \cdot \left(\frac{7+\delta}{11+\delta}\right) \quad \text{for } \alpha=0.76 \qquad\qquad \frac{k_{eq}}{k_{host}} = 3 \cdot \left(\frac{\delta}{2+\delta}\right) \quad \text{for } \alpha=1.00$$

where $\delta = k_{inclusion}/k_{host}$ and $\alpha = \left(r_{inclusion}/R_{host}\right)^2$. These formulations overestimate the equivalent hydraulic conductivity k_{eq} because the flow is not uniform. Moreover, the application of a different grid of 2^{Dn} single elements results in more complex expressions that still fail to capture the physics of the problem. For example, the expression for a grid with $\alpha=0.25$ is:

$$\frac{k_{eq}}{k_{host}} = \frac{(5\delta+3)\left[48(1+7\delta)(1+15\delta)(7+9\delta)(1+\delta)\right]}{\left(156825 \cdot \delta^5 + 1497 \cdot \delta^4 + 590794 \cdot \delta^3 + 250638 \cdot \delta^2 + 35789 \cdot \delta\right)} \qquad (2.15)$$

Figure 2.17 shows the analytical bounds for the equivalent hydraulic conductivity of the system when $\alpha=0.75$. Although they are consistent with Figure 2.1, these bounds do not work well whenever the hydraulic conductivity of the inclusion is greater that of the host.

A semi empirical estimate of the equivalent hydraulic conductivity of cylindrical inclusions (Figure 2.12) arises from inspection of equations 2.14 and 2.15:

$$\frac{k_{equivalent}}{k_{host}} = 2 \cdot A \cdot \frac{\left(B + e^{\frac{4}{25} \cdot B} \cdot \delta \right)}{\left(3 \cdot B + 1 + 2 \cdot e^{\frac{4}{25} \cdot B} \cdot \delta \right)} \tag{2.16}$$

where A varies between from $A=1.5$ for large diameter inclusions and $A \cong 1.4$ for small inclusions, B is a parameter associated to α, varying from $B=0$ for $\alpha=1$ and tends to infinite $B \rightarrow \infty$ for $\alpha=0$ (in practice, $B=100$ is large enough for small α's), and $\delta = k_{inclusion} / k_{host}$ and e is the base of the natural logarithm. The A parameter appears related to B as:

$$A = -0.216 \cdot B^2 + 0.4084 \cdot B + 1.307 \tag{2.17}$$

The numerical finite element method tends to overestimate the equivalent hydraulic conductivity (Figure 2.13) as observed in previous studies (Lachassagne et al. 1990). This phenomenon is also observed in upscaling of two-phase flows and in the boundary of interfaces and zero flux (Moulton et al. 1999; Fredlund et al. 2003; Efendiev et al. 2006). On the other hand, finite difference techniques are subjected to different biases that depend on the intermesh averaging rule. With the usual harmonic averaging rule, finite differences underestimate the equivalent hydraulic conductivity (Lachassagne et al. 1990).
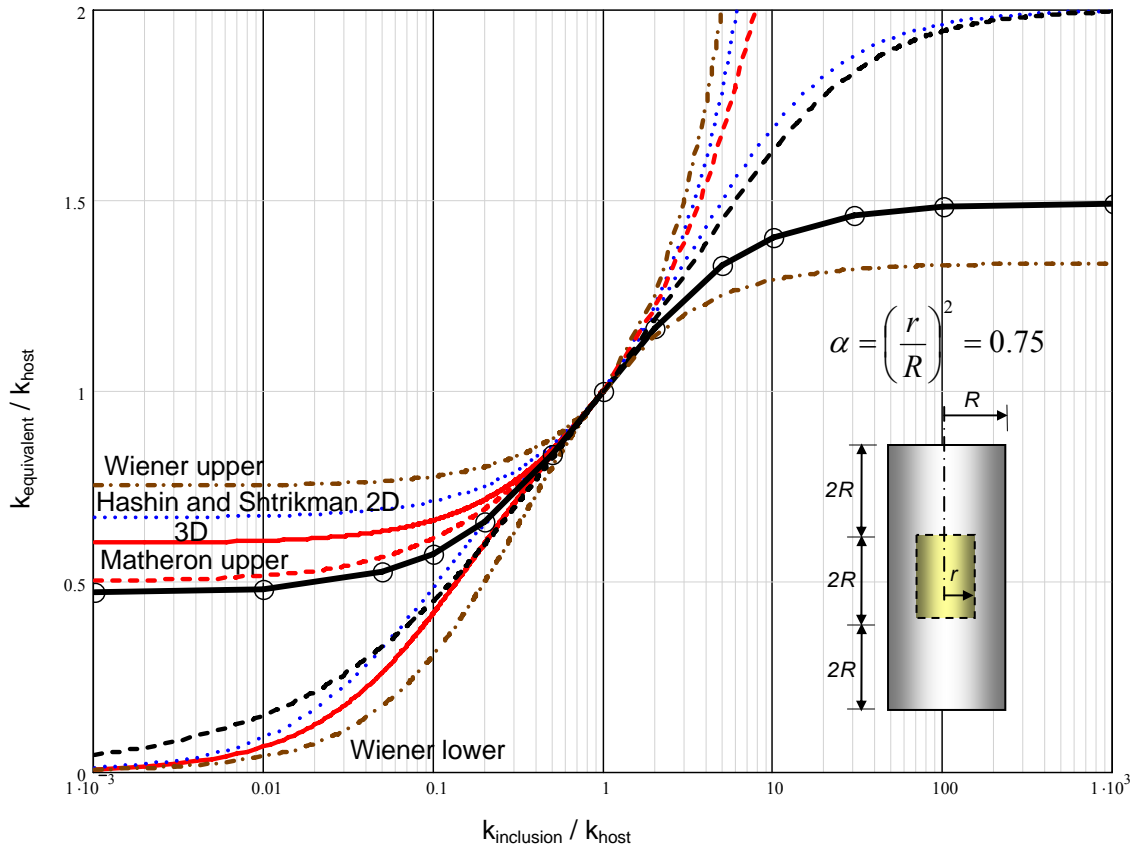
Figure 2.17. Analytical bounds for the equivalent hydraulic conductivity curve when α=0.75.

2.6 SUMMARY AND CONCLUSIONS

The inherent spatial variability in soils affects conduction phenomena. Salient conclusions extracted from analytical, numerical and experimental results are highlighted next:

- The hydraulic conductivity of homogeneous binary mixtures decreases as the mass fraction of the finer component increases, but it soon reaches a

plateau when the mass fraction of the finer grains is sufficient to fill the void space left by the coarser grains.

- The spatial variability in hydraulic conductivity plays a crucial role in flow rate and total head distribution.

- Most analytical bounds and close form solutions are based on volume fraction and fail to capture effects associated to the spatial distribution of hydraulic conductivity, such as percolation effects.

- The analytical Wiener, Hashin and Shtrikman (2D and 3D) and Matheron upper bounds fail to constrain the effective hydraulic conductivity when inclusions have higher hydraulic conductivity than the host medium.

- Renormalization methods take into account the spatial variability of hydraulic conductivity. Yet, they fail to provide simple expressions. A simple, semi empirical formulation is proposed in this study.

- Numerical discretization using finite elements tends to overestimate the equivalent hydraulic conductivity. A detailed justification remains unclear.

- The hydraulic conductivity decreases with increasing variability (as measured by the coefficient of variation COV in log-normal distributions of hydraulic conductivity with the same mean value). This observation applies to both correlated as well as uncorrelated k-fields.

- Correlated random fields exhibit lower hydraulic conductivity than uncorrelated fields with otherwise identical statistics (i.e., exactly the same individual pixel k-values). The development of high-conductivity percolation paths in correlated fields explains this observation.

CHAPTER III

SPATIAL VARIABILITY AND DIFFUSION PHENOMENA

3.1 INTRODUCTION

Diffusion is the time-dependent spatial evolution of a variable towards its steady state condition. The study of diffusion begins in 1826 with Thomas Graham, who publishes a series of papers on gases and aqueous solutions, including laboratory experiments and empirical equations that lead to the first work on diffusion in 1829. In 1855, Adolph Fick develops other diffusion laws for steady state diffusion (Fick's first law) and for non-steady state diffusion (Fick's second law). The diffusion equation has been applied to all kind of physical phenomena such as diffusion in gases, liquids, and solids, self-diffusion of matter (isotope effects), diffusion in ionic solids, diffusion in molecular, valance and polyatomic ionic solids, thermal diffusion, and diffusion processes in biological membranes and inside cells.

The process of consolidation in geotechnical engineering is a case of pressure diffusion. It is related to the dissipation of excess pore pressure, and it depends on the hydraulic conductivity and the skeletal compressibility of soils; both parameters are captured in the corresponding diffusion coefficient herein called the coefficient of consolidation C_v. The theory of consolidation is introduced by Karl Terzaghi in his "theory of clay settlement" in Vienna in 1925.

Previous studies show that the variation in C_v with depth must be accounted for to explain field response (Abbot 1960; Nishimura et al. 2002). However, the proper evaluation of the coefficient of consolidation remains challenging. For instance, Ortega (1996) evaluates C_v at four different scale volumes of lacustrine sediments in Mexico City, and concludes that results are unrealistic when laboratory values are used in larger scale settlement analyses. On the other hand, there are important difficulties in evaluating C_v (Borja 1988; Burns and Mayne 1998; Khemissa and Magnan 2000; Kim and Heydinger 2004).

This chapter starts with a review of previous work in diffusion. Then the forward and associated inverse problems are analyzed in relation to depth-varying C_v. In turn, these developments can permit monitoring and updating the soil model during construction, eventually taking corrective actions in the design. This objective is in line with similar ongoing studies in the context of excavations (Gens et al. 1996; Finno and Calvello 2005).

3.2 THE DIFFUSION EQUATION – PREVIOUS WORK

The classical one dimensional consolidation theory makes the following assumptions: 1) the soil is completely saturated, 2) soil particles and the interstitial fluid are incompressible, 3) Darcy's law is applicable, 4) strains are linearly related to the effective stress and independent of time, and 5) internal effects are disregarded. The resulting diffusion equation is (See Table 2.1):

$$\frac{du_e}{dt} = \frac{d}{dz}\left(C_v(z)\frac{du_e}{dz}\right) \tag{3.1}$$

where $C_v(z)$ is the coefficient of consolidation as a function of depth z, u_e is the excess pore pressure and t is time. Equation 3.1 simplifies when C_v is constant:

$$\frac{du_e}{dt} = C_v \frac{d^2 u_e}{dz^2}$$
(3.2)

The coefficient of consolidation $C_v = k/\gamma_w \cdot m_v$ depends on the hydraulic conductivity of the soil k, the unit weight of water γ_w and the coefficient of volume change m_v. Values of k and m_v can vary significantly depending on the type of soil, stress history, and fabric. Table 3.1 shows typical values of the coefficient of consolidation for different soils. Notice that the wide range of C_v values is not as wide as for k; this implies an underlying global correlation between k and m_v.

Biot (1941) introduces poroelasticity for the analysis of consolidation by combining fluid mass conservation with Darcy's law for laminar flow, and of the momentum balance equations with Hooke's law for elastic deformation. Several studies have extended Biot's theory since (Berryman and Wang 1995; Jeng et al. 1999).

Equation 3.2 can be solved analytically using Fourier transforms, applications of Green's function or Laplace transforms. However, the presence of more than one layer limits the derivation of close form solutions. Instead, numerical analysis is preferred in such cases to solve the forward problem (Abbot 1960; Navy 1962; Schiffman and Gibson 1964; Koppula 1987; Papanicolaou and Diplas 1998; Yang et al. 2004).

Table 3.1. Typical values of the coefficient of consolidation C_v.

Soil	C_v [m²/yr]	References
Boston Blue Clay (CL, marine deposit glacial clay, illite)	12 ± 6	Ladd and Luscher , 1965
Organic Silt (OH)	0.6 – 0.3	Lowe, Zaccheo and Feldman, 1964
Glacial Lake clays (CL)	2.0 – 2.7	Wallace and Otto, 1964
Chicago silty clay (CL)	2.7	Terzaghi and Peck, 1967
Swedish medium sensitive clay (CL-CH)	0.1 – 0.2 (laboratory)	
	0.2 – 1.0 (field)	Holtz and Broms, 1972
San Francisco Bay mud (CL)	0.6 – 1.2	
Maine clay (silty, glacial clay, partially illite)	6.3 – 13	
Normally consolidated stuarine silty clay	3.17 – 32	
Stiff red clay	3.17	Lee, White and Ingles, 1983
Sandy clay	32 – 317	
Silt	317 – 31710	
London clay	1.90 – 6.34	Skempton and Henkel, 1957
Shellhaven postglacial clay	1.27 – 3.81	Skempton and Henkel, 1953
Tillbury postglacial clay	2.85 – 3.49	
Calcareous silt (normally consolidated)	1015	Poulos, 1980
Carbonate silt	222	
Marine clay	634 – 6342	
Boulder clay	63 – 634	Bishop and Henkel, 1962
Boulder clay and residual clay	3.17 – 63	
Adria fine silty sand	0.85 – 1.55 (100-260 kPa)	
	0.54 – 1.57 (260-520 kPa)	
Adria silty clay (CH)	2.08 – 10.1 (50-100 kPa)	
	0.82 – 11.68(100-260 kPa)	
	0.41 – 1.26 (260-520 kPa)	
Adria medium fine sand	1.29 – 3.79 (100-260 kPa)	
	0.69 – 1.89 (260-520 kPa)	Cortellazo, 2002
Malcantone clayey silt and clay (CH)	0.31 – 0.56 (50-100 kPa)	
	0.17 – 0.60 (100-260 kPa)	
	0.24 – 0.38 (260-520 kPa)	
Volta Vaccari soft gray silty clay (CH)	0.6 – 5.36	
Mexico city clay (MH)	0.9 – 1.5	Leonards and Girault, 1961

The most common inverse problem in diffusion is to find the past state of a given system from its current state. There are theorems that demonstrate the uniqueness and existence of solutions when inverting diffusion coefficients (Jones 1963a; Hào 1994; Bal and Chou 2004). Few analytical solutions and inversion methodologies for inverting parabolic equations are presented in the literature (Jones 1963b; Asaoka and Matsuo 1980; Elayyan and Isakov 1997; Liu et al. 1998; Liu and Ball 1999; Isakov and Kindermann 2000; Cai et al. 2004).

However, the inverse problem is affected by ill-conditioning. Moreover, noisy data about the current state severely hinders the ability of finding a useful approximation of the solution (Hào 1994; Yin 1995; Frankel and Lawless 2005). Difficulties are aggregated when the goal includes finding not only the past state but the medium characteristics as well as $C_v(z)$ and even information about the source, common in environmental engineering and thermal applications among others (Bryan and Caudill 1996; Ramm 2001; Tanaka et al. 2005). Successive forward simulation is the most common numerical technique to invert diffusion data (Arai et al. 1984; Shoji et al. 1990; Nishimura et al. 2002).

3.3 FORWARD PROBLEM

This section presents numerical solutions to the consolidation equation. Two-layer, three-layer and linear variation of C_v with double and single drainage are solved and dimensionless charts are drawn to capture a number of common cases in geotechnical engineering.

3.3.1 Code – Validation

The continuous diffusion problem is herein written in discrete form and processed using the construct of matrices and vectors. The general Equation 3.1 written in finite difference form yields:

$$\frac{u_{i,j+1} - u_{i,j}}{\Delta t} = \frac{C_{v\,i+0.5}(u_{i+1,j} - u_{i,j}) - C_{v\,i-0.5}(u_{i,j} - u_{i-1,j})}{\Delta z^2} \tag{3.3}$$

where u is the discrete excess pore pressure u_e, sub indices i and j denote a point in the grid at depth z_i and time t_j, Δt is the time increment and Δz is the depth increment (Figure 3.1). For this explicit scheme, Δt and Δz are selected to satisfy the stability criterion (Press 2002):

$$\max_i(\theta_i) = \max_i\left(\frac{\Delta t \cdot C_{v\,i+1/2}}{\Delta z^2}\right) \le \frac{1}{2} \tag{3.4}$$

If the coefficient of consolidation is constant, Equation 3.3 becomes (refer to Equation 3.2):

$$\frac{u_{i,j+1} - u_{i,j}}{\Delta t} = \frac{C_v(u_{i+1,j} - 2u_{i,j} + u_{i-1,j})}{\Delta z^2} \tag{3.5}$$

Equation 3.3 constitutes an explicit forward time centered space scheme of second order accuracy. It is also possible to derive implicit schemes and Crank-Nicholson schemes. Table 3.2 summarizes the schemes that are used in this work as well as their stability criterion.
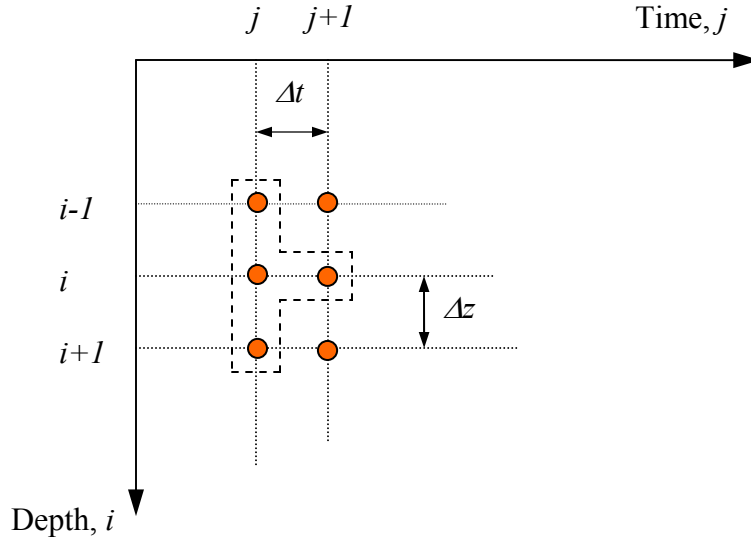
Figure 3.1. Finite difference mesh used to solve the diffusion Equation 3.1. Dash lines indicate the four points of interest in the fully explicit scheme. The orange dots are the six points of interest when solving using Crank-Nicholson scheme.

The schemes in Table 3.2 can be captured in matrix form (Table 3.3). These matrix formulations are coded in MatLab taking advantage of its efficient matrix computations (Appendix B).

Regarding boundary conditions, the initial excess pore pressure distribution u_{e0} is chosen to be constant along the depth, $u_{i,0} = \text{constant} \quad \forall i$ (initial boundary condition), i.e., when a load is apply on top of a consolidating system, the excess pore pressure is constant and equal to the applied load along the depth.

For double drainage, the excess pore pressure at the top and bottom of the consolidating system are zero at all times, $u_{1,j} = u_{M,j} = 0 \quad \forall j$.

Table 3.2. Different discrete solutions to the diffusion equation.

Name of methodology	Equation	Stability criterion
Forward time centered space scheme (explicit method)	$$\frac{u_i^{j+1} - u_i^j}{\Delta t} = \frac{C_{v\,i+0.5}(u_{i+1}^j - u_i^j) - C_{v\,i-0.5}(u_i^j - u_{i-1}^j)}{\Delta z^2}$$	$\max_i(\theta_i) \leq \dfrac{1}{2}$
Implicit method	$$\frac{u_i^{j+1} - u_i^j}{\Delta t} = \frac{C_{v\,i+0.5}(u_{i+1}^{j+1} - u_i^{j+1}) - C_{v\,i-0.5}(u_i^{j+1} - u_{i-1}^{j+1})}{\Delta z^2}$$	Stable
Crank-Nicholson scheme	$$\frac{u_i^{j+1} - u_i^j}{\Delta t} = \frac{C_{v\,i+0.5}(u_{i+1}^{j+1} - u_i^{j+1}) - C_{v\,i-0.5}(u_i^{j+1} - u_{i-1}^{j+1})}{2\Delta z^2} + \frac{C_{v\,i+0.5}(u_{i+1}^j - u_i^j) - C_{v\,i-0.5}(u_i^j - u_{i-1}^j)}{2\Delta z^2}$$	Stable

$\theta_i = \Delta t \cdot C_{v\,i+1/2} / \Delta z^2$

Sources: Press et al. (1992), Hanson (2000) and Class notes on Computational Physics (2001), Numerical PDE class notes (by Prof. Liu 2004). Time is represented by superscript "j" just to save space.

Table 3.3. Discrete solutions to the diffusion equation – Matrix forms.

Name of methodology

Forward time centered space scheme (explicit method)

$$
\begin{Bmatrix} u_{0,j+1} \\ u_{1,j+1} \\ \vdots \\ u_{i-1,j+1} \\ u_{i,j+1} \\ \vdots \\ u_{M-1,j+1} \\ u_{M,j+1} \end{Bmatrix}
=
\begin{bmatrix}
\alpha_0 & \beta_0 & 0 & 0 & 0 & 0 & 0 & 0 \\
\beta_0 & \alpha_1 & \beta_1 & 0 & 0 & 0 & 0 & 0 \\
0 & \beta_1 & \alpha_2 & \beta_2 & 0 & 0 & 0 & 0 \\
0 & 0 & \ddots & \ddots & \ddots & 0 & 0 & 0 \\
0 & 0 & 0 & \ddots & \ddots & \ddots & 0 & 0 \\
0 & 0 & 0 & 0 & \beta_{M-3} & \alpha_{M-2} & \beta_{M-2} & 0 \\
0 & 0 & 0 & 0 & 0 & \beta_{M-2} & \alpha_{M-1} & \beta_{M-1} \\
0 & 0 & 0 & 0 & 0 & 0 & \beta_{M-1} & \alpha_M
\end{bmatrix}
\cdot
\begin{Bmatrix} u_{0,j} \\ u_{1,j} \\ \\ u_{i-1,j} \\ u_{i,j} \\ \vdots \\ u_{M-1,j} \\ u_{M,j} \end{Bmatrix}
$$

where

$$C_{vm\,i} = \frac{C_{v\,i-1} + C_{v\,i}}{2}$$

$$r_i = C_{vm\,i}\frac{\Delta t}{\Delta z^2}$$

$$\beta_i = \frac{r_i}{2} \quad ; \quad \delta_i = \frac{r_i}{2}$$

$$\alpha_i = 1 - \beta_i - \delta_i$$

Implicit method

$$
\begin{Bmatrix} u_{0,j+1} \\ u_{1,j+1} \\ \vdots \\ u_{i-1,j+1} \\ u_{i,j+1} \\ \vdots \\ u_{M-1,j+1} \\ u_{M,j+1} \end{Bmatrix}
=
\begin{bmatrix}
\gamma_0 & -\beta_0 & 0 & 0 & 0 & 0 & 0 & 0 \\
-\beta_0 & \gamma_1 & -\beta_1 & 0 & 0 & 0 & 0 & 0 \\
0 & -\beta_1 & \gamma_2 & -\beta_2 & 0 & 0 & 0 & 0 \\
0 & 0 & \ddots & \ddots & \ddots & 0 & 0 & 0 \\
0 & 0 & 0 & \ddots & \ddots & \ddots & 0 & 0 \\
0 & 0 & 0 & 0 & -\beta_{M-3} & \gamma_{M-2} & -\beta_{M-2} & 0 \\
0 & 0 & 0 & 0 & 0 & -\beta_{M-2} & \gamma_{M-1} & -\beta_{M-1} \\
0 & 0 & 0 & 0 & 0 & 0 & -\beta_{M-1} & \gamma_M
\end{bmatrix}^{-1}
\cdot
\begin{Bmatrix} u_{0,j} \\ u_{1,j} \\ \vdots \\ u_{i-1,j} \\ u_{i,j} \\ \vdots \\ u_{M-1,j} \\ u_{M,j} \end{Bmatrix}
$$

$$\gamma_i = 1 + \beta_i + \delta_i$$

Table 3.3. Continued.

Name of methodology

Crank-Nicholson scheme

$$
\begin{Bmatrix} u_{0,j+1} \\ u_{1,j+1} \\ \vdots \\ u_{i-1,j+1} \\ u_{i,j+1} \\ \vdots \\ u_{M-1,j+1} \\ u_{M,j+1} \end{Bmatrix} =
\begin{bmatrix}
\gamma_0 & -\beta_0 & 0 & 0 & 0 & 0 & 0 & 0 \\
-\beta_0 & \gamma_1 & -\beta_1 & 0 & 0 & 0 & 0 & 0 \\
0 & -\beta_1 & \gamma_2 & -\beta_2 & 0 & 0 & 0 \\
0 & 0 & \ddots & \ddots & \ddots & 0 & 0 & \upsilon \\
0 & 0 & 0 & \ddots & \ddots & \ddots & 0 & 0 \\
0 & 0 & 0 & 0 & -\beta_{M-3} & \gamma_{M-2} & -\beta_{M-2} & 0 \\
0 & 0 & 0 & 0 & 0 & -\beta_{M-2} & \gamma_{M-1} & -\beta_{M-1} \\
0 & 0 & 0 & 0 & 0 & 0 & -\beta_{M-1} & \gamma_M
\end{bmatrix}^{-1}
\begin{bmatrix}
\alpha_0 & \beta_0 & 0 & 0 & 0 & 0 & 0 & 0 \\
\beta_0 & \alpha_1 & \beta_1 & 0 & 0 & 0 & 0 & 0 \\
0 & \beta_1 & \alpha_2 & \beta_2 & 0 & 0 & 0 & 0 \\
0 & 0 & \ddots & \ddots & \ddots & 0 & 0 & 0 \\
0 & 0 & 0 & \ddots & \ddots & \ddots & 0 & 0 \\
0 & 0 & 0 & 0 & \beta_{M-3} & \alpha_{M-2} & \beta_{M-2} & 0 \\
0 & 0 & 0 & 0 & 0 & \beta_{M-2} & \alpha_{M-1} & \beta_{M-1} \\
0 & 0 & 0 & 0 & 0 & 0 & \beta_{M-1} & \alpha_M
\end{bmatrix}
\cdot
\begin{Bmatrix} u_{0,j} \\ u_{1,j} \\ \vdots \\ u_{i-1,j} \\ u_{i,j} \\ \vdots \\ u_{M-1,j} \\ u_{M,j} \end{Bmatrix}
$$

51

When these initial and boundary conditions are incorporated into the matrix forms shown in Table 3.3, the first and last row and column of the matrices are eliminated, and the first and last element of the vectors are eliminated as well (since they are zero). Single drainage conditions imply $u_{M-1,j} = u_{M,j} = 0 \quad \forall j$.

The computer code is validated first for a single layer with constant C_v with depth z (case a in Table 3.4). The layer is discretized in $\Delta z/H = 0.033$. The selected $\theta = 0.4$ satisfies stability criterion for all schemes (Equation 3.4). Results in Figure 3.2 show a perfect match with the theoretical solution.

$$u_e = \sum \frac{2 \cdot u_0}{M} \left(\sin M \frac{z}{H} \right) e^{-M^2 T} \quad \text{where } M = \frac{\pi}{2}(2m+1) \qquad (3.6)$$

3.3.2 Case studies – Charts

Layered media. Several layered media cases are analyzed and summarized in Table 3.4. The evolution in excess pore pressure in depth and time for layered media are computed next (cases b and c in Table 3.4).

Figure 3.3-a shows the results of a two-layer system with $C_{v\,bottom} / C_{v\,top} = 1.4$ and selected $\theta = 1.14$ (case b in Table 3.4). Results confirm that the solution is not stable for explicit methods as this θ parameter does not satisfy the stability criterion. On the other hand, the Crank-Nicholson scheme produces a stable solution, even for such a high θ value (Figure 3.3-b). The figures show the isochrones for dissipation of excess porewater pressure u_e/u_0 at time factors ($T = C_v t/H^2$) T=0, 0.03, 0.06, 0.125, 0.25, 0.50, 1, and 2.
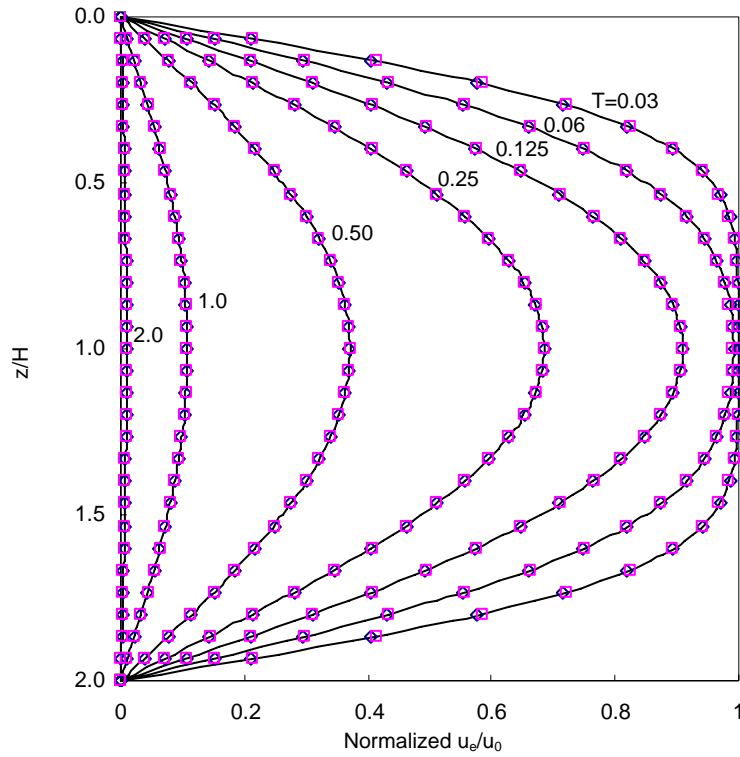
Figure 3.2. Code validation. Explicit scheme (blue rhombuses), Crank Nicholson scheme (pink squares), exact solution (solid black line, first 1000 terms).

Table 3.4. Forward problem – Cases.

Boundary conditions	Initial excess pore pressure distribution	Number of layers	$\beta^{-1} = \dfrac{C_{v\,bottom}}{C_{v\,top}}$	Objectives
Double drainage	Linear along depth	(a) 1 layer	1	Validate the proposed methodology
		(b) 2 layers	1.4	Show instability of some schemes.
		(c) 2 layers	0.6	Show sensitivity to Δt and Δz (refined mesh)
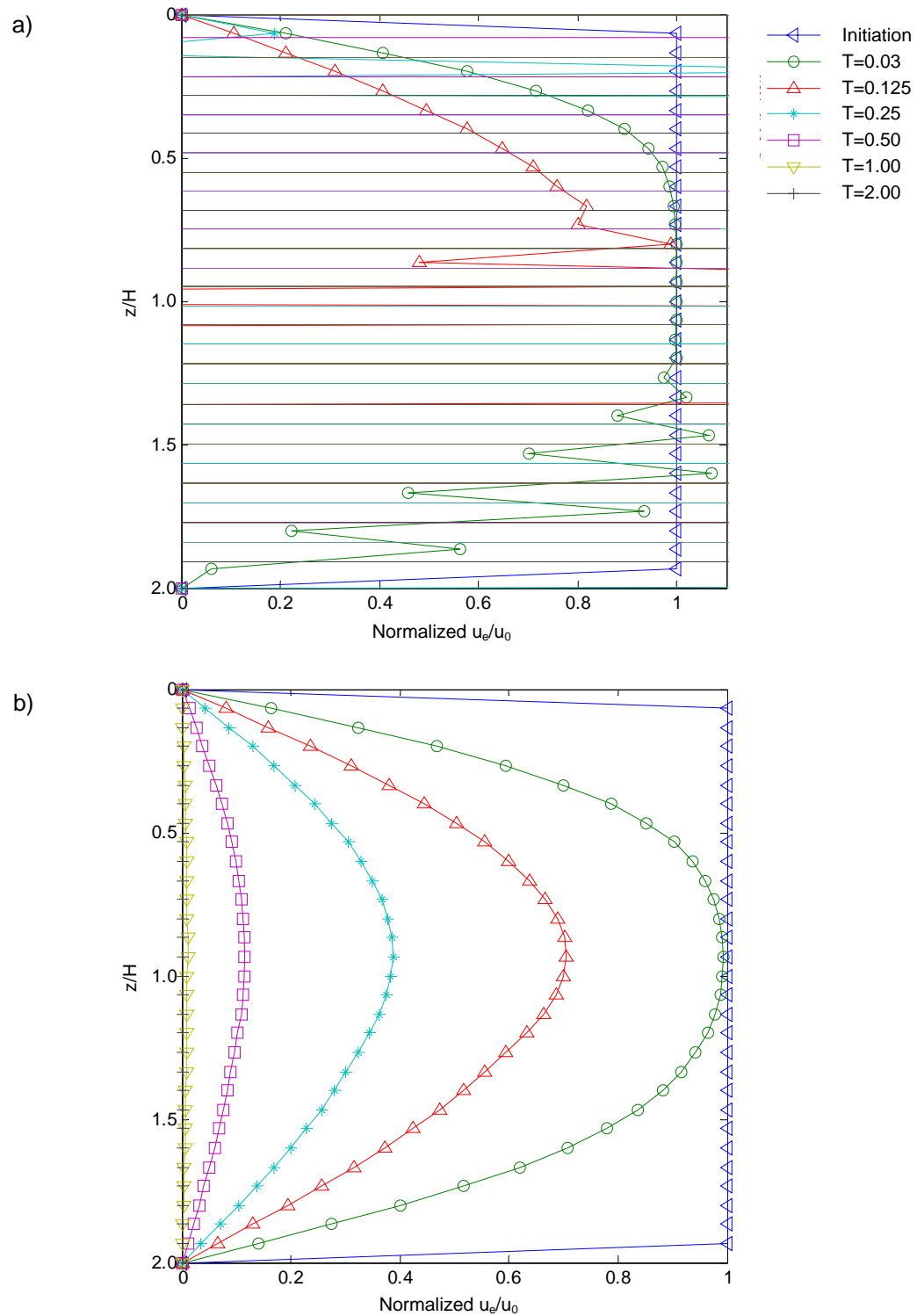
Figure 3.3. Testing for stability with θ=1.14. a) Instability for the explicit scheme, case "b" in Table 3.4. b) The Crank-Nicholson scheme shows a stable solution.

The temporal scale t_f is the time t where more than 99% of the dissipation of u_e is achieved; this temporal scale corresponds to a time factor $T=4$ (i.e., $t_f = 4 \cdot H^2 / C_v$). In case of varying C_v we define

$$T = \min_i \left(\frac{C_{vi} \cdot t}{H^2} \right) \tag{3.7}$$

This time factor T represents an upper bound for excess pore pressure dissipation, in other words, excess pore pressure dissipation would take at most $t_f = H^2 \cdot T / C_{v\,min}$. On the other hand, a lower bound for complete dissipation is the maximum time in each individual layer, $t_f = \max_i \left(H_i^2 \cdot T / C_{vi} \right)$. An effective thickness of a multilayered system and the dimensionless time factor T_{NAFVAC} can be computed as (NAVFAC 1986):

$$T_{NAVFAC} = \frac{C_{v\,ref} \cdot t}{\left(\sum_1^N H_i \cdot \sqrt{\frac{C_{v\,ref}}{C_{vi}}} \right)^2} \tag{3.8}$$

where $C_{v\,ref}$ is a reference coefficient of consolidation (e.g., the value of any layer). We have numerically verified that the time for complete dissipation given by Equation 3.8 falls between the lower and upper bounds. The time factor defined in Equation 3.7 is used in this study in lieu of a rigorous mathematical derivation of Equation 3.8. Additionally, this choice requires further analysis.

For case c in Table 3.4, two-layer sediments with step variation of C_v, such that $C_{v\,bottom} / C_{v\,top} = 0.6$ and selected $\theta=0.4$, the results are stable, even for explicit methods as these parameters satisfy the stability criterion (the implicit and Crank-Nicholson

scheme results stable as well). Figure 3.4 shows the results with the Crank-Nicholson scheme. The solution converges to an asymptotic value as the mesh is refined, in other words, as the ratio $\Delta t/\Delta z$ decreases.
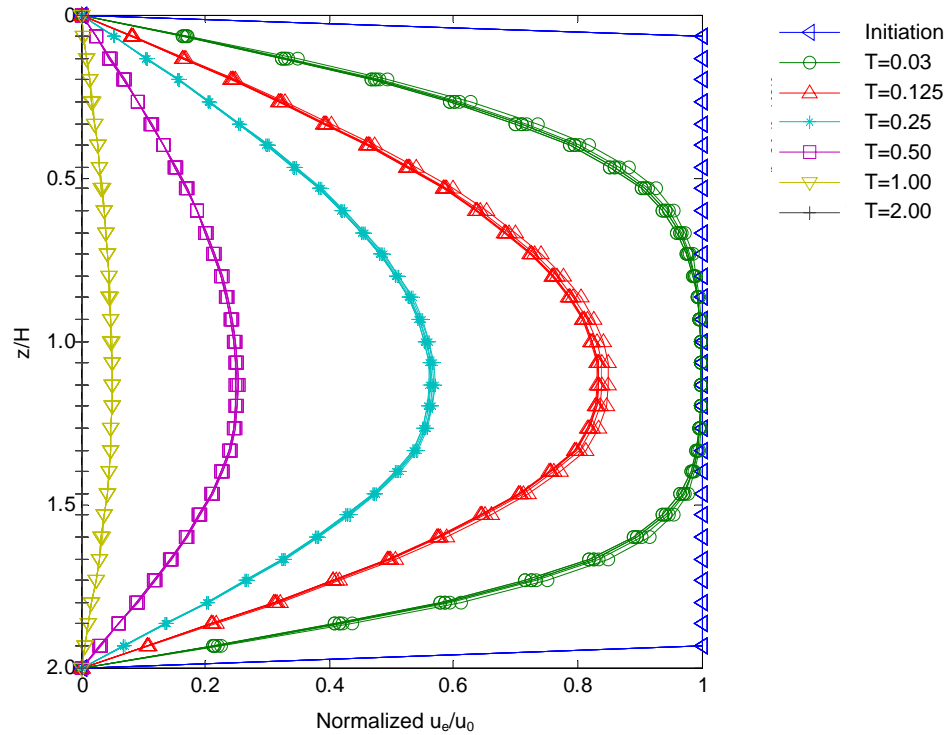
Figure 3.4. Convergence due to mesh refinement. The Crank-Nicholson scheme shows a stable solution ($C_{v\ top}$=0.5 m2/year at z/H=0 through 1.3, $C_{v\ bottom}$ =0.3 m2/year at z/H=1.3 through 2.0).

The rest of this section uses the Crank-Nicholson scheme since it results in a stable solution of second order accuracy in time and space, and it inherently satisfies the laplacian across the boundary at any given time. Two dimensionless parameters

$\alpha = z_1 / z_{total}$ and $\beta = C_{v\,top} / C_{v\,bottom}$ are defined to present the data in general terms (Figure 3.5).

$$\alpha = \frac{z_1}{z_{total}}$$

$$\beta = \frac{C_{v\,top}}{C_{v\,bottom}}$$
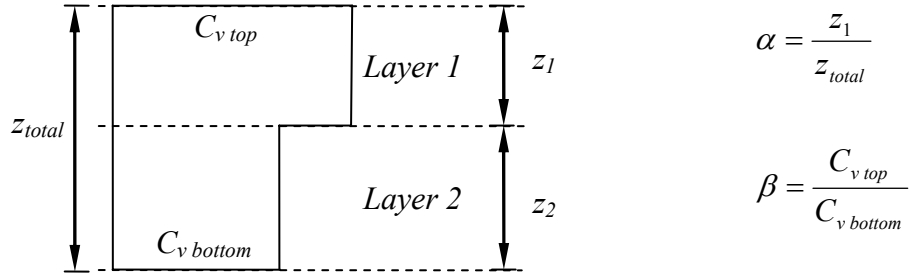
Figure 3.5. Dimensionless ratio α and β for a bi-layer system.

Figure 3.6 shows the normalized excess porewater pressure u_e / u_0 profiles with depth at selected times using the dimensionless ratios α, β, $T = C_{v\,min} \cdot t / H^2$ and z/H, for a constant initial excess pore pressure $u_e(t = 0) = u_0$, and double drainage, $H = z_{total}/2$. The degree of consolidation at any given depth and time is computed as

$$U_z = 1 - (u_e / u_0) \tag{3.9}$$

where u_e / u_0 is the normalized excess porewater pressure shown in the charts (Figure 3.6). In addition, any problem with linear initial excess porewater pressure can be solved using the charts if there is double drainage; just multiply the value u_e / u_0 from the chart by the initial excess porewater pressure.
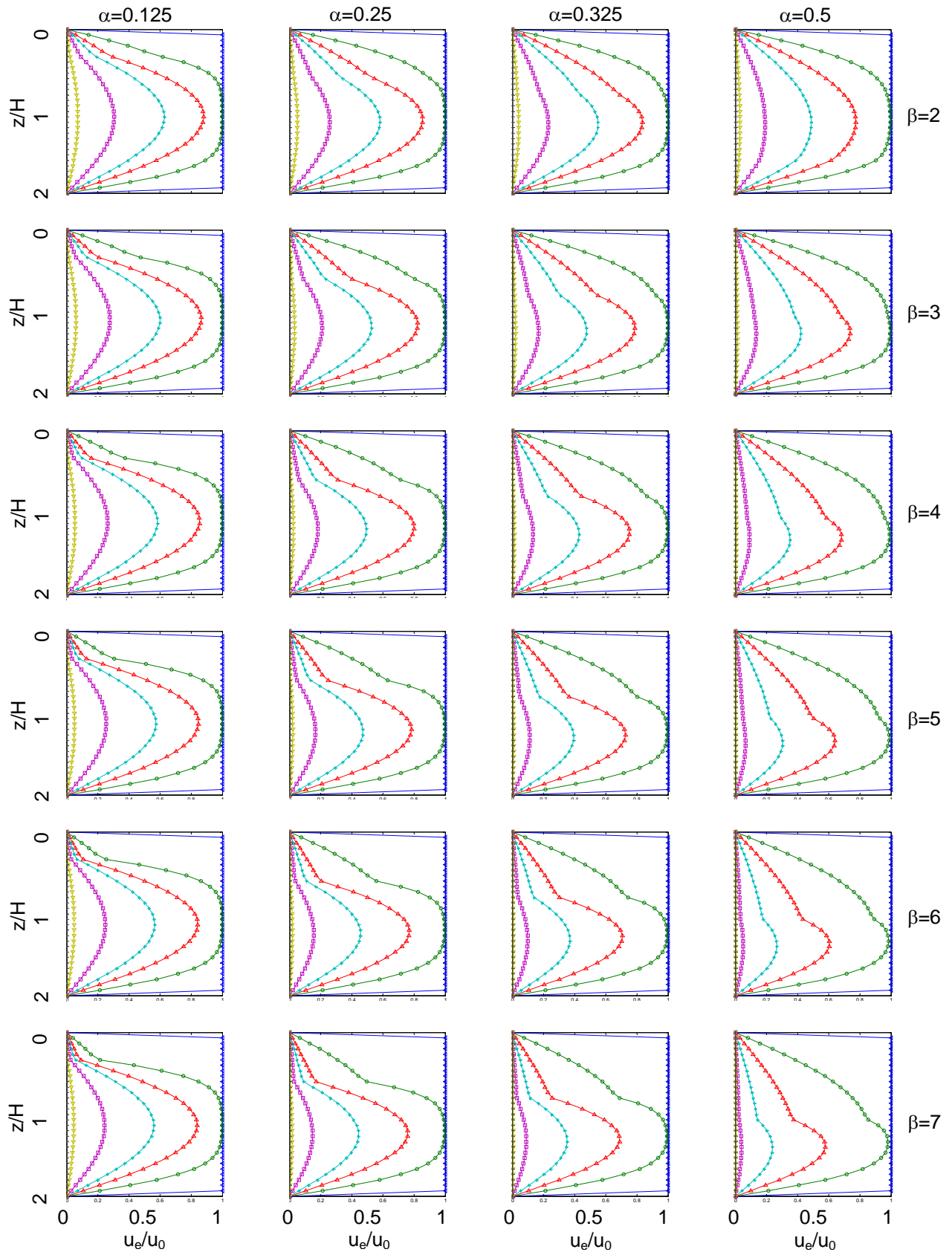
Figure 3.6. Charts for bi-layer systems. Isochrones at T: 0.03125, 0.125, 0.25, 0.50, 1.0 and 2.0.
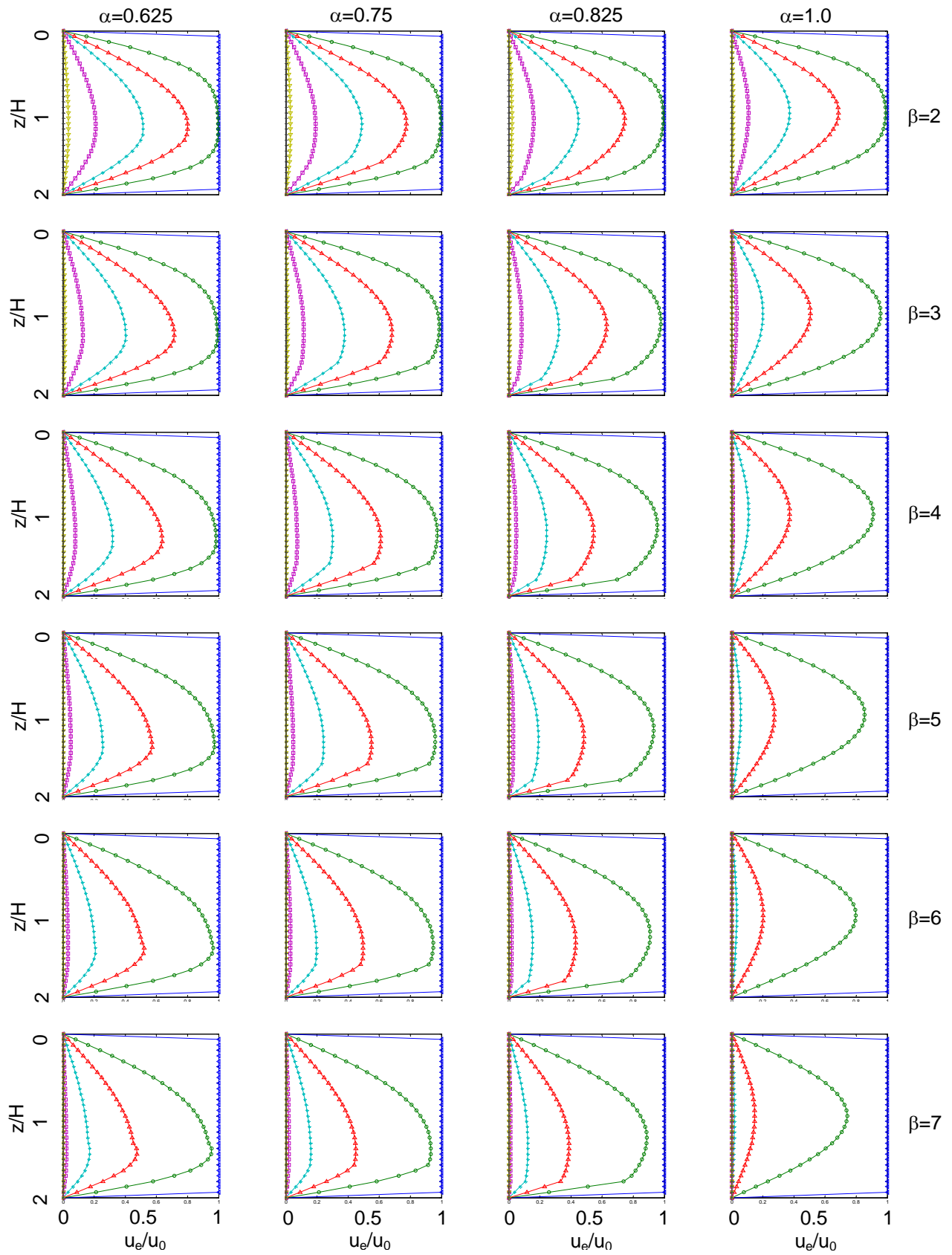
Figure 3.6. Continued.

The dissipation in the higher C_v layer (the top layer) takes place much faster as β increases, yet, it is restricted by the layer of lower C_v. The restriction in dissipation of u_e is more apparent as α increases, since a greater portion of the consolidating system has lower C_v. Moreover, the gradient at the interface $\partial u / d(z/H) \neq 0$; therefore, water flow takes place across the interface for all α and β values, indicating interaction between layers. Clearly, $\partial u / d(z/H) \rightarrow 0$ as $\beta \rightarrow \infty$ and dissipation becomes single drainage.

A single drainage condition can be also solved using charts in Figure 3.6 as follows:

1. Identify the set of charts with closest β.

2. In these charts, find the normalized depth H_n where $\partial u / d(z/H) = 0$. This normalized depth can be assumed at the impervious boundary. (H_n is the single drainage path thickness).

3. If α<0.5, then discard the lower part of the chart; if α>0.5, then discard the upper part of the chart and flip accordingly.

4. Recompute the vertical axis for the "new" converted chart: the normalized depth as z/H_n if $\alpha < 0.5$ or as $z/(2\text{-}H_n)$ if $\alpha > 0.5$, and the new ratio $\alpha_n = 2 \cdot \alpha / z_n$, and the new isochrones as $T_{iso\,n} = T_{iso} / 4$.

5. Use the "new" chart as directed previously.

A solved example is presented in Figure 3.7.

a)

Sand		
Clay 1, $C_{v\ top} = 1.8$ m^2/yr	3m	
Clay 2, $C_{v\ botton} = 0.3$ m^2/yr	1m	
Impervious intact rock		
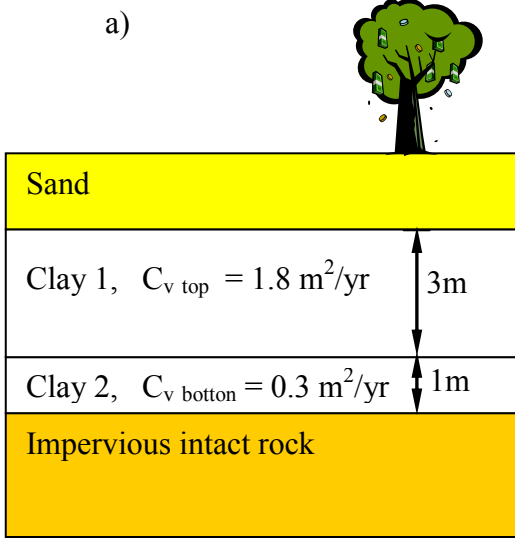
Consider a soil profile a). The new ratios for this problem are α_n =3m/4m=0.75 and β_n=1.8m^2/yr/0.3m^2/yr=6, and H_n=4.
Identify in Figure 3.6, the charts corresponding to β=6. By inspection, the chart for α=0.5 may be useful; $\partial u / d(z/H) = 0$ at $z/H \cong 1.35$, so z_n=1.35. It is now possible to draw the new normalized depth z/H_n. In the figure, it is also possible to discover that α_n=2·0.5/1.35=0.75 as we wanted. The last task is to properly convert the isochrones, for example, the isochrone corresponding to T_{iso}=0.29 in the original chart, would be $T_{iso\ n}$=0.29/4=0.07 in the new converted chart (Figure 3.7-b).

b)
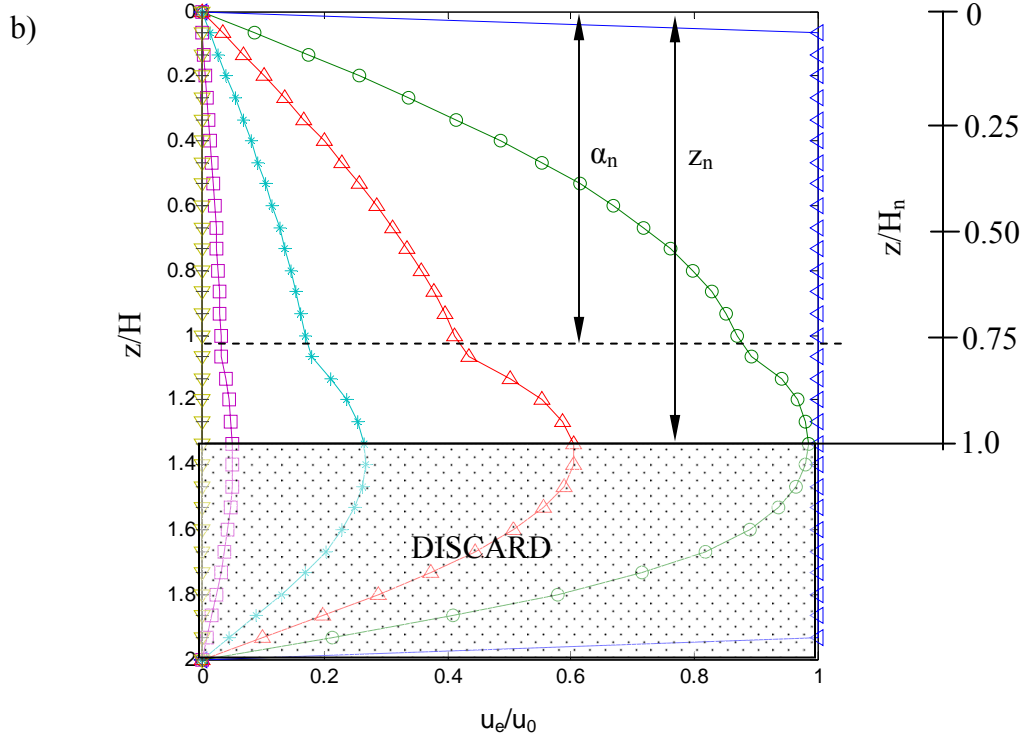
Figure 3.7. Application of the design charts – Example: single drainage path, bi-layer system, with ratio α_n=0.75 and β_n=6.

61

Linearly varying C_v. Charts in Figure 3.8 are computed for a linear variation of the coefficient of consolidation, initial excess pore pressure u_0 and double drainage. This is the typical case for weathered/residual soil profiles; the inverted variation is valid for sedimentary soils. The dimensionless parameter $\delta = C_{v\,top}/C_{v\,bottom}$ captures the linear variation between the top and bottom C_v. Isochrones for dissipation of normalized excess porewater pressure u_e/u_0 at Time factors T= 0.0006, 0.04, 0.14, 0.29 0.57, 1.15 and 2.3 are presented.

It can be seen that as $\delta = C_{v\,top}/C_{v\,bottom}$ increases, the system tends to behave as a single drainage one; however, the gradual variation of C_v may better reflect deposits formed by weathering of intact rock, where no definite interface between layers is noticeable.

3.4 INVERSE PROBLEM

This section starts with a brief review of inversion techniques. The revolution in sensor and information technology has made possible extensive monitoring during construction, coupled with inversion analysis to extract "the true field parameter", eventually leading to design optimization (Gioda and Sakurai 1987; Zhang et al. 1998; Finno and Calvello 2005). In light of these developments, the purpose of this section is to explore the invertibility of in situ coefficient of consolidation profiles. Then, an inversion methodology is proposed herein, and several cases are analyzed. Limitations and possible practical implications are discussed at the end of this section.

$$\delta = \frac{C_{v\,top}}{C_{v\,botton}}$$

Dimensionless parameter capturing linear variation of coefficient of consolidation
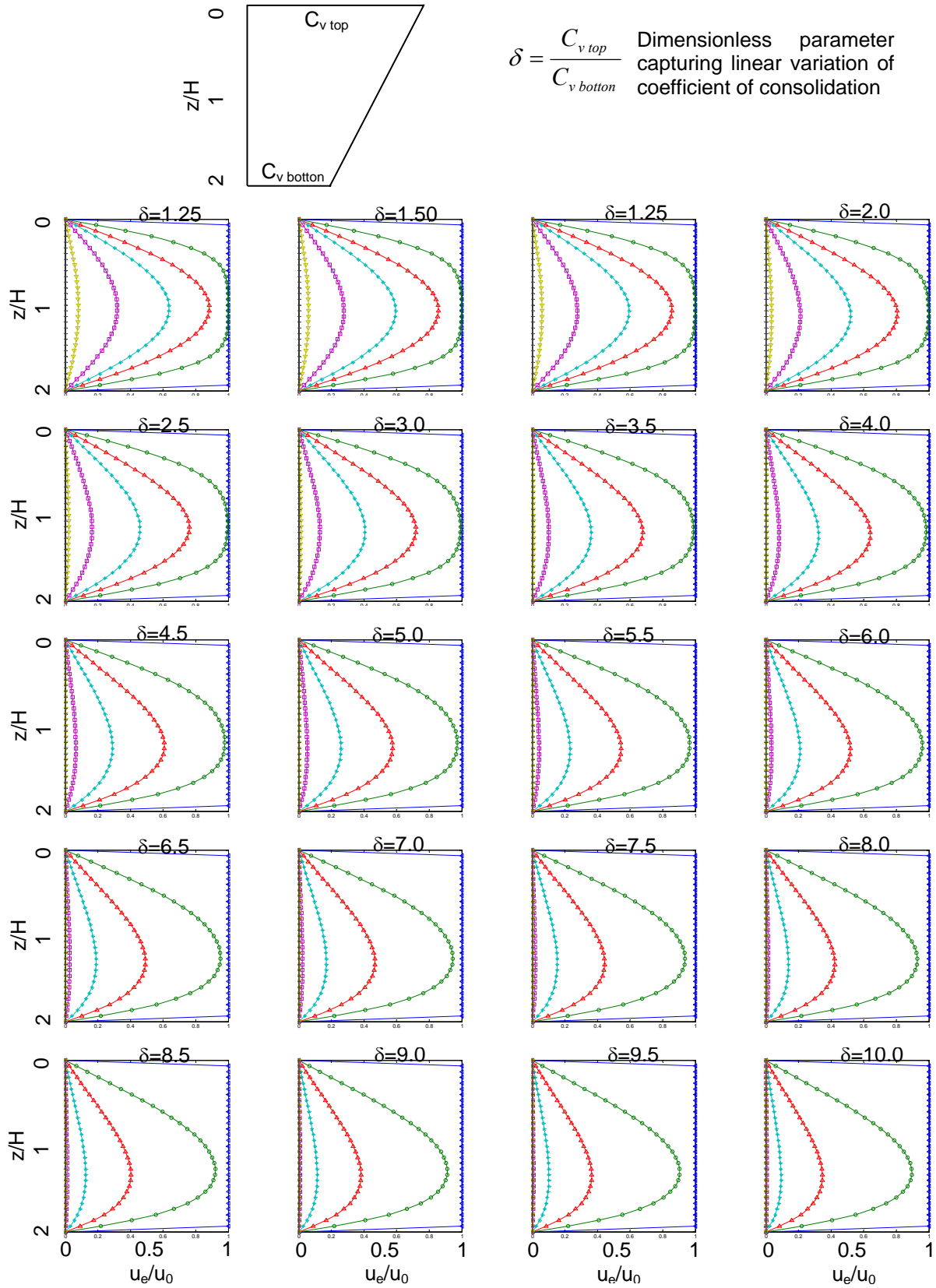
Figure 3.8. Charts for linear varying systems. T: 0.0006, 0.04, 0.29, 0.57, 1.15 and 2.3.

3.4.1 Theory of inverse problem solving

The goal of inverse problem solving is to determine the values of unknown model parameters from measured quantities by assuming a model that relates the two. A simple and versatile, yet computer-intensive approach is the solution by successive forward simulation. Alternatively, once the forward problem is expressed in a matrix form, the inverse problem becomes the algebraic problem of matrix inversion.

The general forward problem has the following matrix form:

$$\underline{y} = \underline{\underline{h}} \cdot \underline{x} \tag{3.10}$$

where $\underline{x}$ represents the input vector (i.e., unknown parameters), $\underline{y}$ the output vector (i.e., measured quantities) and $\underline{\underline{h}}$ is the transformation matrix, the model in matrix form.

There are a number of techniques used to find the unknowns parameters (Press 2002; Santamarina and Fratta 2005); three are tested in this work: 1) Direct Inversion (DI), 2) Least Squares Solution (LSS), and 3) Regularized Least Squares Solution (RLSS).

If the transformation matrix $\underline{\underline{h}}$ is invertible, then the Direct Inversion method is applicable, and the unknown parameters are obtained as:

$$\underline{x} = \underline{\underline{h}}^{-1} \cdot \underline{y} \tag{3.11}$$

However, $\underline{\underline{h}}$ is rarely invertible. Consequently, a pseudo inverse of $\underline{\underline{h}}$ is computed instead of $\underline{\underline{h}}^{-1}$.

The Least Squares Solution LSS starts with the error vector $\underline{e}$, where e_i is the difference between the ith measured value y_i and the estimated value, and finds the pseudo inverse by minimizing ($\underline{e}^T \underline{e}$). This leads to the following solution:

$$\underline{x} = (\underline{\underline{h}}^T \cdot \underline{\underline{h}})^{-1} \cdot \underline{\underline{h}}^T \cdot \underline{y} \tag{3.12}$$

Additional information about the unknown parameters may be incorporated during the inversion. For example, one may assume that the unknown vector varies linearly (first derivative is a constant) or smoothly (second derivative is zero). Such information can be added through a regularization matrix $\underline{\underline{R}}$ leading to the Regularized Lest Squares Solution RLSS:

$$\underline{x} = (\underline{\underline{h}}^T \cdot \underline{\underline{h}} + \lambda \cdot \underline{\underline{R}}^T \cdot \underline{\underline{R}})^{-1} \cdot \underline{\underline{h}}^T \cdot \underline{y} \tag{3.13}$$

where λ is the nonnegative regularization coefficient. The matrix $\underline{\underline{R}}$ often results from finite difference approximations (Tikhonov regularization – Press 2002; Santamarina and Fratta 2005). The RLS solution requires the selection of λ. Its optimal value depends on the characteristics of the problem, the quality of the data and the adequacy of the assumed model (Santamarina and Fratta 2005). Moreover, in most cases, the analyst has some information about the solution; for example the minimum and maximum values that each unknown can physically reaches, the relative magnitude of parameters, or a prevailing trend in the solution. The optimal value for λ is chosen by monitoring all this information. In simulated the diffusion problem, the true values $\underline{C_v}^{<true>}$ (equivalent to $\underline{x}^{<true>}$ in this case) can be compared to the inverted values $\underline{C_v}$ (equivalent to $\underline{x}$ in this case) for

different λ values. Furthermore, the evolution in $\underline{C}_v$ and in the norm of the residuals

$|\underline{e}| = \underline{e}^T \cdot \underline{e} = \left| \underline{\Delta u} - \underline{\underline{h}} \cdot \underline{C}_v \right|$ can be plotted versus different λ values.

3.4.2 Inversion of coefficient of consolidation profiles

The matrix forms of Equation 3.1 from finite differences (Table 3.3) constitute the forward problem and they allow us to generate synthetic "measured" data of the excess pore pressure vector $\underline{u}$. Then, the goal is to determine the C_v profiles versus depth from these "measured" data.

The finite difference equation is expressed in matrix form in order to use matrix-based inversion methods:

$$\underline{\Delta u} = \underline{\underline{h}} \cdot \underline{C}_v \qquad (3.14)$$

where $\underline{\Delta u}$ is the vector of excess pore pressure differences between two given times; and the vector $\underline{C}_v$ captures the C_v profile. The finite difference form of the diffusion equation used herein is:

$$\frac{u_{i,j+1} - u_{i,j}}{\Delta t} = \frac{C_{v\,i}(u_{i+1,j} - 2u_{i,j} + u_{i-1,j})}{\Delta z^2} \qquad (3.15)$$

where $C_{v\,i}$ is the local average,

$$C_{v\,i} = \frac{C_{v\,i+0.5} + C_{v\,i-0.5}}{2} \qquad (3.16)$$

From Equation 3.15,

$$u_{i,j+1} - u_{i,j} = \frac{\Delta t}{\Delta z^2} \cdot (u_{i+1,j} - 2u_{i,j} + u_{i-1,j}) \cdot C_{vi} \qquad (3.17)$$

This expression can be written in matrix form,

$$
\begin{Bmatrix}
u_{0,j+1} - u_{0,j} \\
u_{1,j+1} - u_{1,j} \\
... \\
u_{i-1,j+1} - u_{i-1,j} \\
u_{i,j+1} - u_{i,j} \\
u_{i+1,j+1} - u_{i+1,j} \\
... \\
u_{M,j+1} - u_{M,j}
\end{Bmatrix}
= dia\left[\frac{\Delta t}{\Delta z^2} \cdot
\begin{bmatrix}
1 & 0 & 0 & ... & ... & 0 & 0 & 0 \\
1 & -2 & 1 & 0 & ... & 0 & 0 & 0 \\
0 & 1 & -2 & 1 & ... & 0 & 0 & 0 \\
... & ... & ... & ... & ... & ... & ... & ... \\
0 & 0 & 0 & 0 & ... & 1 & -2 & 1 \\
0 & 0 & 0 & 0 & ... & 0 & 0 & 1
\end{bmatrix}
\cdot
\begin{Bmatrix}
u_{0,j} \\
u_{1,j} \\
... \\
u_{i-1,j} \\
u_{i,j} \\
u_{i+1,j} \\
... \\
u_{M,j}
\end{Bmatrix}
\right] \cdot
\begin{Bmatrix}
C_{v0} \\
C_{v1} \\
... \\
C_{vi-1} \\
C_{vi} \\
C_{vi+1} \\
... \\
C_{vM}
\end{Bmatrix}
$$

$$\underline{\Delta u} \qquad = \qquad \underline{\underline{h}} \qquad \cdot \quad \underline{C_v}$$

$$(3.18)$$

In Equation 3.18, the operator *dia[ ]* creates a diagonal matrix $\underline{\underline{h}}$ whose elements are the values of the vector between brackets.

For the case of double drainage conditions, $u_{0,j}$ and $u_{M,j}$ are zero for all j, and Equation 3.18 is modified for this boundary condition, yielding:

$$
\begin{Bmatrix}
u_{1,j+1} - u_{1,j} \\
u_{2,j+1} - u_{2,j} \\
... \\
u_{i-1,j+1} - u_{i-1,j} \\
u_{i,j+1} - u_{i,j} \\
u_{i+1,j+1} - u_{i+1,j} \\
... \\
u_{M-1,j+1} - u_{M-1,j}
\end{Bmatrix}
= dia \left| \frac{\Delta t}{\Delta z^2} \right| \cdot
\left(
\begin{bmatrix}
-2 & 1 & 0 & ... & ... & 0 & 0 & 0 \\
1 & -2 & 1 & 0 & ... & 0 & 0 & 0 \\
0 & 1 & -2 & 1 & ... & 0 & 0 & 0 \\
... & ... & ... & ... & ... & ... & ... & ... \\
0 & 0 & 0 & 0 & ... & 1 & -2 & 1 \\
0 & 0 & 0 & 0 & ... & 0 & 1 & -2
\end{bmatrix}
\cdot
\begin{Bmatrix}
u_{1,j} \\
u_{2,j} \\
... \\
u_{i-1,j} \\
u_{i,j} \\
u_{i+1,j} \\
... \\
u_{M-1,j}
\end{Bmatrix}
\right)
\cdot
\begin{Bmatrix}
C_{v1} \\
C_{v2} \\
... \\
C_{vi-1} \\
C_{v\ i} \\
C_{vi+1} \\
... \\
C_{v\ M-1}
\end{Bmatrix}
$$

$$\underline{\Delta u} \quad = \quad \underline{\underline{h}} \quad\cdot\quad \underline{C_v}$$

(3.19)

For the case of sediments on an impermeable lower boundary, an imaginary lower node is assumed with equal excess pore pressure, $u_{M-1,j} = u_{M+1,j}$ (i.e., no drainage). Then Equation 3.18 becomes:

$$
\begin{Bmatrix}
u_{1,j+1} - u_{1,j} \\
u_{2,j+1} - u_{2,j} \\
... \\
u_{i-1,j+1} - u_{i-1,j} \\
u_{i,j+1} - u_{i,j} \\
u_{i+1,j+1} - u_{i+1,j} \\
... \\
u_{M-1,j+1} - u_{M-1,j}
\end{Bmatrix}
= dia \left| \frac{\Delta t}{\Delta z^2} \right| \cdot
\left(
\begin{bmatrix}
-2 & 1 & 0 & ... & ... & 0 & 0 & 0 \\
1 & -2 & 1 & 0 & ... & 0 & 0 & 0 \\
0 & 1 & -2 & 1 & ... & 0 & 0 & 0 \\
... & ... & ... & ... & ... & ... & ... & ... \\
0 & 0 & 0 & 0 & ... & 1 & -2 & 1 \\
0 & 0 & 0 & 0 & ... & 0 & 2 & -2
\end{bmatrix}
\cdot
\begin{Bmatrix}
u_{1,j} \\
u_{2,j} \\
... \\
u_{j-1,j} \\
u_{j,j} \\
u_{j+1,j} \\
... \\
u_{M-1,j}
\end{Bmatrix}
\right)
\cdot
\begin{Bmatrix}
C_{v1} \\
C_{v2} \\
... \\
C_{vi-1} \\
C_{v\ i} \\
C_{vi+1} \\
... \\
C_{v\ M-1}
\end{Bmatrix}
$$

$$\underline{\Delta u} \quad = \quad \underline{\underline{h}} \quad\cdot\quad \underline{C_v}$$

(3.20)

Notice that the procedure is completely independent of the initial excess pore pressure distribution.

The regularization matrix selected for this study is built to promote linear variation in C_v:

$$\underline{\underline{R}} = \begin{bmatrix} -1 & 1 & 0 & 0 & \dots & 0 & 0 & 0 & 0 \\ 0 & -1 & 1 & 0 & \dots & 0 & 0 & 0 & 0 \\ 0 & 0 & -1 & 1 & \dots & 0 & 0 & 0 & 0 \\ 0 & 0 & 0 & -1 & \dots & 0 & 0 & 0 & 0 \\ \dots & \dots & \dots & \dots & \dots & \dots & \dots & \dots & \dots \\ 0 & 0 & 0 & 0 & \dots & -1 & 1 & 0 & 0 \\ 0 & 0 & 0 & 0 & \dots & 0 & -1 & 1 & 0 \\ 0 & 0 & 0 & 0 & \dots & 0 & 0 & -1 & 1 \\ 0 & 0 & 0 & 0 & \dots & 0 & 0 & 1 & -1 \end{bmatrix} \tag{3.21}$$

Figure 3.9 summarizes the proposed methodology. Knowing $\underline{\Delta u}$ at selected times, Equations 3.19 or 3.20 are used to implement DI, LSS or RLSS inversion techniques as described in Section 3.4.1.

3.4.3 Numerical examples

Several examples with the two boundary conditions are solved to analyze the characteristics and reliability of the proposed methodology, and its numerical behavior (Table 3.5).
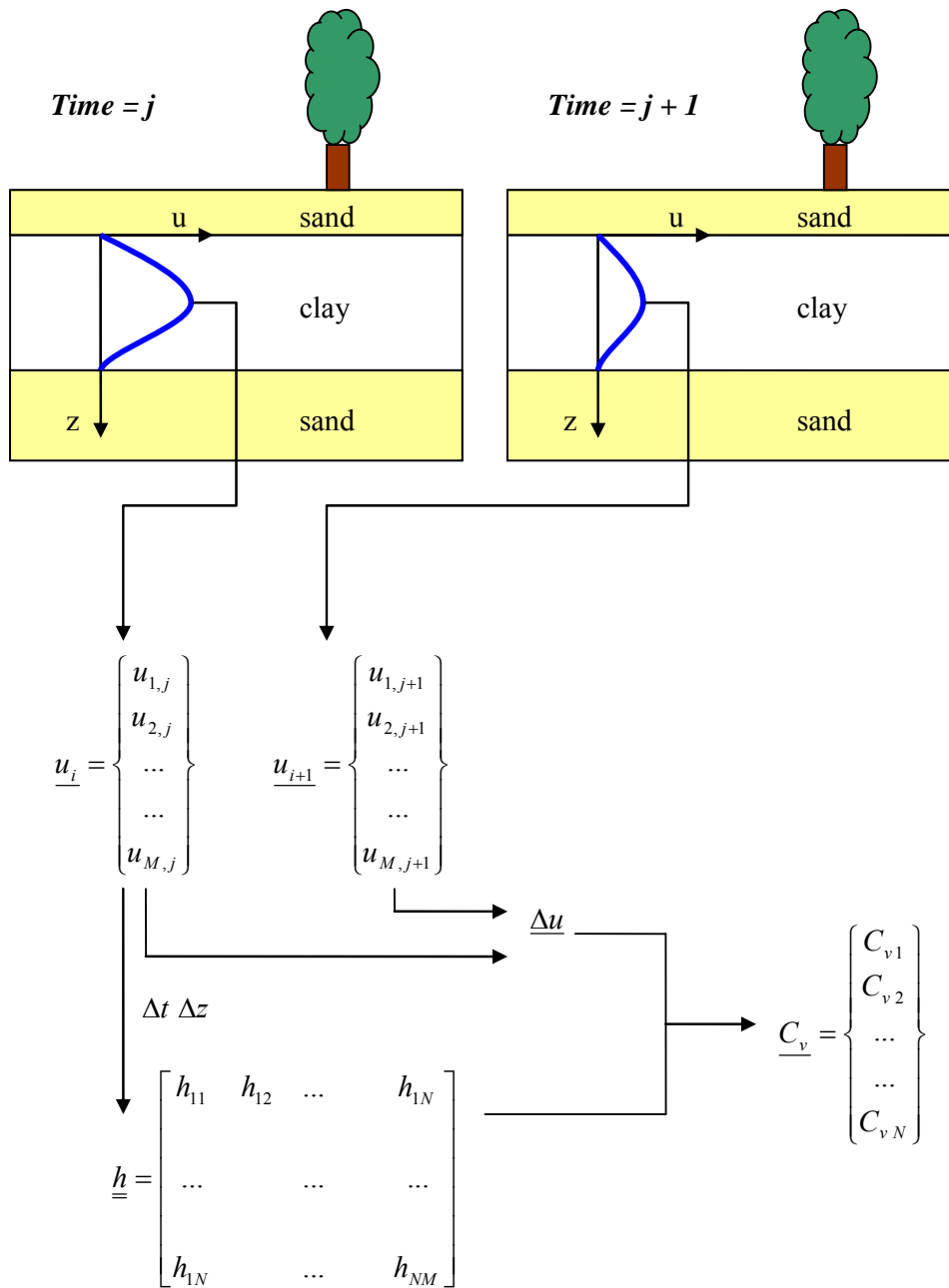
Figure 3.9. Proposed inversion methodology to find the coefficient of consolidation from excess pore pressure data.

Table 3.5. Inverse problem – Cases.

Boundary conditions	Initial excess pore pressure distribution	Number of layers		$\beta^{-1} = \dfrac{C_{v\,bottom}}{C_{v\,top}}$	Objectives
I Double drainage	Rectangular	(a) 1 layer		n/a	- Validate the proposed methodology
		(b) 2 layers		3	- Show the behavior of the answer
		(c) 3 layers		0.4 and 0.67	
		(d) a layer		Linear variation of C_v	
	Triangular	(a) 1 layer		n/a	- Show independency of the initial excess pore pressure distribution
		(b) 2 layers		0.5	- Show sensitivity to Δt and Δz
II Single drainage	Rectangular	(a) 1 layer		n/a	- Validate the proposed methodology - Show influence of T over the inversion
		(b) 2 layers		2	- Show the behavior of the answer for different contrast in C_v
		(c) 2 layers		5	
		(d) 2 layers		10	- Show influence of T over the inversion

Double drainage. Four situations are analyzed all for a uniform initial excess pore pressure: (a) a constant C_v layer; (b) two layers, with different C_v; (c) three layers with different C_v; and (d) linear varying C_v with depth. In all cases, the artificially generated excess pore pressure data are contaminated with random noise. The level of noise is either 1.0 % or 0.5 % in the numerically simulated "measurements".

The time interval under consideration ranges between T= 0.136 and T=0.137. Figure 3.10-a shows inverted C_v results obtained for case (a) in Table 3.5. The value of C_v is normalized with respect to the actual value. The optimal value of λ for the RLSS is determined as shown in Figure 3.11: the goal is to satisfy the data (minimum $\underline{e}^T \cdot \underline{e}$) and the regularization criterion $\min(\underline{u} - \underline{\underline{R}} \cdot \underline{u})$, while obtaining physically meaningful values of C_v.

Figure 3.10 shows the results obtained for the first four cases in Table 3.5. It can be concluded that the RLSS gives a reasonable approximation to true values of C_v. However, the prediction weakens when sudden variations of C_v are attempted (Figure 3.10-c). For the case of linear variation of C_v (Figure 3.10-d), the computed values of C_v tend to be more accurate and more independent of the noise level in $\underline{u}$. Finally, a smoother variation in the C_v values along depth is more easily inverted.

Noise level = 0.5% in u_e data   Noise level = 1.0% in u_e data

72
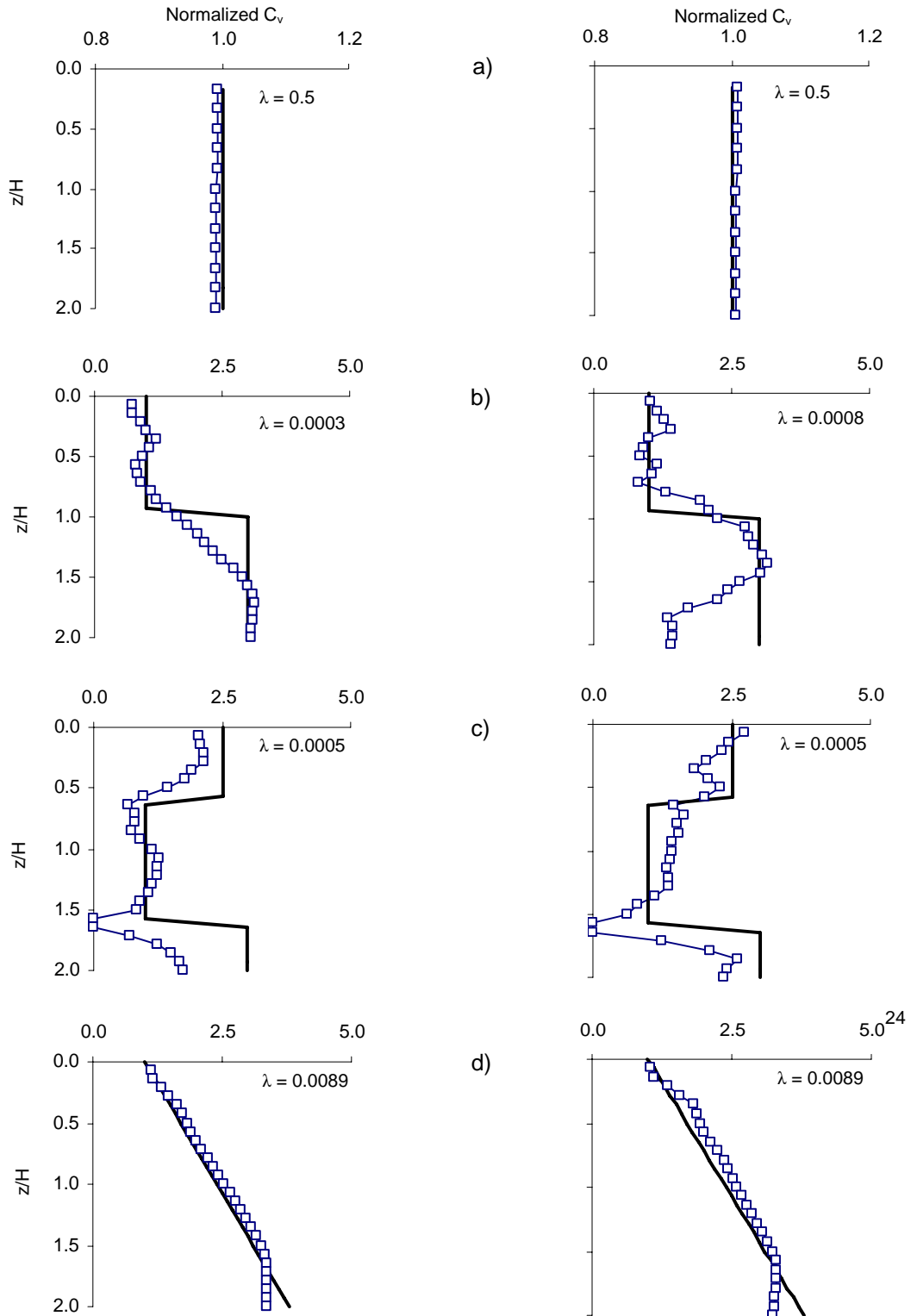
Figure 3.10. Inversion results for double drainage and two noise levels. a) Single C_v layer, using RLSS (squares). The "perfect solution" should be 1 (solid lines). b) Two layers. c) Three layers. Notice different coefficients of regularization λ. d) Linearly increasing coefficient of consolidation C_v.
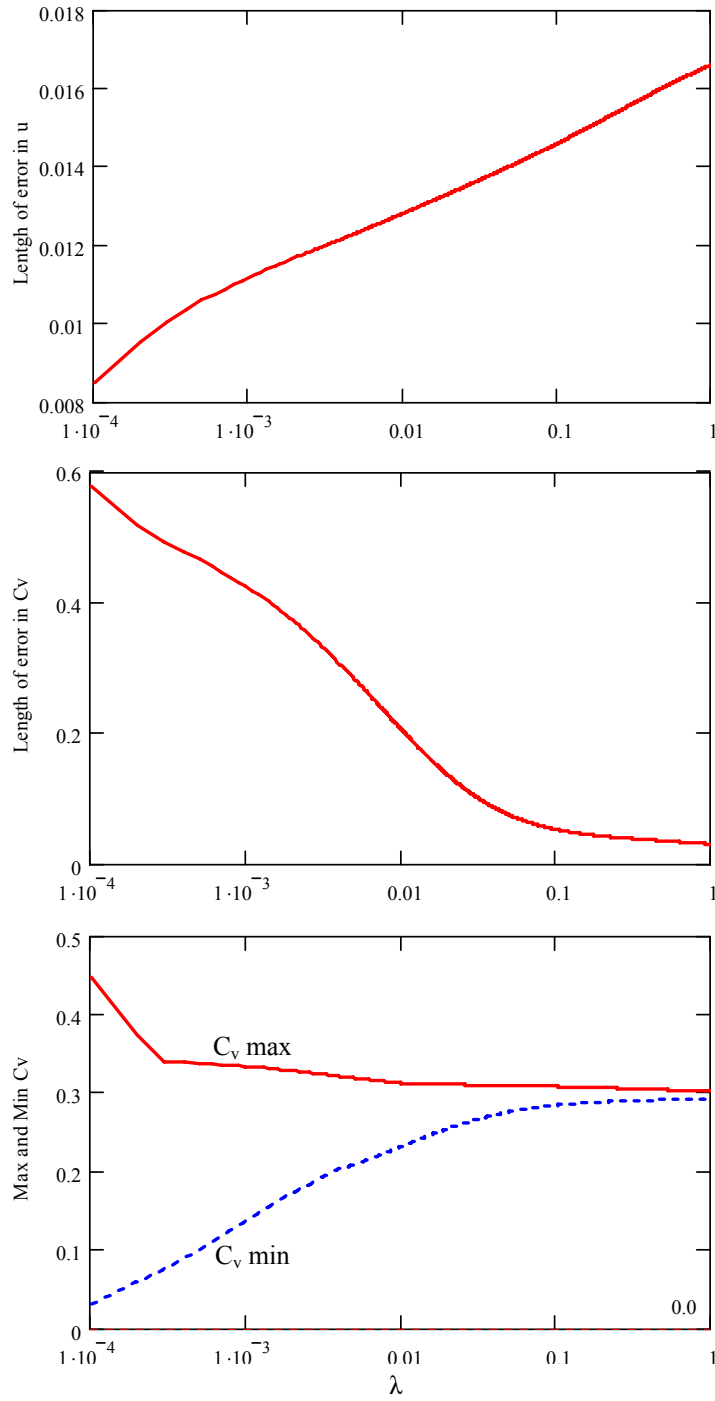
Figure 3.11. Determination of non-negative regularization coefficient λ for the case of a triangular initial excess pore pressure distribution (single clay layer).

Initial pore pressure distribution. The forward finite difference computation can be applied to any initial pore pressure distribution. Therefore, one must wonder whether the proposed inversion applies as well. Two double drainage cases are analyzed with initial triangular excess pore pressure distribution: (a) a single layer with constant C_v, (b) a two-layer system with $C_{v\,bottom}/C_{v\,top} = 0.5$ (see Table 3.5, Boundary condition I, Triangular initial excess pore pressure distribution).

The time interval under consideration ranges between T= 0.136 and T=0.137. Figure 3.12-a shows the results for the single layer. The C_v profile is adequately determined from the vector of $\underline{\Delta u}$ regardless of the initial pore pressure distribution. Note that drainage condition at boundaries must be known to define $\underline{\underline{h}}$ (Equation 3.20).

Figure 3.12-b summarizes a series of results for different Δt that were employed in the computation. The inversion is not sensitive to the chosen Δt and it seems to be independent of the stability criterion given for the forward simulation in Equation 3.3. Besides the time savings with matrix inversion techniques, the independency between Δt and Δz is an advantage over the successive forward simulation technique. When the forward simulation uses the less-stable explicit form of the finite difference method, the solution may be unstable and could never be reached.

The matrix inversion does not work for large Δt or Δz values. Hence, the time and depth increments have to be chosen within meaningful physical limits of the studied process. For example, it does not make sense to choose a Δt of the same order of magnitude as the consolidation time (i.e., H^2/C_v).
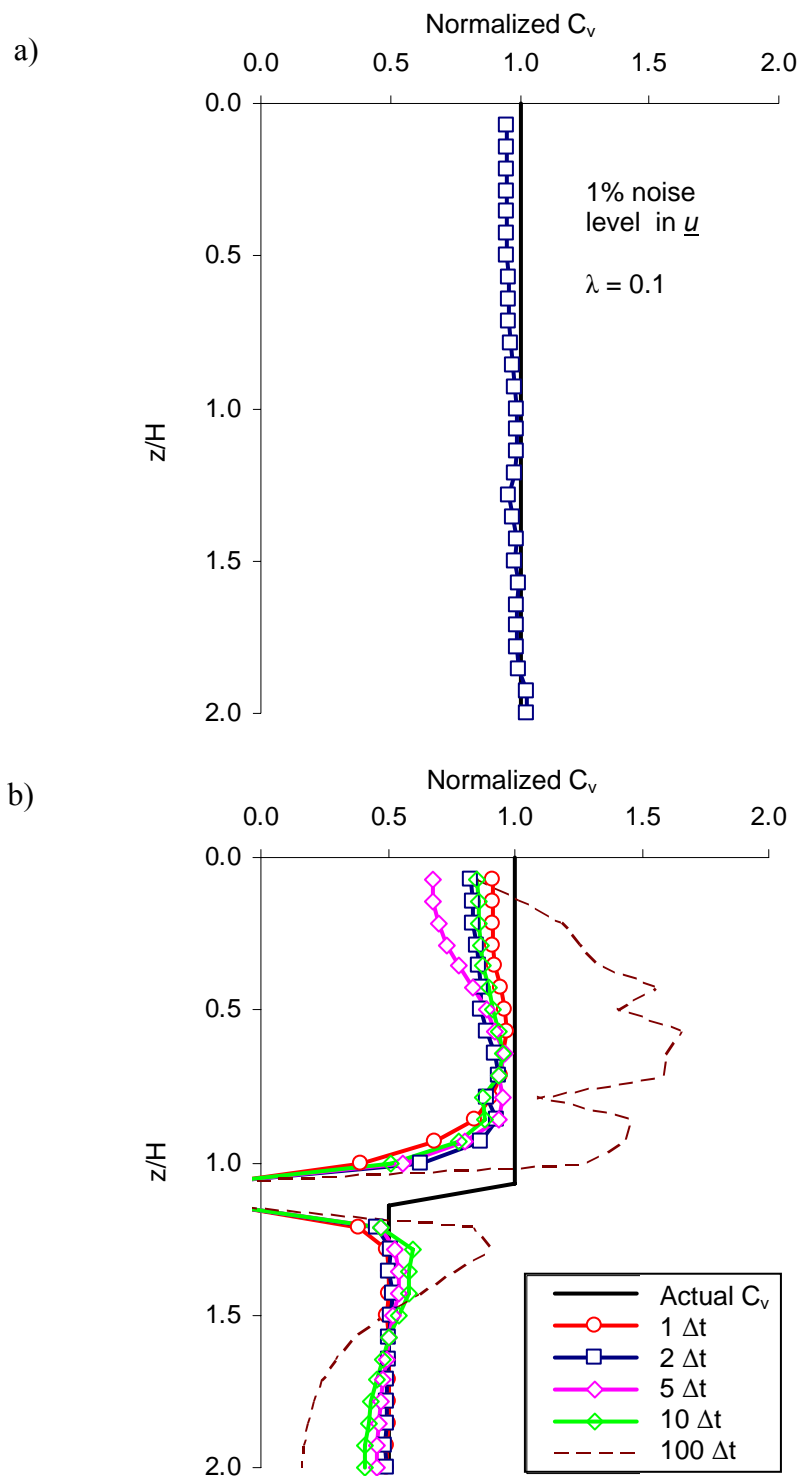
Figure 3.12. RLSS inversion results for triangular initial excess pore pressure distribution and double drainage. a) Single layer. b) Two-layer systems. Several Δt values are used in the inversion.

Single drainage. Four new cases are analyzed for uniform initial excess pore pressure: (a) a single layer with a constant C_v is solved to validate the proposed methodology using Equation 3.20 for simple drainage; (b) a two-layer system with $C_{v\,bottom}/C_{v\,top} = 2$; (c) a two-layer system with $C_{v\,bottom}/C_{v\,top} = 5$; and (d) a two-layer sediments with $C_{v\,bottom}/C_{v\,top} = 10$ (see Table 3.5, Boundary condition II, rectangular initial excess pore pressure distribution). These cases allow us to see the behavior of the inversion for different contrast in the C_v values along depth. In all cases, the analysis is performed for a time factor T=0.136 and with the same noise level 0.025% in the simulated measurements.

Figure 3.13-a shows the results for the single layer case (a). Figure 3.13-b shows a summary of the results using the RLSS method for cases (b), (c) and (d). It can be noticed that the larger the relation between upper and lower C_v values, the bigger the dispersion of the results becomes. In addition, the estimation of an adequate value of regularization coefficient λ becomes more difficult.

3.4.4 Observations and implications on inversion

It is not possible to invert the problem with only one excess pore pressure profile gathered at a selected time to obtain $C_v(z)$. Instead, it is necessary to consider either two sets of data, measured at two different times t_j and t_{j+1}, or the applied load (i.e., known a u_e at time t=0) and a u_e profile at a later time.
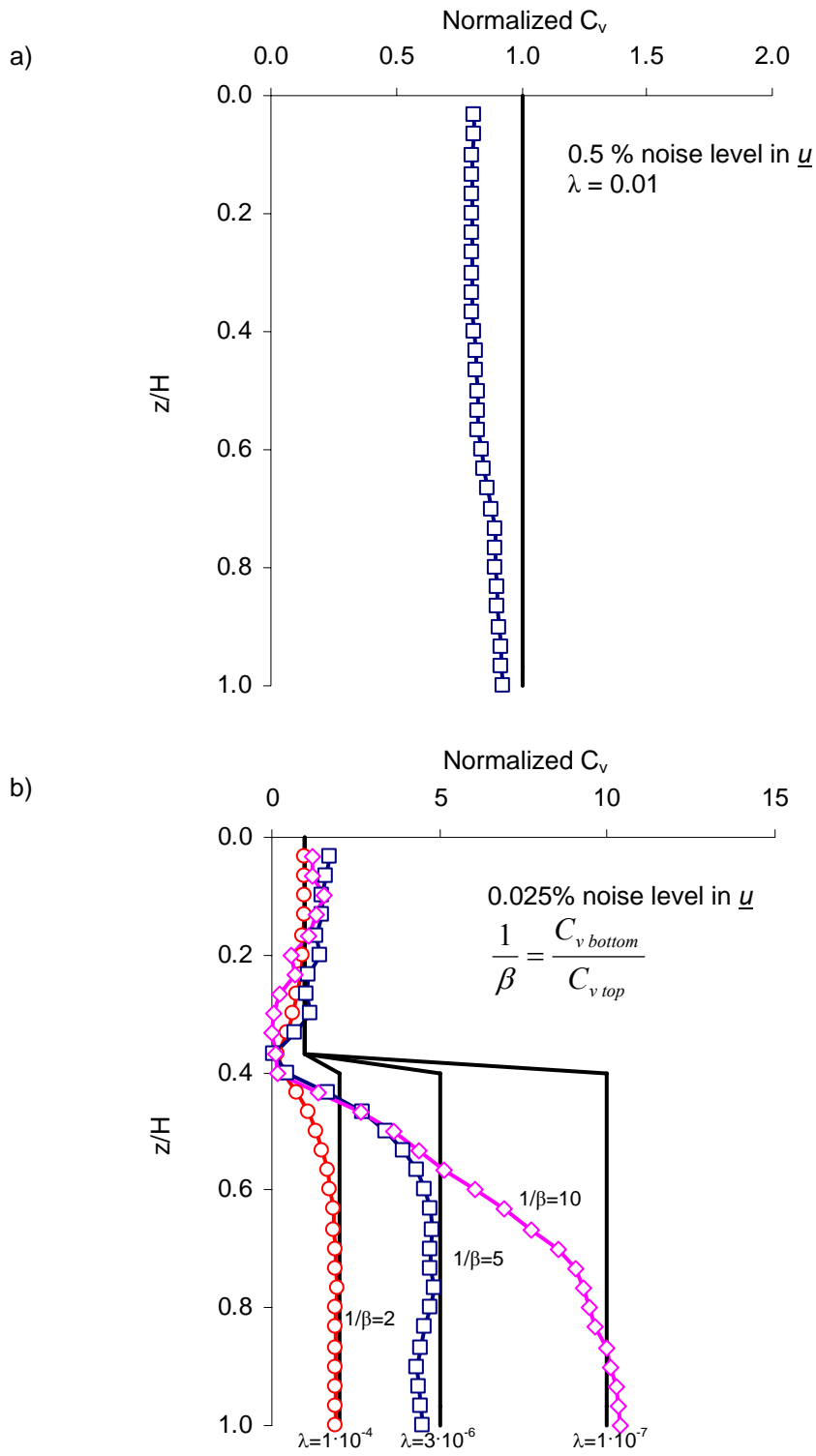
Figure 3.13. Inversion results for single drainage (at T=0.136). a) Single layer. b) Summary of the results using RLSS methodology for two layers with different C_v.

The oscillation in the inversion of C_v observed at the interface in two-layer systems, is a consequence of the first order accuracy of the model used, which in fact does not satisfy the maximum principle (Thomas 1995); however, the inversion self-heals in the process due to the small domain of dependence (i.e., this explicit model uses only information from three discrete points). An alternative model for the matrix $\underline{\underline{h}}$ could be obtained by considering a scheme with higher order of accuracy such as the implicit scheme (Table 3.3). The algebraic manipulation of the implicit scheme for double drainage leads to:

$$
\begin{Bmatrix} C_{v1} \\ C_{v2} \\ \dots \\ C_{v\,i-1} \\ C_{v\,i} \\ C_{v\,i+1} \\ \dots \\ C_{v\,M-1} \end{Bmatrix}
= \frac{\Delta t}{\Delta z^2} \cdot
\begin{bmatrix}
u_{1,j}-\dfrac{u_{2,j}}{2} & 0 & 0 & \dots & \dots & 0 & 0 & 0 \\
-\dfrac{u_{1,j}}{2} & u_{2,j}-\dfrac{u_{3,j}}{2} & 1 & 0 & \dots & 0 & 0 & 0 \\
0 & -\dfrac{u_{2,j}}{2} & u_{3,j}-\dfrac{u_{4,j}}{2} & 1 & \dots & 0 & 0 & 0 \\
\dots & \dots & \dots & \dots & \dots & \dots & \dots & \dots \\
0 & 0 & 0 & 0 & \dots & \dfrac{u_{M-3,j}}{2} & u_{M-2,j}-\dfrac{u_{M-1,j}}{2} & 0 \\
0 & 0 & 0 & 0 & \dots & 0 & \dfrac{u_{M-2,j}}{2} & u_{M-1,j}-\dfrac{u_{M,j}}{2}
\end{bmatrix}
\cdot
\begin{Bmatrix} u_{1,j+1}-u_{1,j} \\ u_{2,j+1}-u_{2,j} \\ \dots \\ u_{i-1,j+1}-u_{i-1,j} \\ u_{i,j+1}-u_{i,j} \\ u_{i+1,j+1}-u_{i+1,j} \\ \dots \\ u_{M-1,j+1}-u_{M-1,j} \end{Bmatrix}
$$

$$\underline{C_v} \quad = \quad \underline{\underline{h}}^{-1} \quad \cdot \quad \underline{\Delta u}$$

$$(3.22)$$

Equation 3.22 provides more accurate results for smooth variations of the coefficient of consolidation with depth. However, it tends to smoothen the solution, even without regularization, due to the infinite domain of dependence (i.e., the scheme considers

information from all the discrete points in the domain). Consequently it can not handle step variations of C_v more precisely than Equation 3.19.

Information about initial conditions is gradually lost as time passes (T increases). The influence of time when the data are collected to solve for C_v is explored in Figure 3.14: double drainage, two-layer system with different $C_{v\,bottom}/C_{v\,top}$ ratios. The same matrix inversion methodology is used. The data $\underline{u}$ do not include noise. Figure 3.14 shows the computed C_v at the midpoint of each layer versus the dimensionless time factor T. Results show that inversion is not possible or accurate at the very beginning of the consolidation process (because $\underline{\varDelta u}$ becomes very small and leads to singularities) or late in the process (numerical error magnification). In other words, information is lacking in both extremes of time $T \to 0$ or $T \to \infty$.

The inversion weakens when the ratio between coefficients of consolidation increases (Figure 3.14). A larger error is induced over the bottom layer (higher C_v) because $\underline{\varDelta u}$ becomes smaller.

The error in the inverted C_v is computed versus the time factor T for the case of a single layer on an impermeable bed (single drainage conditions), and noisy $\underline{u}$ data. A comparison of these errors with the time factor at different noise levels is shown in Figure 3.15. Previous observations are corroborated with these results. Furthermore, the addition of random noise causes high errors in the inverted C_v profiles, even at small time factor values. Therefore, the inversion problem is sensitive to the presence of noise in $\underline{u}$, particularly when u_e values are measured after $T>1$.
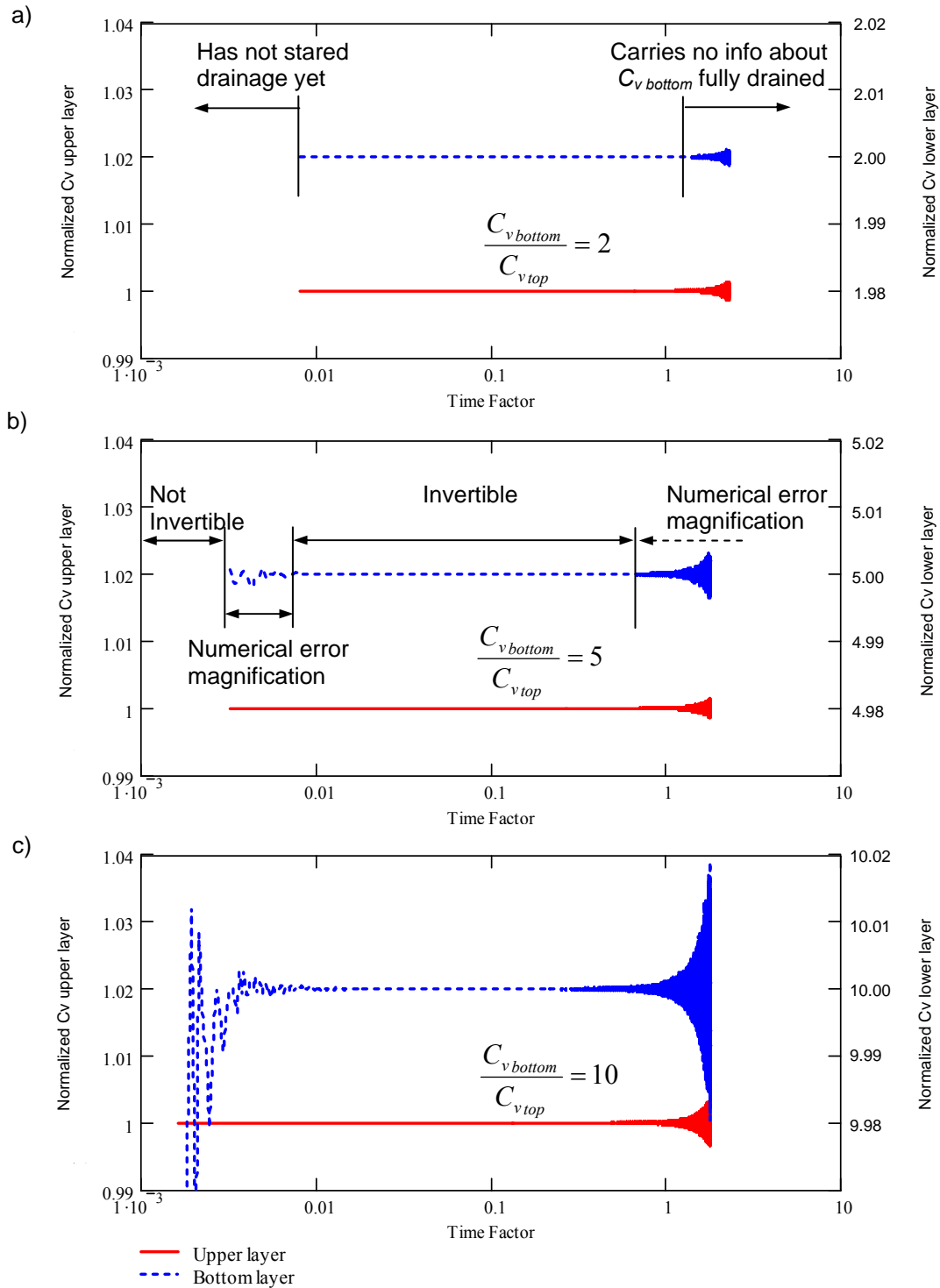
Figure 3.14. Inversion of C_v at different times (Single drainage, two-layer sediments, no noise. a) β=0.5 and Δt=0.15yr. b) β=0.2 and Δt=0.06yr and c) β=0.1 and Δt=0.03yr.
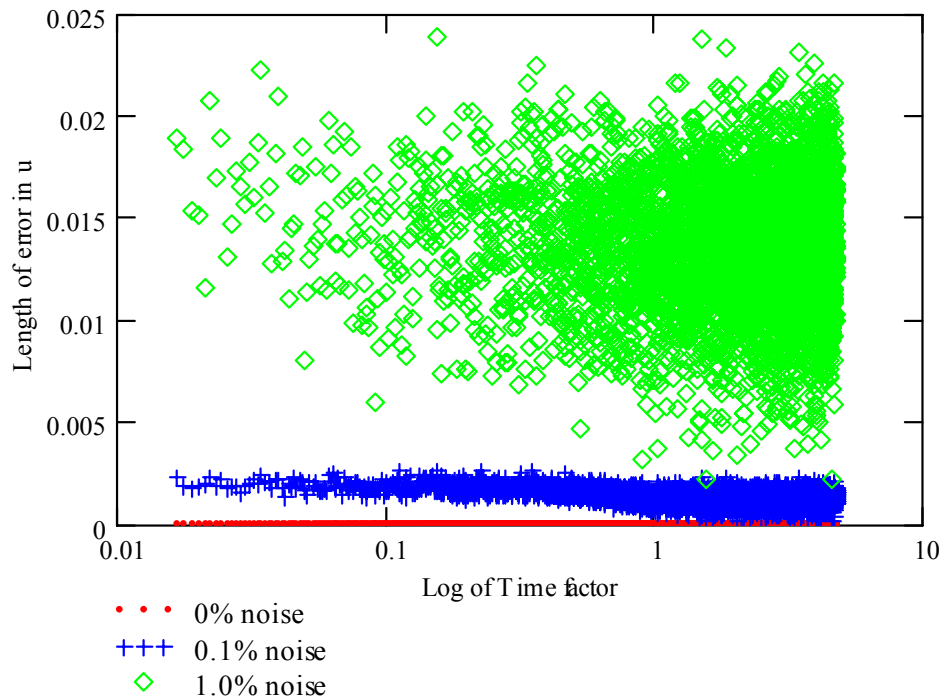
Figure 3.15. Error in the excess pore pressure for the single layer problem, with single drainage and constant initial excess pore pressure, for different noise levels: 0.0 %, 0.1 % and 1.0 %.

3.5 APPLICATIONS IN PRACTICE – DISCUSSION

Several numerical schemes are tested and the Crank-Nicholson scheme has proven to be valuable since results are unconditionally stable for the forward problem. However, it is computationally more expensive than other schemes.

The inverse approach explored above can be applied to real situations where field $\underline{u}$ data is available to infer the in situ values of C_v and its spatial variability. However, extensive field monitoring is required. Piezometric data at one location for long periods of time can also be used, and complemented with sedimentation data.

Knowing two sets of $\underline{u}$ along depth at two different times is the minimum requirement to find C_v. The step-by-step procedure for inverting field data follows (Figure 3.16, case: three $\underline{u}$ profiles separated by Δt): 1) arrange excess pore pressure u values in three vectors $\underline{u}_j$, $\underline{u}_{j+1}$ and $\underline{u}_{j+2}$ for each time j, $j+1$ and $j+2$, 2) build a sub-matrix $\underline{\underline{h}}_k$ with the first pair of $\underline{u}$ (i.e., $\underline{u}_j$ and $\underline{u}_{j+1}$) and with their corresponding Δt and Δz following Equation 3.19 or Equation 3.20 depending on the boundary conditions, 3) repeat the procedure for a second $\underline{u}$ pair, either for $\underline{u}_{j+1}$ and $\underline{u}_{j+1}$ obtaining sub-matrix $\underline{\underline{h}}_{k+1}$, or for $\underline{u}_j$ and $\underline{u}_{j+2}$ obtaining $\underline{\underline{h}}_{k+2}$; use the corresponding Δt between measurements, 4) build the matrix $\underline{\underline{h}}$ stacking the sub-matrices, and the vector $\underline{\Delta u}$ stacking the corresponding $\underline{\Delta u}_k$ vectors in the same order as $\underline{\underline{h}}$, 5) find the solution for C_v using LSS and RLSS (DI is not applicable because $\underline{\underline{h}}$ will not be square). Notice that Δz is the same in all cases, but Δt can vary.

3.6 CONCLUSIONS

The effect of the inherent spatial variability in soils on diffusion problems was addressed in this chapter, for the special case of 1-D consolidation. Both forward and inverse conditions are investigated through numerical simulations. The following conclusions are drawn:

- The dissipation in the higher Cv layer takes place faster as $\beta = C_{v\,top}/C_{v\,bottom}$ in bi-layer systems and $\delta = C_{v\,top}/C_{v\,bottom}$ in linearly-varying systems increases, yet, it is restricted by the layer of lower coefficient of consolidation.

83
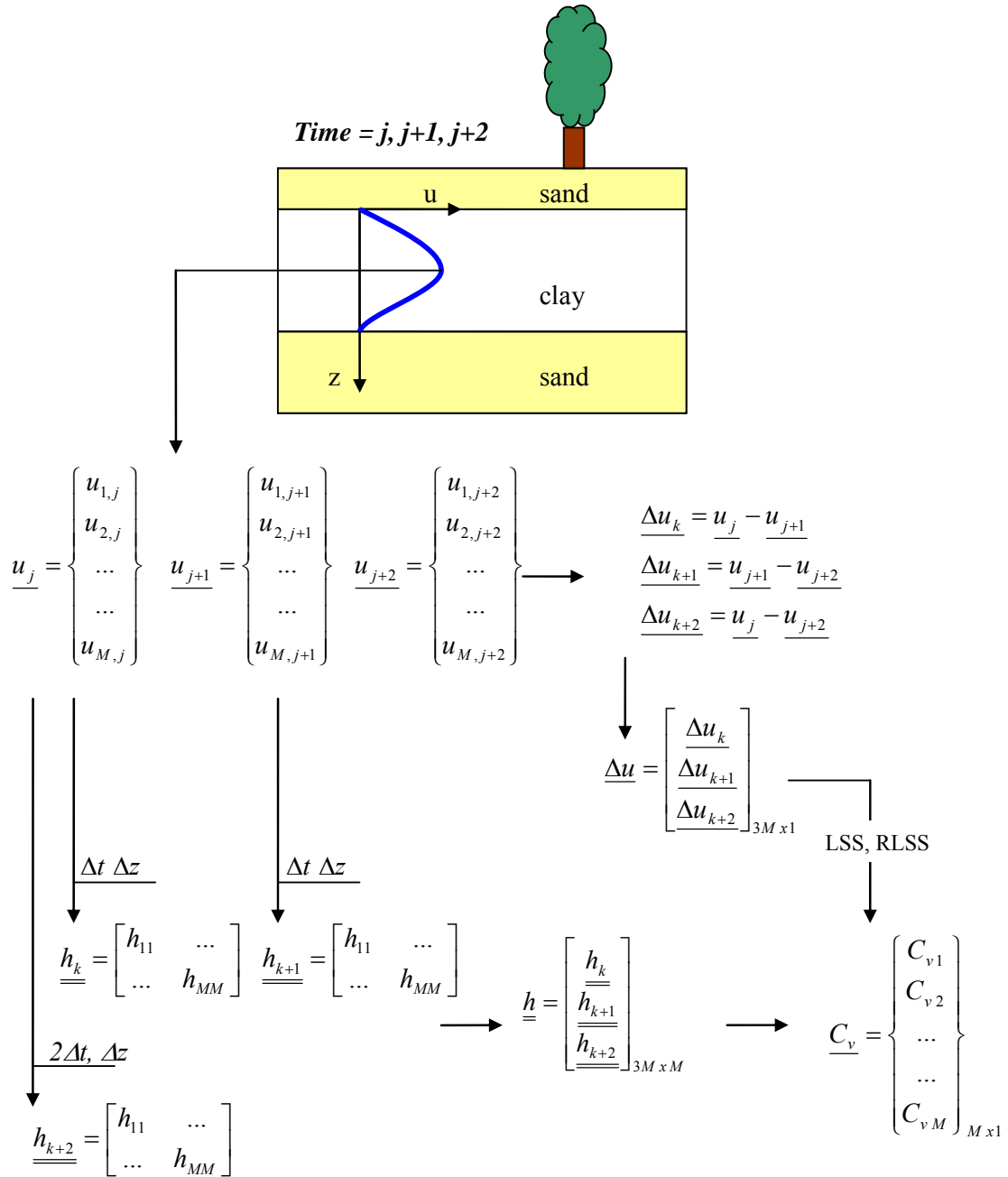
Figure 3.16. Implementation – Proposed methodology to find the coefficient of consolidation from multiple excess pore pressure data.

- The $\partial u / d(z/H) \neq 0$ at the interface between layers indicates that water flow is taking place at the interface, and thus, interaction between layers occurs.

- The time and depth variation of excess pore pressure can be used to infer the coefficient of consolidation C_v and its spatial variation in the subsurface.

- The data can be inverted using a finite difference approximation even when the convergence in the forward numerical solution is unstable.

- This inverse problem is highly sensitive to the presence of noise.

- Regularized least squares is generally preferred, and it reduces the effects of noise in the data. The value of the optimal regularization coefficient λ depends on the noise level and C_v profile.

- The u_e-profile lacks information at very short or very large T values. Therefore, the inversion of C_v improves with data gathered at intermediate T values.

- The uncertainty in inverted values increases with increasing range of C_v values in the soil profile.

CHAPTER IV

TERMINAL DENSITY – IMPLICATIONS TO DYNAMIC SETTLEMENT

4.1 INTRODUCTION

There are five states or phases of matter: Bose-Einstein condensate, solid, liquid, gas, and plasma. The extreme zero-energy Bose-Einstein condensates consist of unexcited, cold atoms with distinct geometry and density at near absolute zero temperature. At warmer temperatures, solids hold their own shape while liquids acquire the geometry of the container; both have a well defined density and present low compressibility. On the other hand, gases have neither a fixed geometry nor density, and can fill a container of any size and shape. Finally, plasmas are made of free electrons and ions (e.g., Northern Lights) and are obtained from gases at high energy. Energy in the form of temperature, pressure or vibrations prompts phase transformations. Figure 4.1 summarizes the states of matter in relation to energy level.

Soils are particulate materials made of solid mineral grains and fluids (gases and liquids). Particulate materials behave like no other material at any phase condition. They can respond as solids when confined, flow like liquids on a ramp and occupy different volume like gases (Savage 1994; van Hecke 2005). In particular, it is not possible to define a characteristic stable density for soils in most cases (Makse and Kurchan 2002).
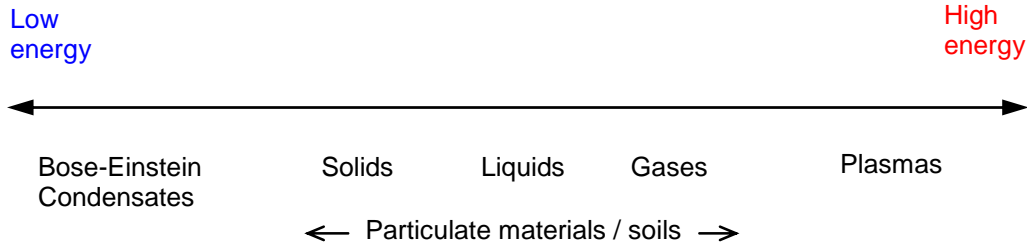
Figure 4.1. States of matter in Nature and their inherent energy level. Soils are mixtures of solids, liquids and gases; yet, soil properties differ from each of its components.

Instead, it appears that each process prompts a characteristic density and internal fabric if extended long enough. The associated fabric condition supports continuation of the process at constant volume or "terminal density" ρ_t. We can readily identify various examples of process-dependant terminal densities.

Large-strain monotonic loading. Figure 4.2 shows a schematic representation of the fundamental results obtained by Casagrande in 1936. Loose and dense specimens tend to reach the same critical state void ratio e_{cs} and residual strength τ_{cs} upon large-strain shearing. The values of e_{cs} and τ_{cs} are functions of the mean effective stress, and define the critical state line *CSL* in the *e-p'-q* space (Schofield and Wroth 1968). The critical state void ratio or critical density is an example of terminal density for shearing processes at large-strain.

Intense vibration (and loading) versus vibration-less fabric formation. Processes involving vibrated granular materials exhibit a steady state density reached at certain acceleration and frequency of vibration (Nowak et al. 1998; Brey et al. 2000; Prados et al.

87

2000). In particular, the procedural definitions of the maximum and minimum void ratios e_{max} and e_{min} are also the terminal densities for the processes specified in ASTM D 4254 and ASTM D 4253 respectively.

Quasistatic loading. A loaded soil deforms and settles a finite quantity, defining a new final density, in this case $e_t=f(e_0, C_c, C_r, \Delta\sigma')$.

Impact based remolding. Each Proctor curve represents the terminal densities for a given imposed energy as a function of moisture content.
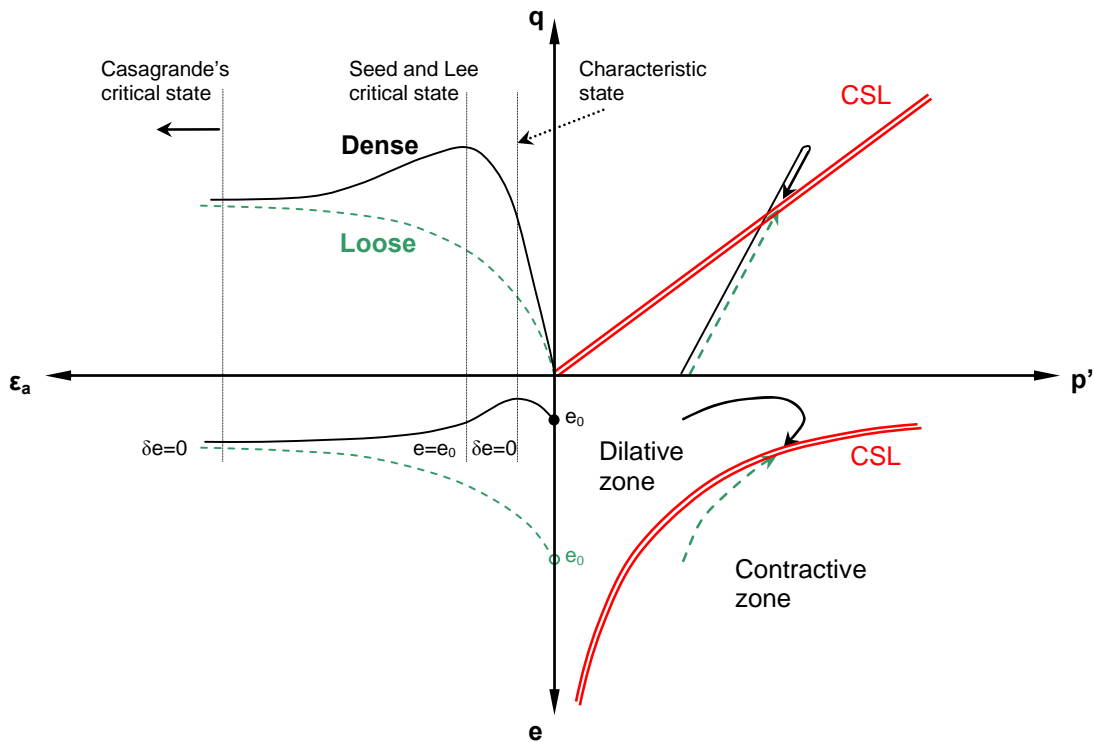
Figure 4.2. Typical stress-strain-strength response for dense and loose packings.

Particle crushing. Massive crushing in sands occurs at high stresses, say 7MPa to 15MPa (Terzaghi et al. 1996; Nakata et al. 2001). Particle crushing contributes to volume contraction and affects dilatancy (Valdes 2002). The volume contraction due to crushing redistributes force chains, which leads to new crushing. The terminal density ρ_t is attained when the process stabilizes and no more crushing occurs.

The hypothesis in this chapter is that there exists a unique terminal density for every process imposed on a given granular material. The research starts with a comparative study of monotonic and cyclic loading. Then, the concept of terminal density is applied to the analysis of seismic induced settlement.

4.2 TERMINAL DENSITY – MONOTONIC VERSUS CYLIC PROCESSES

Monotonic and repetitive cyclic processes lead to different terminal densities. Consider the monotonic loading data in Figure 4.3. Contraction takes place at small-to-intermediate strains, typically $\gamma < 0.1$, even in large-strain dilative soils (i.e., the large-strain behavior is dependent of the initial void ratio e_0 and the initial effective stress σ_0'). These results suggest that small-to-intermediate stain contraction should be expected in most sands.

Shear induced volume change in soils with void ratio $e < e_{cs}$ is the result of two competing mechanisms: 1) slip down and 2) roll-over (Dafalias 1993; Ishihara 1996; Mueth et al. 2000). The slip down movement of particles provokes an overall volume contraction, while the roll over mechanism produces an increase in the total volume, i.e., dilation. The cyclic strain level plays a critical role on the attainable terminal density and
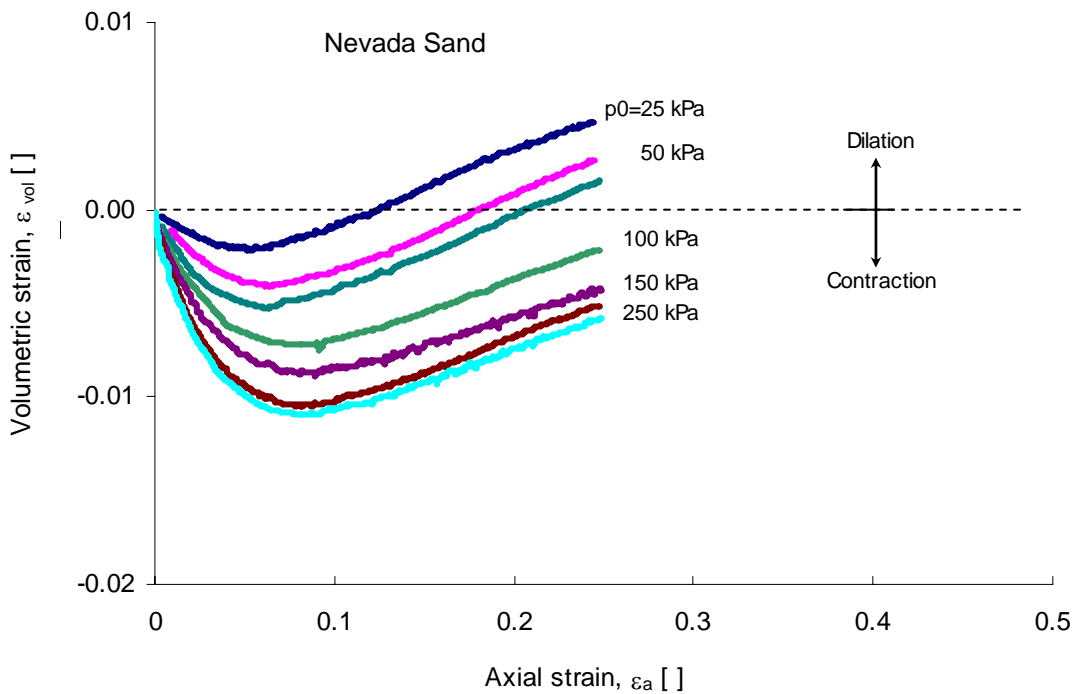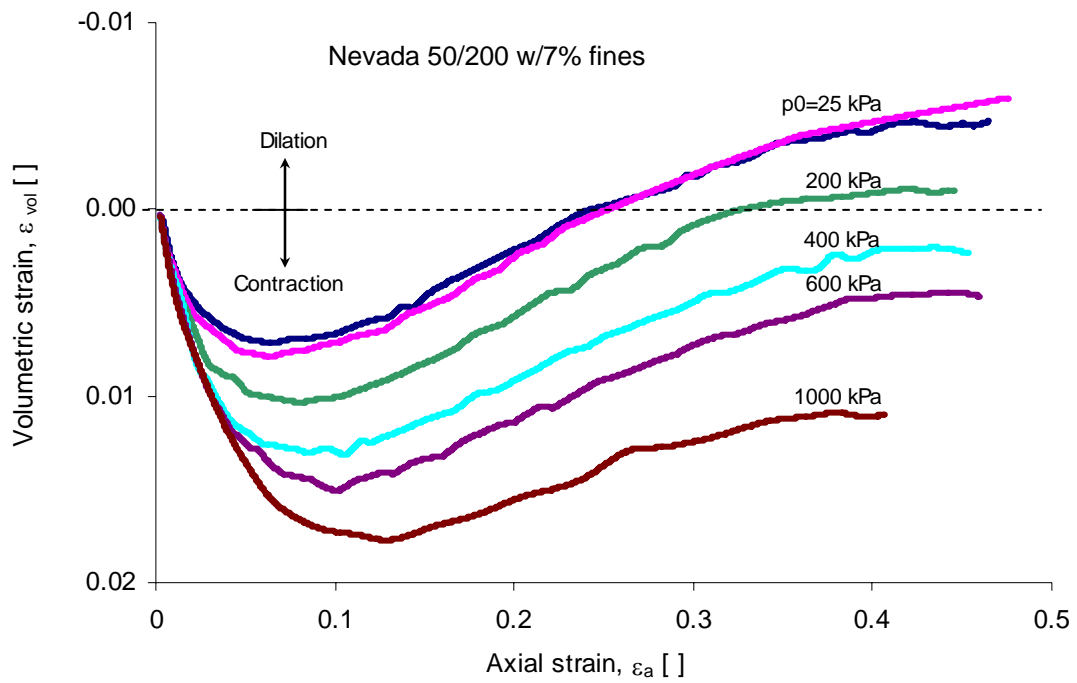
Figure 4.3. Example of initial densification in dilative soils: Nevada sand (data from Yamamuro et al. 1999, Nevada 50/200 w/7% fines; and Norris 1999, Nevada sand) .

the rate of volume change. Then, what is terminal density that a sand can reach when a small-to-intermediate strain cyclic load is applied under drained conditions?

In this section, we explore in detail early volume contraction in monotonic loading. Then, we investigate its implications on terminal density during small-to-intermediate strain cyclic loading.

4.2.1 Monotonic loading – Early volume contraction – Numerical

Consider the early contraction portion in Figure 4.3. The influence of initial void ratio is revealed using the NorSand model (Jefferies and Shuttle 2002, 2005). A consolidated drained axial compression triaxial test is simulated using typical sand parameters, Γ=0.817, slope λ=0.014 (in base e=2.718), rigidity index I_r=600, and Poisson's ratio ν=0.2. Figure 4.4 shows the simulated typical response of the dilative sandy soil at different initial void ratios. For a constant confining stress (σ_h'=300kPa), the soil reaches the minimum void ratio (called characteristic state) at a larger strain level for looser sands (i.e., higher initial void ratio). The dashed line in the figure indicates such points where $\partial e/\partial \varepsilon = 0$ (refer to Figure 4.2 for a definition of characteristic state).

Simulations using the Cam Clay model show similar results on the early contractive behavior of dense (i.e., overconsolidated) soils up to the characteristic state (programmed in Mathcad by A. Bayoumi, 2006). In this case, the soil parameters corresponds to a sand with M=1.24, λ=0.014, κ=0.0024, ν=0.28 and Γ=0.391 at 1kPa. Figure 4.5 shows a summary of these results (24 runs). The initial void ratio e_0 and the void ratio at maximum contraction e_{mc} are presented for different initial void ratios and

91
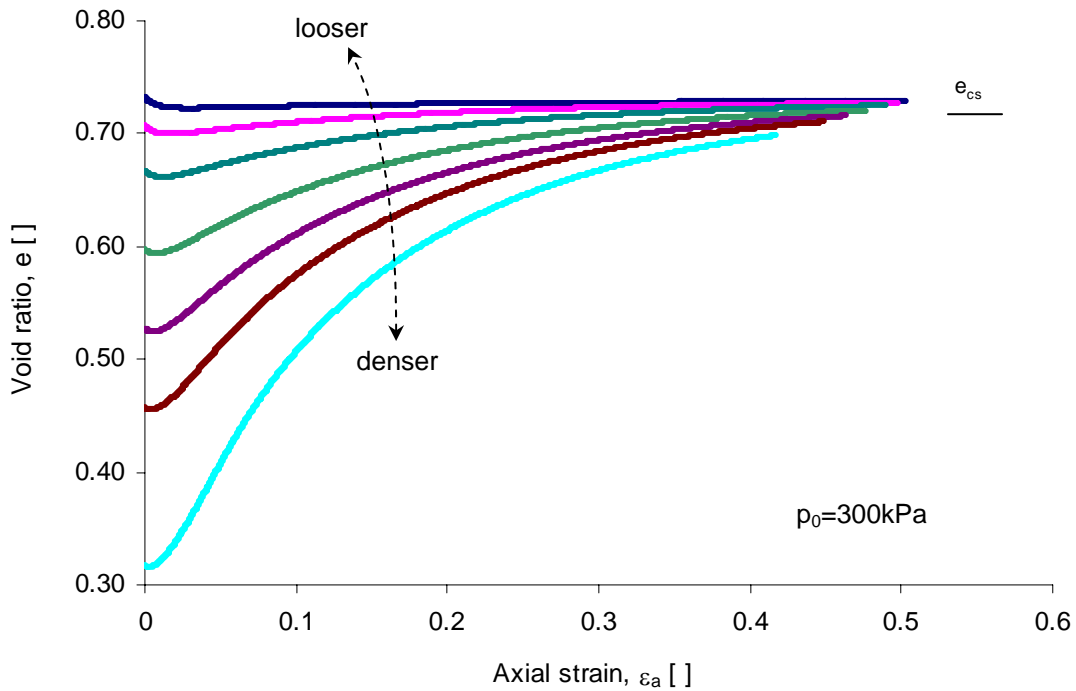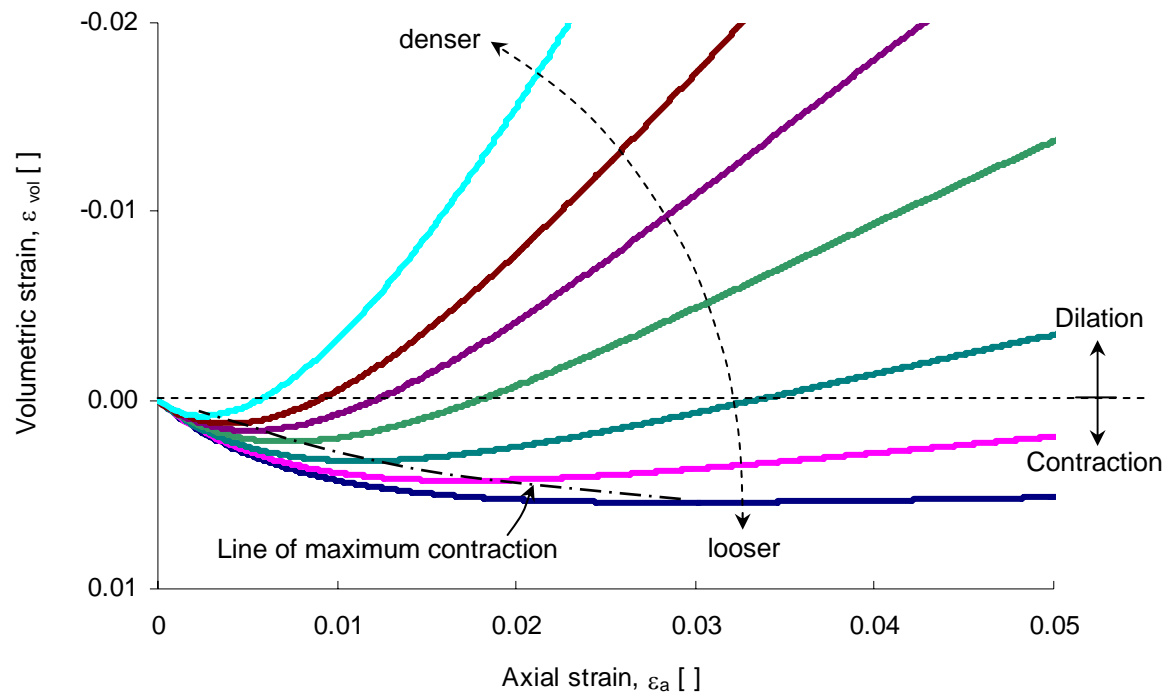
Figure 4.4. Effect of initial void ratio on contractive behavior of dilative sands – Numerical simulations (NorSand model with Γ=0.817, λ=0.014, I_r=600, and ν=0.2).

initial mean effective stress. The void ratios between the e_0 and e_{mc} at different shear strain levels are also shown.
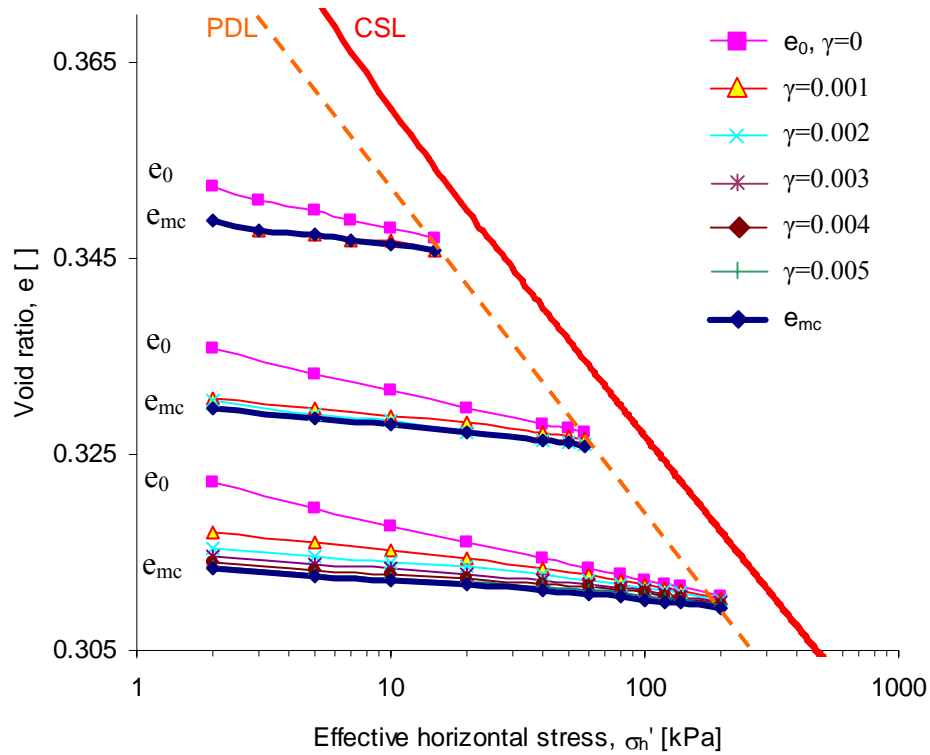
Figure 4.5. Evolution of void ratio e during axial compression before dilation as a function of initial void ratio and effective confinement σ_h' – Numerical simulations (Cam clay model with M=1.24, λ=0.014, κ=0.0024 Γ=0.391, and v=0.28).

The following observations can be made: 1) shear-based densification is possible in large-strain dilative soils, since there is contraction at small-to-intermediate strains, 2) a looser soil reaches the characteristic state at higher strain levels, 3) the terminal void

93

ratio at a given shear strain level decreases as the initial void ratio decreases (whenever below the strain level of characteristic state), 4) between the critical state line *CSL* and the pure dilation line *PDL*, there exists a region where there is no detectable contraction, 5) the higher the initial mean effective stress p_o', the lower the incremental densification. In other words, the change in void ratio in the strain range below the corresponding characteristic state is larger at lower confinement, 6) however, for a low void ratio soil, the material experiences contraction for a larger range of shear strain than for a high void ratio soil as a result of overconsolidation (Figure 4.5), 7) there is not a single terminal density line. In fact, terminal density lines associated to each shear level depends on the initial void ratio, the amount of shear strain imposed and the confining pressure.

The general observation is that the larger the shear strain, the larger the contraction the soil experiences before its threshold strain for contraction.

4.2.2 Cyclic loading – Small-to-intermediate strain – Numerical

The implications of early volume contraction on small-to-intermediate cyclic straining are explored using numerical simulations first.

The question addressed in this section centers on the maximum density o minimum void ratio attainable in cyclic drained axial contraction triaxial tests, for a given initial void ratio and a certain effective stress. The simulation sequence follows. A specimen with initial void ratio $e_0^{<0>}$ is sheared in a simulated axial compression triaxial test. The void ratio is obtained as a function of axial strain. Then, a new test is run on a specimen with initial void ratio equal to the minimum void ratio in the first test

94

$e_0^{<1>} = e_{min}^{<0>}$. The process is repeated until no more contraction is induced by shearing, in which case densification no longer takes place.

A drained axial compression triaxial test is simulated using typical sand NorSand parameters (Γ=0.817, slope λ=0.014, rigidity index I_r=600, and Poisson's ratio ν=0.2). Figure 4.6-a shows the first 20 cycles for a specimen with initial void ratio $e_0^{<0>} = 0.747$ and initial mean effective stress p_0'=100kPa. The enlarged view shows the numerical procedure followed to obtain the maximum attainable density.

For comparison, the simulation is repeated by starting the next cycle at the void ratio reached at different fixed strain levels. Figure 4.6-b, Figure 4.6-c and Figure 4.6-d show the evolution of densification for cyclic peak strain ε_a=0.5%, 1.5% and 5% in all cases for specimens with initial void ratio $e_0^{<0>} = 0.747$. Figure 4.7 presents the variation of void ratio with the number of cycles for all four cases; the bottom line (green rhombus) represents the desired lower bound attained by reversal at the optimum minimum strain.

This approach has limitations. For example, dynamic effects are not captured with the NorSand model and zero volumetric strain ε_{vol}=0 during reversal rarely happens. However, results support insightful observations. Small-to-intermediate cyclic strain loading can bring a soil well into the dilative zone by reducing its initial void ratio. The lower bound found in these simulations corresponds to cyclic straining to the characteristic state in each cycle, and produces maximum densification in the smallest number of events. Figure 4.6-d suggests that practical applications would better operate at $\varepsilon<\varepsilon_{opt}$ than $\varepsilon>\varepsilon_{opt}$ to attain maximum densification. Different terminal densities are reached as a function of cyclic strain amplitude.
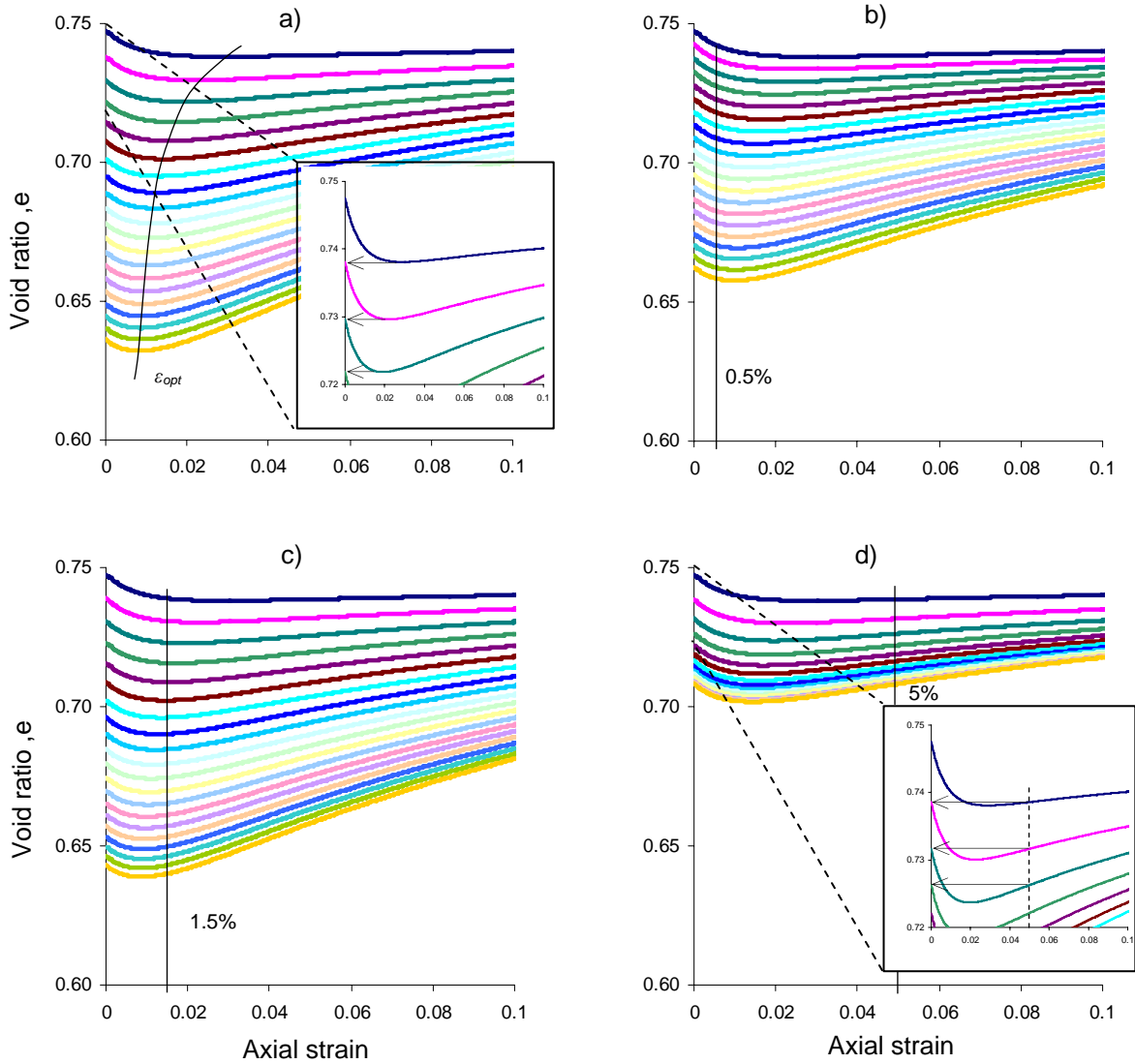
Figure 4.6. Numerical cyclic strain tests (NorSand model): a) Lower bound at ε_{opt}. b) Fixed ε_a=0.5%, c) Fixed ε_a=1.5%, and d) Fixed ε_a=5%.
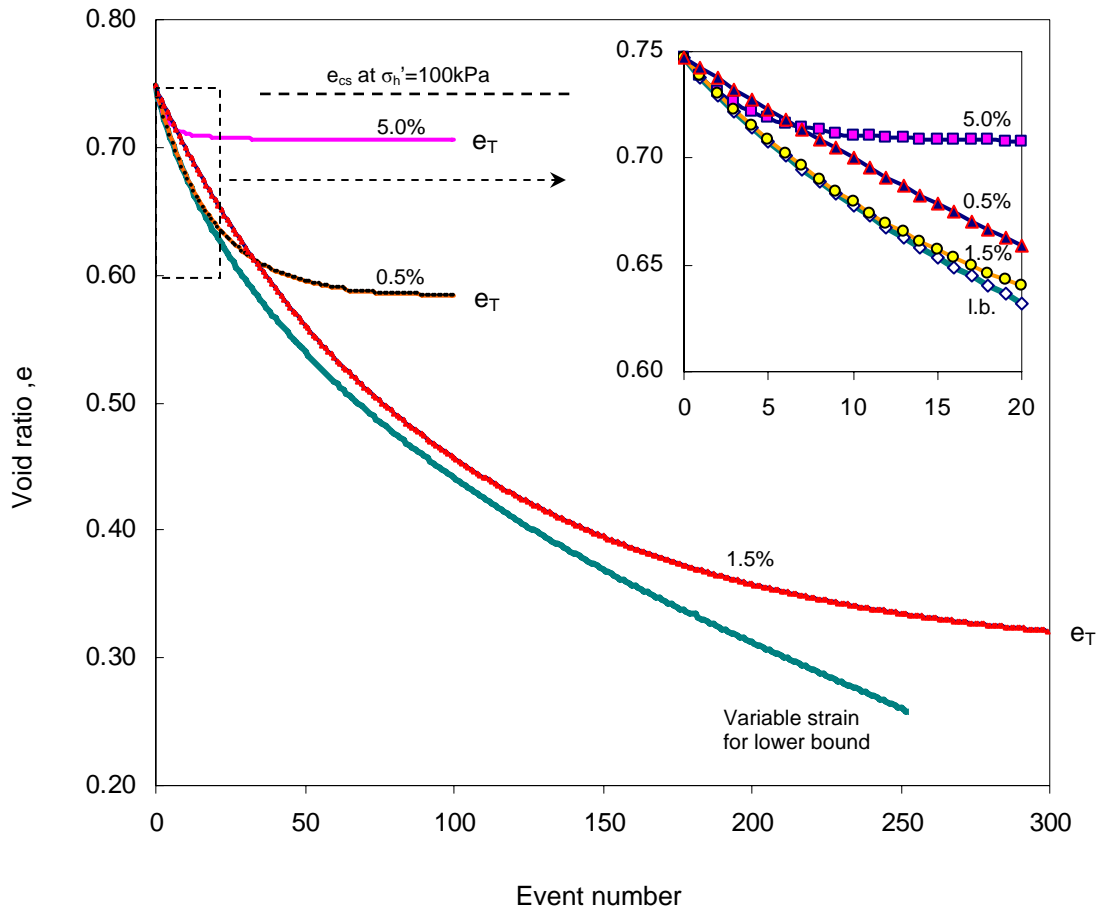
Figure 4.7. Void ratio vs. number of events for each imposed cyclic strain levels: lower bound at ε_{opt}, fixed ε_a=0.5%, fixed ε_a=1.5%, and fixed ε_a=5.0%.

4.2.3 Cyclic loading – Small-to-intermediate strain – Experimental Drained

The experimental validation of the previous numerical results is implemented using Nevada sand subjected to an isotropic effective stress of p_0'=100kPa (D_{50}=0.16mm, C_u=1.8). Tests are conducted by means of a triaxial device modified to produce axial strain controlled cyclic tests. The goals are to impose the same axial strain in each cycle

97

and to monitor the volumetric strain in drained conditions. The volume change in saturated specimens is measured using a pipette connected to the samples. Figure 4.8 shows the evolution in void ratio for two levels of peak-to-peak cyclic strain, one below ε_{opt} (ε_a=0.5%) and the other near ε_{opt} (ε_a=1.5%). The change in void ratio with the number of cycles is linear in semi-logarithmic scale for the first ~100 cycles, and tends to reach asymptotic terminal density values.

As observed in the numerical simulations, the rate of volume reduction with the number of cycles is higher when $\varepsilon_a \cong \varepsilon_{opt}$. The initial void ratio results smaller than the procedurally defined minimum void ratio due to specimen preparation.

4.2.4 Cyclic loading – Small-to-intermediate strain – Experimental Undrained

Numerical and experimental results highlight that dilative granular media can experience significant contraction when subjected to cyclic straining at small-to-intermediate strains. Therefore, it is possible and necessary to define terminal densities as a function of the imposed cyclic strain level.

An important implication of these results relates to the cyclic undrained response as a function of the imposed strain level and mean effective stress. In particular, it is anticipated that a dilative soil (at large-strain) can build up positive porewater pressure if a dynamic undrained loading imposes strains of proper amplitude (See classical results in Castro 1969).
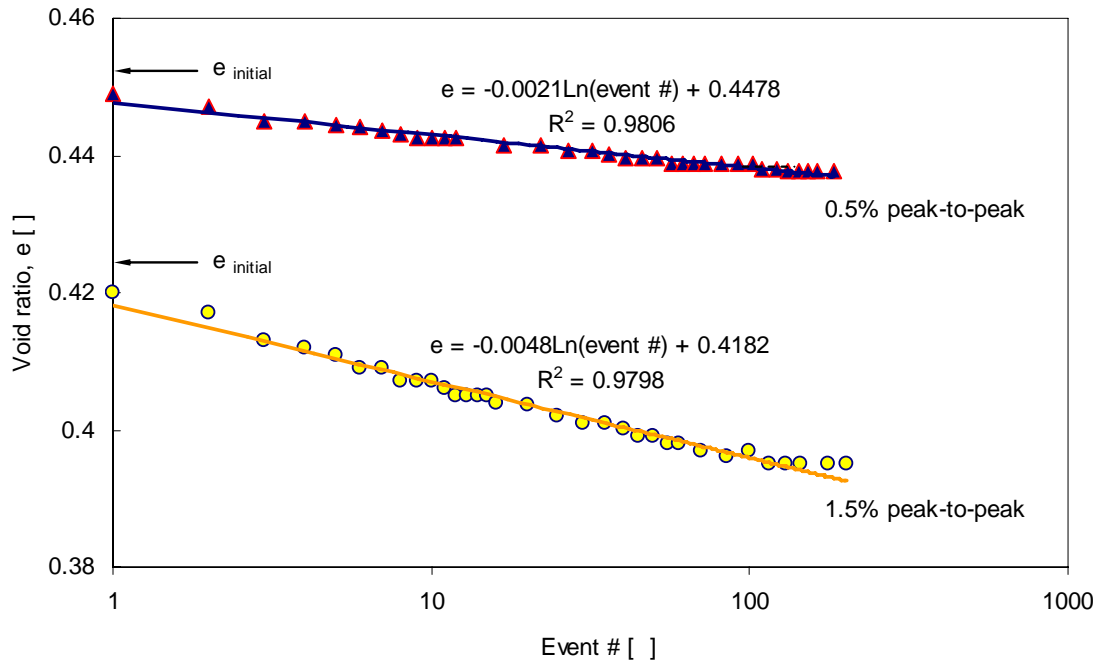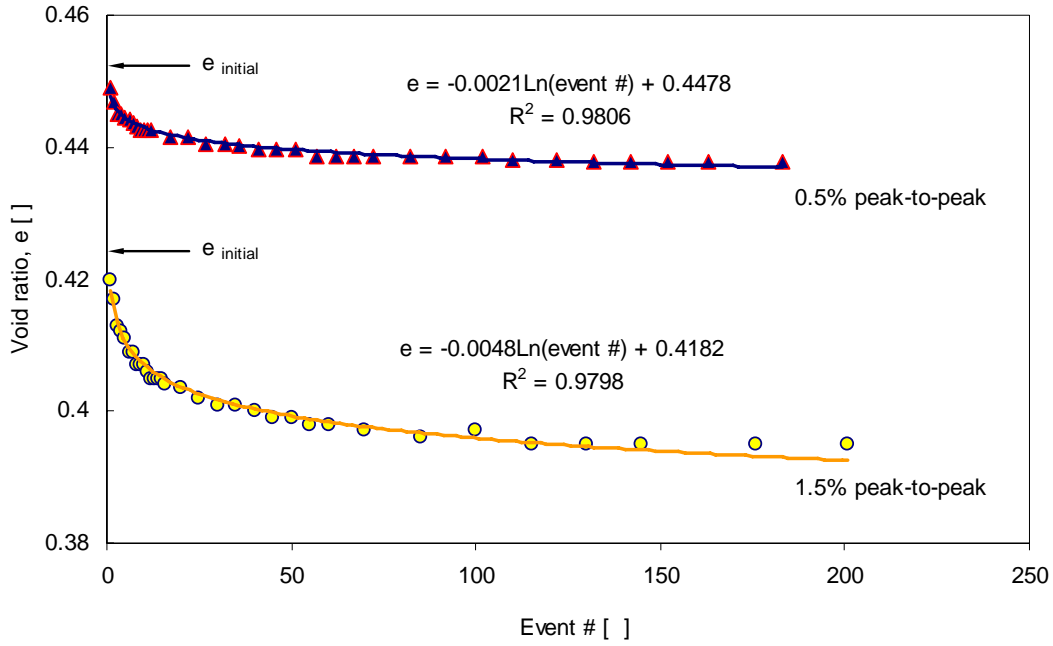
Figure 4.8. Drained cyclic triaxial tests on Nevada sand for two fixed peak-to-peak axial strain levels (p0'=100kPa , ecs=0.9).

99

This phenomenon is herein revisited in the context of terminal densities. Strain controlled axial compression cyclic triaxial tests are performed on three different sands: Nevada Sand, Ottawa Sand and Ticino Sand (see Table 4.1). Specimens are prepared at low initial void ratios, to ensure $e_0 << e_{cs}$ (large-strain dilative region). Once prepared, specimens are tested at different confinements. The peak-to-peak axial strain is ε_a=0.005 in all tests (note that $\varepsilon_a < \varepsilon_{opt}$). Strain cycles are repeated until the excess pore pressure u_e equals the vertical effective stress σ_0' or the test is stopped at 40 cycles. This test sequence is considered *"one event"*. Drainage is allowed at the end of each event and the change in volume is measured. Afterwards, a new undrained event is imposed on the same specimen.

Table 4.1. Material properties for the different tested sands.

Material	e_{min}	e_{max}	$\gamma_{d,max}$ [kN/m^3]	$\gamma_{d.min}$ [kN/m^3]	G_s	Critical State parameters
Nevada sand D_{50} = 0.16 mm C_u=1.8	0.516	0.894	17.29	13.84	2.68 2.67	φ_{cs} = 31° Γ = 1.04 λ = 0.071
	0.55	0.87	16.75	13.89		
	0.511	0.887	17.33	13.87		
	0.533	0.888	17.09	13.87		
	0.54	0.87	16.85	13.89		
Ottawa 20-30 D_{50} = 0.72 mm C_u=1.4	0.50	0.80	17.33	14.44	2.65	φ_{cs} = 31° Γ = 0.802 λ = 0.05
	0.502	0.742	17.30	14.92		
	0.50	0.80	17.3	14.5		
Sand 106 D_{50} = 0.21 mm C_u=2.8	-	0.77	-	14.7	2.66	φ_{cs} = 38°
Ticino Sand D_{50} = 0.58 mm C_u=1.5	0.574	0.99	16.56	13.1	2.66	φ_{cs} = 37° Γ = 1.05 λ = 0.053

Note: $\gamma_{d\,min/\,max} = \dfrac{\gamma_w G_s}{e_{max/\,min} + 1}$

Data collected during one event is shown in Figure 4.9. These typical signals show the imposed cyclic vertical strain, excess porewater pressure and deviatory stress q with the number of cycles, and their variation with effective mean stress p' and vertical strain. As the number of compression-extension cycles increases, the excess porewater pressure increases while the deviatory stress decreases. The critical state line with slope M bounds the stress path in the q-p' space.

The condition of zero effective stress is reached in multiple successive events imposed onto the same specimen (see also Youd 1984; Scott 1986; Lee 2003).

The change in volume during drainage after each event is plotted as a function of event number in Figure 4.10. The change in volume decreases as the event number increases. There is a linear relationship between void ratio at the end of each event and the square root of the event number. Each point in the figure is the result of the cumulative contraction in otherwise dilative soils. Figure 4.11 summarizes the terminal void ratios reached by the three sands under the test conditions described previously.

All eleven specimens are on the dilative side, yet, early cyclic events at small-to-intermediate cyclic strain systematically reach to $u_e = \sigma_0'$ condition. Therefore, it is shown that repetitive strain cycles at the proper strain level can lead to the accumulation of positive excess porewater pressure u_e, even in dilative soils. While these specimens would eventually dilate at large monotonic strains, the existence of interfaces of high hydraulic conductivity contrast may lead to the formation of water gaps and the complete loss of shear strength at the interlayer. Experimental and field evidence of water gap

formation is documented in the literature (Youd 1984; Fiegel and Kutter 1994; Kokusho and Kojima 2002).
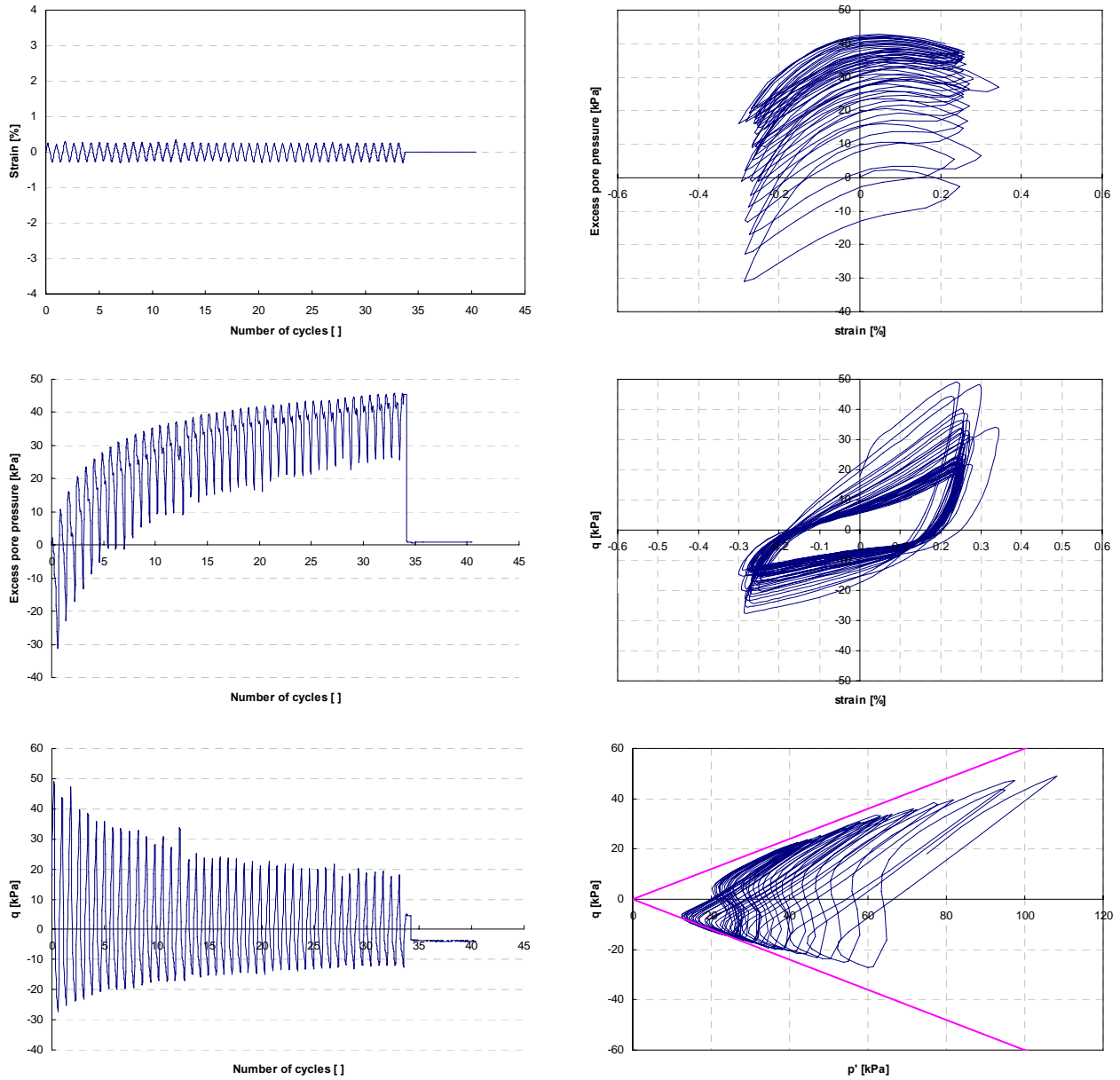
Figure 4.9. Example of cyclic undrained triaxial test on Nevada sand (po'=50 kPa, e=0.68).
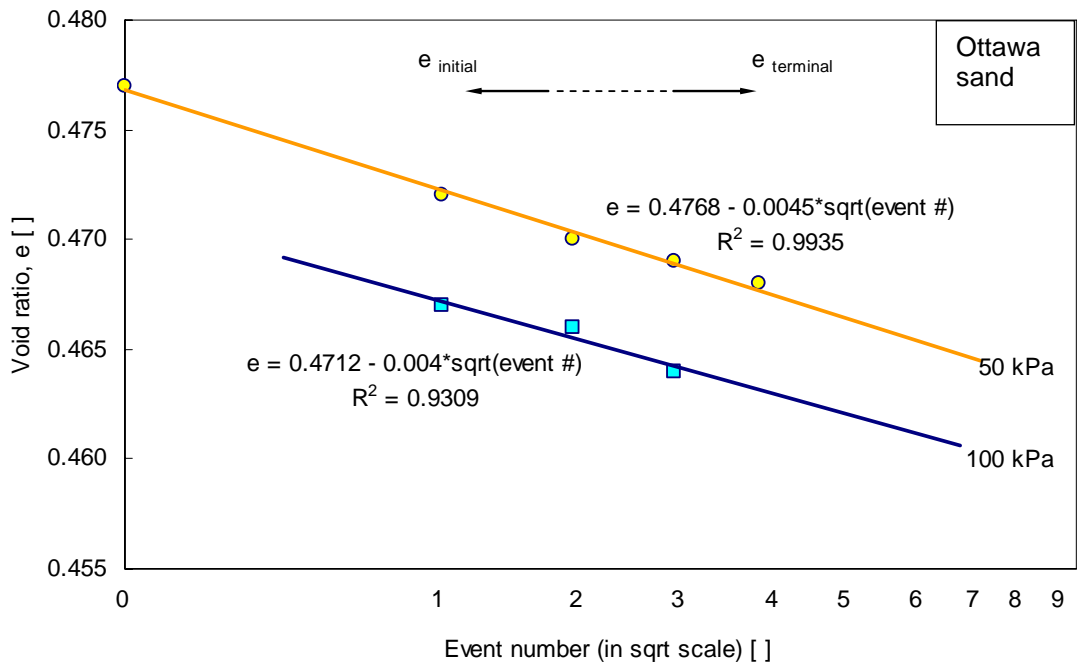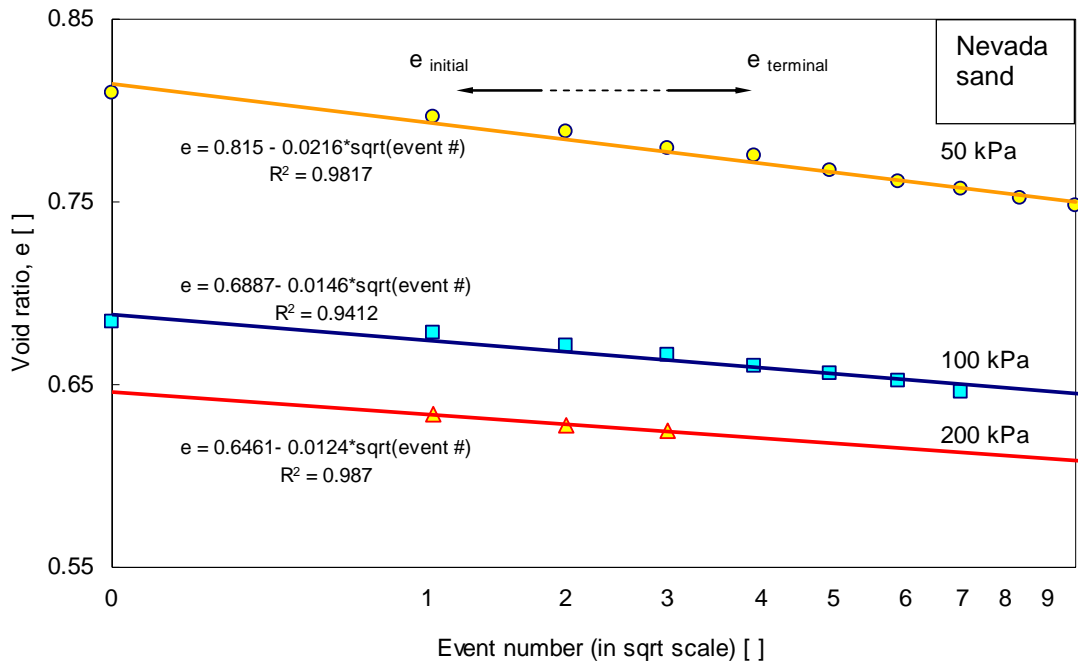
Figure 4.10. Reaching terminal density in cyclic events. Void ratio as function of the event number for different confinements. (Nevada sand and Ottawa sand shown).
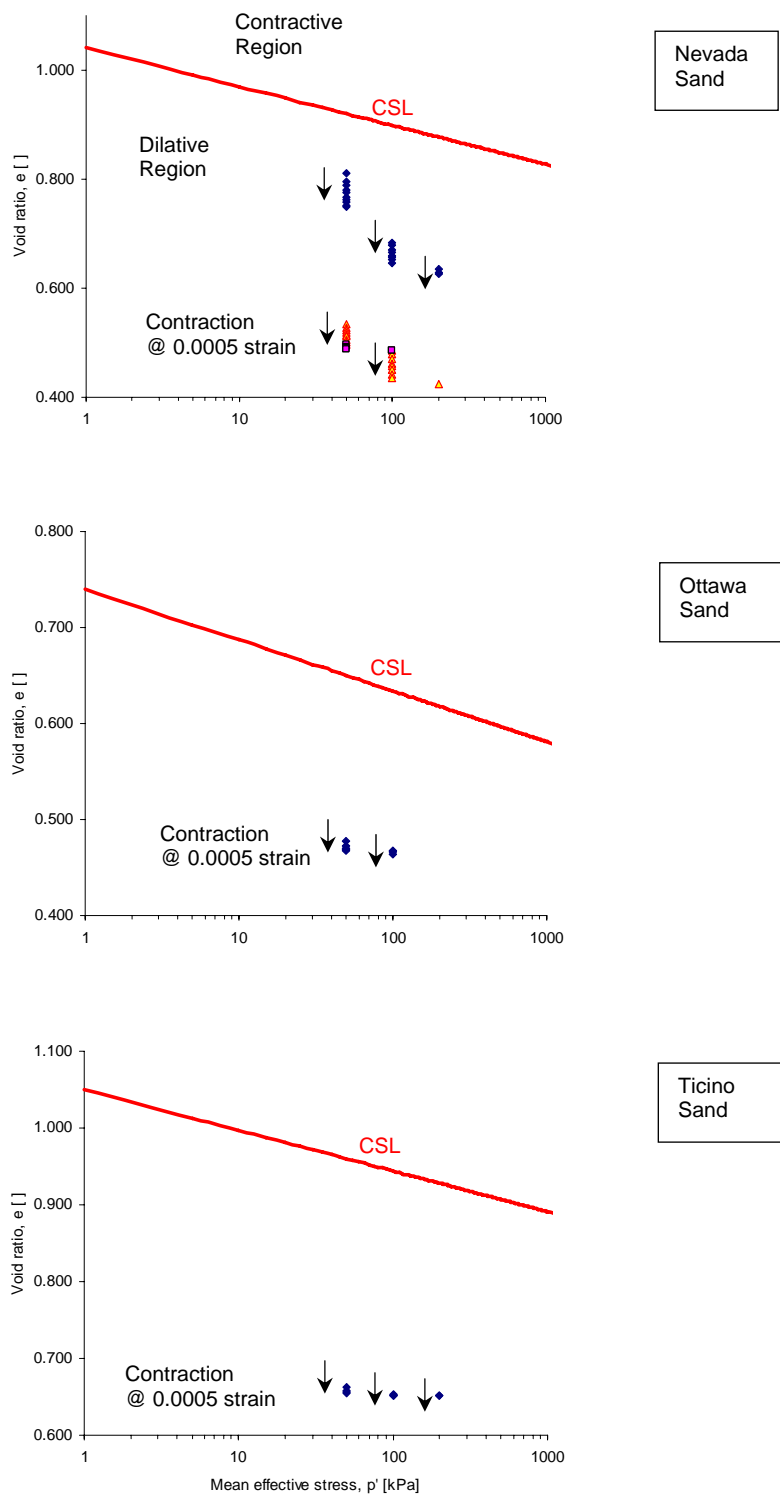
Figure 4.11. Summary plot of initial and terminal void ratio for Nevada, Ottawa and Ticino sands.

4.3 TERMINAL DENSITY AND SETTLEMENT

The dynamic effects caused by earthquakes tend to cause volume contraction and earthquake induced settlements. The new density can be framed as a step in the path towards terminal density (e.g. Figure 4.10). However, the prediction of vertical deformation due to earthquakes remains difficult, and estimation errors have been reported in the order of 25% to 50% or even more in some cases (Kramer 1996; Vincens et al. 2003; Stewart et al. 2004a). Furthermore, different mechanisms may apply depending on the degree of saturation of the soil.

Several places have experienced liquefaction and earthquake induced settlement. For instance, in San Fernando Earthquake, 1971, the ground settlement was of 6.4cm, with a peak acceleration of 0.45 g. (Seed and Silver 1972). During May 5, 1986 Malatya earthquake, among other damages, the settlement of the Sürgü dam was 15cm in the upstream part of the crest (Özkan et al. 1996). In 1995, extensive soil liquefaction on Port and Rokko Islands was observed during the Kobe earthquake resulting in ground settlement of 20cm to 50cm (Bardet et al. 1997; Soga 1998). During the Turkey earthquake in August 24, 1999, at 50 kilometers east of Izmit, settlements as large as 1.5m were observed (Erdik 2000). What would be the settlement in these sites if another earthquake arrives?

An experimental study is conducted next to understand the evolution of settlement in a liquefiable soil, due to repetitive dynamic events, i.e., simulated earthquakes.

4.3.1 Experiment

The experimental setup consists of two plexiglass tubes, 81.44 mm of inner diameter that act as containers for the two sand columns to be simultaneously excited. Different drainage conditions are tested as part of the study in view of the possible beneficial effects of vertical drains. This is accomplished by testing the sand in one continuous impervious tube while the other one has small diameter holes around its circumference. These holes are vertically spaced every 20mm (½ radii). Capillary forces and static hydraulic gradients are avoided by placing a bigger concentric tube surrounding the perforated plexiglass tube. The water level is the same in the inner tube and in the annular space. This design allows for excess pore pressure dissipation only in the vertical direction towards the surface of the sand column in the continuous tube, while excess pore pressure u_e can dissipate in both radial and vertical directions in the perforated tube. The continuous and the perforated tubes have an overflow mechanism that keeps the water level equal in both sand columns (see Figure 4.12). The plungers of vertical LVDT rest on perforated light discs on the surface of both sand columns. Finally, a pendular mass hanging from the ceiling is used in pendular motion to hit the common base of the tubes. Each impact is an event. Events are repeated every one minute.

The sand specimens in both columns are prepared by the water pluviation method. Initially, the tubes are partially filled with de-aired water. Dry sand is slowly poured or sprinkled from the top of the tubes. The water level rises while the soil is rained into the tubes and the level of water above the sand surface guaranties terminal velocity for particles falling down prior to sediment contact. A very loose formation is obtained using
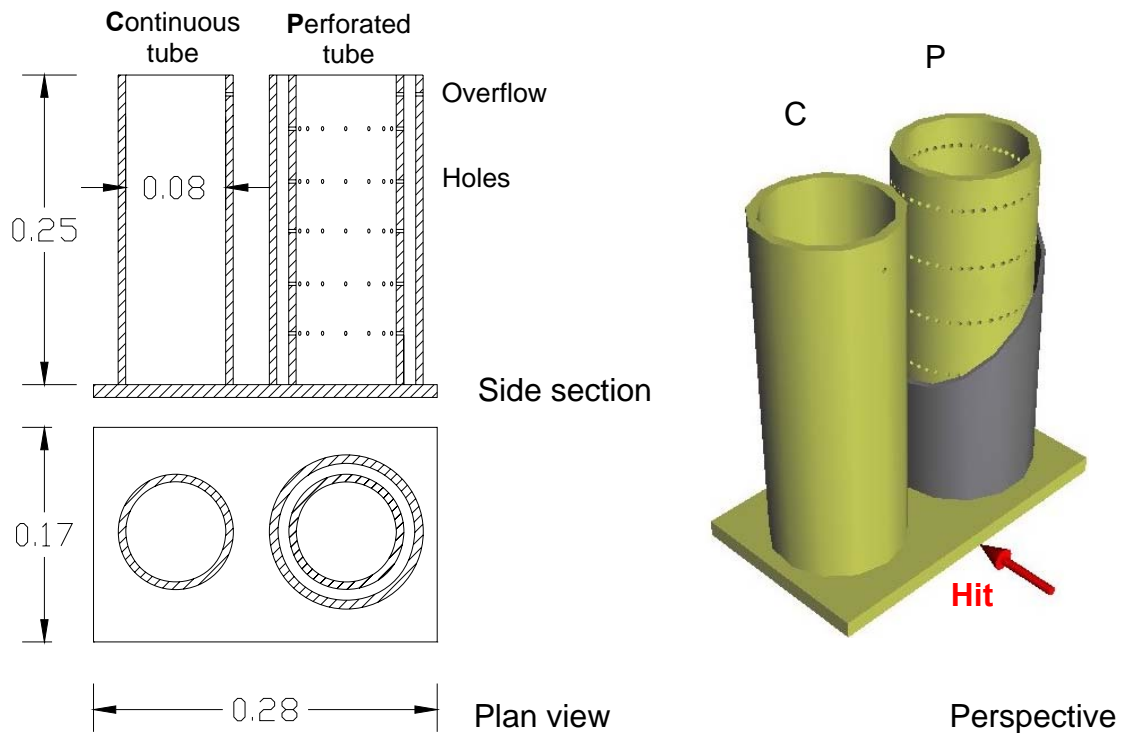
Figure 4.12. Terminal density and settlement. Experimental setup (dimensions in meters).

this method. The three different sands tested following the same procedure are: 1) Nevada sand, 2) Ottawa 20-30 sand, and 3) a crushed granitic sand 106. Table 4.1 summarizes the relevant soil parameters.

Figure 4.13 shows typical results. Specimens tested in the perforated and continuous tubes exhibit similar behavior. The first few events produce higher settlements than the subsequent ones do. The settlement in perforated tubes is slightly smaller than in the continuous tube but it tends to equalize as the number of events increases. This observation is in agreement with the case history of blast densification in

Mt. St. Helen's, Washington (Hachey et al. 1994), but it disagrees with other references (Lyman 1942; Massarch 2001).

Figure 4.13 shows that most of the settlement occurs in the first 30 events, and continues decreasing asymptotically with increasing number of events.
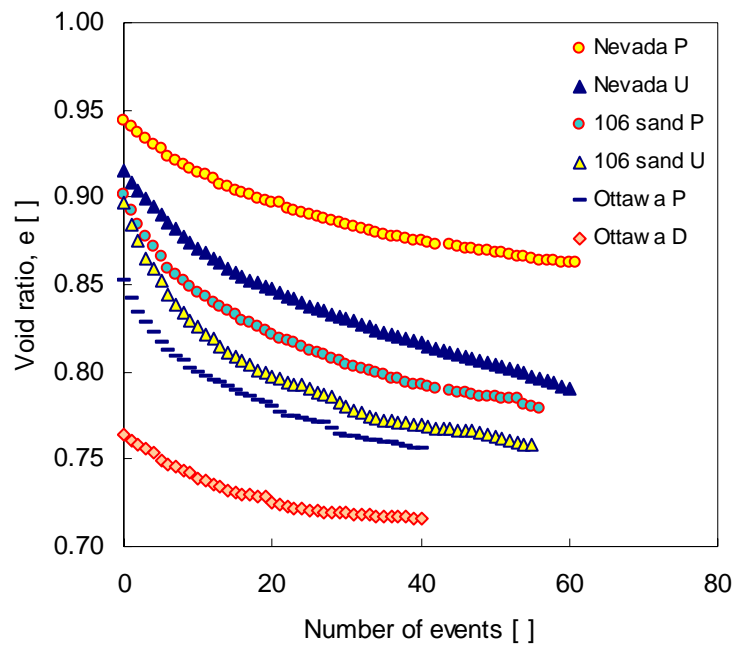
Figure 4.13. Void ratio evolution as a function of the number of events for the three sands tested in the continuous and perforated tubes.

The average relative density D_R at the end of each event is plotted with respect to the initial relative density before the event. Typical results are shown in Figure 4.14. It is observed that the change in relative density decrease for each event, hence, the soil is approaching its terminal density for the given process.
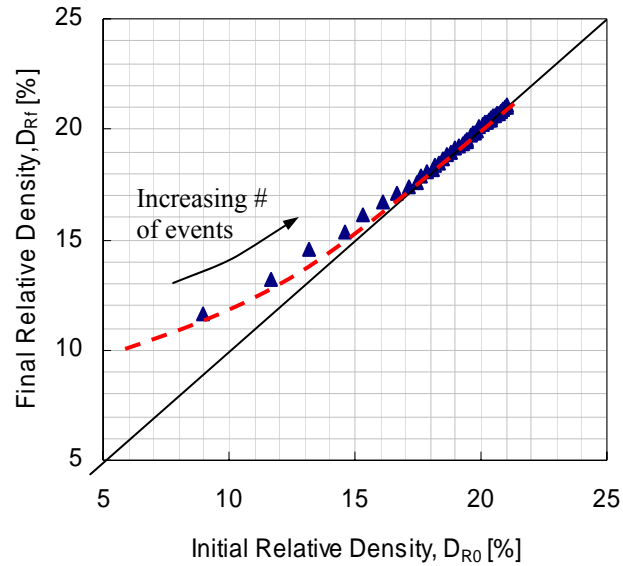
Figure 4.14. Typical evolution of the relative density with the numbers of events with respect to the previous state.

4.3.2 Settlement analysis

Previous laboratory studies suggest that the volumetric strain in saturated soils increases with increasing earthquake induced peak strain and decreasing relative density, as shown in Figure 4.15 (Tatsuoka et al. 1984; Tokimatsu and Seed 1987; Chien et al. 2002). Certainly, a soil with low relative density D_R most likely presents $e_0 > e_{cs}$, it falls in the contractive zone (Figure 4.2) and consequently, the lower relative density, the higher the volumetric change is as inferred from Figure 4.14. However, a high relative density soil may fall in the dilate zone $e_0 < e_{cs}$, and therefore, data in Figure 4.15-c as does not have a proper physical explanation for two reasons: First, a dilative soil contracts at peak large-strain; and second, the steady state volumetric change seems to be reached at the
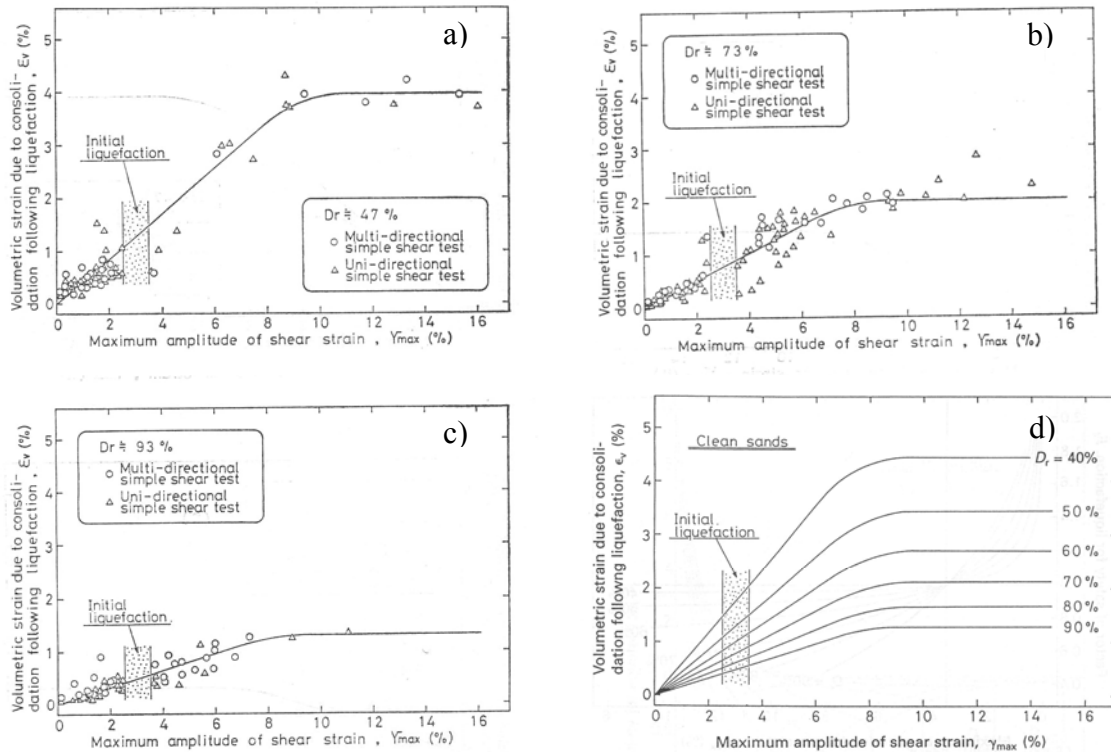
Figure 4.15. Volume change vs. maximum induced shear strain for clean sand. a) Relative density DR=47%. b) DR=73%. c) DR=93% (Nagase and Ishihara 1988). d) Summary plot (Ishihara and Yoshimine 1992).

same threshold maximum shear strain independently of the relative density D_R. These studies suggest that the settlement of saturated sands subjected to cyclic shear is governed by the initial relative density of the soil, the maximum shear strain induced by the event, and the amount of excess porewater pressure that the event generates. Some authors argue that settlement is neither influenced by the initial effective overburden stress nor by the mechanism that causes the porewater pressure generation (Tatsuoka et al. 1984;

Tokimatsu and Seed 1987). These apparent contradictions find a physical explanation in the lessons learned in previous sections: a large-strain dilative soil can densify when subjected to small-to-intermediate cyclic strain. Furthermore, the maximum or peak shear strain may not prevail over a larger number of smaller cyclic strains and thus, paths similar to the ones shown in Figure 4.6 develop. The settlement is indeed not influenced by the porewater pressure generation mechanism; however the initial effective overburden stress must have an influence as evidence in Figure 4.3 and Figure 4.5.

It is also observed that no significant volume change is achieved until a certain threshold cyclic stress ratio is reached (Tokimatsu and Seed 1987; Chern and Lin 1994; Ishihara 1996; Hsu and Vucetic 2004). In fact, the volumetric contraction observed at small-to-intermediate strains results usually small, while it becomes significant in repetitive events (cyclic loading). The volume change is uniquely correlated to the level of porewater pressure that develops regardless of load irregularity or whether it is a single or multi-directional loading condition (Chen 1988; Nagase and Ishihara 1988).

The post liquefaction volumetric strain can be related to the initial relative density of the sand and the factor of safety against liquefaction defined as (Ishihara 1996)

$$F_l = \frac{\tau_{max,l} / \sigma_v'}{\tau_{max} / \sigma_v'} \tag{4.1}$$

where τ_{max} is the maximum shear stress, σ_v' is the effective vertical stress and τ_{max} / σ_v' is the applied stress ratio, and the subindex l denotes the state at liquefaction (Ishihara and Yoshimine 1992; Chien et al. 2002). Figure 4.16 shows such relation.
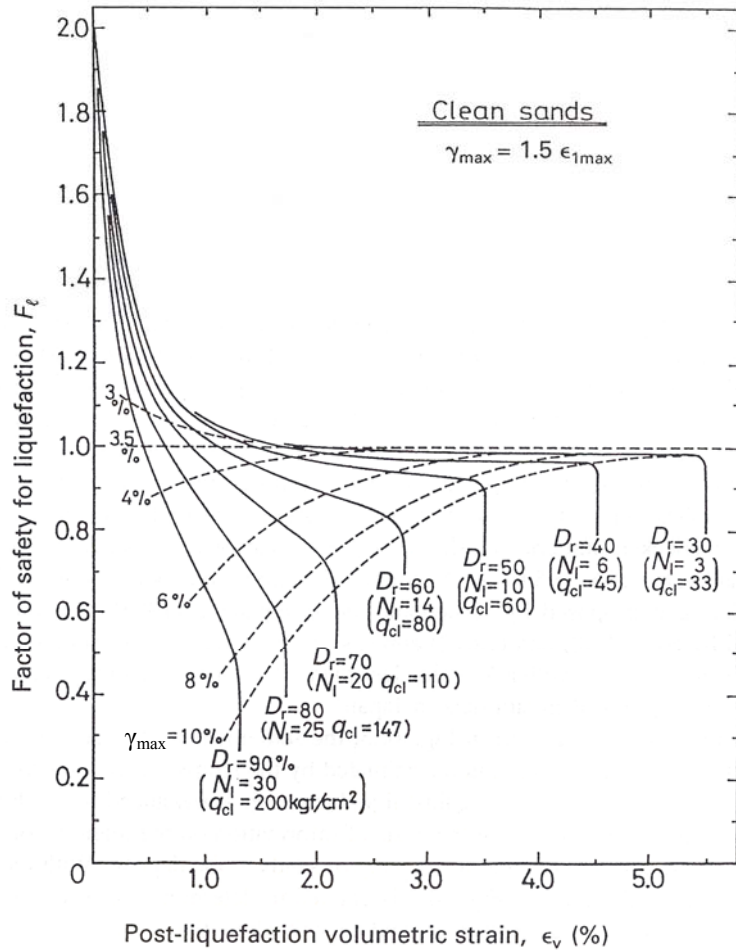
Figure 4.16. Post-liquefaction volumetric strain as a function of initial relative density and factor of safety against liquefaction (Ishihara and Yoshimine 1992).

The integration of the predicted volumetric strain over the thickness of the liquefied layer gives the ground surface settlement.

The rate of settlement is governed by the reconsolidation characteristics. Reconsolidation begins at the bottom of the liquefied layer and proceeds upward combining process such as stokes sedimentation and consolidation (Whitman et al. 1982;

Youd 1984; Scott 1986; Stewart et al. 2004b; Santamarina and Lee 2006). Therefore, the earthquake duration and the settlement duration can have different time scales, as the settlement time due to reconsolidation will be governed by sedimentation path, hydraulic conductivity, and compressibility of the soil.

On the other hand, dry sands densify during earthquakes as well. The term "seismic compression" is used to describe volumetric strain accumulation in unsaturated soils during earthquakes (Stewart and Whang 2003; Stewart et al. 2004a). Previous laboratory-based investigations of seismic compression include studies on both clean sands and soils containing fines. The settlement depends on the current relative density, amplitude of cyclic strain induced in the sand, number of cycles (i.e., duration of the dynamic event) of the shear strain during the earthquake (Silver and Seed 1971).

An estimation of cyclic strain can be computed as (Seed and Idriss 1971; Seed and Silver 1972; Pyke et al. 1975; Tokimatsu and Seed 1987; Stewart and Whang 2003):

$$\gamma_{cyc} = 0.65 \frac{a_{PGA}}{g} \frac{\sigma_v r_d}{G_{\gamma\ cyc}} \tag{4.2}$$

where a_{PGA} is the peak ground acceleration at the surface, g is the acceleration of gravity, σ_v is the total vertical stress, r_d is the stress reduction factor that accounts for depth (i.e., r_d is 1 at the surface and decreases with depth, 0.9 at 10m (Iwasaki et al. 1978), and $G_{\gamma\ cyc}$ is the shear modulus of the soil at $\gamma = \gamma_{cyc}$ (Silver and Seed 1971; Liu et al. 2001). The value of γ_{cyc} is found by iteration due to the dependency of the shear modulus on the strain level and the effective stress. Then, the volumetric stain due to densification is found using Figure 4.17 knowing γ_{cyc} and the initial relative density (or SPT blowcounts).

113
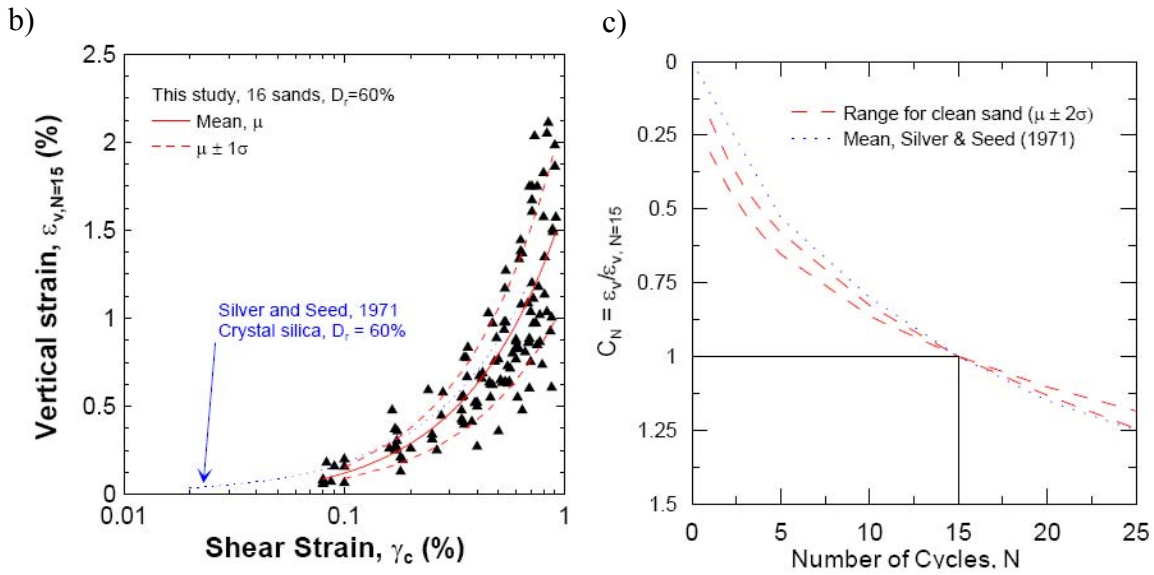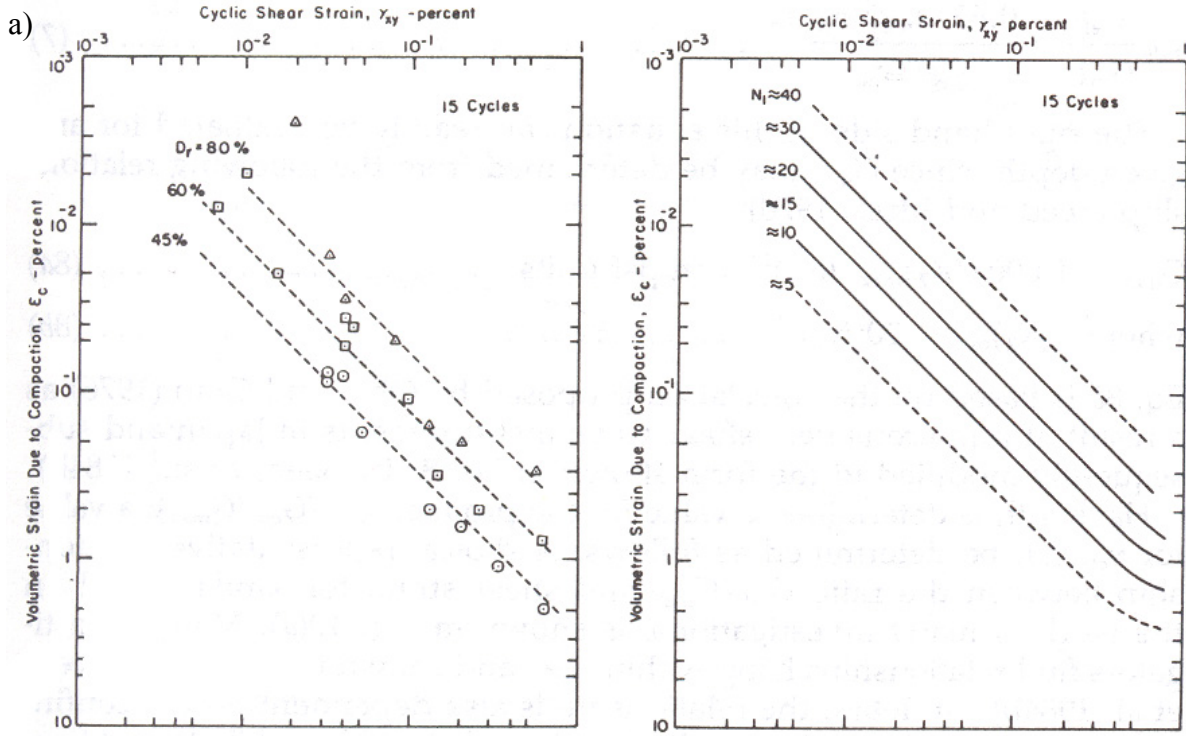
Figure 4.17. Volumetric strain as a function of shear strain. a) Volumetric strain and shear strain for dry sands and modification for SPT-N values (Tokimatsu and Seed 1987, after Silver and Seed, 1971). b) New findings (Stewart and Whang 2003). c) Correction factor (Stewart et al. 2004a).

The figure corresponds to an earthquake magnitude $M= 7.5$ and 15 strain cycles. The volumetric strain can then be scaled to different earthquake magnitudes (Table 4.2) and adjusted for the actual number of cycles with the correction factor C_N (Pradel 1998; Stewart et al. 2004a). The correction factor is a practical way to tie any process to a reference process occurring at 15 cycles; C_N results a universal conversion for processes that reaches it terminal density by following an evolution similar to Figure 4.13. For small-to-intermediate strain amplitude, C_N must be greater than one; this factor captures the further densification a dilative soil may experience if $\varepsilon_a \leq \varepsilon_{opt}$ in cyclic events (Figure 4.6-b and –c).

Table 4.2. Correction factors for different Earthquake magnitudes on volumetric strain ratio for dry sands (Source: Tokimatsu and Seed, 1987)

Earthquake magnitude	Number of representative cycles at 0.65 t_{max}	Volumetric strain ratio
8.5	26	1.25
7.5	15	1.00
6.75	10	0.85
6	5	0.60
5.25	2-3	0.40

4.4 CONCLUSIONS

Results from this study support the following conclusions:

- There exists a single terminal density ρ_t for every granular material and every process. There is and associated fabric condition (presumed – not observed) at the terminal density that supports the continuation of the process at constant volume.

- Numerical and experimental results highlight that large-strain dilative granular media can experience significant contraction when subjected to cyclic straining at small-to-intermediate strains.

- Terminal densities associated to each process must be defined as a function of the imposed cyclic strain level and confining pressure. Consequently, the amount of settlement depends on the initial void ratio, the number of events (i.e., earthquakes), the state of stress, and the amount of shear imposed.

- The change in relative density in cyclic shearing decreases with the number of events and diminishes for higher values of relative density.

- The evolution of settlement in slightly affected by drainage conditions and tends to equalize for higher number of events.

- Repetitive small-to-intermediate strain undrained shear events on a dilative soil can cause the accumulation of positive excess porewater

116

pressure, and therefore a dilative soil may loose shear strength. In this case draining water may accumulate at interfaces between layers and generate water gaps. A complete loss of shear strength at the water film may develop.

CHAPTER V

BLAST DENSIFICATION STUDY – PART 1:

SITE AND SOIL CHARACTERIZATION

5.1 INTRODUCTION: TEST SITE DESCRIPTION

An unprecedented blast densification field study is conducted at a test site in South Carolina, on the coastal geological province. The formation consists of a relatively new deposit from the Pleistocene (Quaternary). Figure 5.1 shows the location of the test site. The study is contracted by GeoSyntec Inc. (R. Bachus and T. Hebeler).

The earthquake hazard in the region is high. There is a 23% probability of a magnitude $M \geq 4.75$ earthquake in the next 50 years (U.S. Department of the Interior 2005). The expected peak ground acceleration at the site, according to the 1996-2002 USGS hazard maps is $a_{PGA}=0.75 \cdot g$ for a 2% of probability of exceedance in 50 years (U.S. Department of the Interior 2005). Figure 5.2 provides further details about the seismicity at the site.

The site is being considered for a landfill. The soil layer between depths $z \cong 8m$ and $z \cong 12m$ is assumed to be liquefiable throughout the site. Given the layer depth and the aerial extent involved, blast densification is believed to be the most economically viable soil improvement alternative to enhance the liquefaction resistance. The purpose of this
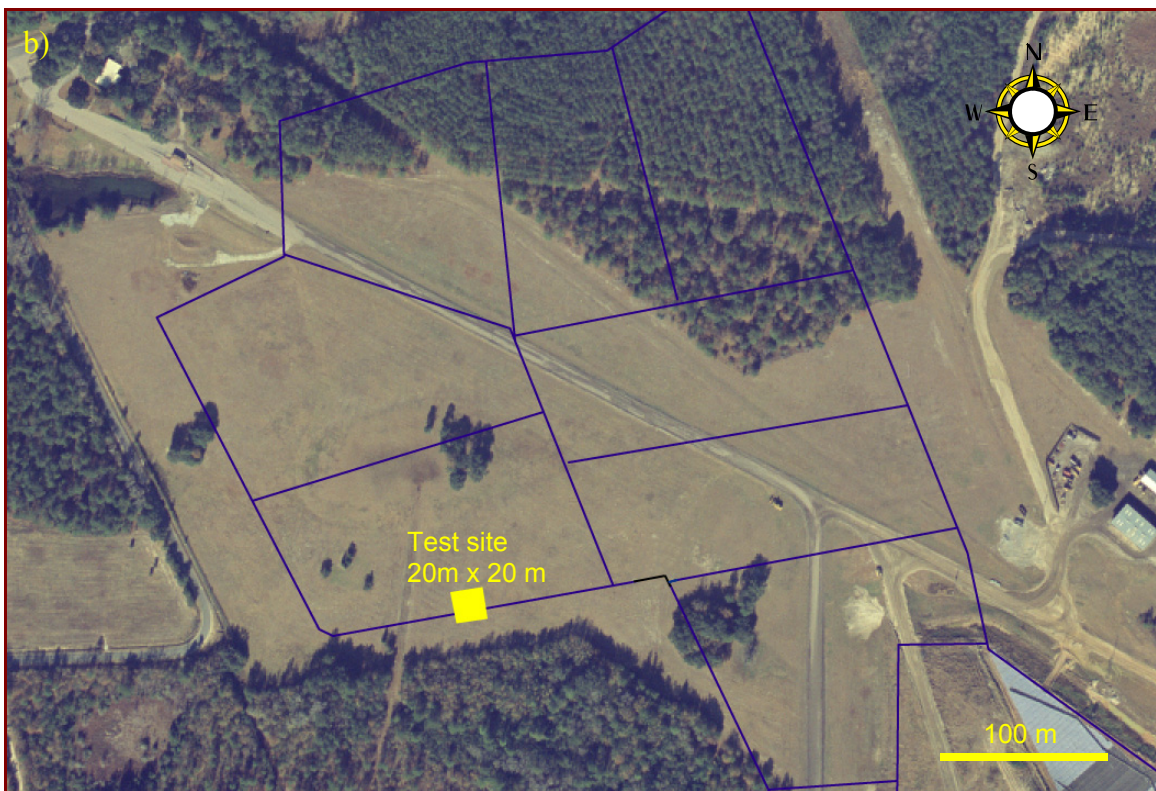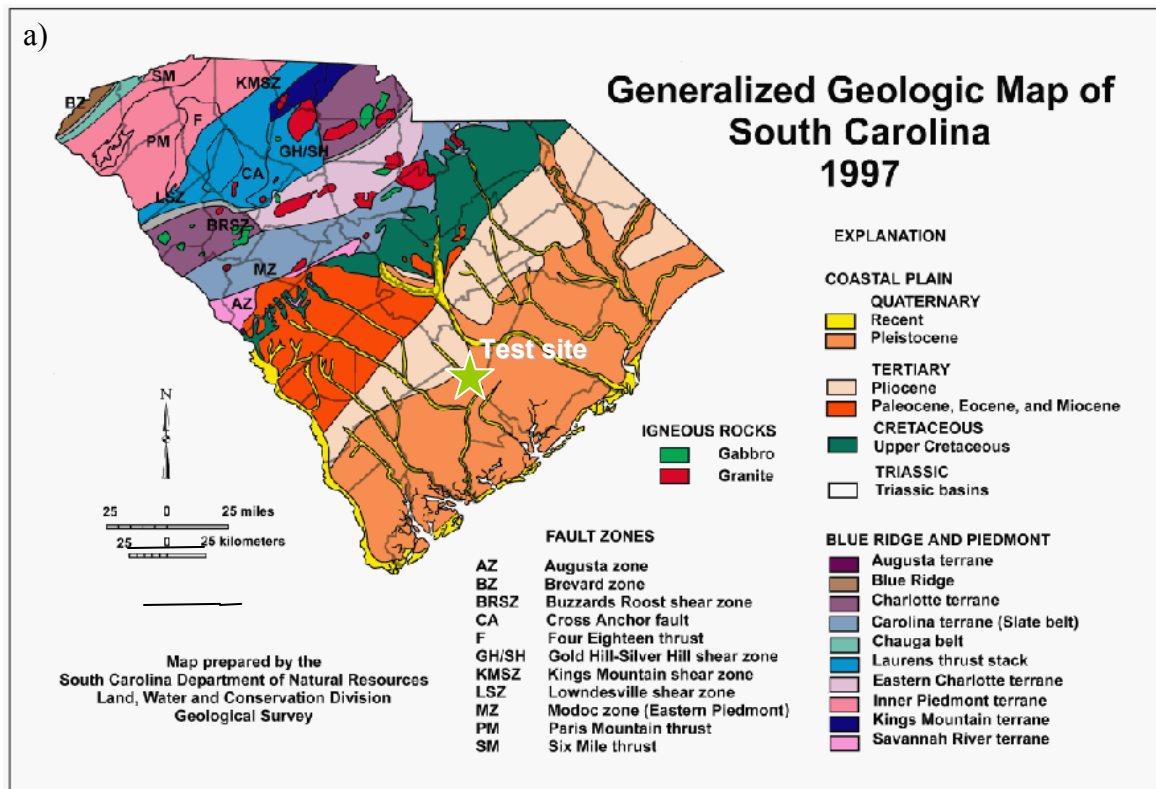
Figure 5.1. a) Location of the test site on the coastal plain. b) Layout of the ~20m x 20m test site.

119
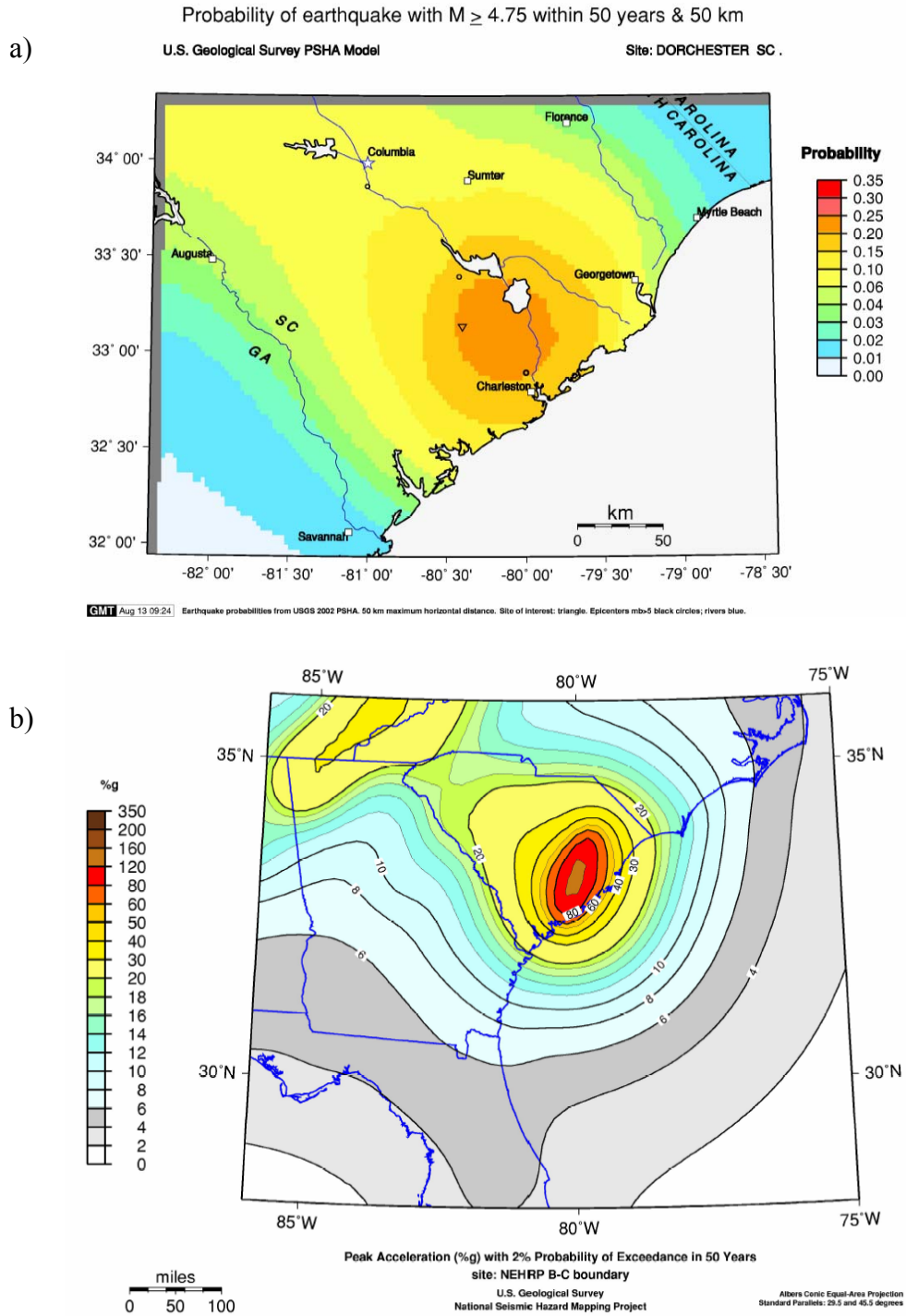
Figure 5.2. Site seismicity. a) Probability distribution of earthquakes Magnitude 4.75 or greater within the next 50 years. b) Peak ground acceleration PGA (%g) with 2% probability of exceedance in the next 50 years (U.S. Department of the Interior 2005).

study is to assess its technical suitability and to provide guidelines for optimal implementation. The study is reported in two Chapters. This chapter presents the results of the comprehensive laboratory and field characterization conducted as part of this investigation.

5.2 LABORATORY STUDY

The laboratory soil characterization program evaluates all layers, with emphasis on the fine sands encountered between depths $z\cong8m$ and $z\cong12m$. The study encompasses index properties, conduction and diffusion, small and large strain parameters and geophysical properties. Results are summarized in Table 5.1 and in Table 5.2. Tests are conducted in collaboration with Jong-Sub Lee and Angel Palomino (Particulate Media Research Laboratory – Georgia Institute of Technology).

5.2.1 Index properties

There are five distinguishable layers at the site, and specimens from six different depths are tested: P1, and B1 through B5 (Figure 5.3). P1 denotes the upper sands which are immediately below the surface ($z=0m$ to $z\cong0.60m$ below ground surface). They are tan and dry-to-moist depending on depth from the water table. The B1, B2, and B3 specimens consist of a very white, fine, clean sand (i.e., $z\cong6.0$ to 7.3-7.6 m below ground surface). This group presents small variations, some of which can be observed during drilling (e.g., coloration). However, they can be treated basically as the same soil unit. The B4 specimen corresponds to a very fine "black sand" that extends from depths $z\cong7.6m$ to $z\cong10.7-13.0m$. Finally, B5 is a fossiliferous marl layer below the black sand; it

Table 5.1. Summary of soil parameters and some soil properties.

Sample →	B1	B2	B3	B4 Field condition	B4 washed	B5
Depths [m]	2	4	6	10		13
Classification						
#4 Passing [%]	100.0	100.0	100.0	100.0	100.0	100.0
#200 Passing [%]	0.71	1.17	0.58	0.73	3.76	2.06
D_{60} [mm]	0.20	0.20	0.32	0.22	0.21	0.21
D_{50} [mm]	0.19	0.19	0.29	0.21	0.19	0.20
D_{30} [mm]	0.18	0.18	0.22	0.17	0.17	0.17
D_{10} [mm]	0.16	0.16	0.17	0.15	0.12	0.15
$C_u = D_{60}/D_{10}$	1.25	1.25	1.88	1.47	1.75	1.40
$C_{cur} = \dfrac{D_{30}^2}{(D_{10} \cdot D_{60})}$	1.01	1.01	0.89	0.88	1.15	0.92
USCS	SP	SP	SP	SP	SP	SP
w [%]	26.8	32.5	25.5	28.9		32.9
e_0	0.715	0.868	0.681	0.772		0.878
σ_{fluid} [S/m] (@200 MHz)	0.041	0.044	0.082	1.23		0.310
Particle Shape (soil retained on sieve #100)						
Sphericity	S = 0.60 (average of all samples)					
Roundness	R = 0.15 (average of all samples)					

Note: "Field condition" refers to disturbed specimens obtained from split barrels samplers; "washed" indicates specimens whose fines have been washed out.

Table 5.2. Some soil parameters and properties for the representative soil layers.

Sample →	B2	B4 (soils of most interest)	
Specific gravity, G_s	2.65	2.67	
Minimum dry unit weight, γ_{min} [kN/m^3]	11.93	12.50	
Maximum void ratio, e_{max}	1.179	1.096	
Minimum void ratio, e_{min}	0.54	0.52	
Estimated in-situ Dr [%]	48	54 – 58	
k [cm/s]	$4\times10^{-5} – 6\times10^{-4}$	$1.5\times10^{-5} – 7\times10^{-3}$	
pH		4.11 (acidic)	(Fisher Scientific Accumet AR50 pH Meter)
Velocity – Stress trends			
α	36 (D_R=52%)	45 89 51	(D_R=35%) (D_R=47% - oven dried) (D_R=62%)
β	0.312 (D_R=52%)	0.296 0.234 0.289	(D_R=35%) (D_R=47% - oven dried) (D_R=62%)
Critical State Soil parameters			
Γ (intercept)	1.232 1.313 1.037	1.165 1.205 1.037	Measured From e_{max} ,e_{min} and C_u Estimated from R and S
λ (slope)	0.113 0.096 0.240	0.138 0.086 0.200	Measured From e_{max} and e_{min} From Γ and e_{min}
ϕ_{cs}	32˚	33˚ - 40˚	
Oedometer			
C_c (last loading stage)	0.0347 (D_R=52%)	0.0528 0.0728 0.0347	(D_R=35%) (D_R=47%-oven dried) (D_R=62%)
C_r (last unloading state)	0.00291(D_R=52%)	0.0036 0.0028 0.0021	(D_R=35%) (D_R=47%-oven dried) (D_R=62%)
C_c/C_r	16 (D_R=52%)	15 26 16	(D_R=35%) (D_R=47%-oven dried) (D_R=62%)

has shell fragments and a greenish/olive-gray color. At the time of testing, the ground-water table depth is z_w=0.8–1.5m below the surface.
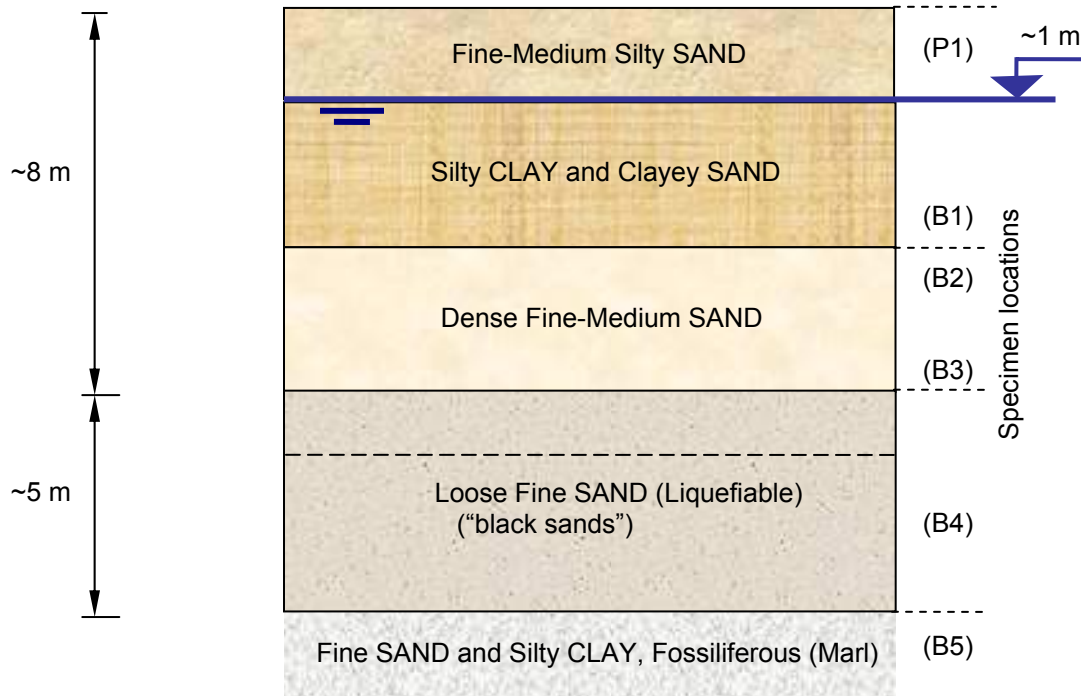
Figure 5.3. Representative soil profile.

Grain size distribution curves are shown in Figure 5.4 (mean size D_{50}=0.19mm to 0.29mm; coefficient of uniformity C_u=1.25 to 1.88). These are poorly graded sands which fall under the SP category according to the unified soil classification system USCS.

Particle shape, i.e., sphericity, angularity and roughness, emerges as a significant parameter in the behavior of sands (Santamarina and Cho 2004). Particle shape is characterized using a Leica MZ6 microscope (20x-to-100x) and recorded with a

Qimaging Micropublisher digital camera. Selected images are shown in Figure 5.5. The particle geometry is determined by visual matching with the chart shown in Figure 5.6. Particle shape matching shows similar roundness (*R=0.1*) and sphericity (*S=0.6*) for all layers, indicating subrounded to angular shape particles.
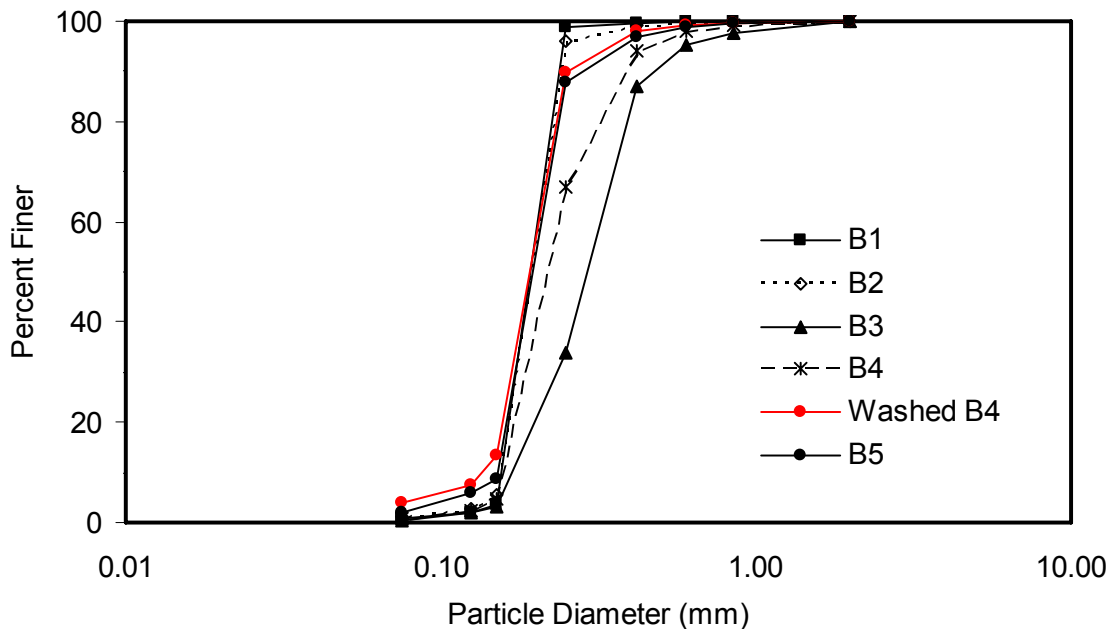
Figure 5.4. Typical grain size distribution for all specimens.

Images of B4 specimens demonstrate the existence of small black particles attached to the larger particles. The presence of organic material in the fines portion of this soil (passing Sieve #200) was confirmed using the hydrogen peroxide effervescence index test, although this test has only a limited action on undecomposed plant remains like roots and fibers (Head 1992). The organic content of the soil determined by the LaMotte organic matter soil test kit is 1% of the material passing sieve #20. The fine and

organic materials in B4 are observed in a scanning electron microscope as well (Figure 5.7). Fibrous, thread-like inclusions can be seen connecting clay particles at magnifications 7000x and 30000x. SEM x-ray spectrum analysis detected the presence of silica; therefore, not all of the fines are organic in nature.

The specific gravity G_s is determined by the Pycnometer method (ASTM D854-92–oven dried specimen). The measured value G_s=2.65 to 2.67 is compatible with quartz and feldspar (silica) minerals.

The maximum void ratio attained for B4 sands is e_{max}=1.1 (graduated cylinder, Method C – ASTM 4254). The minimum void ratio is e_{min}=0.5 (modified procedure of the compaction based Method 2A – ASTM 4253). Particle shape and the coefficient of uniformity permit estimating extreme void ratios (Figure 5.8). The estimated minimum void ratio $e_{min}\cong0.5$ and maximum void ratio $e_{max}\cong1.0$ are in agreement with the measure values for specimens B2 and B4 (Table 5.2).

The pH of the pore fluid in sediments B4 is determined using a Fisher Scientific Accumet AR50 pH Meter. The measured valued pH=4.11 indicates acidic pore fluid. A low pH is usually associated with the presence of organic matter (Head 1992).

5.2.2 Hydraulic conductivity

The hydraulic conductivity k is measured using rigid wall permeametry (ASTM D5084-Method B: Falling Head – Constant Tailwater). Measured values presented in Figure 5.9 show a range between k=1x10^{-5}cm/s and k=1x10^{-2}cm/s.
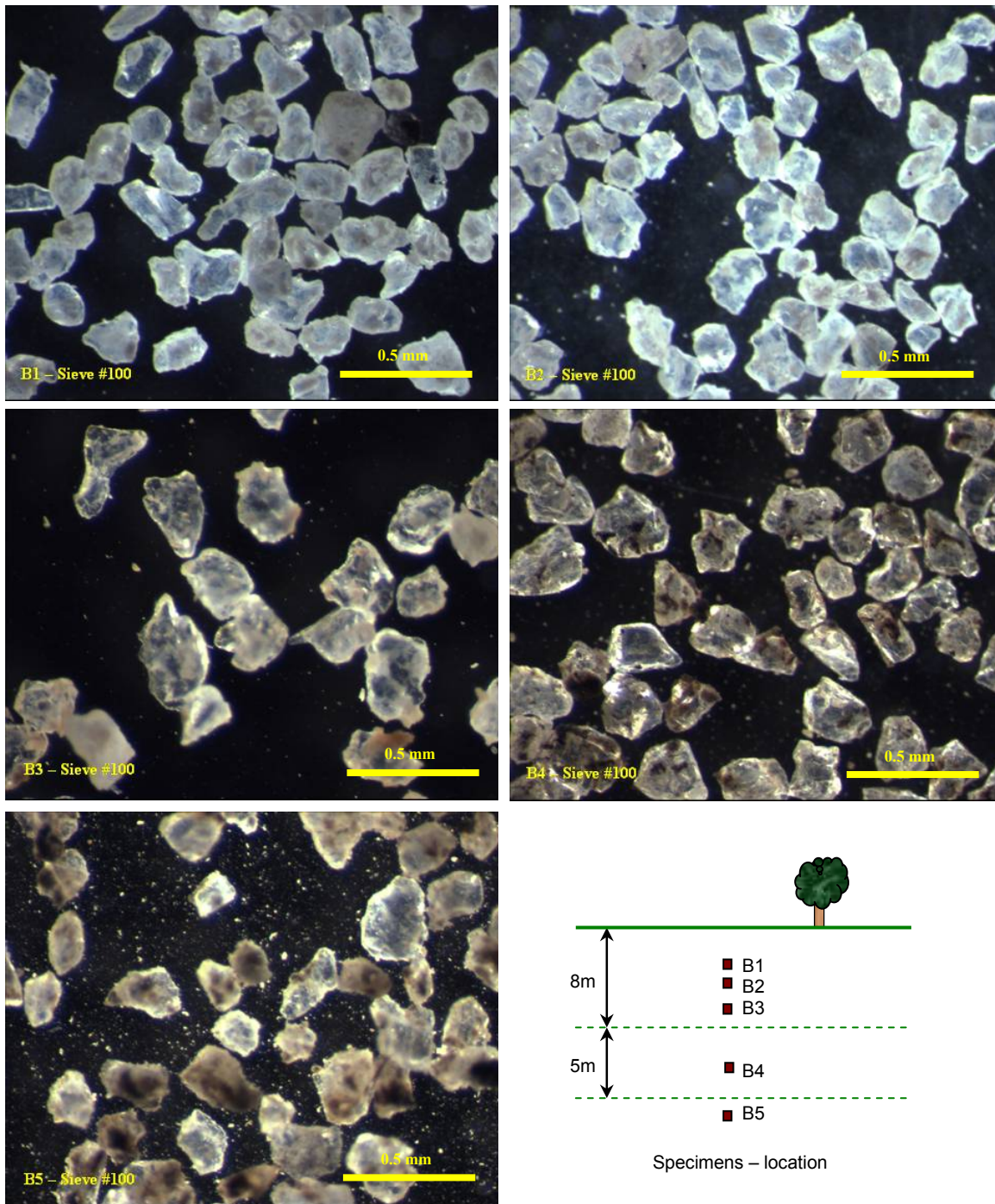
Figure 5.5. Micro-photographs of the soil samples corresponding to the fraction retained on sieve #100, including a magnification of the black fine particles found in B4 specimens.

$$S = \frac{r_{max}}{r_{min}}$$

$$R = \frac{\sum r_i / N}{r_{max}}$$
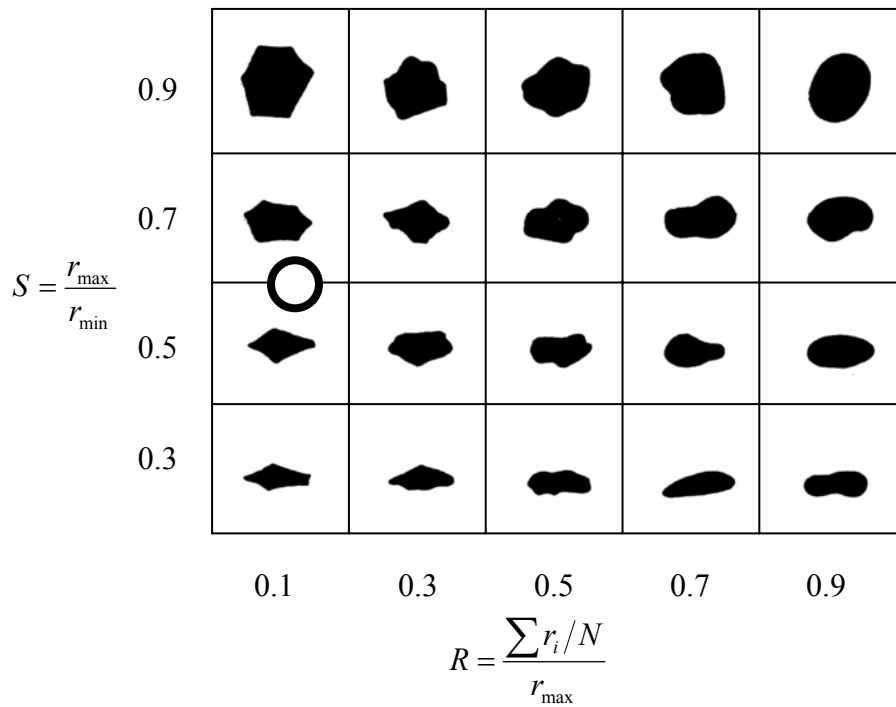
Figure 5.6. Sphericity and roundness for all sands estimated from the microphotographs (chart by Krumbein and Sloss 1963).
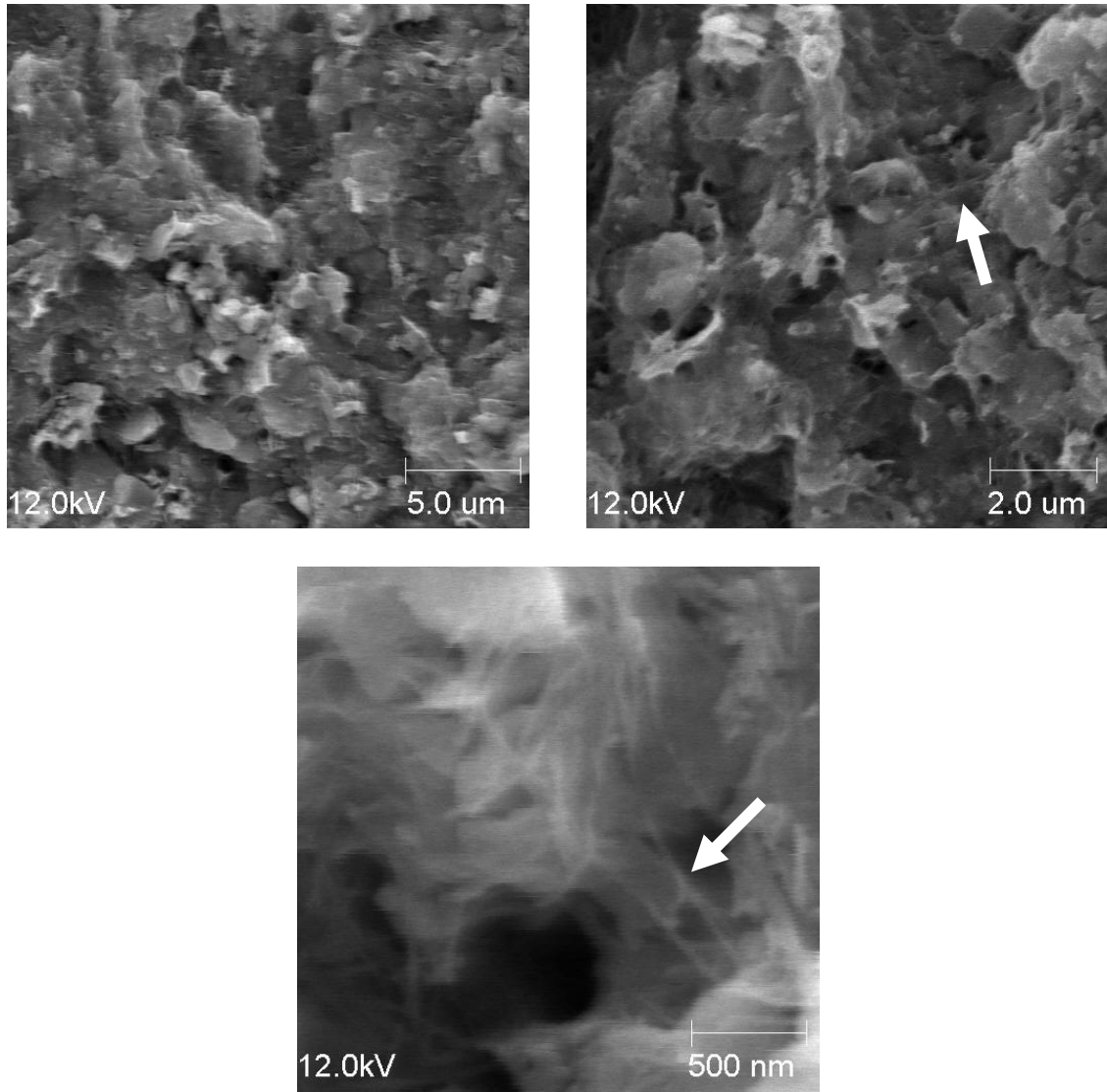
Figure 5.7. SEM microphotographs at different magnifications.
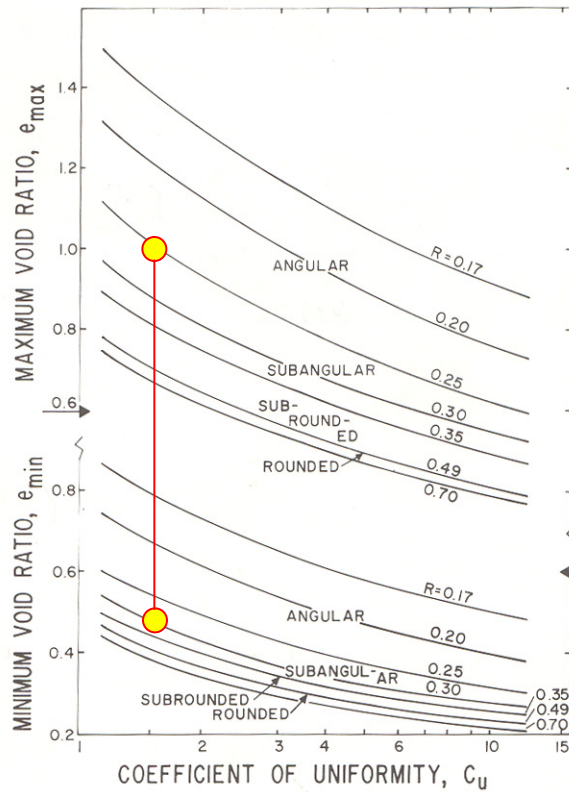
Figure 5.8. Particle shape, coefficient of uniformity and extreme void ratios (Youd, 1973; see also Maida, 2002).

Furthermore, there is a significant increase in hydraulic conductivity for specimen B4 when it is oven-dried prior to testing (more than two orders of magnitude). This highlights the role of the organic matter present in this layer.

The specimen B2 contains clay balls and nodules. The spatial distribution of these inclusions has a significant effect on the measurements (refer to results in Chapter II).

For reference, the Hazen equation predicts a value $c \cdot D_{10}^2 \approx 2.3 \times 10^{-2}$ cm/sec for the most commonly used value of the coefficient $c=100/(cm.sec)$.
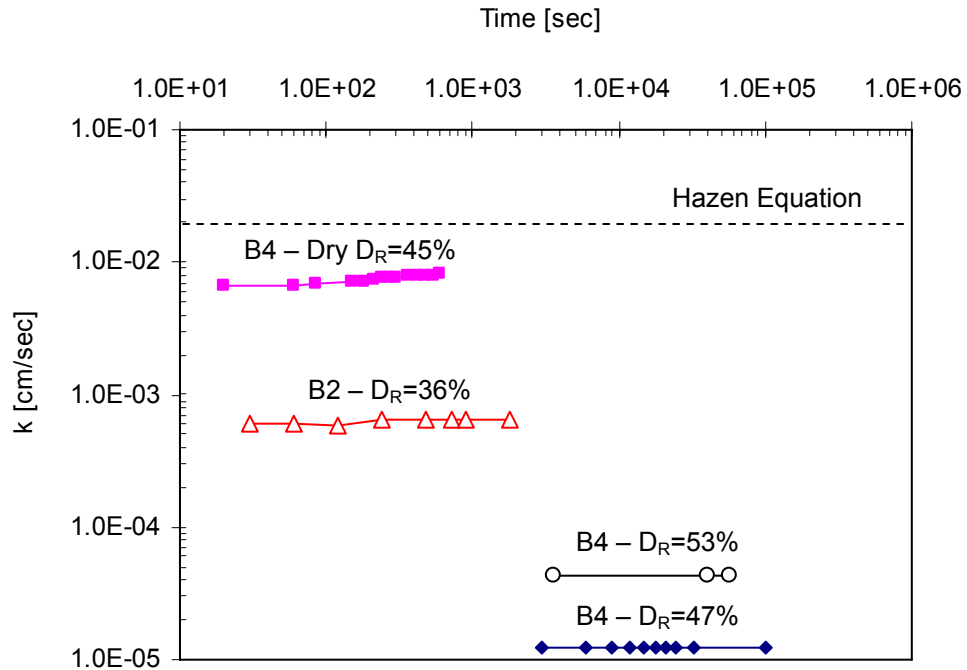
Figure 5.9. Hydraulic conductivity. Note the large increase in hydraulic conductivity when specimen B4 is oven-dried prior testing.

5.2.3 Quasistatic tests

The measured zero lateral strain K_0 loading compressibility and large-strain critical state parameters are documented next.

Zero lateral strain K_0 loading. Load-deformation under zero lateral strain is studied using oedometer cells. Typical load-deformation results are shown in Figure 5.10 (Table 5.2). Each loading stage is applied for 10-20 minutes in specimens B2 and B4, (the load is sustained for one hour in specimen B4-D_R=47%, specimen prepared with oven-dried, and re-saturated soil). Some remarks follow.
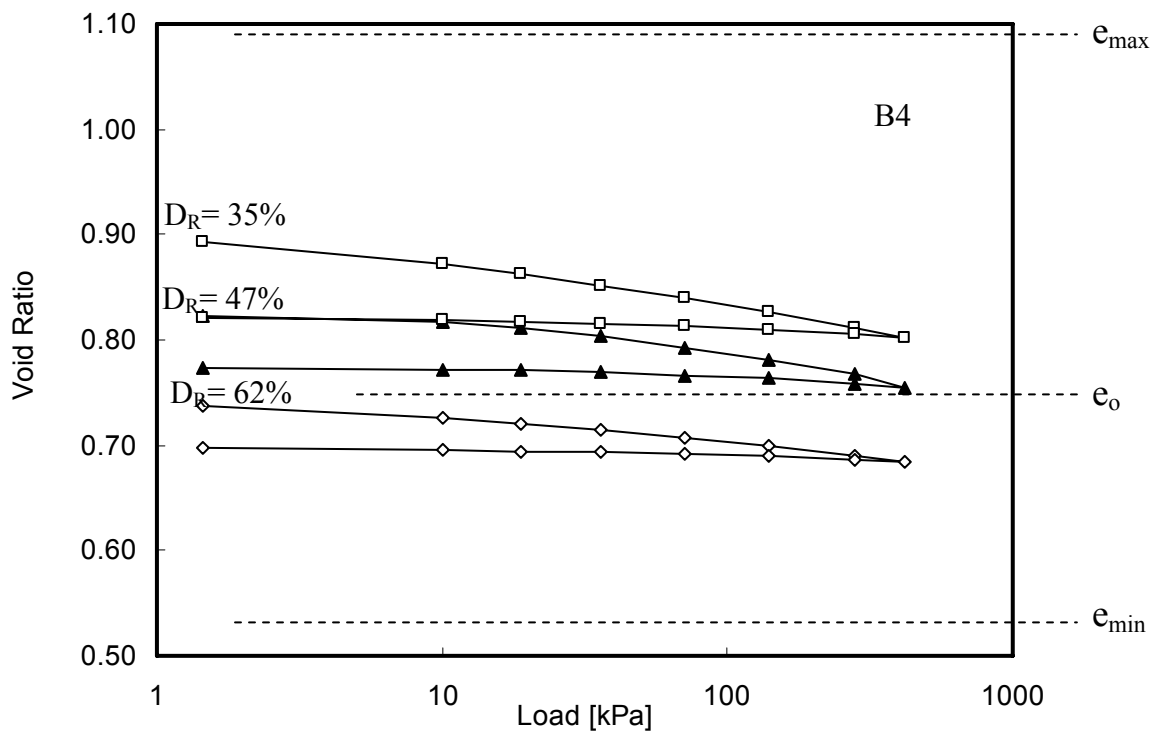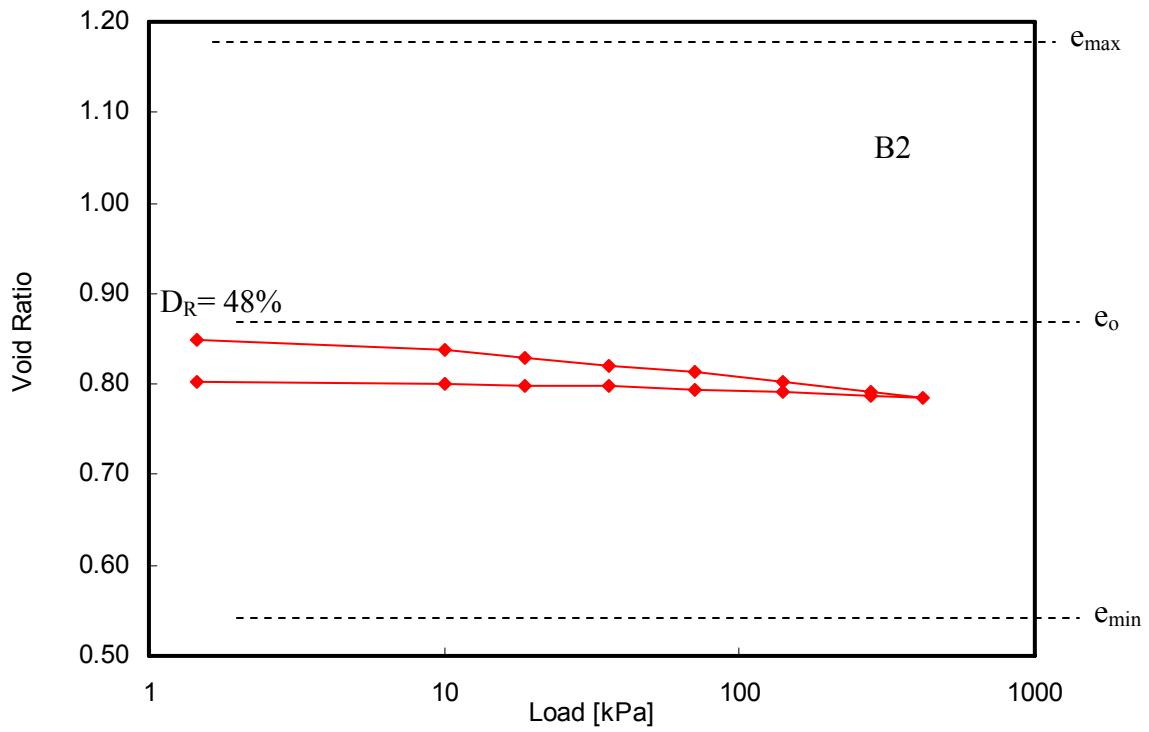
Figure 5.10. Oedometer test results on specimens B2 and B4.

The compression index C_c decreases as the relative density D_R increases, ranging from C_c=0.0347 to C_c=0.0528. Nevertheless, the compression index C_c increases for oven-dried specimens, resulting C_c=0.0728.

The recompression index C_r ranges between C_r=0.0021 and C_r=0.0036, and it increases with decreasing relative density.

The coefficient of consolidation C_v for the B4 loose fine sandy layer is estimated from load-deformation data shown in Figure 5.11. The inferred value is C_v=5.7m^2/yr (log time method). For comparison, C_v is computed from the compression index C_c and the hydraulic conductivity k as:

$$C_v = \frac{k}{\gamma_w \cdot \left(\frac{0.435 \cdot C_c}{(1+e_0) \cdot \sigma_{avg}} \right)}$$

(5.1)

Resulting in $1.062x10^{-3} \frac{m^2}{yr} \leq C_v \leq 2.33x10^{-3} \frac{m^2}{yr}$ if k=1x10^{-5} cm/sec. Due to the large variation of the hydraulic conductivity k, the value of C_v could vary in result up to 3 orders of magnitude. Differences between measured and predicted values may reflect the contribution of creep to pressure diffusion.

The laboratory time scale is ~2minutes at all relative density D_R in Figure 5.11.

The range $e_{min} - e_{max}$ is superimposed on Figure 5.10. It can be concluded that preloading is not an effective approach to densify the "black sands".
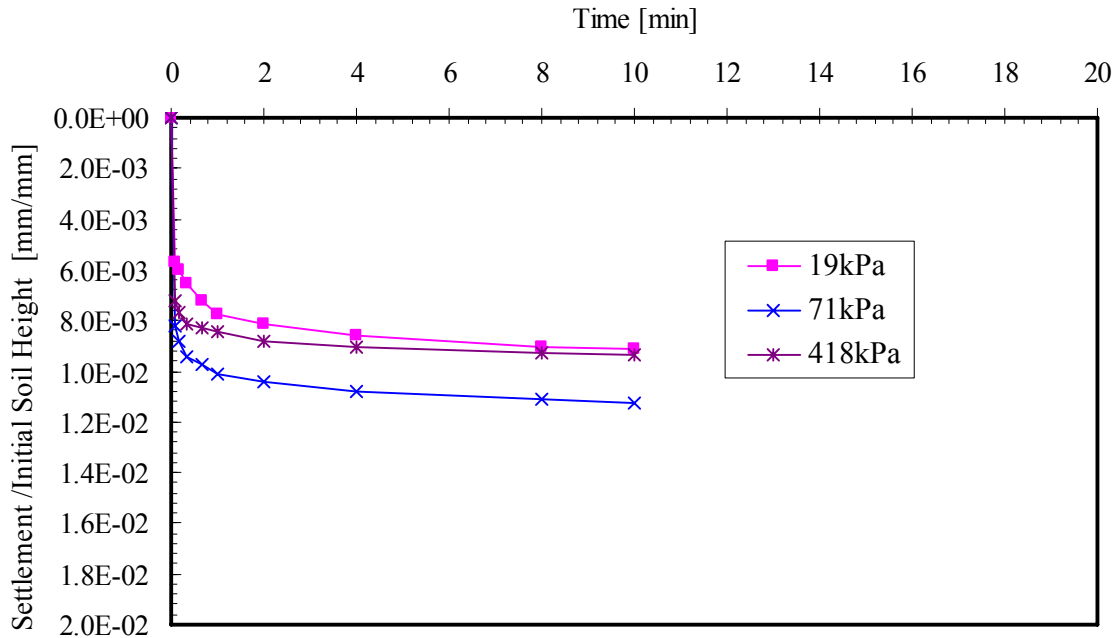
Figure 5.11. Time rate effects observed in oedometer tests (B4 at DR=47%, Oven dry specimen). Initial Soil Height =18.50mm.

Critical state. The critical state is the most robust criterion for strength design including post-liquefaction strength. Critical state soil parameters are found following the simplified method proposed by Santamarina and Cho (2001). The resulting critical state lines are shown in Figure 5.12. The inverted *p'-e* critical state parameters are Γ=1.232 (intercept at *p'*=1kPa), and compression index λ=0.049 (in natural logarithmic scale) for specimen B2; and Γ=1.165 and λ=0.06 for specimen B4. The simplified critical state method renders critical state friction angles φ_{cs}=32° for B2, and φ_{cs}=33°–40° for B4.
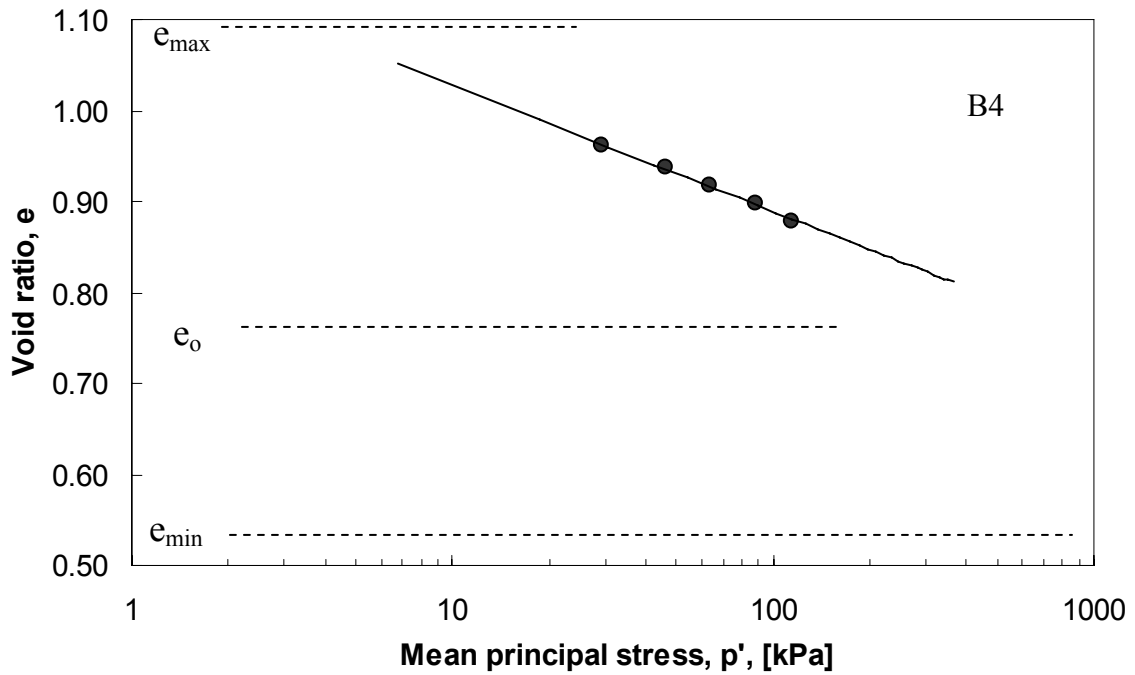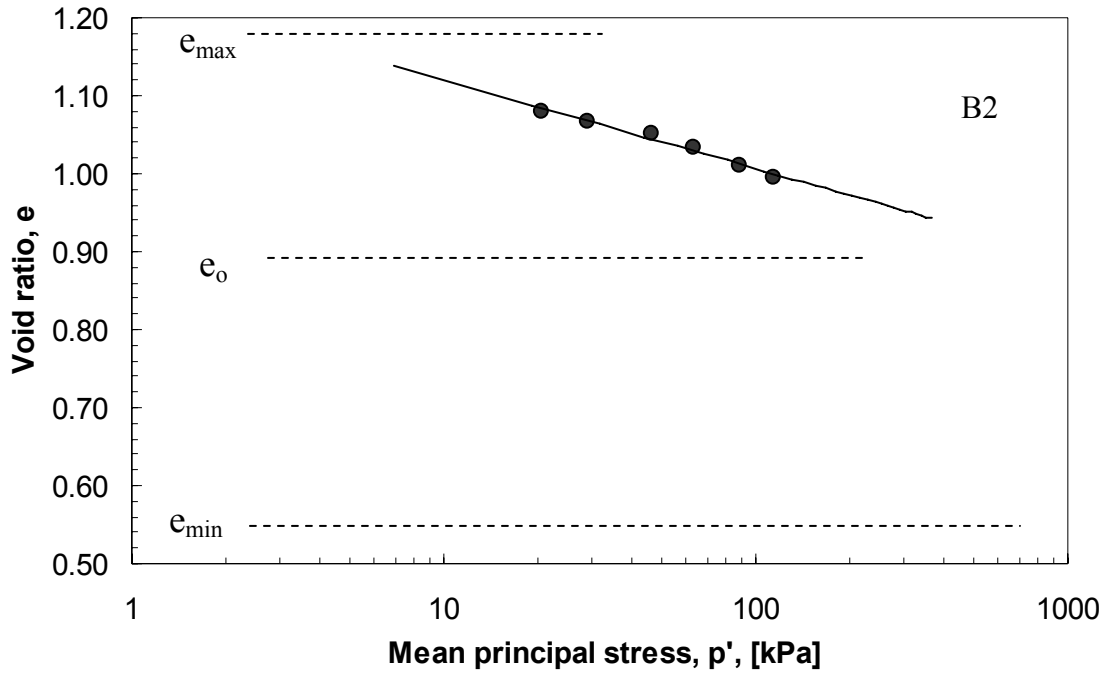
Figure 5.12. Critical state lines in the e vs. p' space for specimens B2 and B4.
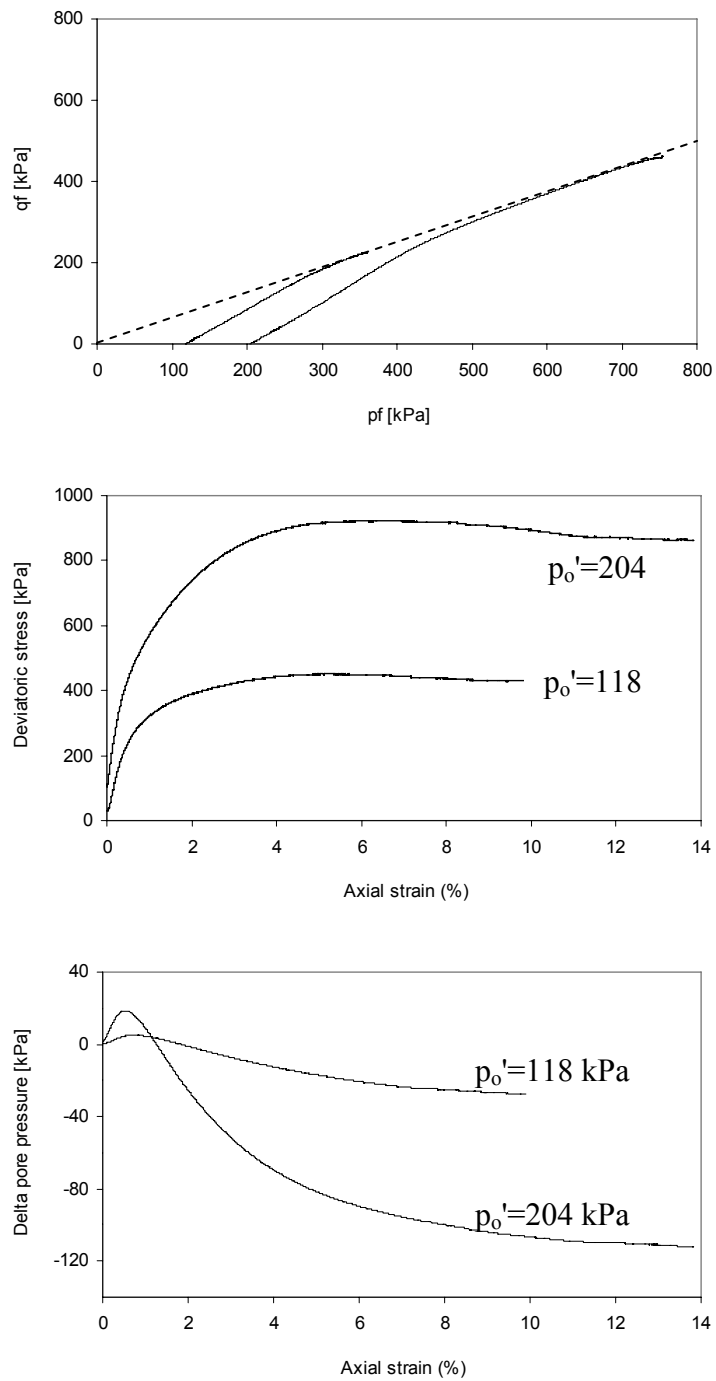
Figure 5.13. CU Triaxial test on B4 specimen (isotropically consolidated, followed by undrained deviatory loading). For p_0'=118kPa, e=0.79 and D_R=53%, and for p_0'=1204kPa, e=0.70 and D_R=69%.

To address concerns related to fine segregation, undrained triaxial tests are conducted on specimens B4 with black fines to determine the *q-p'* critical state strength parameter *M* (Figure 5.13). The measured critical state friction angle is φ_{cs} =17° for B4, which is significantly lower than friction angles obtained by the simplified method.

5.2.4 Dynamic tests

Strain controlled, undrained dynamic cyclic triaxial tests are conducted on specimens B2 and B4 using a modified triaxial device. The peak-to-peak axial strain level is fixed at ε_a=0.01. This is the strain amplitude caused by a harmonic motion with amplitude a_{PGA}=0.26g and frequency ω=2Hz in a *H*=12m soil column, $\varepsilon = a_{PGA}/(\omega^2 \cdot H)$.

Results in Figure 5.14 show a vertical strain time series and the associated variations in excess porewater pressure and deviatory stress *q*. Related plots are shown as well. Results indicate that as the number of compression-extension cycles increases, the excess porewater pressure increases while the deviatory stress decreases. The critical state line with slope *M* bounds the stress path in the *q-p'* space.

Cyclic tests are stopped whenever liquefaction is achieved (i.e., u_R=1), or after 70 cycles, whichever happens first. Each completed test is called an "event". Once the test is stopped, drainage is allowed and the volumetric strain is determined. Figure 5.15 shows the evolution in void ratio *e* with the number of events. It resembles the "terminal density" graph in Figure 4.10. The terminal void ratio for this soil and process is e_T=0.87.

The number of cycles required to achieve a certain level of excess pore pressure relative to the liquefaction condition u_L, namely $u_R=u_{measured}/u_L$ is plotted versus void
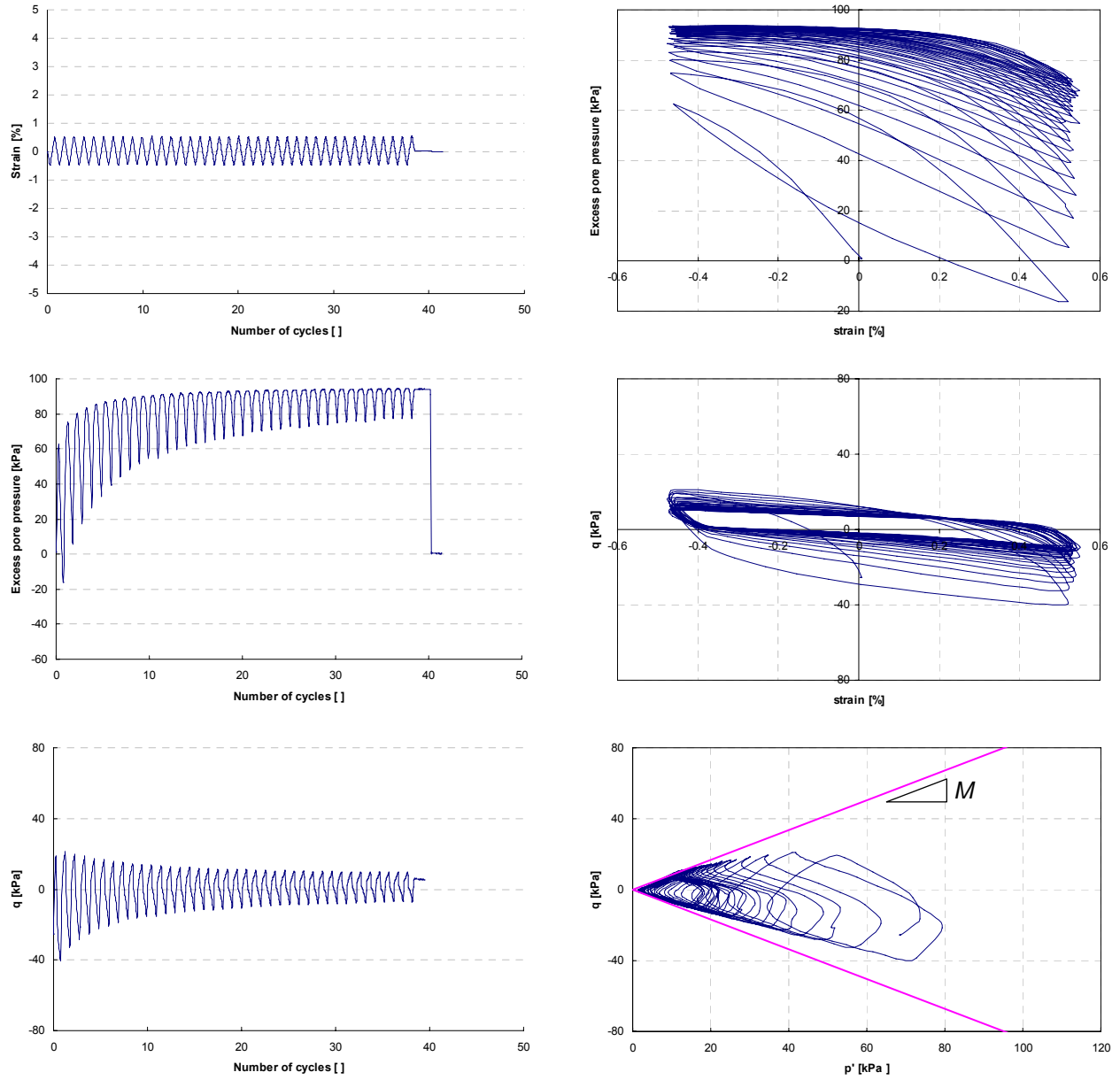
Figure 5.14. Typical dynamic cyclic triaxial test results on B4 specimens (σ_confinement=100kPa, e=0.847).
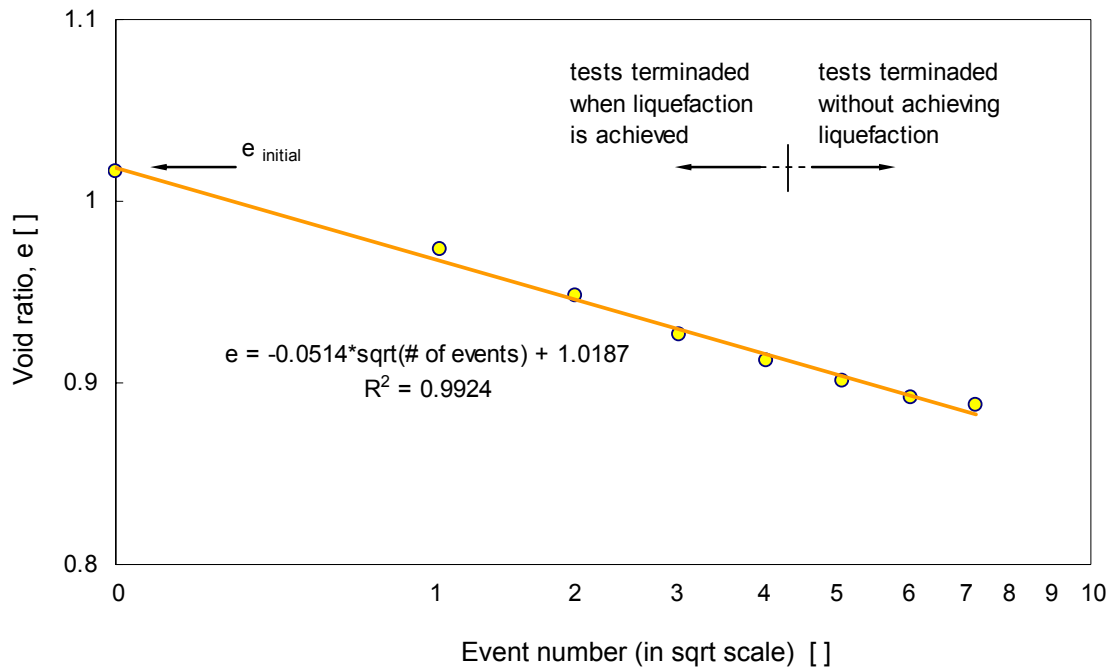
Figure 5.15. Terminal density. Void ratio as a function of event number.

ratio e for each event in Figure 5.16. The graph reveals that a void ratio $e<0.9$ is sufficient

to prevent massive liquefaction in the B4 soil since a very large number of cycles would

be required to build excess pore pressure.

139
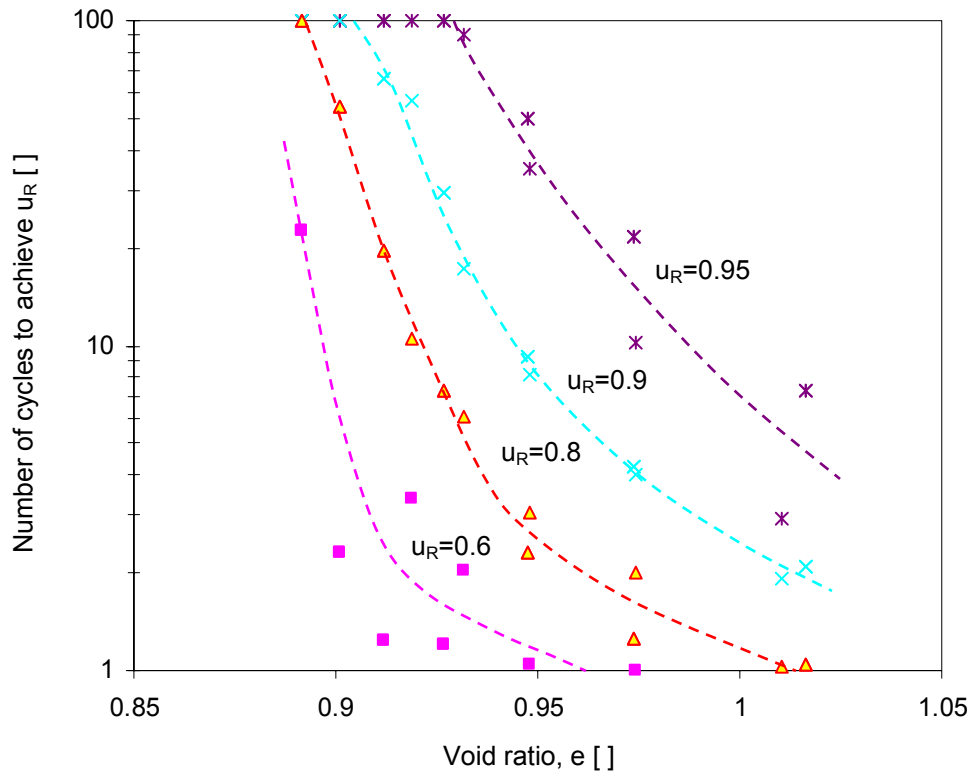
Figure 5.16. Number of cycles required to achieve a certain liquefiable excess pore pressure $u_R = u_{measured}/u_L$ versus void ratio (data gathered with two B4 specimens).

5.2.5 Geophysical tests

Geophysical parameters are gathered in the laboratory in view of potential field characterization and process monitoring strategies. Tests include shear wave and electromagnetic wave propagation.

Shear wave velocity. The shear wave velocity V_s is a measure of the soil skeletal stiffness G_{max} and mass density ρ. The oedometer cell (Section 5.3.2) is instrumented with bender elements to monitor the shear wave velocity and its variation as a function of

effective stress. The shear wave travels through the specimen, excites the lower bender element (i.e., receiver), and its signal is recorded. The procedure is repeated at each loading step, during loading and unloading (instrumentation details and interpretation can be found in Lee and Santamarina, 2005). Figure 5.17 shows a typical set of time series; the first signal is the input step function (i.e., source) As the load increases, the travel time decreases, and the shear wave velocity increases.

Velocity-stress plots are summarized in Figure 5.18. The shear wave velocity V_s increases as a power function of the effective mean stress in the polarization plane σ_m' (Stokoe et al. 1991),

$$V_s = \alpha \cdot \left(\frac{\sigma_m'}{kPa} \right)^{\beta}$$

(5.2)

This model fits the data with α and β values summarized in Table 5.2 for different relative densities. Values are compatible with similar values found for comparable sands (Fernandez 2000). In agreement with previous studies, α increases and β decreases as the relative density decreases. Both values are in agreement with uncemented, not preloaded sandy soil (Santamarina et al. 2001 – Figure 5.19).

Electromagnetic properties. The electromagnetic properties of these soils are investigated to assess the possible utilization of GPR in the field. Measurements include pore fluid and soil-water mixture characterization. The pore fluid conductivity σ_f is measured by extracting pore fluid by dilution with the addition of a one pore-volume of deionized water; then, assuming low ionic concentration and a linear concentration-conductivity relation, the measured conductivity is doubled. The electrical conductivity

141
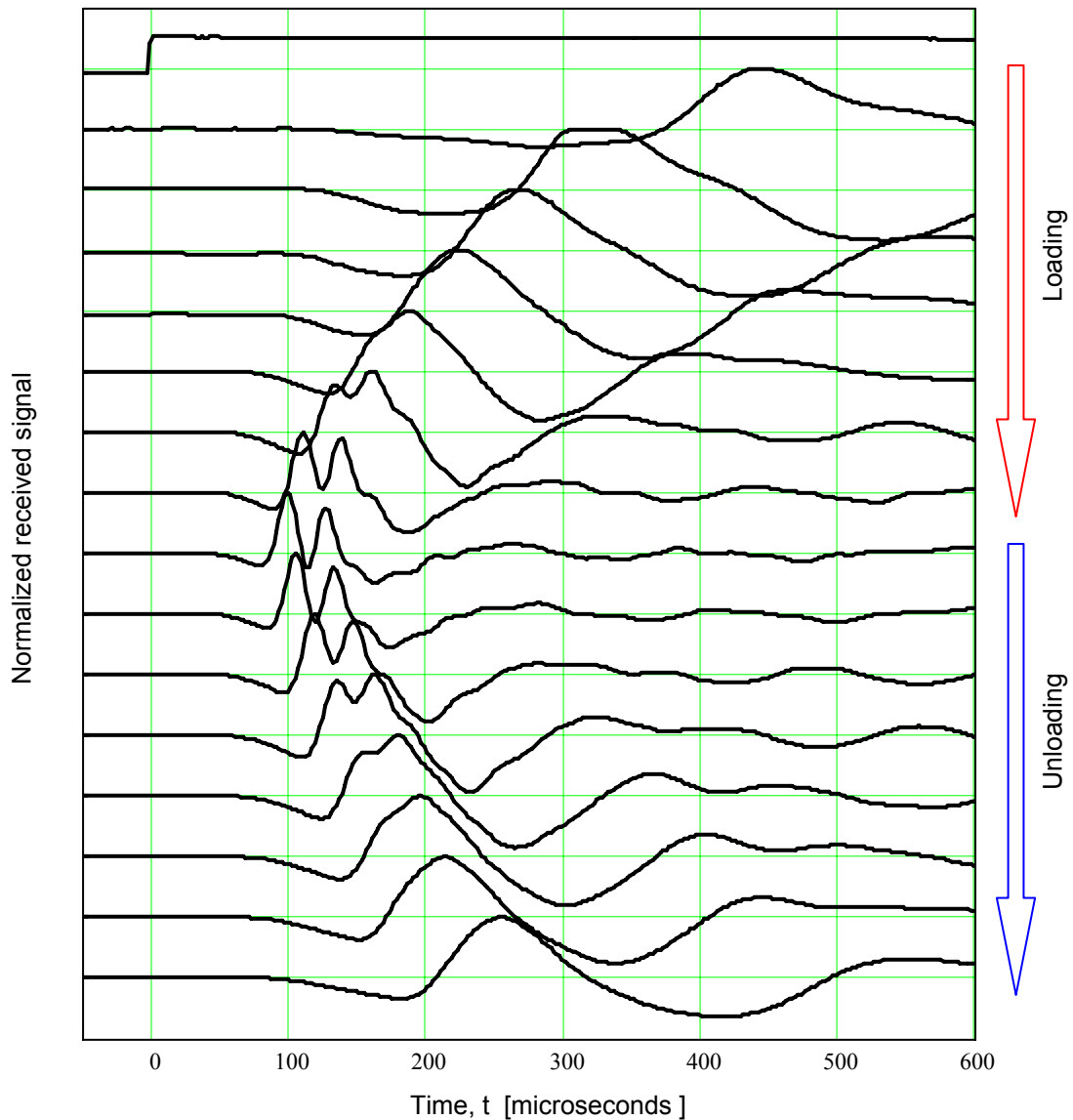
Figure 5.17. Shear wave velocity measurement in oedometer cell. (D_R= 62%, B4 – field conditions).

increases with depth from σ_{el}=0.041 S/m for the B1 horizon to σ_{el}=1.23 S/m for B4 (Table 5.1). The high conductivity of the pore fluid in the B4 layer is surprising. For comparison, the conductivity of fresh water is σ_{el}=10^{-3} S/m while the conductivity of seawater is σ_{el}=4 S/m.
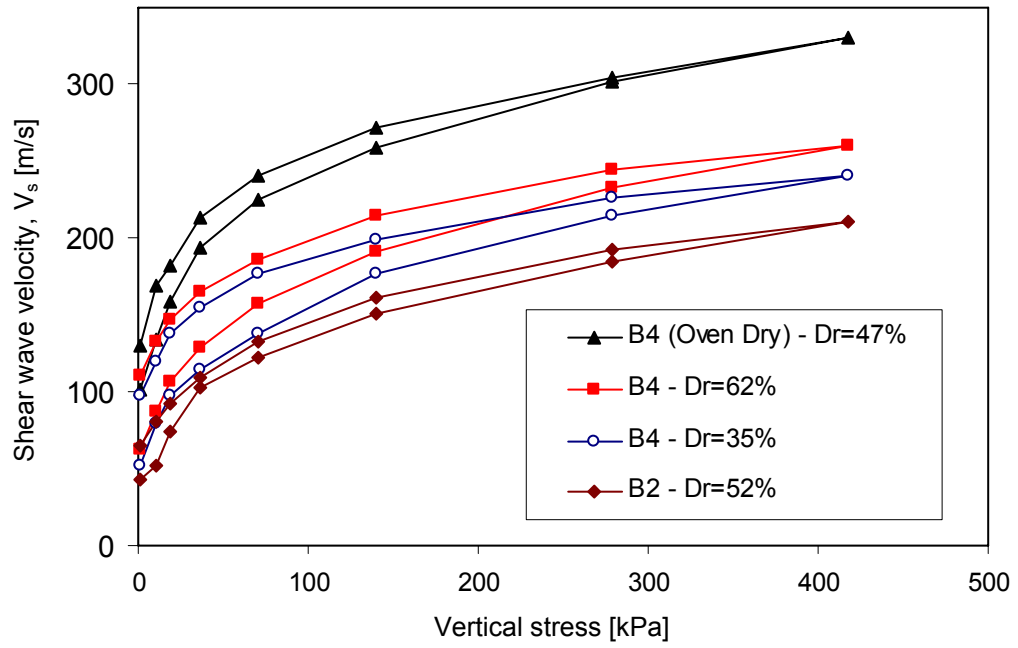
Figure 5.18. Shear wave velocity versus vertical stress.

$$\beta = 0.36 - \alpha / 700$$
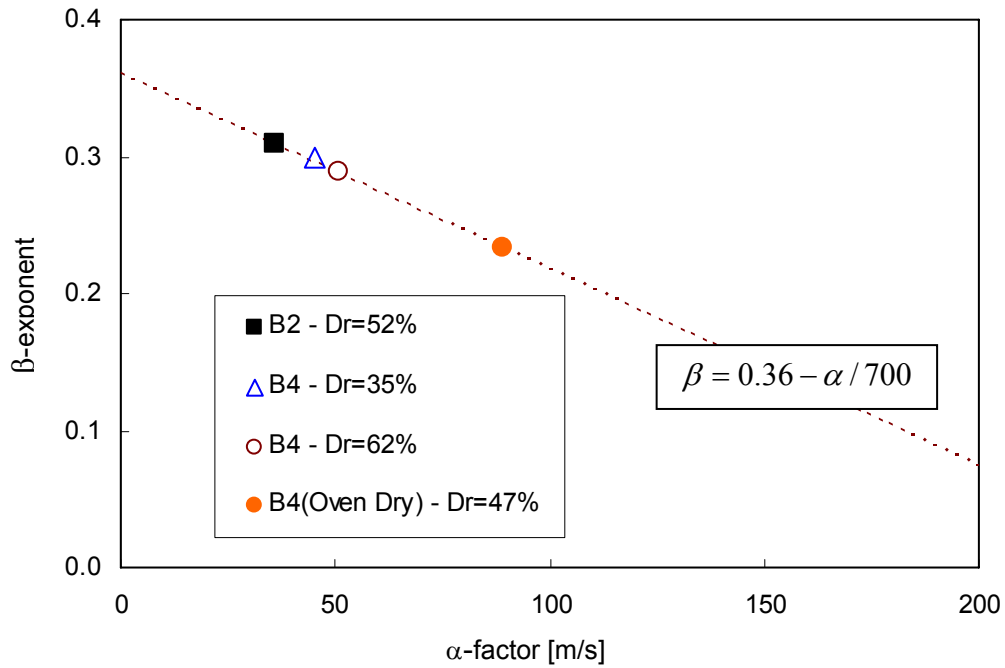
Figure 5.19. Comparison with published database (trendline from Santamarina et al. 2001).

143

The soil-water mixture conductivity σ_{mix} (a function of the ionic concentration in the pore fluid) and permittivity κ' (a function of the volumetric water content) are measured using a HP 8752A Network Analyzer between 20MHz and 1.3GHz; this frequency range is relevant to ground penetrating radar. Results are presented in Figure 5.20. Specimens are preserved at their "natural moisture".

5.3 FIELD CHARACTERIZATION

The field site characterization involves topographic surveys, cone penetration CPTu, spectral analysis of surface waves SASW, seismic refraction, and ground penetrating radar GPR. Salient results are summarized next.

5.3.1 Cone penetration test

The CPT soundings shown in Figure 5.21 are gathered at several locations in the 20mx20m test site. There is a relatively small horizontal variation in soil parameters. Notice the very weak contractive sediments between depths $z\cong7.5m$ and $z\cong12m$, as confirmed by both low tip resistance q_t and high positive excess porewater pressure u.

5.3.2 Ground penetration test

An extensive GPR survey of the test area and its vicinity is conducted using 200 MHz antennae and a spacing of 2 m, with a side step of either 0.50 m or 0.90 m (Figure 5.22-a). Figure 5.22-b displays a typical GPR profile that shows the horizontally stratified profile. The first strong signal corresponds to the direct wave that propagates in air; the second arrival is the reflection from the ground water table (GWT). Signals vanish after 250 ns and no reflection can be identified thereafter.

144
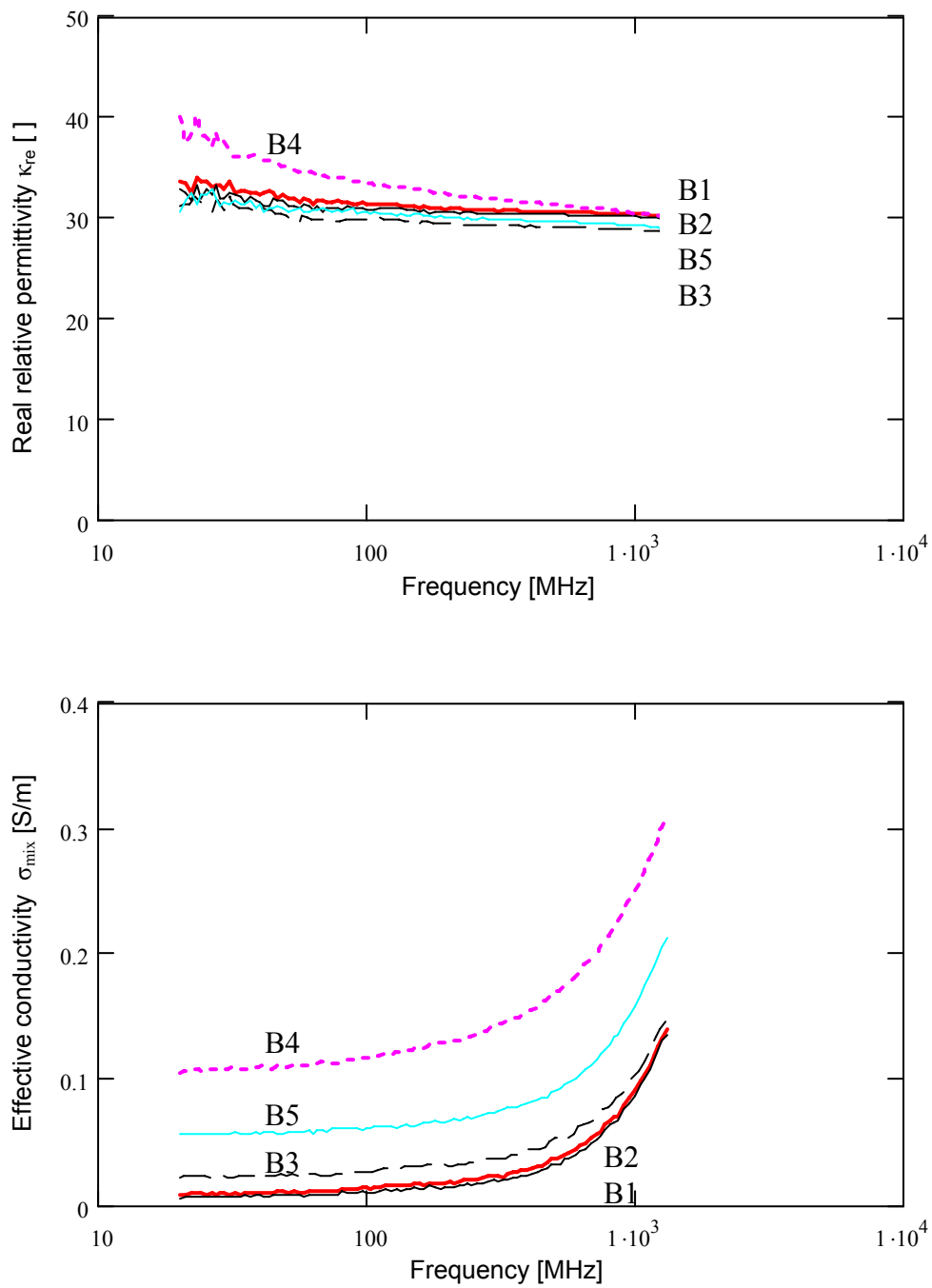
Figure 5.20. Soil-water mixture electrical conductivity and permittivity as a function of frequency.
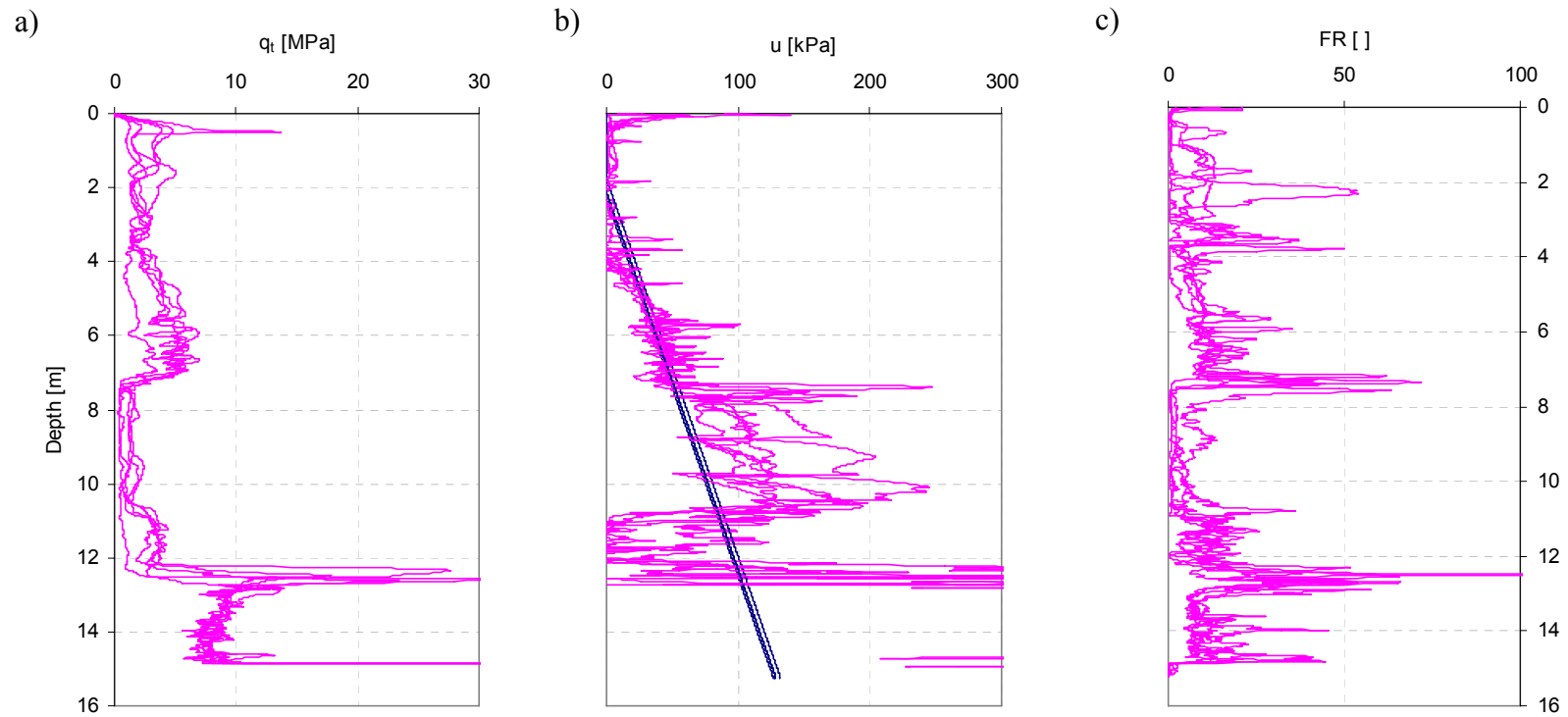
Figure 5.21. Representative CPT data. a) Tip resistance q_t. b) Porewater pressure u. c) Friction ratio FR. The soundings are conducted at different locations within the 20m by 20m test site. Notice the relatively small horizontal variation in soil parameters and the weak contractive sediments found between depths z~8m and z~12m (data provided by T. Hebeler – GeoSyntec Inc.).

a) Plan view

• GPR survey lines

Distance in meters

Antennae

2.0m

Line 6

Side step

b) Side view GPR
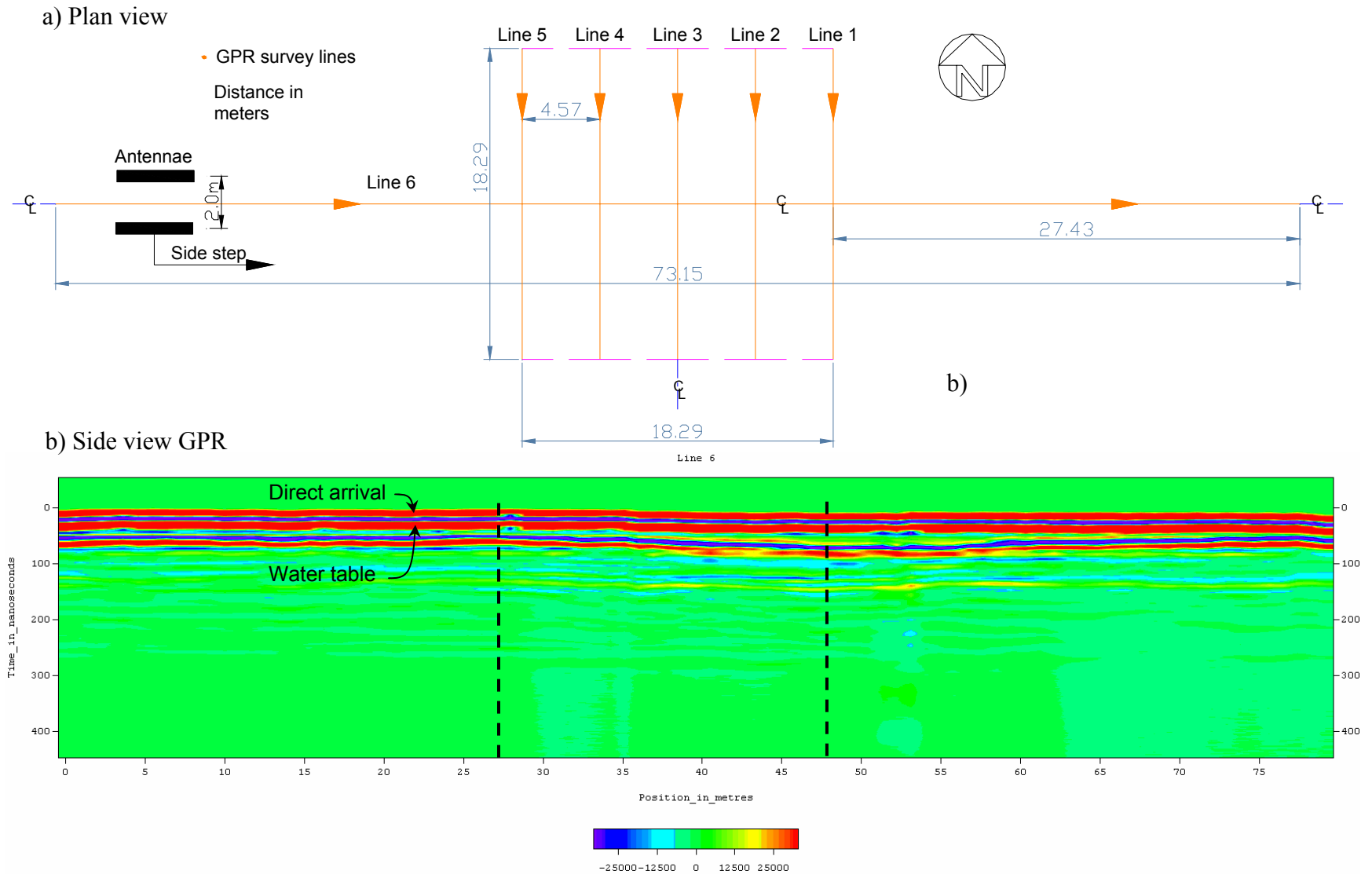
Figure 5.22. GPR profile (Line 6). The dashed lines indicate the 20m test site.

A common midpoint GPR survey (CMP) is conducted to infer the variation of local porosity with depth. This test consists of gradually moving the receiver and transmitter antennae equal distances away from a common mid-point (Figure 5.23). This technique permits the evaluation of local propagation velocity at different elevations from the analysis of the ensuing hyperbolic records in the presence of clear reflectors. In this study, the CMP survey is conducted using the 200 MHz antennae and increasing the offset every 0.60 m (i.e., antennae spacing of 1.2 m; 1.8 m, 3.4 m, etc.). Data are interpreted following normal move out NMO correction in a horizontally stratified profile ($t^2 - x^2$ velocity analysis that assumes a hyperbolic function in the time delays due to the offset) and the method of constant velocity scan CVS. Figure 5.23 shows agreement between velocity profiles obtained with the two techniques. The velocity profile inverted from data collected before blasting confirms the presence of a high velocity upper layer (the P1 layer) on top of lower velocity layers (B1 through B3).

Given the velocity profile and the time for maximum penetration (t~250ns), it is concluded that GPR cannot penetrate the subsurface beyond ~8m; thus, the B4 horizon can not be explored with surface-based GPR.

5.3.3 SASW and Seismic refraction

A spectral analysis of surface wave SASW is implemented by S. Yoon using array-based surface wave methods. A harmonic source (APS Dynamics, Inc. Model 400 Electro-Seis electromechanical shaker) is used to generate the active Rayleigh wave field. Typical measurements span from ~4 Hz to ~100 Hz. A non-uniform linear array of 15 Wilcoxon Research 731A Ultra-Quiet, Ultra-Low-Frequency seismic accelerometers is

a)

b)
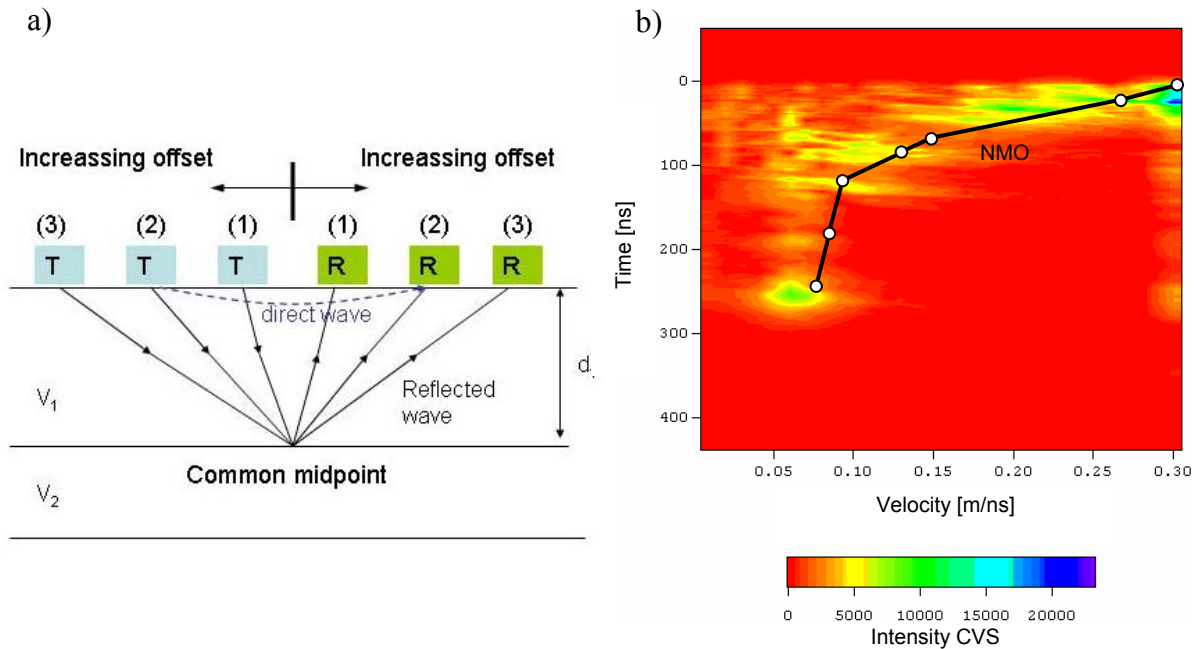
Figure 5.23 Common midpoint test using GPR. a) Common midpoint sketch. b) Results – Comparison between velocity analysis with CVS and NMO ($t^2 – x^2$ velocity analysis).

deployed. A circular array is deployed for passive surface wave tests. The data acquisition system is a modular Hewlett-Packard VXI multi-channel digital signal analyzer, complemented with a signal conditioner, and a laptop computer. Further details on the methodology and the hardware can be found in Yoon (2005).

The shear wave velocity profile inferred from SASW is shown in Figure 5.24. It highlights a low velocity region V_s<150m/s at depths z~7.5 to z~12m, in agreement with CPT results in Figure 5.21.

Finally, a 12 channel Bison Seismograph is used to conduct high resolution seismic refraction surveys. The spacing between each of the 12 geophones is 1.067m, and

a sledge hammer is used as a source. A set of signals is presented in Figure 5.25. No strong refraction is detected. The data show a P-wave velocity V_P=160 m/s in the unsaturated upper layer. The prevalent Raleigh wave velocity is V_R=95 m/s and corresponds to a wavelength $\lambda_R \cong 1.4$m, thus, the very shallow unsaturated upper layer.
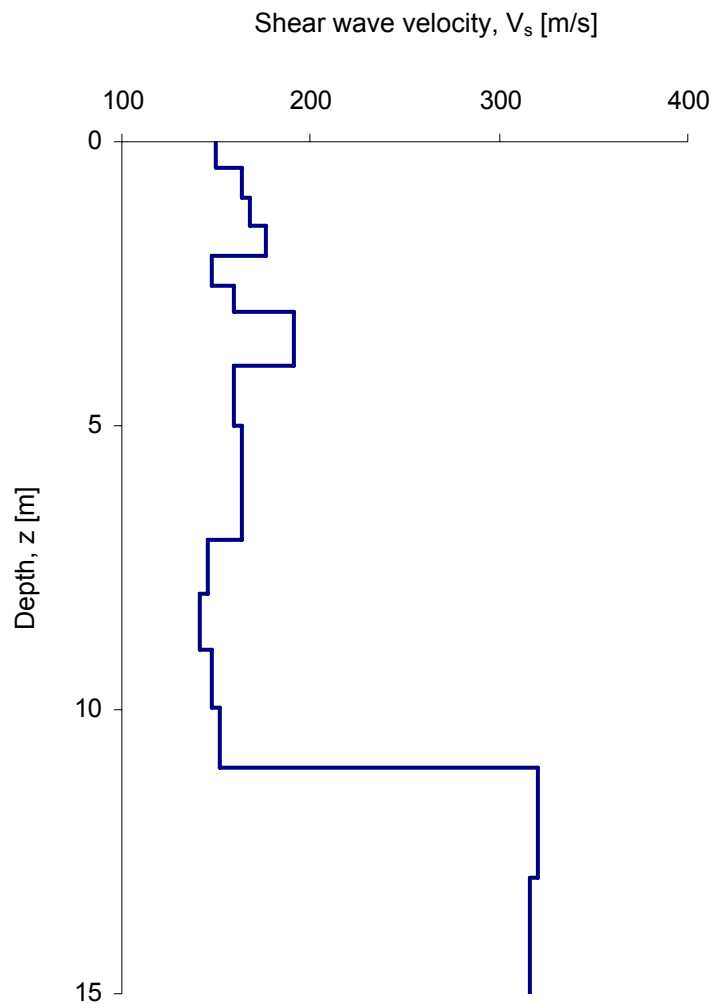
Figure 5.24. S-wave velocity profile from SASW (data gathered by Sungsoo Yoon).
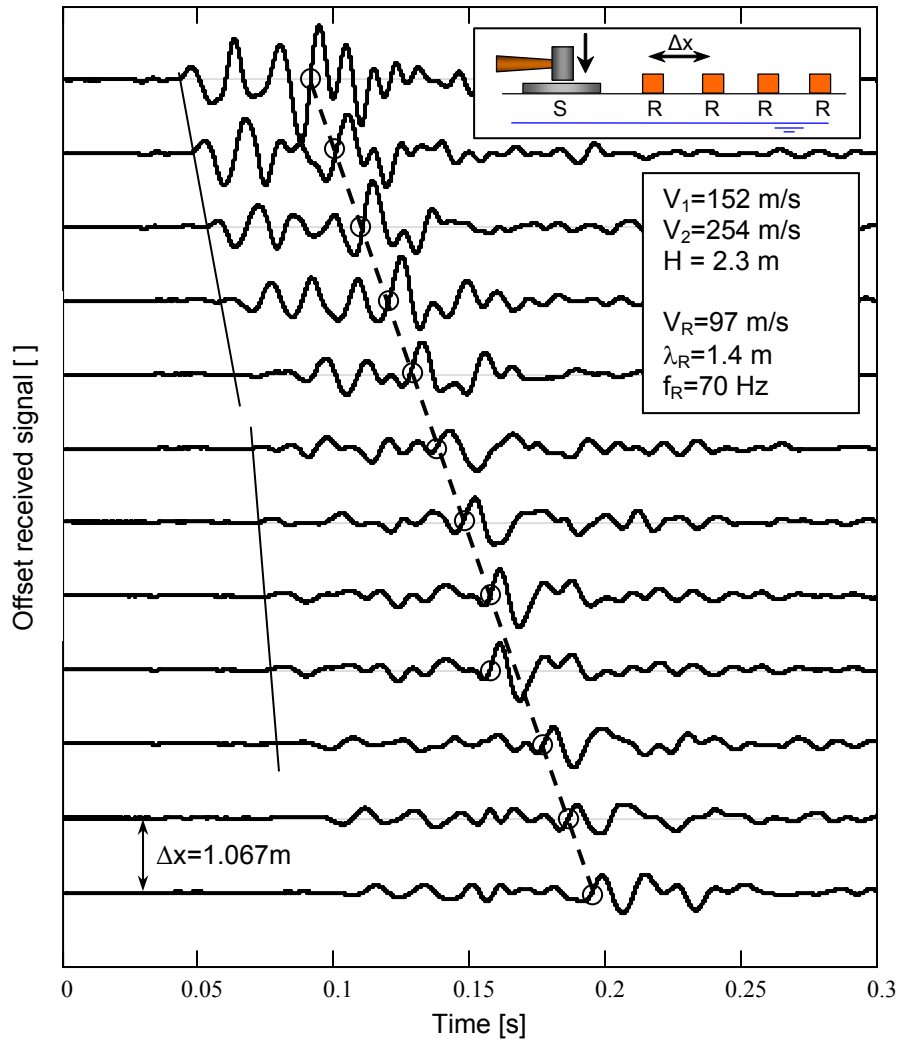
Figure 5.25. Seismic survey line – Center Line of test site (source at 9.1 m away from the first geophone, the top signal). Geophone separation is 0.91 m (Record SM3).

151

5.4 DISCUSSION

The characteristic relaxation time for excess porewater pressure diffusion can be estimated as $t = H^2/C_v$. For a drainage path H=2m and $1.062x10^{-3}\frac{m^2}{yr} \leq C_v \leq 2.33\frac{m^2}{yr}$, the pressure diffusion time can extend from 1.7yrs to 3700yrs. Alternatively, data in Figure 5.11 gathered for a H_2=18.5 mm can be scaled by H_1^2/H_2^2. For H_2=6m, the observed ~2minutes time scale in the laboratory corresponds to ~0.5yrs in the field as $t_2 = t_{1.}\left(H_2^2/H_1^2\right)$. In either case, these results suggest that post-blasting settlement will not be instantaneous.

The study of critical state parameters permit assessing whether the soil will tend to dilate or to contract upon shearing, and the corresponding development of positive or negative excess porewater pressure under undrained loading. The measured critical state parameters Γ and compression index λ are compatible with the values for e_{max}, e_{min} and C_u as summarized in Table 5.2 (Cho 2001),

$$\Gamma = 1.136 \cdot e_{max} - 0.397 \cdot e_{min} - 0.103136 \cdot C_u + 0.317 \qquad (5.3)$$

$$\lambda = 0.15 \cdot \left(e_{max} - e_{min}\right) \qquad (5.4)$$

The critical state friction angle φ_{cs} measured in triaxial tests and using the simplified method are in agreement with values predicted from roundness R (Narsilio and Santamarina 2004; Santamarina and Cho 2004; Cho et al. 2006):

$$\phi_{cs} = 42 - 17 \cdot R \qquad (5.5)$$

The determination of the in situ void ratio presents great uncertainty. When the in situ void ratio e_0=0.78 estimated from the recovered moisture content (assuming complete saturation) is compared against the critical state line, it is concluded that these soils will tend to dilate at large strains. Therefore, although they may experience large deformations under cyclic loading, they are not expected to liquefy. Furthermore, the calculated in situ void ratio may be higher than the measured one if water drained out during sampling. On the other hand, black fines segregate during testing and are purposely removed before running the simplified critical state tests (applies both to friction angle and e-p' test). This may explain the high e_{cs} values that are measured as compared to e_0. In turn, this situation aggravates the potential for liquefaction in the B4 horizon.

The liquefaction potential assessment procedure proposed by Youd et al. (2001) is used to evaluate the liquefaction resistance at the site based on CPT data (Figure 5.21) and a peak ground acceleration as small as a_{PGA}=0.26g The layer between depths z≅7.5m and z≅12m is predicted to be "extremely liquefiable" (at the time of CPT testing, the ground-water table was z=0.8m to 1.5 m below the surface). However, the age of sediment, the lack of historical evidence of past liquefaction events in the vicinity, and e_0<e_{cs} contradict this assessment.

The application of GPR to this site is limited by the penetration depth of the electromagnetic waves in the soil mass. The penetration of GPR for a 100dB A/D board can be computed as follows:

$$skin\ depth = \frac{R_{16}}{\frac{\omega \cdot \sqrt{\kappa_{re}}}{c} \cdot \sqrt{\frac{1}{2} \cdot \left[\sqrt{1 + \left(\kappa_{re} \Big/ \frac{\sigma}{\varepsilon_0 \cdot \omega} \right)^2} - 1 \right]}} \qquad (5.6)$$

where σ is the electrical conductivity of the soil-fluid mixture, ω is the frequency, κ_{re} is the real relative permittivity, and the factor R_{16}=11.052 corresponds to a 16-bit card. The skin depth computed with Equation 5.6 and data in Figure 5.20 is plotted in Figure 5.26 as a function of frequency. In agreement with field results (Figure 5.22), surface-based GPR will not penetrate the weak B4 layer at $z \cong 7.5m$ to $z \cong 12m$ (conductivity-based determinations may be more applicable).
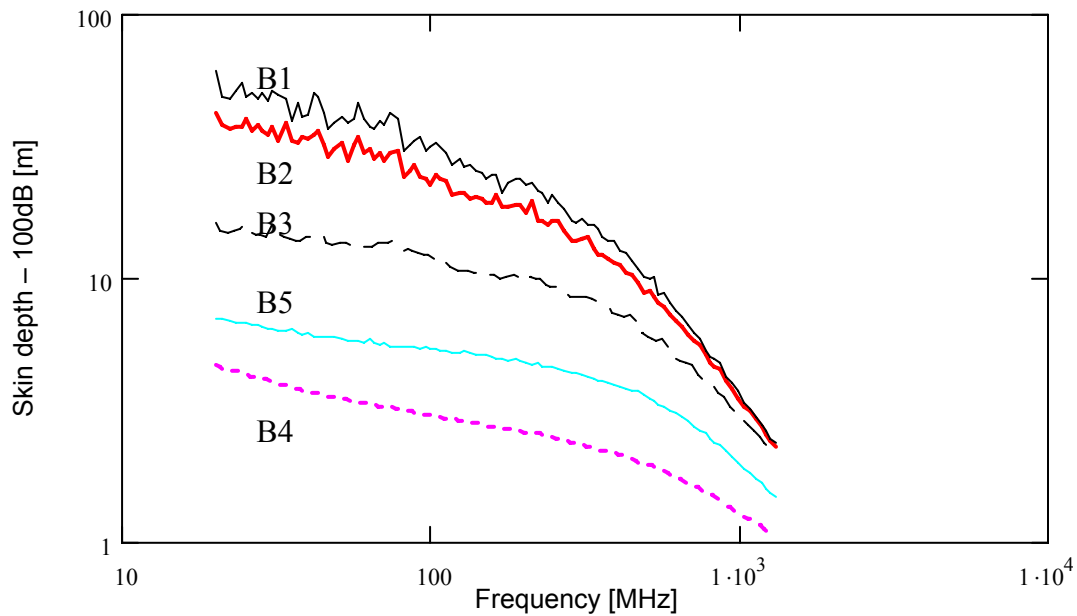
Figure 5.26. Electromagnetic penetration depth as a function of frequency for the 5 specimens (for a 100dB system).

5.5 SUMMARY AND CONCLUSIONS

A comprehensive laboratory and field soil characterization program is conducted for the test site. The deposit formed during the Pleistocene and it is located in a high seismicity zone. The soil profile can be described as a three layer system, where the intermediate layer at depths $z \cong 7.5m$ to $z \cong 12m$ is very liquefiable. Conclusions from this study follow:

- The site is dominated by poorly graded subrounded to angular sands and index properties (Coefficient of uniformity, sphericity and roundness) properly account for macroscale properties (e_{min}, e_{max}, Γ, λ, α, and β).

- Electrical conductivity values are low in the upper layers, but surprisingly high in the lower black sand. Surface-based GPR cannot be used to explore and monitor deep blasting effects.

- CPTu soundings reveal weak contractive sediments between 7.5m and 12m, where the black sand layer is found. SASW shows low stiffness at the same depths.

- Preloading is not an effective approach to densify the black sands.

- The age of the material, the lack of historical evidence of past liquefaction events in the vicinity of the site, and apparent $e_0 < e_{cs}$ suggest low liquefaction risk. However, CPT and SASW data point to a highly liquefaction potential in the black sand layer.

CHAPTER VI

BLAST DENSIFICATION STUDY – PART 2:

FULL SCALE MULTI-INSTRUMENTED CASE HISTORY

6.1 INTRODUCTION: THE BLAST DENSIFICATION TECHNIQUE

Blast densification, also known as explosive densification or deep blasting, has been used to densify loose, saturated, sandy soils since the middle 1930's (Wild 1961; Hall 1962; Solymar 1984; Raju and Gudehus 1994; Gnadhi et al. 1999; La Fosse 2002). Blasting does not require special construction machinery and it may be effective for deep compaction of uncemented granular deposits over large areas.

The soils must be saturated, otherwise damping is high and only a local effect is achieved; soils must be free draining so particles can rearrange. The clay content has to be less than 5 to 10% and the silt content has to be less than 70 to 80%, otherwise liquefaction cannot be achieved and drainage is restricted (Narin van Court and Mitchell 1994).

Typically, blast densification is used when the relative density is less than $D_R \leq 50\% - 60\%$. However, soils with higher D_R may be blast-densified if the confining stress and is high.

Blast densification has been successfully used in the past in several dam sites in Canada, India, Nigeria, Pakistan, and U.S.A. (Lyman 1942; Hall 1962; Solymar 1984), transmission towers in Massachusetts (Wild 1961), thermal power plants (Gnadhi et al. 1999), airport related projects (Fordham et al. 1991; La Fosse 2002), mines (Raju and Gudehus 1994), offshore platforms and manmade islands (Rogers et al. 1990; Jefferies and Rogers 1993; Baxter 1999), liquefaction and earthquake experiments (Byrne et al. 2000; Robertson et al. 2000; Al-Qasimi et al. 2005).

The large release of energy when the detonation takes place creates a radial shock wave that hits a soil element in compression, immediately followed by the rarefaction wave front (Charlie et al. 1985; Dowding and Hryciw 1986; Narin van Court and Mitchell 1998). The repetition of compression and tension cycles and the excess water pressure generated due to the large volumetric strains induced by gas expansion separate interparticle contacts, and promote the densification of loose sandy deposits. The porewater pressure typically increases to reach the overburden pressure, the compressive forces transmitted between soil grains vanish, the shear resistance is completely lost and the soil liquefies. After liquefaction, the particles resettle into a denser configuration, and further compression takes place as the excess porewater pressures dissipates (Mitchell 1981; Narin van Court 1997).

The densification may be increased when a detonation takes place in a previously blasted soil while the porewater pressure is still elevated (Ivanov 1983; Minaev 1993). In this case, the initially low shear resistance facilitates vibration-induced compaction.

The penetration resistance increases by 50% to 200%. This increase is not immediate after blasting but typically occurs few weeks or months later. Settlement occurs almost immediately after blasting and reaches 2% to 10% of the treated layer thickness (Ivanov 1983; Narin van Court and Mitchell 1998).

6.2 BLAST DENSIFICATION DESIGN

The design of blast densification has developed from experience rather than theory. The main design variables include: 1) weight of explosives, 2) spacing and pattern of boreholes (distribution of charges in triangular or square grid patterns, use of decks to vertically distribute charge), 3) depth of explosives, 4) number of coverages, 5) blasting sequence, and 6) delay time. A compilation of semi-empirical formulations guidelines is presented in Table 6.1. Larger charges affect greater volume but do not necessarily increase densification; instead, detonating small charges at the same points, allowing time for drainage between detonations is more effective (Terzaghi et al. 1996). Obviously, charges should not be too large to cause surface blow up.

Undrained shaking typically results in settlements greater than in drained conditions especially if the soil liquefies (Section 4.3.1, Figure 4.12, see also Hachey et al. 1994). Therefore, the soil to be treated and the overlying soil layers should be relatively free draining to shorten the densification time. Increasing fine contents reduces densification.

Soils with CPT tip resistance q_t > 20MPa tend to loosen during blasting. Fair to good densification is achieved when q_t <15MPa, while good to very good densification is attained when q_t < 10MPa (Narin van Court 2003).

Table 6.1. Blast densification – Design.

Charges size	Depth	Spacing horizontally	Detonation Interval	Detonation sequence	Number of coverages	Results	Reference
$W = 0.10 \cdot H_w^{2.46}$ (concentrated or point charges, diameter > length)	$dc = 1.8 \cdot W^{1/3}$	Maximum grid pattern $S = 4 \cdot W^{1/3}$					Ivanov (1967)
1 to 12 kg 8 to 850 gm/m3 10 to 30 gm/m3	$>{}^1\!/_4$ depth to bottom of layer to be treated, ½ to ¾ of depth common	5 -15 m	Hours to days.		1 to 5 usually 2 to 3	$\Delta s = H \cdot 0.02 \quad to \quad H \cdot 0.10$	Mitchell, J. K. (1981)
At Karnafuli Dam $D_{10} = 0.18$ mm, $C_u = 2$ 30% special gelatin dynamite, 3.6 Kg. each.	3, 6, and 11 m	6 m	4 hours.			Porosity changed from 47% to 43%.	Terzaghi et al. (1996)
Hopkinson's Number (Ivanov, 1967) $HN = \dfrac{W^{1/3}}{R}$ The excess pore pressure is a function of HN. Recommended values of HN: Van Impe = 0.15 Van Court = 0.50 Ivanov = 0.2 to 0.5 but if concentrated charge are not used, = 0.5 to 1.2 Optimum charge = 10 kg TNT (Ivanov, 1983)	R or 2/3 depth to bottom of layer to be treated.	R	Not clear. Preliminary test explosives needed.	Polish experience: Going from the edges, inwards		See plot in page 29, "Soil improvement techniques and their evolution" Settlement $\Delta s = H \cdot [2.73 + 0.9\ln(HN)]$	Van Impe, W. F. (1989); Narin Van Court (2003); Narin Van Court (1997); Narin van Court, and Mitchell (1998)

Table 6.1. Continued

Normalized weight (Dembicki et al, 1992) $$NW = \dfrac{\left(\dfrac{W}{L_c}\right)^{1/2}}{R}$$ Recommended NW Dembicki et al (1992) = 0.3 to 0.6 = 0.4 to 0.7 is better.	Imioled (1992) suggest $$H_B = 1.48 \cdot Q^{1/2}$$ $$H_I = 2.63 \cdot C^{1/3}$$	Square or equilateral triangles.				May not be valid for different geometries (patterns) and site conditions	Narin van Court, and Mitchell (1998); Narin Van Court (2003)
Energy input attenuation $$E_1 = \Sigma\left(\dfrac{W_i}{R_{vi}^{\,2}}\right)$$ 4 to 7 kg per sublayer, depending on spacing. E1 at the center of the grid should be 350 to 3500. For very loose soils ($q_0 < 5$ MPa) $350 < E1 < 1000$; for loose to medium ($5 < q_0 > 15$ MPa), $1500 < E1 < 3500$. For 2 coverages, $750 < E1\ f < 1500$. No mayor dependency on σ'_v	Layers $> 7 – 8$ m should be divided in sublayers of 5-6 m thick.	Square grid 4.5 to 11 m more effectiveness 4.5 to 6 m	Several minutes between detonations (controlled by the dissipation of pore pressure), allow enough time to achieve 120 -150% of initial pressure.	It should proceed outward, from center to outside.	1 or more. 2 are recommended The final charge spacing is accomplished by placing the charges for each coverage on grids with the spacing equal to 1.4 times the final spacing. If 3 coverages needed, 2 first with twice the final spacing and the last one with 1.4	Predicted final q tip in CPT cone: $$q_{1,f} = 0.450 \cdot q_{1,0}^{0.500} \cdot E_1^{0.321}$$ $$R^2 = 0.64$$ $$q_{1,f} = 0.195 \cdot q_0^{0.478} \cdot E_1^{0.330} \cdot \sigma_v'^{\,0.175}$$ $$R^2 = 0.66$$ $$q_{1,f} = 0.404 \cdot q_{1,0}^{0.525} \cdot E_1^{0.327}$$ $$R^2 = 0.64$$	Narin Van Court (2003)

160

Notation:

HN [kg] = Charge weight	**H [m] = layer thickness treated**
R [m] = effective radius in plan = ½ grid spacing	H_b [m] = minimum distance from ground surface to top of charge
L_c [m] = charge length	H_w [m] = water depth.
W_i [grams] = weight of individual charges around a point in the soil mass	Q [kg/m] = charge loading density
R_{vi} [m] = minimum vector distance from charge to a point in the soil mass	C [kg] = concentrated charge
Δs [m] = settlement	S [m] = spacing

The upper 1m to 3m of soil may be loosened because of the upward seepage forces of the escaping water. Sand boils spread a loose layer of fine sand and silt across the surface. Therefore, the upper layers may require post-blasting compaction. Alternatively, a temporary 3m thick layer of gravel placed on top mitigates those effects (Narin van Court 2003).

6.3 CASE HISTORY - DESCRIPTION

An initial pilot program is designed to densify a 18.3m x 18.3m area in the test site characterized in Chapter V (Figure 5.1). The loose sandy layer between $z=8m$ and $z=12m$ below the ground surface is the target layer to be densified by blasting. The field study is contracted by GeoSyntec Consultants Inc. (Robert Bachus and Tamara Hebeler). Tae Sup Yun collaborates in the implementation.

The blast design is based on guidelines listed in Table 6.1 and it yields individual charges ranging from 20kg to 34kg of explosive placed at a depth $z=10m$, in a square grid pattern with a fix spacing of approximately 9.1m. Two initial coverages are followed by another two similar coverages but with smaller individual charges of 11kg. Figure 6.1 shows the aerial distribution of the four blast coverages, which take place on the following dates: November 21st 2003 (1:06pm), December 23rd 2003 (12:19pm), June 4th 2004 (2:06pm), and August 5th 2004 (10:07am). The first coverage consists of nine holes, distributed in three rows and three columns occupying 18.2m x 18.2m of aerial space, and 9m of spacing between charges; the mass of explosives W per hole is $W \cong 19kg$ (open circles in Figure 6.1). The second coverage involves sixteen holes in a four-by-four hole grid, with individual charges $W \cong 34kg$ (black circles). The third coverage is arranged into

a two-by-three grid, with individual charges $W \cong 11$kg (rhombus). The fourth and last coverage consists of seven charges, in a three-by-three grid (two explosives are missing in the grid), with $W \cong 11$kg (stars). The third and fourth blast coverages are performed in a sequence of three detonations, with a difference of about 10 minutes in between. Table 6.2 summarizes information about the four blast coverages.

Plan view   Indivicual charges = 11000 grams.
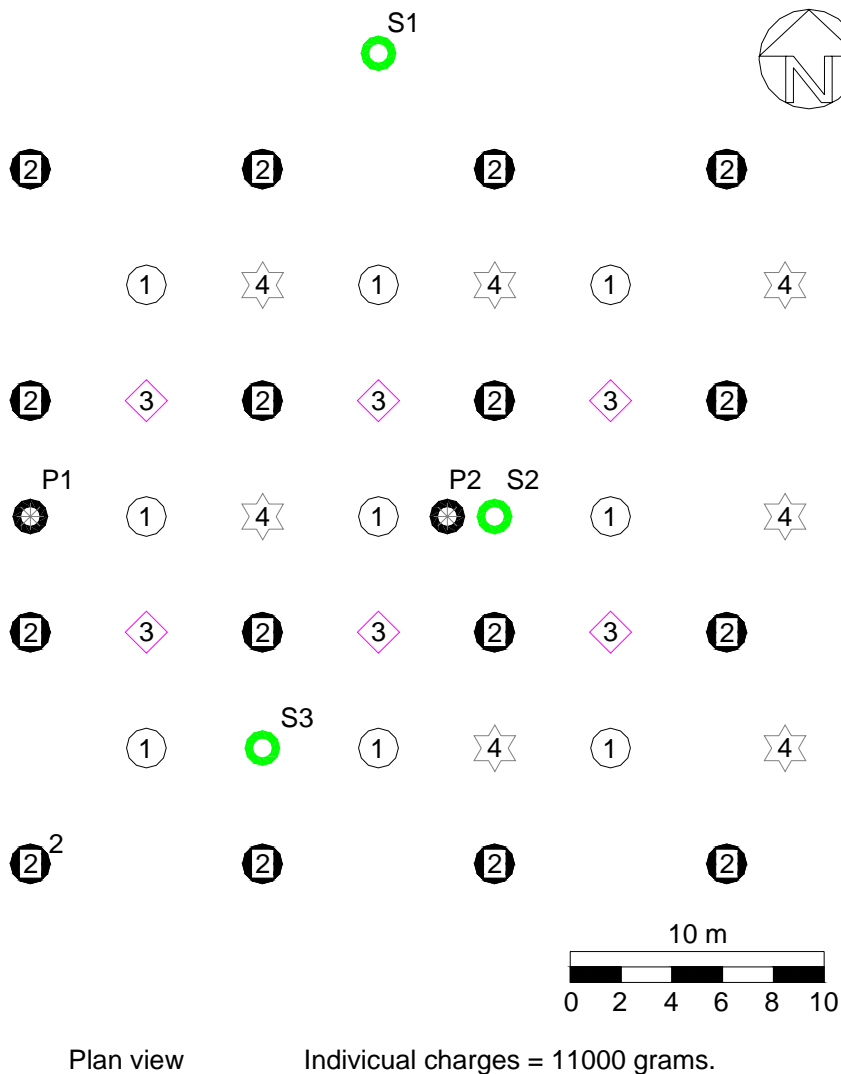
Figure 6.1. Site geometry. Location of the explosives (four coverages), piezometers (P1 and P2), and Sondex systems (S1, S2 and S3). The explosives are buried ~10.0 m in depth.

Table 6.2. Field tests – Blast coverages.

Blast Coverage	Grid	# of charges	Individual charge	Explosive type / Depth	Delay sequence detonation
1st	3 rows 3 columns (square)	9	19 kg	Hydromite 860 / 10m	100 ms between rows
2nd	4 rows 4 columns (square)	16 (+1*)	34 kg	Hydromite 860 / 10m	50 ms between rows
3rd	2 rows 3 columns (square)	6	11 kg	Hydromite 860 / 10m	10 minutes between rows
4th	3 rows 3 columns (square)	7	11kg	Hydromite 860 / 10m	10 minutes between rows

* A single charge is detonated firstly due to detonation failure of one of the charges during the first coverage.

Details of explosive installation are shown in Figure 6.2. A borehole is predrilled and encased, the explosive (Hydromite 860) is lowered to the desired depth ($z \cong 10m$) and the rest of the borehole is backfilled with gravel.

6.4 MONITORING BLASTING EVENTS

Measurements are taken during and after each of the four blast coverages. They include: 1) ground surface settlement using standard surveying equipment, 2) subsurface settlements using three Sondex systems S1, S2 and S3, 3) vibration assessment using geophones and a 12 channel seismograph, 4) penetration studies using CPTu cones are conducted before and after blasting, 5) ground penetrating radar GPR, 6) spectral analysis of surface waves SASW, and 7) porewater pressure using two vibrating wire piezometers P1 and P2. This section contains representative results from each of the measurements, and their physical interpretation.
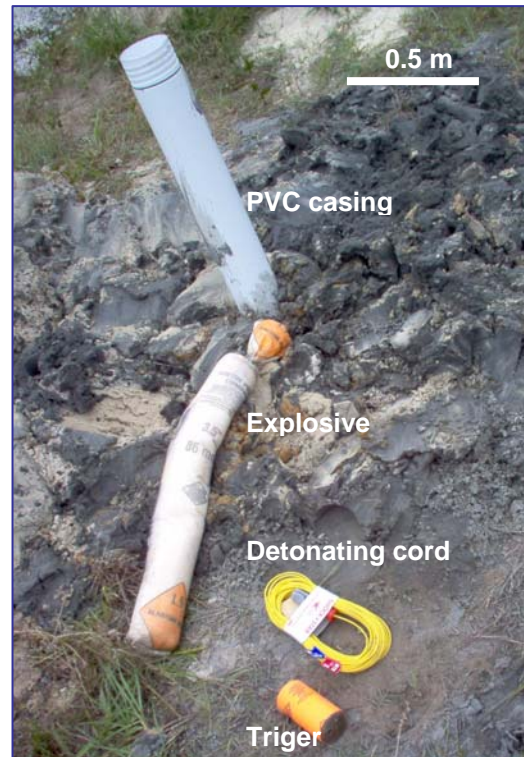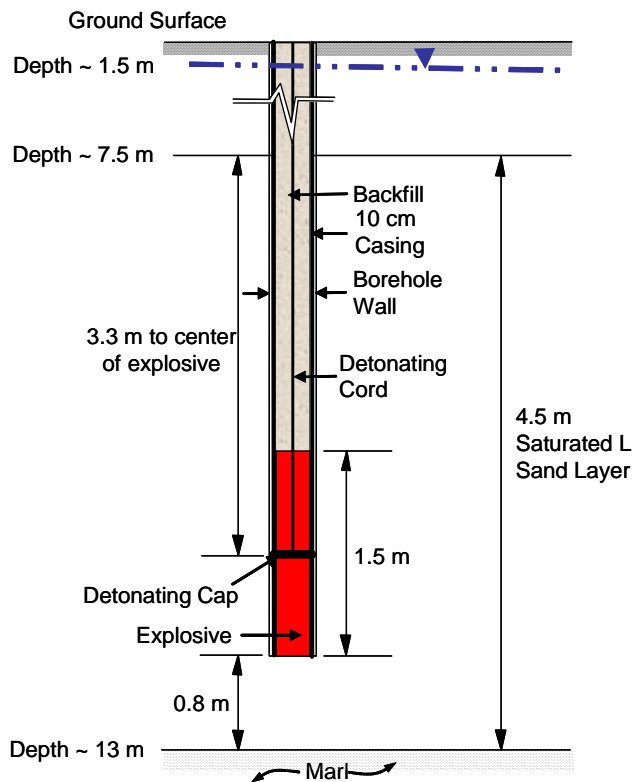
Figure 6.2. Details of explosive installations.

6.4.1 Surface settlement

Standard topographic surveys are conducted before, during and after each of the blast coverages. Emphasis is placed on the 18.3 m x 18.3 m test site and the surrounding area (Figure 6.3). The evolution in time of ground elevation along Line 3 is shown in Figure 6.4. The four wider lines show the maximum recorded settlement a month or more after each blast. The grey areas indicate the zones where the explosives are detonated (Figure 6.1). The affected surface extends a distance similar to the blasting depth outside the blasting zone in each direction; for example, the blasting zone is 18.3m x 18.3m and surface settlement is observed in a 38m x 38m area (blasting depth z=10m, Figure 6.5).
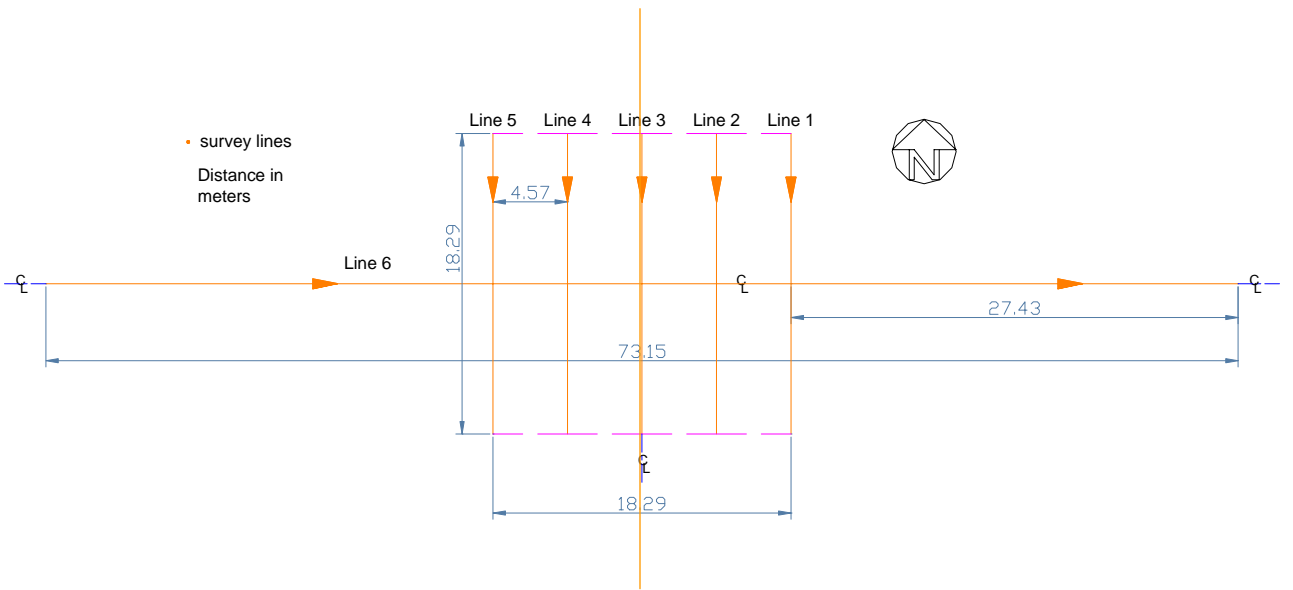
Figure 6.3. Topographic (and GPR) survey lines. The doted lines identify the ~18.3 m x 18.3 m test site.
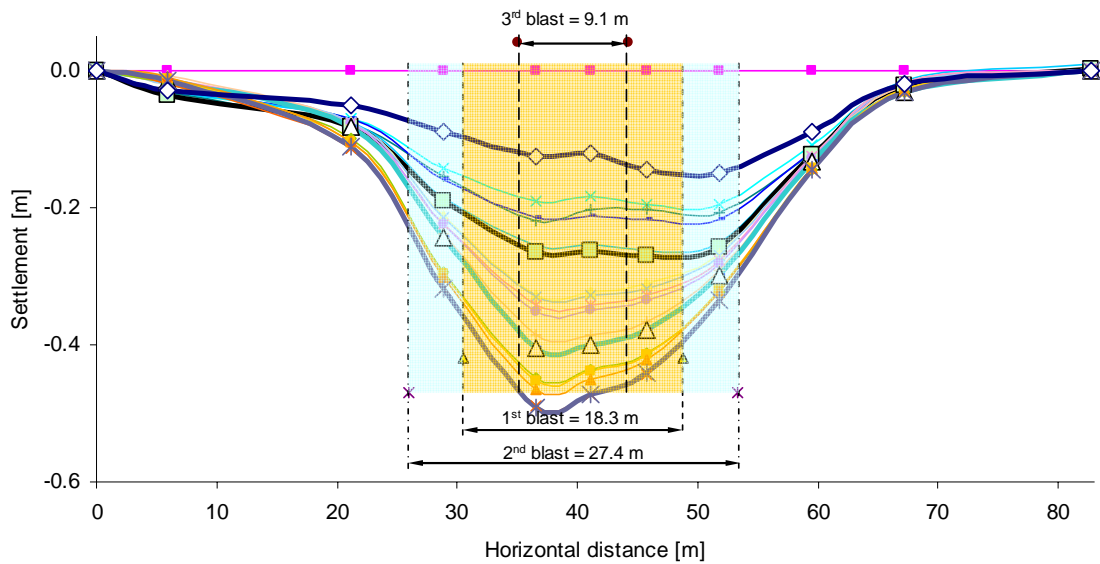
Figure 6.4. Surface settlement. The settlements measured at different times are shown. The highlighted lines correspond to the maximum recorded settlement after each blast.

166
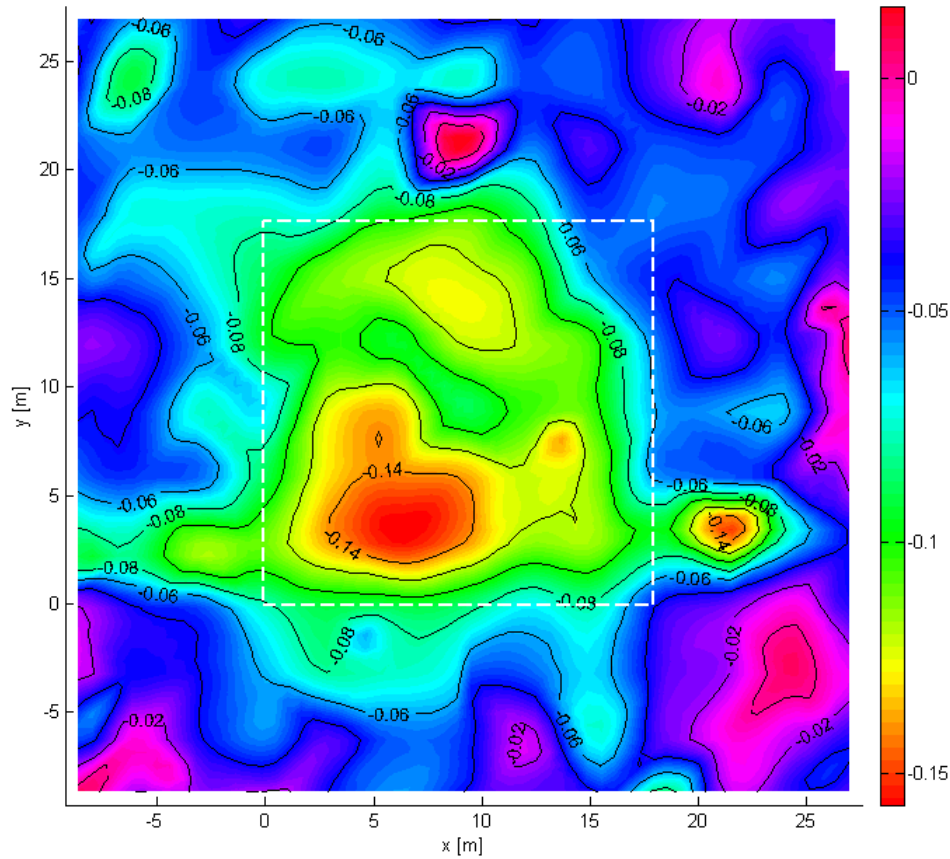
Figure 6.5. Settlement one month after the first blast coverage. The white dashed line indicates the test site.

The topography of the affected area, as suggested by surface settlement, is related to the location of explosives. The maximum recorded settlement after each blast coverage and the location of the explosives (white circles) are shown in Figure 6.6. The figure that corresponds to the first blast shows the blasting zone (18.3m x 18.3m) and the surrounding area, while the rests of the plots show the 18.3m x 18.3m blasting zone only. The settlement after the second blast is quite uniform due to the uniform distribution of
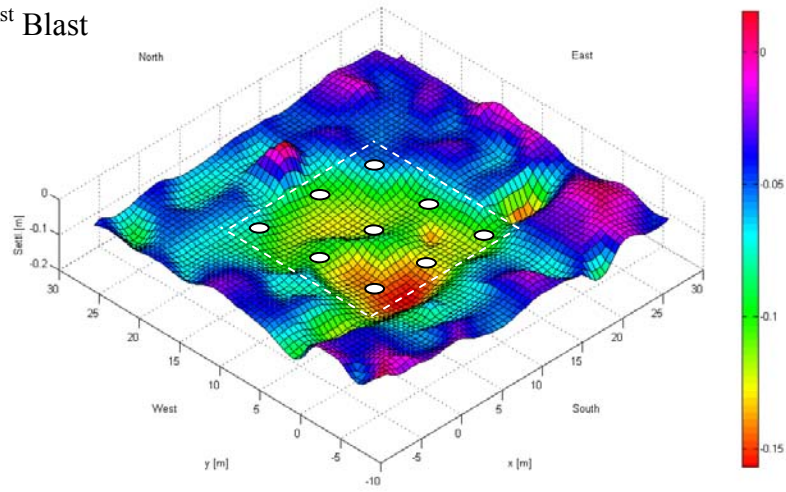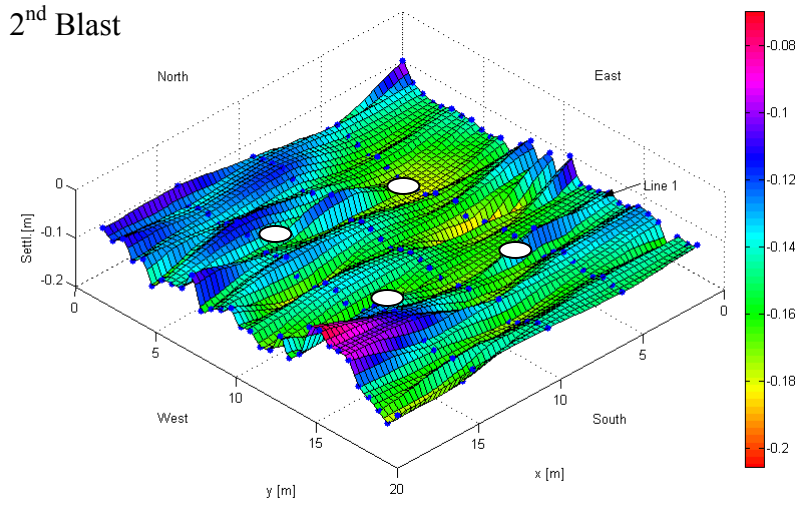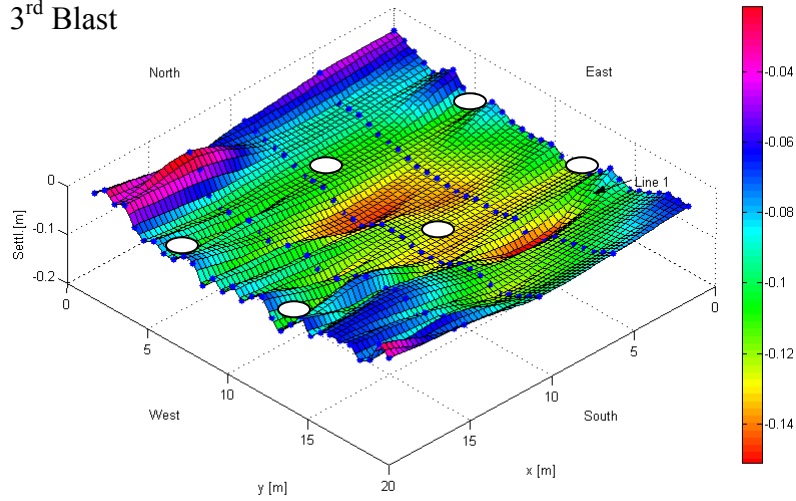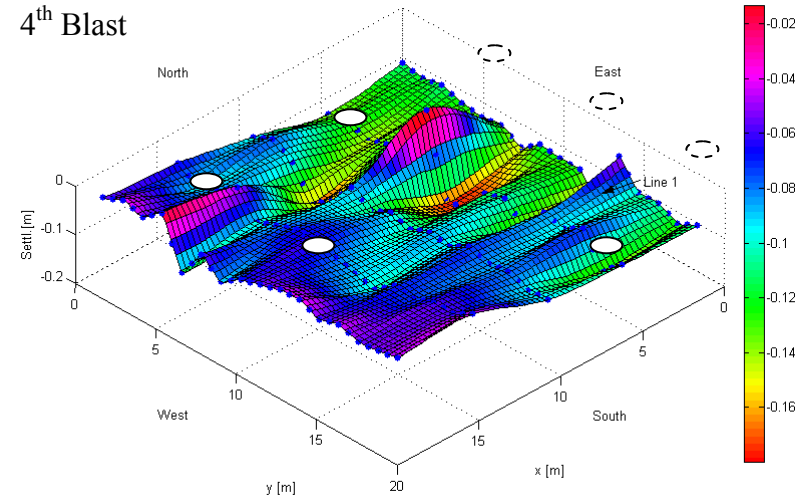
Figure 6.6. Settlement after the each blast of the test site. The white circles show the location of the explosives.

the explosive charges. However, the settlement in the third blast shows a half-cylindrical shape; and for the fourth blast, bigger settlements occur where there is a denser configuration of explosives (towards the East).

Figure 6.7 shows the evolution of cumulative surface settlement with time. The settlement for each blast event is shown in Figure 6.8. The curve that corresponds to the first blast is estimated based on the settlement that occurs after 44,000 minutes.

Water flows out of boreholes after each blast. The duration of water flow decrease with subsequent blast: 12 hours, 4 hours, 5 minutes and 0 – 5 minutes for the 1st through the 4th blast respectively. Settlement and the duration of water flow confirm that densification is not immediate, as reported by several researchers, but rather related to the time scale for porewater pressure dissipation after blasting.
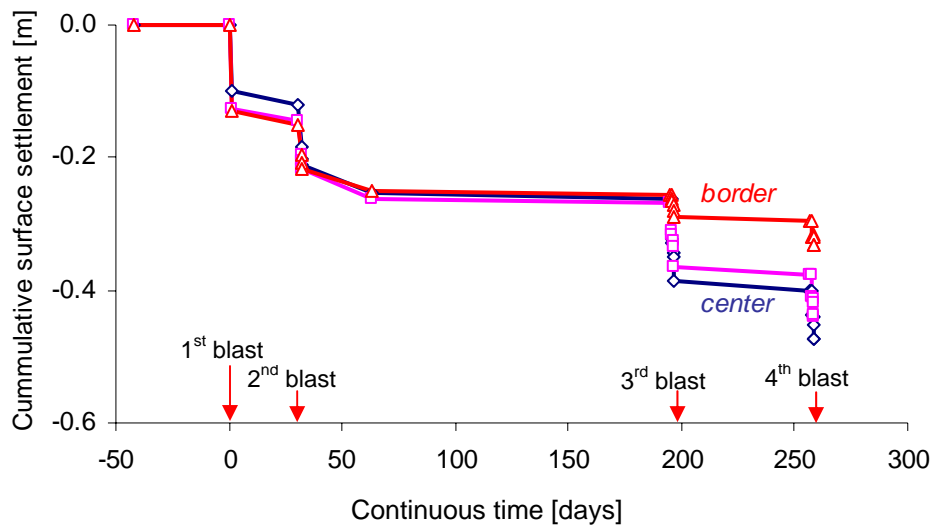
Figure 6.7. Settlement of the ground surface versus time.

169
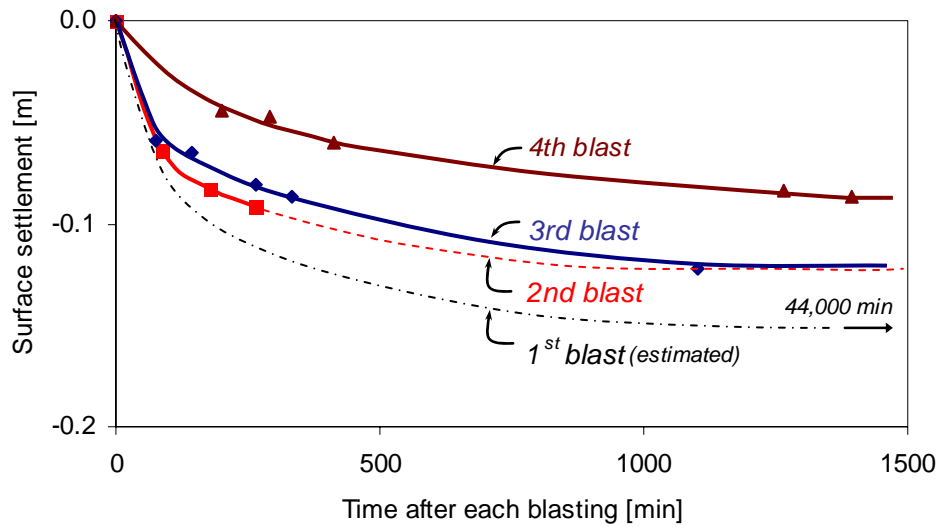
Figure 6.8. Settlement of the ground surface versus time for the individual events.

6.4.2 Subsurface settlement

Sondex systems are used to monitor subsurface ground deformation. Figure 6.9 shows a picture of the device and a schematic diagram that explains its operation. A corrugated pipe with periodic metallic sensing rings is embedded into the soil and its vertical deformation is measured by detecting the location of rings with a torpedo-type probe. The installation of the corrugated pipe is achieved by pushing down on a bottom plate. It is expected that this procedure causes extension in the pipe and leads to lock it in tension.

Sondex measurements are taken at three locations: 1) outside the test site S1, yet in the area of influence of the explosives, 2) at the center of the test site S2, and 3) at the border of the test site S3 (Figure 6.1). Displacement profiles for S3 are shown in Figure

6.10. Most of the vertical deformation accumulates in the lower loose layer ($z \cong 7\text{m}$ to $z \cong 12\text{m}$), while the upper layers ($z \leq 7\,\text{m}$) behave as a rigid block. Figure 6.11 shows the time variation of the subsurface rings at initial depth $z=1.4\text{m}$ in all three Sondex units. Results are analogous to the surface settlement (Figure 6.7).
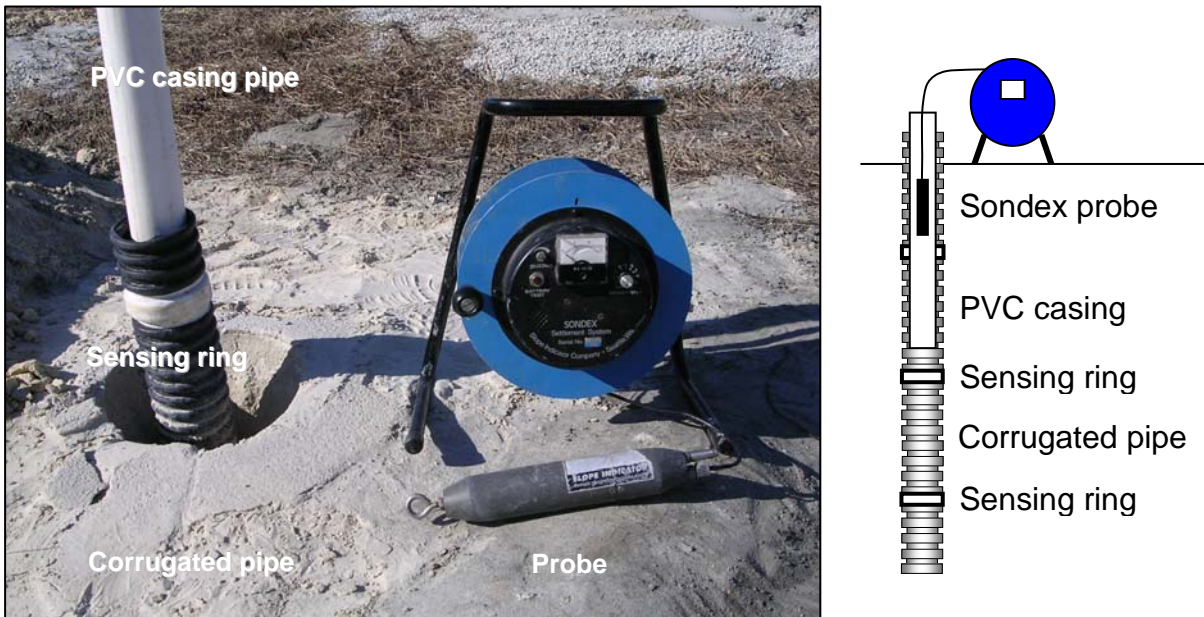
Figure 6.9. Sondex. Measurement of vertical strain with depth.

6.4.3 Vibration assessment

The vibrations caused by the explosions are measured using geophones placed in three directions *x*, *y* and *z* at four stations 1, 2, 3 and 4, and connected to a 12 channel Bison seismograph (Figure 6.12). Each station is 3m apart from each other. Figure 6.13 shows typical signatures gathered during a blast event. The compressional wave velocity is $V_P \cong 1500\text{m/s}$ as expected for saturated soil (Figure 6.14 – the ground water level is at
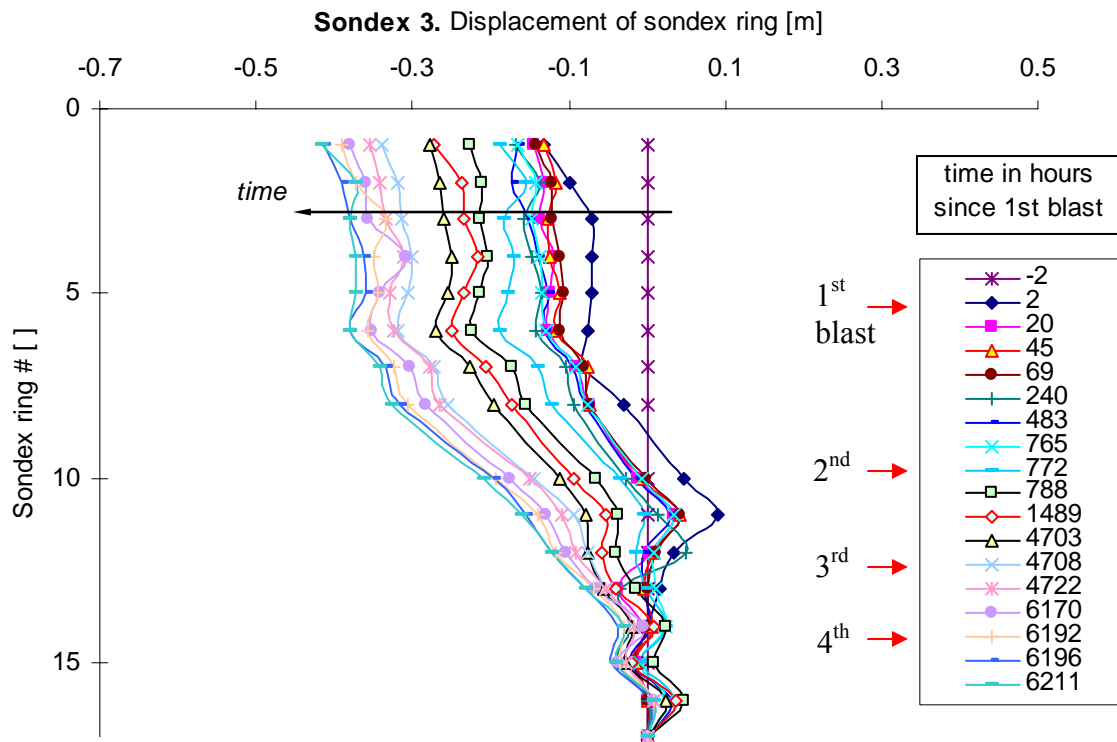
Figure 6.10. Typical Sondex measurements for the S3 unit installed in the border of the test site.
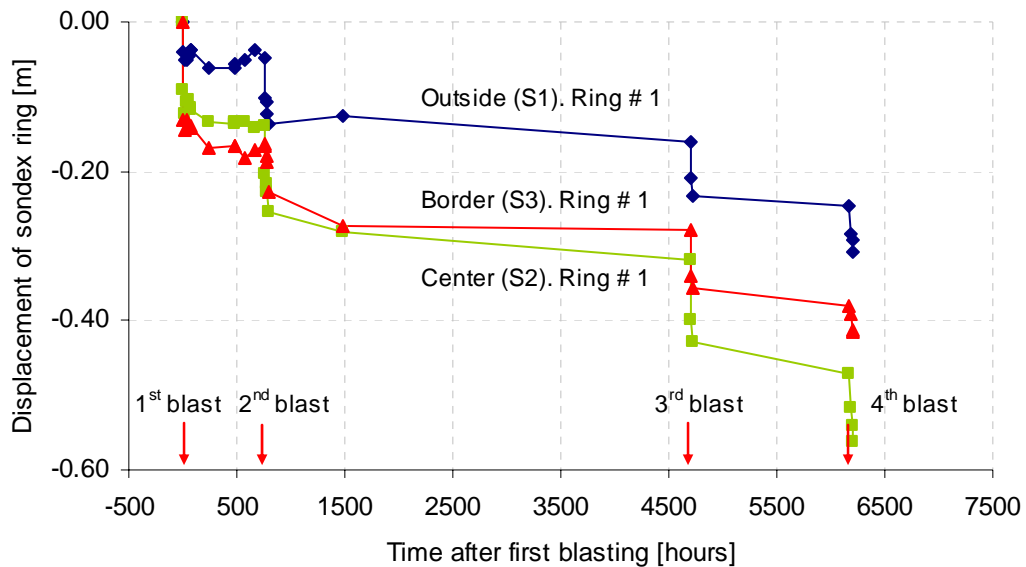
Figure 6.11. Sondex measurements as a function of time. Only Ring#1 is shown (initial depth z≈1.4m).

z≅1.0m with respect to the surface). Surface vibrations continue for about 0.5 seconds after blasting. The attenuation of surface vibrations is computed in the frequency and time domains and corresponds to a damping ratio $D \cong 8\%$ (Figure 6.15).

Seismic signals clearly show the detonation delays (Figure 6.16). The blast design requires detonations every 50ms for this coverage. The delay observed in records must be corrected for the relative position of the sensors with respect to each detonation.

Hodographs are used to investigate the extent of induced shear effects due to imposed detonation delays and sequences. The hodographs look alike at the four 3D geophone stations due to the small separation distance between stations. Figure 6.17 shows a set of hodographs; notice the prevailing energy content in the vertical direction (z-direction) in comparison to the horizontal directions. In fact, there is no evidence in these data that time delay has produced significant transverse vibrations.
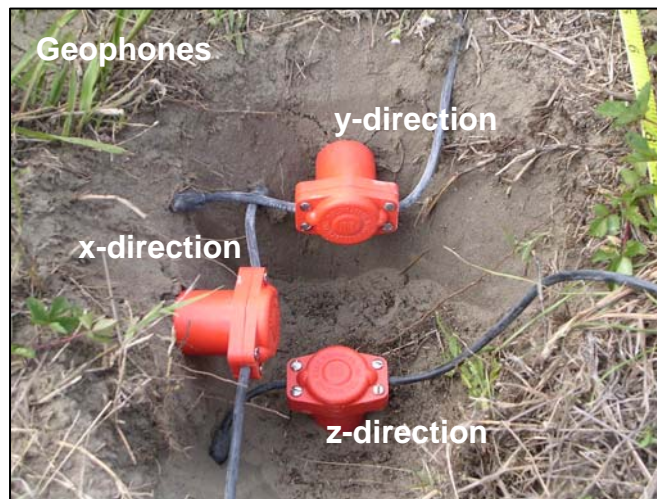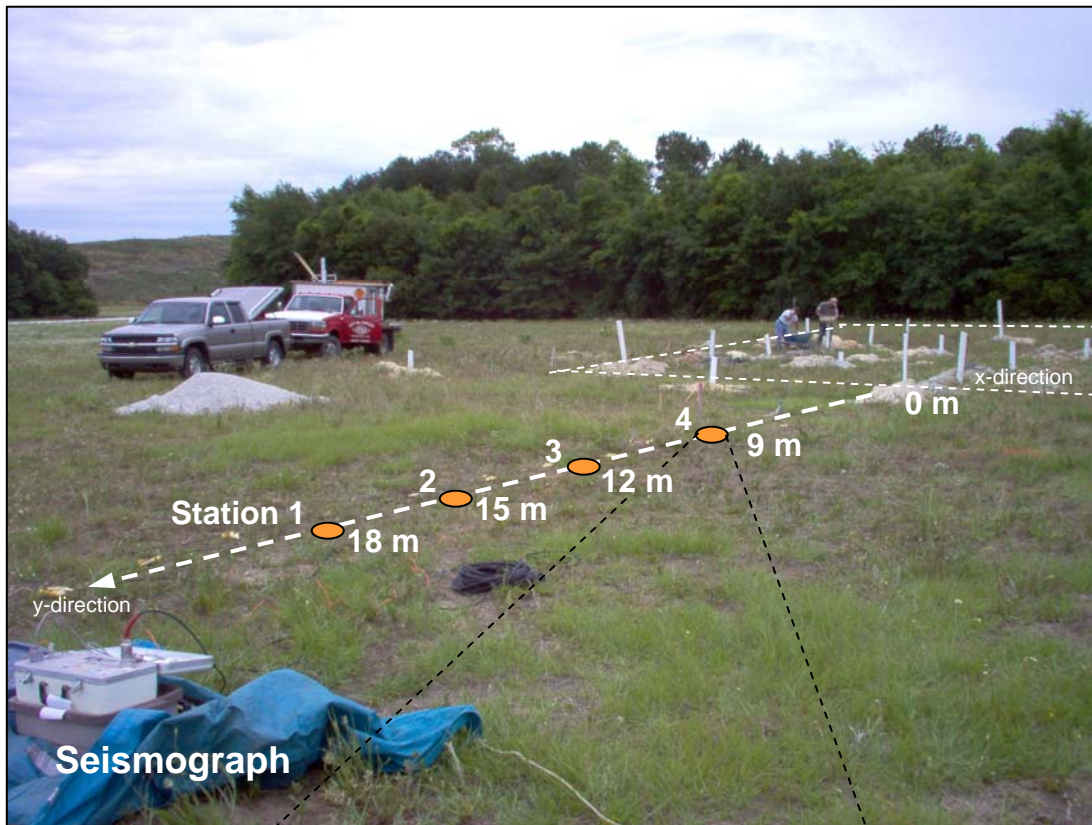
Figure 6.12. Vibration assessment using geophones in 3 directions at four stations.
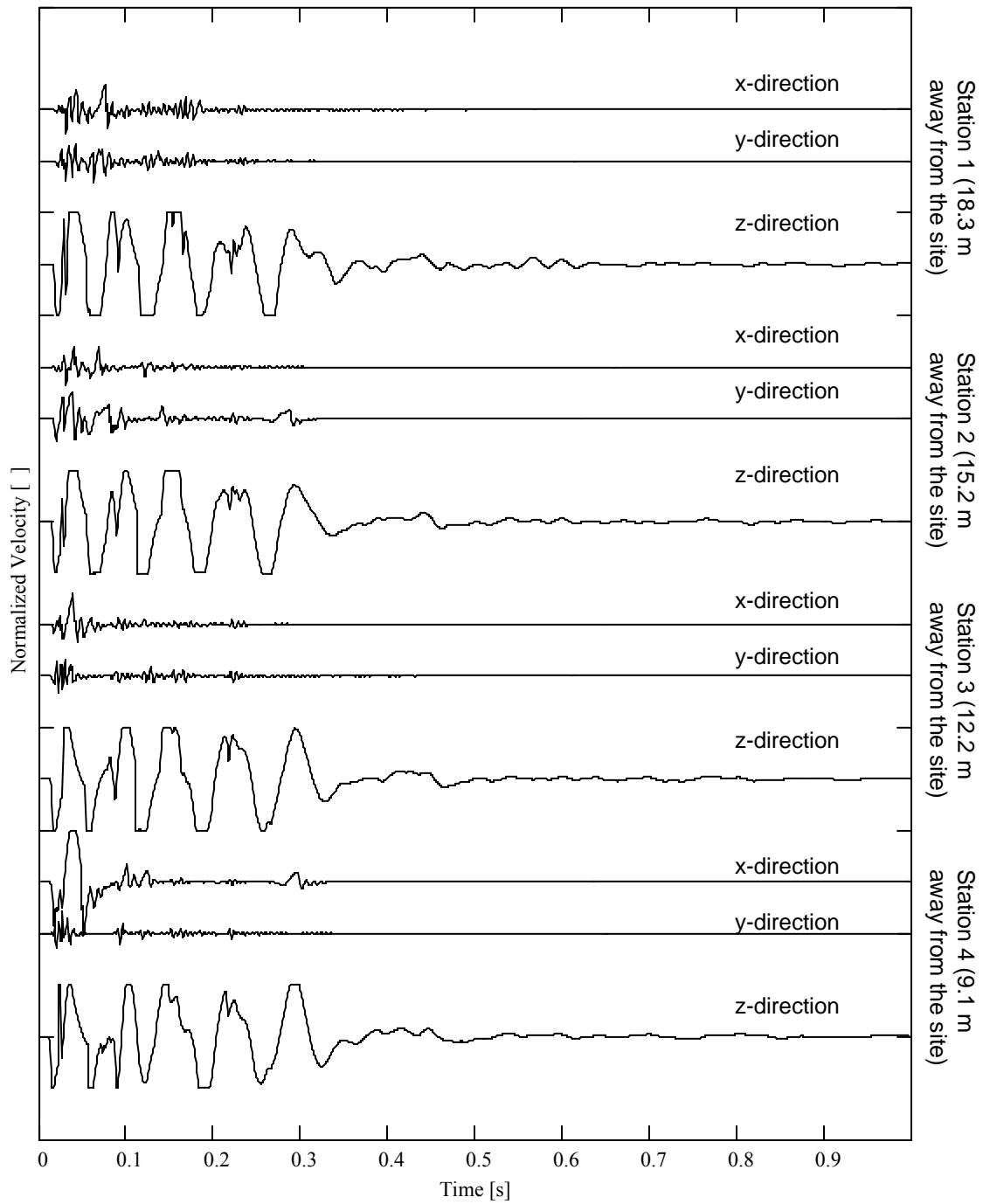
Figure 6.13. Typical measured signals in the 3 directions. Saturation could not be avoided in the vertical direction due to the proximity to the blasts. These records correspond to the second blast coverage.
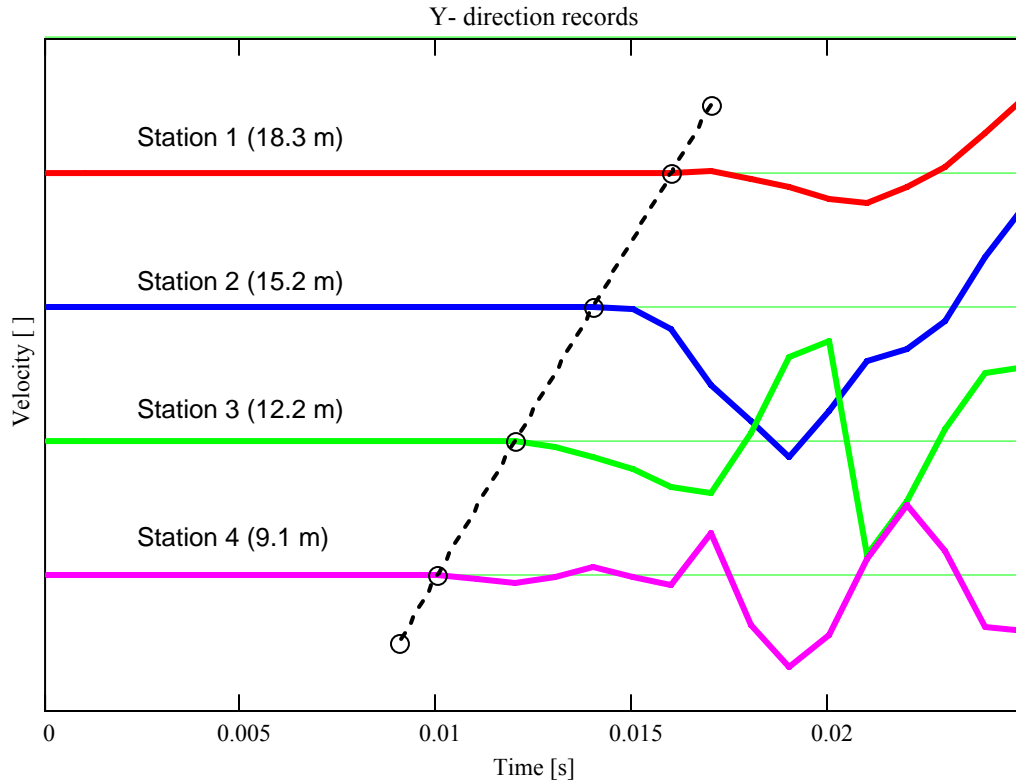
Figure 6.14. P-wave velocity determination. (second blast coverage, y-direction)
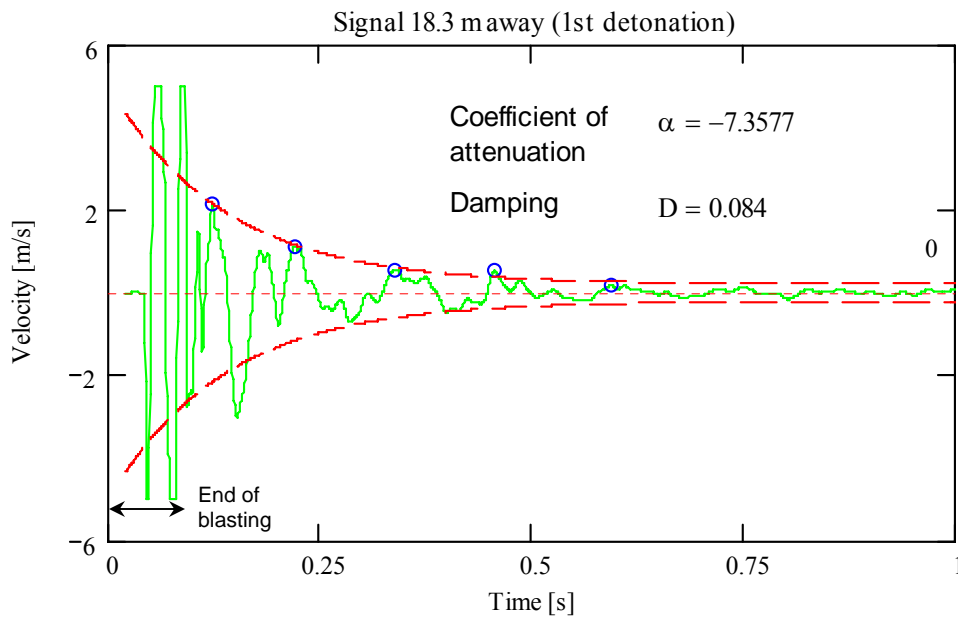
Figure 6.15. Example of damping determination in the time domain (third blast coverage, first detonation).

176
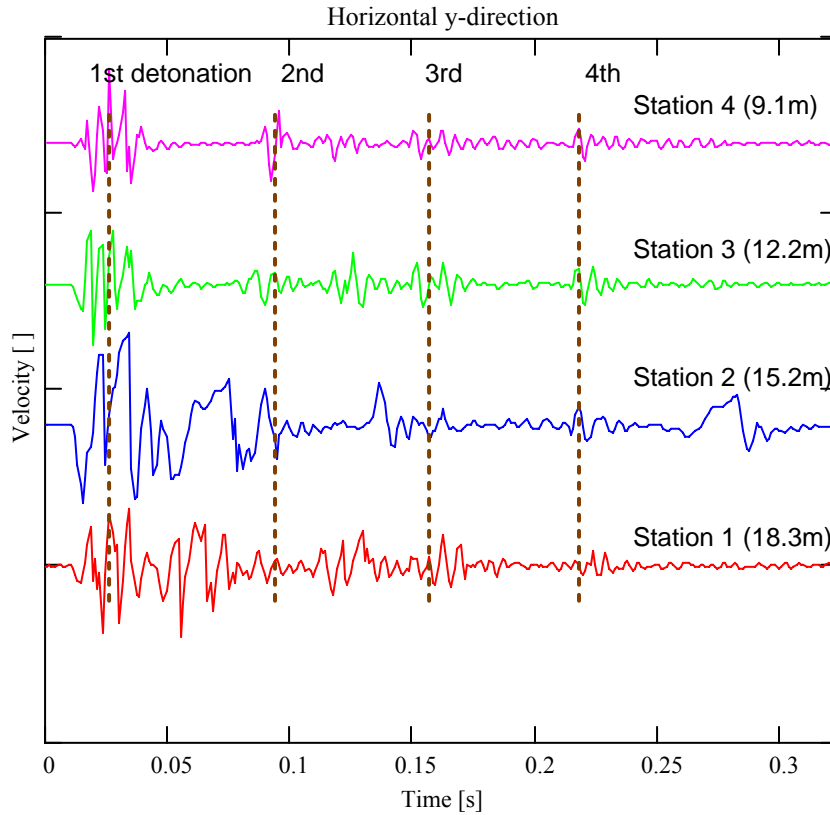
Figure 6.16. Identification of the several detonations in a given blast (second blast coverage).

6.4.4 Penetration tests

Figure 6.18 shows CPT tip resistance q_t at three different locations within the test site. Each panel shows four CPT profiles each gathered at least one month after each of the blast coverages. The improvement in tip resistance in the weak layer ($z=8m$ to $z=12m$) is either null or very small. Moreover, location (c) shows that the layer loses some strength.
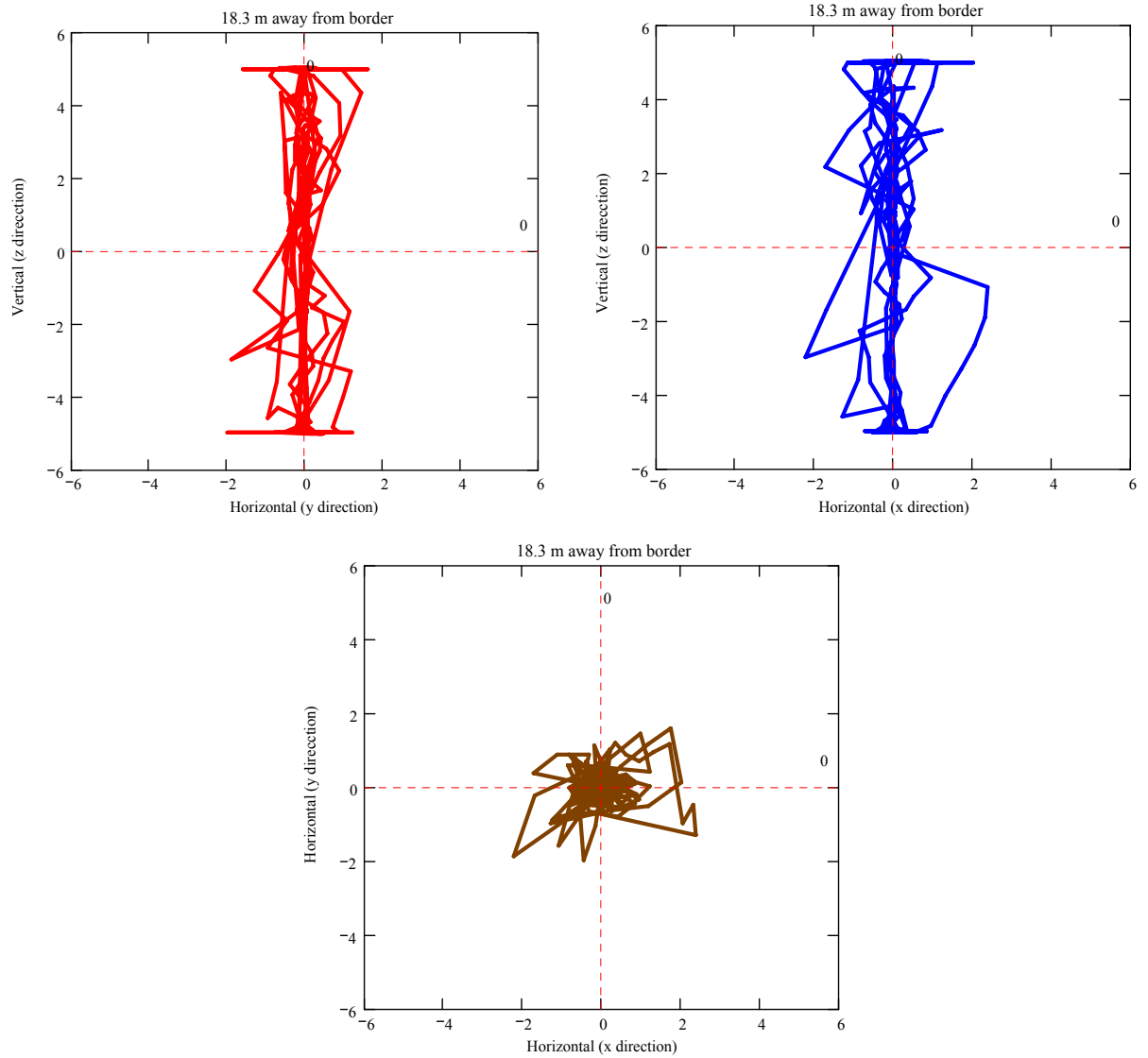
Figure 6.17. Typical hodographs (second coverage, station 1 located 18.3m away from the border of blasting zone).
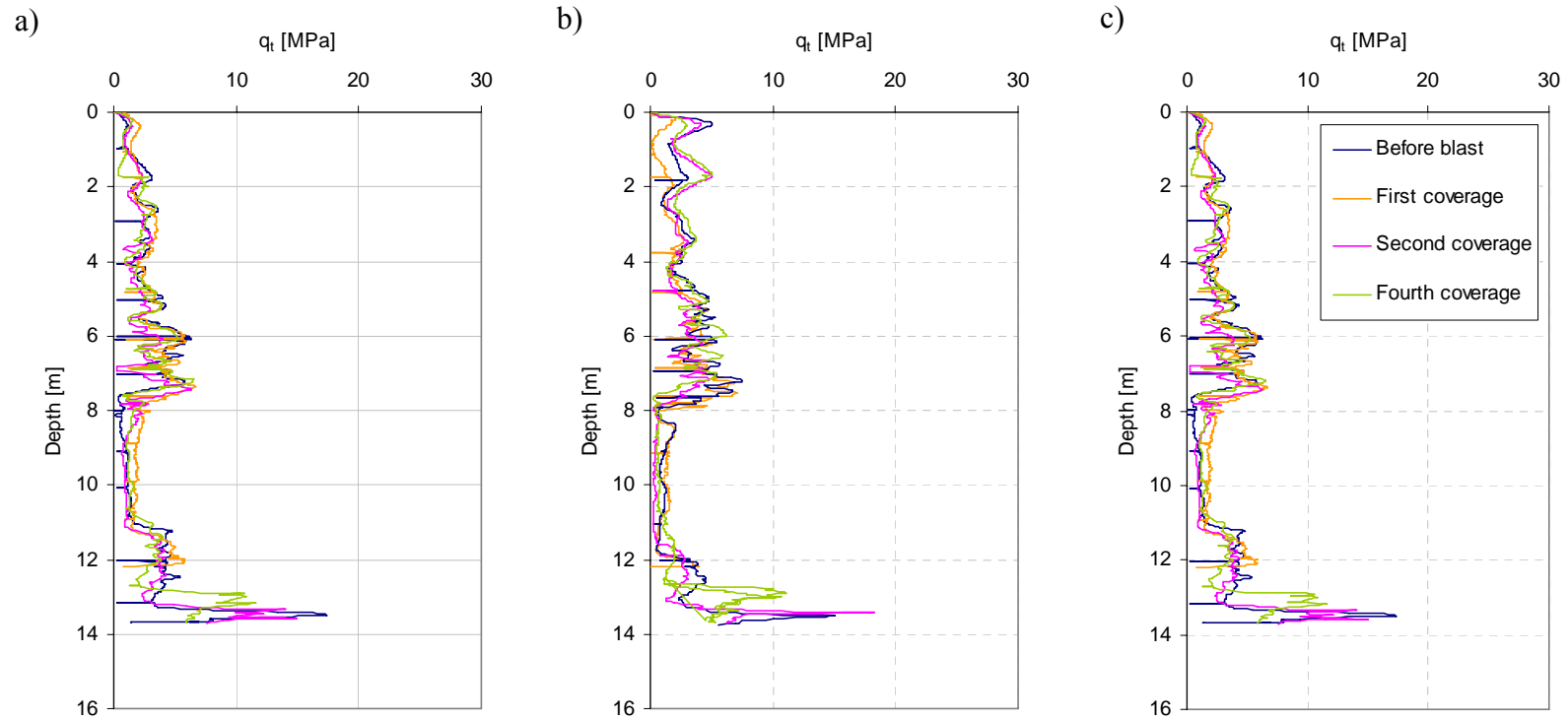
Figure 6.18. CPT data: tip resistance q_t and its evolution with time. a) b) and c) correspond to different locations in the 20m by 20 m test site. There are four records for each location, that correspond to end of each of the blast coverages (except third one). There is a relatively small improvement in the weak layer (z=8m to z=12m). Moreover, c) shows that layer losses some strength (data gathered by G. Hebeler, T. Hebeler and R. Kulasingam).

179

6.4.5 Ground Penetration Radar (GPR) images

GPR runs are conducted along the same lines used for the topographic surveys in Figure 6.3, in an effort to monitor subsurface changes through non-destructive and non-invasive procedures (see for example Kayen et al. 2005). Figure 6.19 shows typical GPR profiles before and 20hrs after a single blast coverage. Signals are enhanced by applying a composite gain consisting of a linear and an exponential time gain with the purpose of compensating for spherical spreading losses and exponential ohmic dissipation of energy. The gain function is

$$g(t) = \left(1 + \frac{\tau}{\tau_w}\right) \cdot e^{\beta \cdot \tau} \tag{6.1}$$

where $\tau = (t - (\tau_w - t_0))$, τ_w is the pulse width (500 in this case), t_0 is the time zero, $\beta = \alpha \cdot v / 8.69$, α=50 dB/m is the radar wave attenuation for this device, and v=0.07m/ns is radar wave velocity. The last measurable reflector (at around 200 ns) corresponds to the top of the loose layer based on CMP analysis performed in Chapter V (Section 5.3.2, Figure 5.21). Peaks and valleys in corresponding signals occur at the same times. Therefore, the similarity between the two plots confirms that the upper ~7m settles as a rigid body in agreement with Sondex data (Figure 6.10).

Before second blast coverage, Line 4 (refer to Figure 6.3)

20hrs after second blast coverage, Line 4 (refer to Figure 6.3)
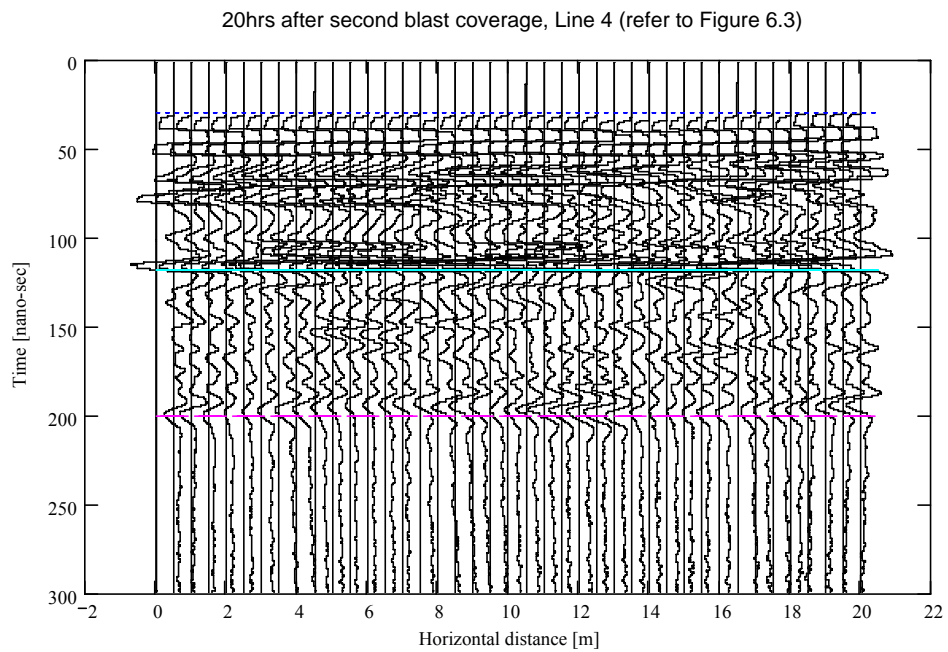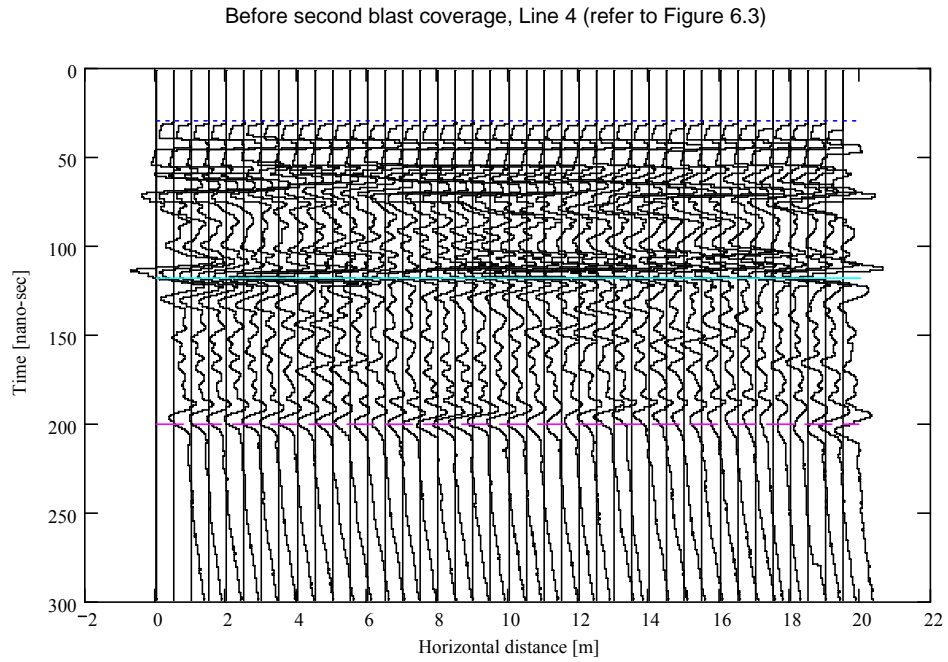
Figure 6.19. Typical GPR enhanced signal profiles. The last reflection at ~200ns corresponds to the top of the lower very loose sand layer (GPR with 200MHz antennae, second blast coverage).

181

6.4.6 Shear wave velocity with SASW

The spectral analysis of surface waves permits inferring the evolution in S-wave velocity profiles at the test site before and after blast coverages. Figure 6.20 shows the S-wave velocity profile for the 3rd blast, and its evolution with time. Consider the upper 12.0 m. The S-wave velocity drops dramatically in the lower very loose sandy layer (depth z=8.0m through z=12.0 m) were the explosives are detonated, up to z=5.0m during the first hours after the detonation. This result reflects the decrease in effective stress in the loose layer due to the increase in pore pressure. Twenty hours after the blast, more than 90% of the excess pore pressure has dissipated and the V_s has recovered to the V_s levels before blasting. Two months later, the V_s profile shows an improvement of ~50%.

6.4.7 Porewater pressure

Two vibrating wire piezometers are installed; one, just outside of the test site (P1, z=10.5m – Figure 6.1) and the other, at the center (P2, z=11.5m –Figure 6.1). P1 provides information about the influence distance from the detonation points, while P2 monitors the pore pressure generation and dissipation. Figure 6.21 shows a schematic drawing of their installation. The borehole is drilled and encased with a one inch diameter PVC pipe which is slotted in the bottom one meter. The vibrating wire piezometer is lowered to the desired depth. Sequences of coarse to medium sand and bentonite are used to fill and seal the pipe, to ensure that pressure readings correspond to the pore pressure at the installation depth.
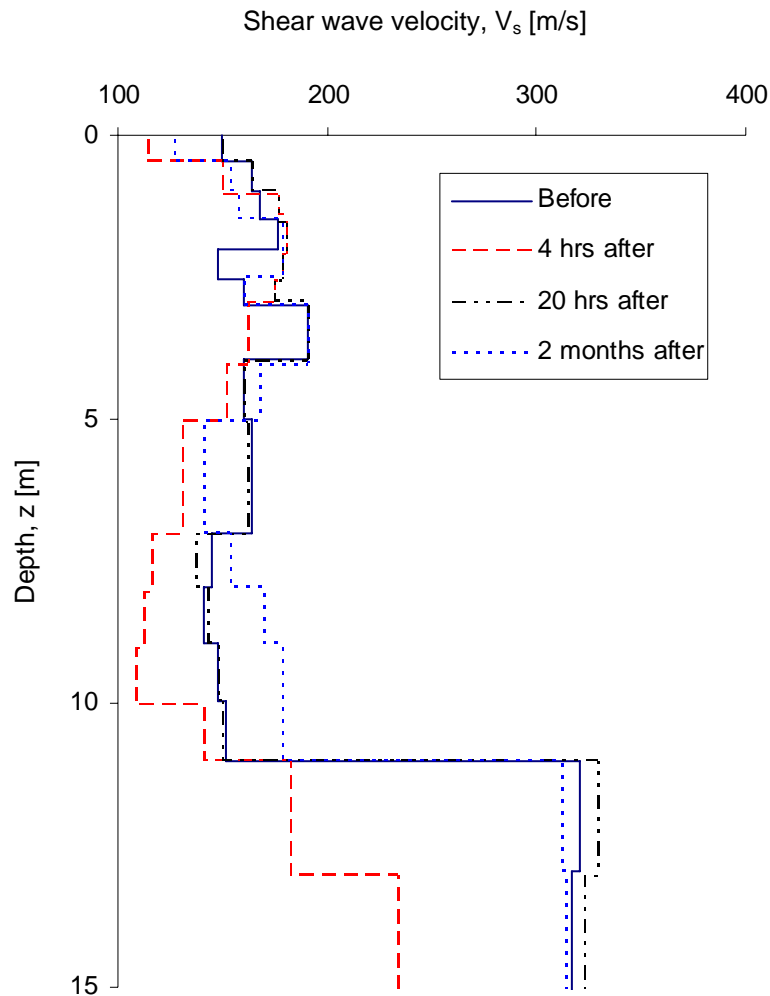
Figure 6.20. S-wave velocity profile from SASW and its evolution with time after the 3rd blasting. The depths of interest is z<12m (data gathered by Sungsoo Yoon).

The pore pressure is measured every 2 seconds during the first hour and every 2 minutes thereafter. Data are collected with a VW mini-logger manufactured by Slope indicator. Data for the three detonations during the fourth blast coverage are plotted in Figure 6.22. Details of the detonation sequence and distances between piezometers and

183

explosive charges are summarized in Table 6.3. The pore pressure for full liquefaction u_L is calculated using the expected in situ void ratio values and highlighted in the figure. The P2 piezometer, located at the center of the site, shows that liquefaction is attained during the second detonation. On the other hand, full liquefaction is attained at the P1 location during the third detonation.
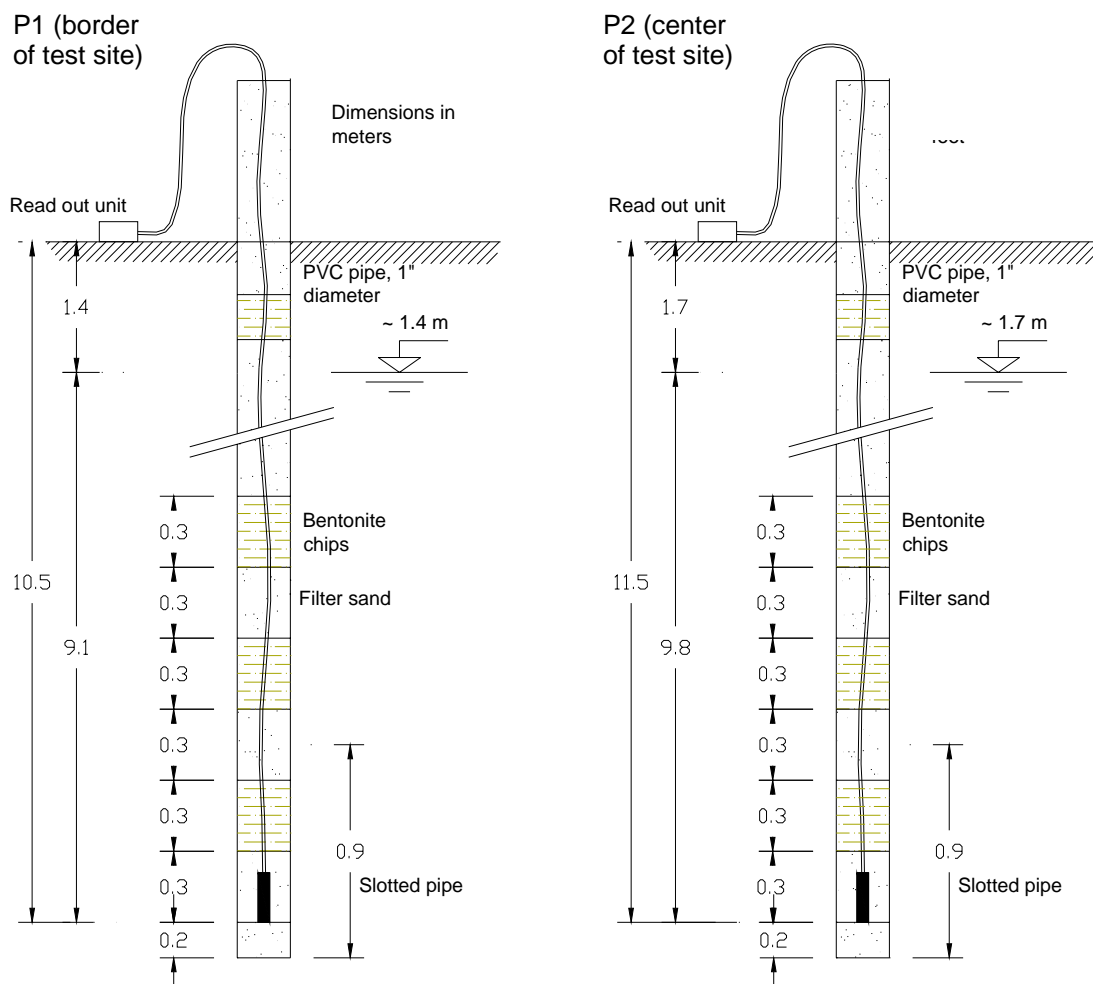
Figure 6.21. Installation of the two porewater pressure vibrating wire transducers. Sequences of coarse sand (#4) and bentonite chips are used to seal and to backfill the one inch diameter PVC pipe, which is slotted in the bottom meter.

184
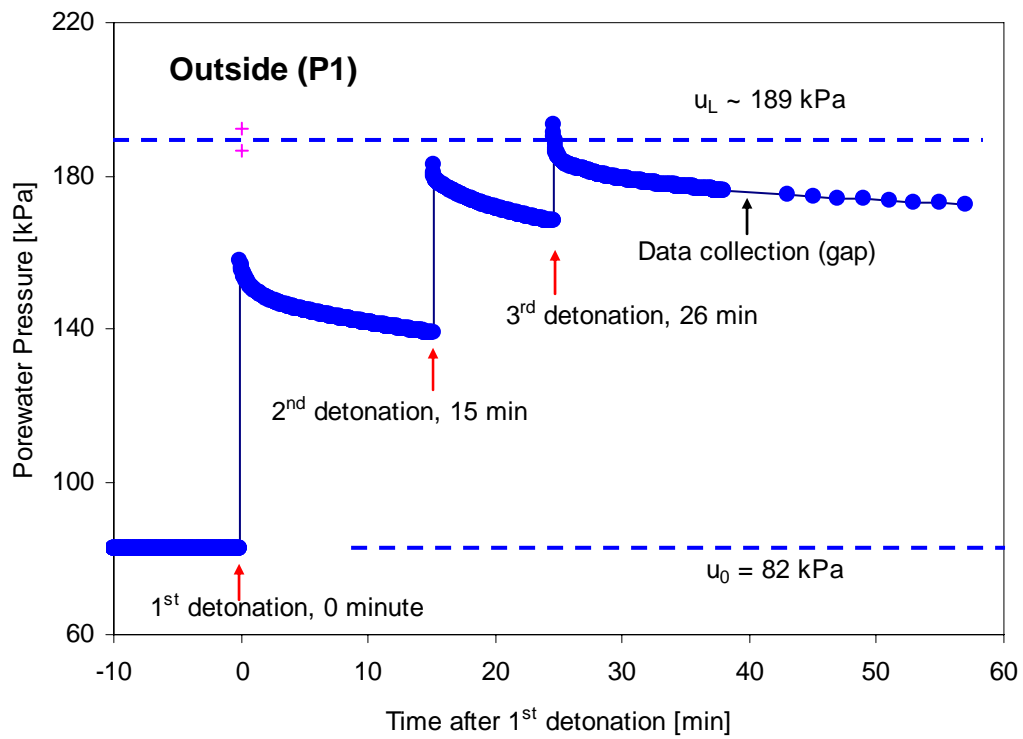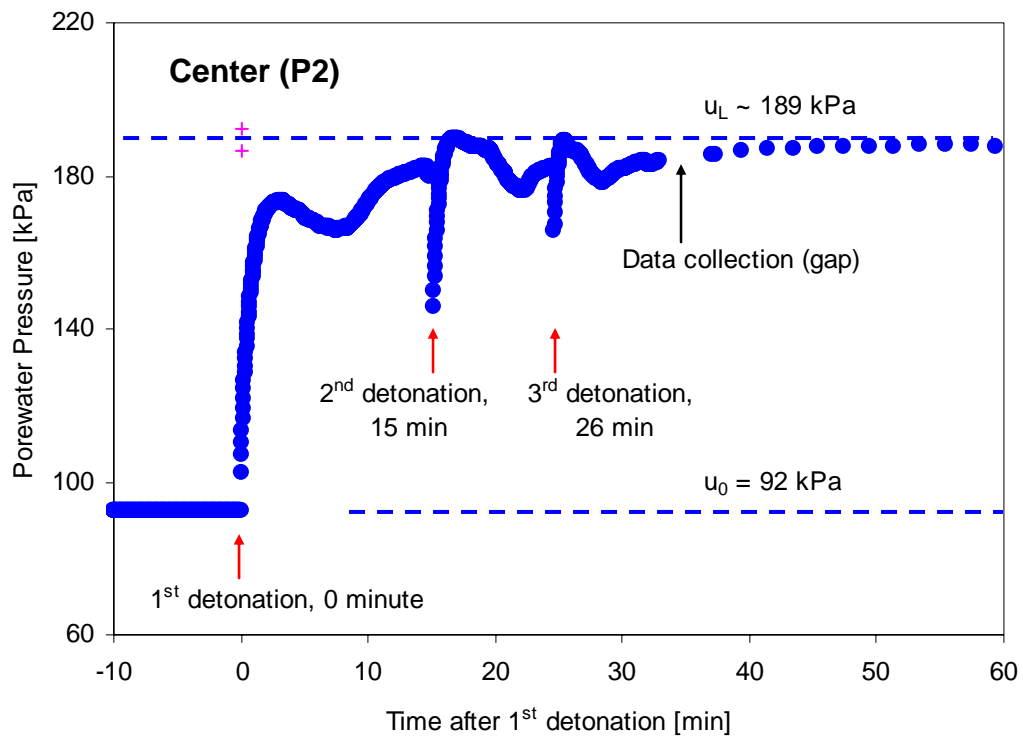
Figure 6.22. Pore pressure measurements during the fourth blast coverage.

185

Table 6.3. Details of detonation sequence and distances to piezometers – Fourth blast coverage.

	Time	# of charges	Distance to P1	Distance to P2
1st detonation	10:07 am	3	28.9 m	10.7 m
2nd detonation	10:22 am	2	15.2 m	9.1 m
3rd detonation	10:33 am	2	9.1 m	9.1 m

6.5 ANALYSES AND DISCUSSION

The following observations can be made from the data gathered from the field study:

Sondex and GPR measurements show that densification takes place primarily in the loose sandy layer (z=8m to z=12m, Figure 6.10 and Figure 6.11) while the upper layer (z<8m) settles as a rigid block.

The variation of settlement with time observed on the surface is in agreement with the one observed in the upper rings of Sondex systems.

GPR images show that blast densification is magnifies some of the initially subtle reflectors in the upper layer (i.e., thin seams of soil), probably induced by water and fines migration from the lower layer after blast-induced liquefaction (Figure 6.19).

Settlement of ~0.12m and decreasing is registered after each blast. This corresponds to a volumetric change of about 3% in the lower layer (z=8m to z=12m).

The total settlement S after the four blast coverages is $S \cong 0.50$m. This represents volumetric a strain of $\varepsilon_v \cong 12\%$ in the lower layer (H=4m) and a decrease in void ratio

186

$\Delta e = \varepsilon_v \cdot (1 + e_0) \cong 0.21$ if $e_0 = 0.77$; or $\Delta e \cong 0.23$ if $e_0 = 0.92$. In either case, a change in void ratio in ~0.2 must bring the soil into the dilative region and significantly lower the liquefaction susceptibility.

Surface settlement extends beyond the blasting area by approximately the blasting depth in each direction (Figure 6.4). The maximum recorded settlements after blasting are near the location of the explosives (Figure 6.6). More uniform explosive distribution renders a more uniform surface settlement (Figure 6.6). Larger settlements occur where there is a denser configuration of explosives (Figure 6.6).

The amount of densification and the amount of water that escapes through borings decrease with successive blast events. This is in agreement with the development of a densification front observed in 1g models (Santamarina and Lee 2006 – Figure 6.8).

The decreasing duration of water flowing out of boreholes after each blast is consistent with the decrease in attained settlement, in agreement with the terminal density framework (Chapter IV).

Settlement is not immediate (Figure 6.8). In fact, the duration of liquefaction and drainage are related to the time scale for excess porewater pressure dissipation after blasting.

In agreement with saturation conditions, the measured compressional wave velocity is $V_P = 1500$m/s (Figure 6.14). No shock wave effects are apparent away form the basting zone.

Surface vibrations after blasting decrease with a high damping ratio D≅8% (Figure 6.15) in part due to large strain phenomena involved as well as geometric spreading and radiation.

Hodographs highlight the preponderant energy content in vertical particle motion (Figure 6.17). The ratio of horizontal-to-vertical particle motion is ~0.4. The theoretical ratio in surfaces wave is 0.6 (Richart et al. 1970).

Blasting sequence and delays do not seem to affect hodographs. Nevertheless, a careful analysis of hodographs for the first few milliseconds after the first detonation reveals a slight tendency to transverse shear in the direction of the detonation sequence. In other words, if one can detonate the first row of charges followed a few milliseconds later by the second row of charges to the right (x-direction), then, more movement develops in the x-direction with respect to the y-direction for the first few milliseconds after the detonation; thereafter, no predominant shear vibration is detected. This suggests that time delay is not effective in causing shear motion. This observation requires further field and numerical investigation.

CPT soundings do not show soil improvement due to blast densification. The in situ relative density D_R can be computed from the tip cone resistance q_t through the normalized tip cone resistance q_{c1} (Kulhawy and Mayne 1990):

$$D_R = 100\sqrt{\frac{q_t/Pa}{\frac{(\sigma'_{vo}/Pa)^{0.5}}{305 \cdot OCR^{0.2}}}} \qquad (6.2)$$

σ'_{vo} is the in situ overburden effective stress, *OCR* is the overconsolidation ratio and *Pa* is the atmospheric pressure *Pa*=100kPa (Figure 6.23). This analysis predicts that the in situ relative density for the loose sandy layer (z=8m to z=12m) ranges between D_R=20% and D_R=40%. The tip cone resistance is not affected by changes in relative density in this range. A qualitative experiment on specimens B4 is performed to confirm these observations and to investigate the effects of the number of liquefaction events on penetration resistance. The experimental set up is shown in Figure 6.25-a. Figure 6.25-b shows details of the minicone used in these tests (60º angle tip, diameter=11mm). The average measured penetration resistance exhibited by the minicone is plotted against the number of liquefaction events imposed on the specimen. The cone tip resistance does not change for the first few events (low D_R range) but later increases with the number of liquefaction events (when large D_R, reaching terminal density). There are cases in the literature where it took 5.5 years for the tip resistance to reach pre-blast values (Charlie et al. 1992; Jefferies and Rogers 1993) and while q_t never reached pre-blast values in blast densified medium dense sands (Hryciw 1986).

The S-wave velocity drops dramatically in the loose sandy layer (depth z=8.0m to z=12.0m) immediately after detonation (<1 hour, inferred from Figure 6.20). Then, V_s decreases in the upper layers up to z=5.0m, four hours after the detonation (Figure 6.20). These results are in agreement with the decreasing in the decreasing effective stress in upper layers produced by the upward flow of the excess pore fluid from the lower layer.
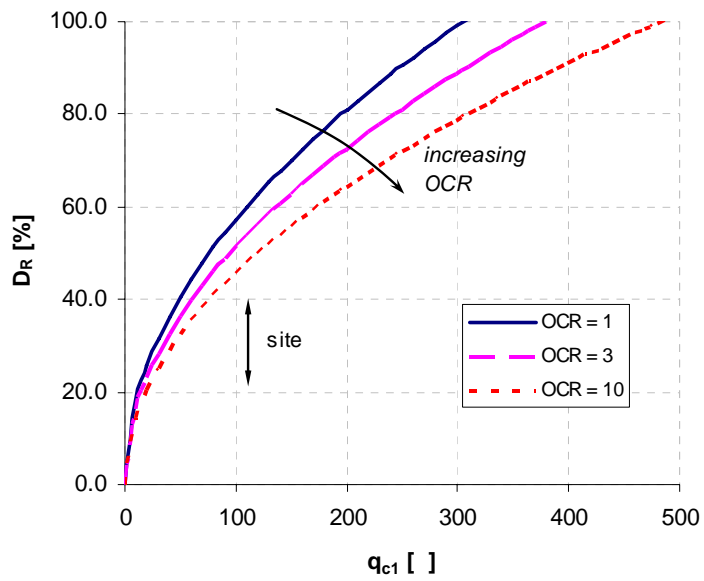
Figure 6.23. Relative density and CPT tip resistance (Equation 6.2).
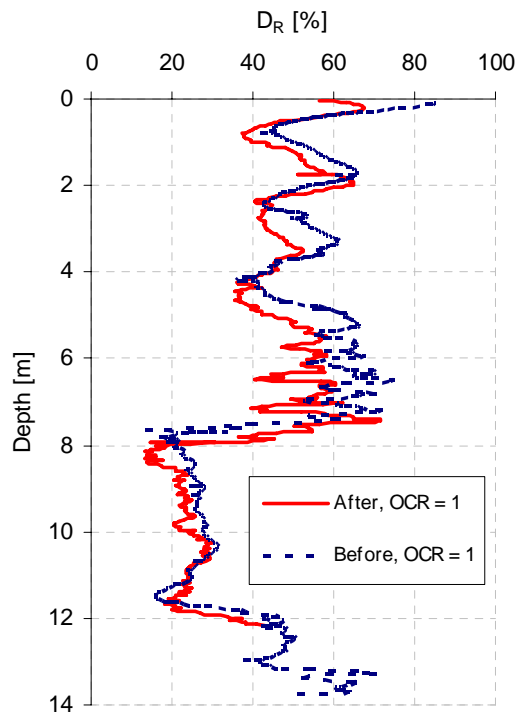
Figure 6.24. Relative density-CPT correlation for C1 sounding (second blast coverage).
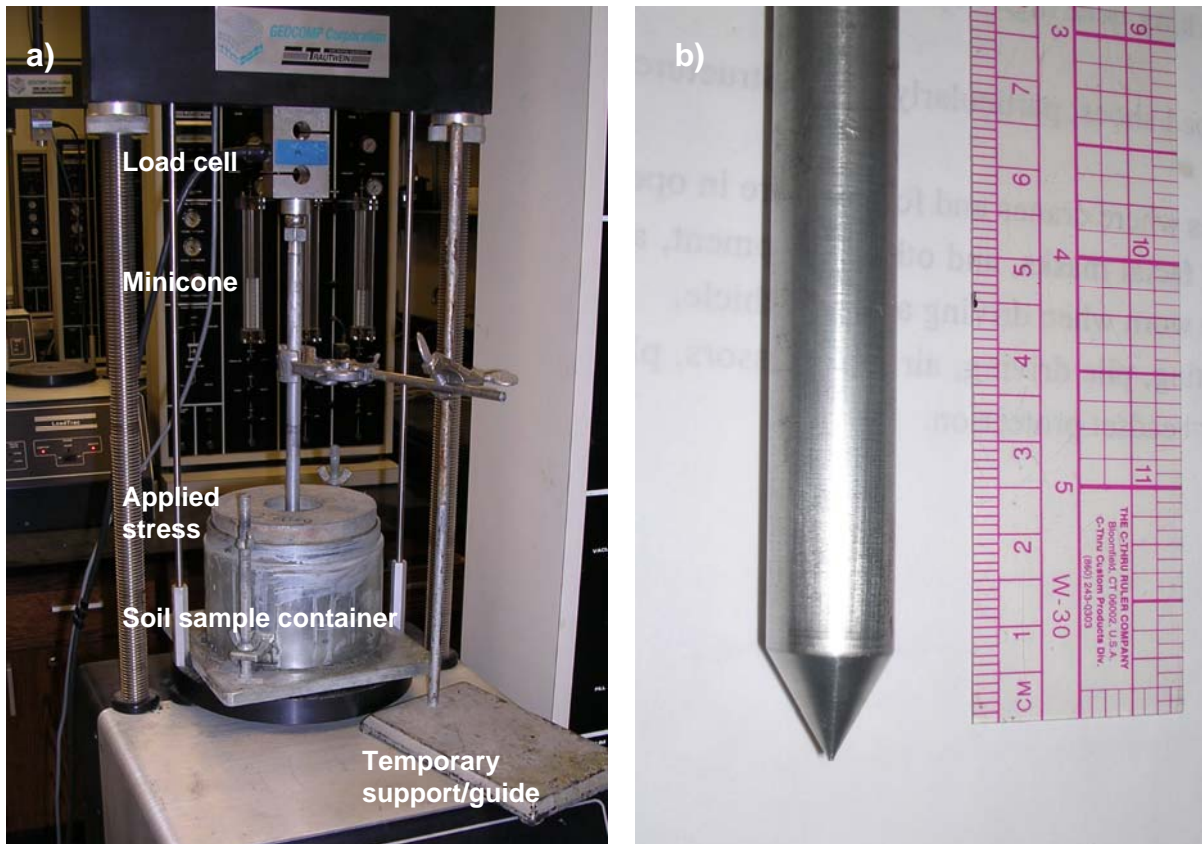
Figure 6.25. Study of relative density effect on CPT penetration resistance. a) Experimental setup. b)

Minicone. Axial stress is applied to achieve some confinement.
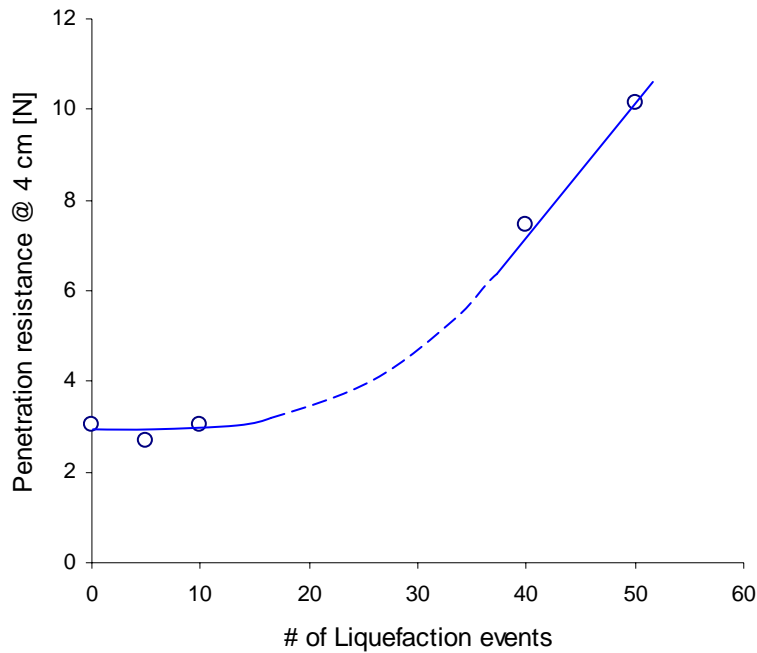
Figure 6.26. Change in mean tip resistance with increasing number of liquefaction events and increasing relative density.

The evolution of settlement and excess pore pressure at the center of the test site is plotted against time in Figure 6.27 (see Figure 6.6 and Figure 6.22): the excess pore pressure is reduced by 90% in 24hrs (much shorter time than predicted for consolidation). In the same period of time only 60% of the total settlement takes place. Settlement curves versus time shown in Figure 6.4, Figure 6.7 and Figure 6.11 show that settlement continues long after the excess pore pressure decreases to 10% of initial excess pressure. This suggests that other settlement processes are involved besides resedimentation and consolidation.
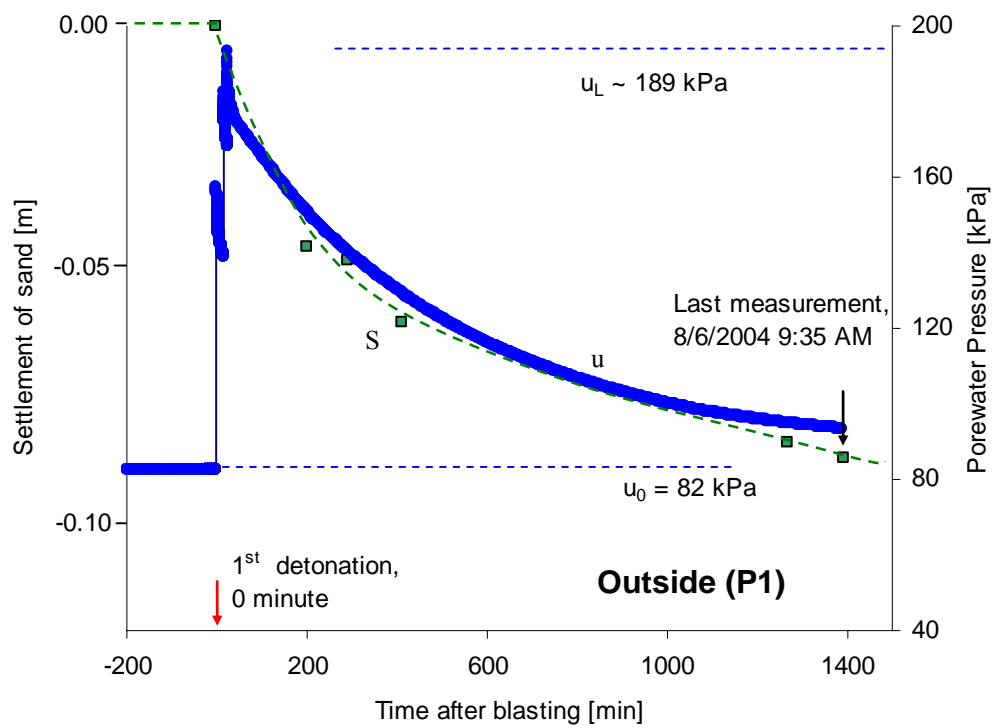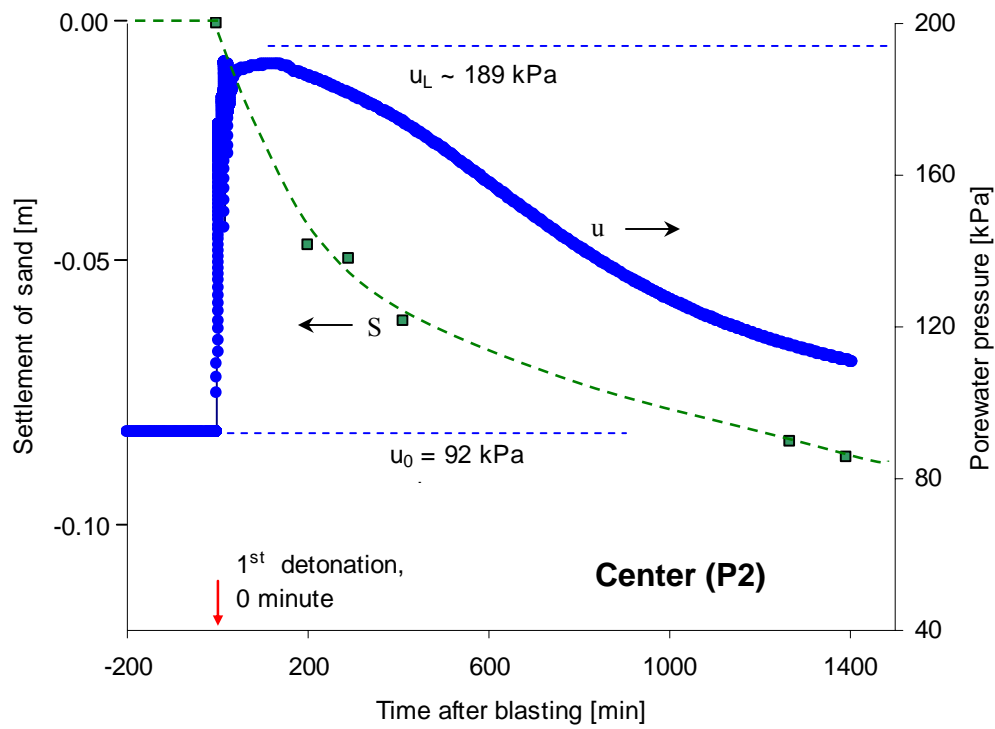
Figure 6.27. Maximum settlement and pore pressure dissipation (fourth blast coverage).

193

Even after the fourth blast coverage, the measured peak excess pore pressure during detonation reaches the vertical effective stress, which would not be expected from a dilative soil subjected to large-strain. Two hypotheses are made: First, the increase in pore pressure is due to gas expansion following explosions. Second, a mechanism of cyclic small-to-intermediate strain densification causes excess pore pressure (Sections 4.2.2 and 4.2.4). The decreasing duration of water flow observed during the fourth blast coverage would agree with the first hypothesis. The second hypothesis would require small-to-intermediate cyclic strains; however, the number of cycles is small in Figure 6.15.

The shear stiffness (from V_s) recovers at T_{90}. Thereafter, V_s increases by about 50% in the following two months (Figure 6.20). This time-dependent gain may be due to dissipation of excess pore pressure, precipitation of salts, densification, creep, stress redistribution and aging effects. There exists inconsistency between CPTu tip resistance and V_s data one month after blasting.

A detonation can cause liquefaction 15m away from the blasting charges, even for relatively small individual charges (W=11kg, Figure 6.22 and Table 6.3).

The timing and duration of water flow out of pipes suggest strong effects of spatial variability and development of percolation paths.

CHAPTER VII

CONCLUSIONS AND RECOMENDATIONS

7.1 CONCLUSIONS

Soils are complex, and inherently variable materials. This research address the effects of the ubiquitous spatial variability of hydraulic conductivity and excess pore pressure diffusivity, and introduces the conceptual framework of terminal density to gain further insight into soil behavior. In addition, an unprecedented blast densification field study is analyzed in detail, and measurements interpreted in terms of terminal density and the interplay between conduction and diffusion phenomena.

The investigation has involved the complementary use of analytical solutions, numerical simulations, laboratory experimentation and field monitoring. Results include effective medium parameters, procedures to assess depth-varying diffusivity, guidelines to take into consideration spatial variability in geotechnical design, and a renewed understanding of blast densification. The main conclusions from this study follow.

Conduction in spatially varying media. The hydraulic conductivity of homogeneous binary mixtures decreases as the mass fraction of the finer component increases, but it soon reaches a plateau when the mass fraction of the finer grains is sufficient to fill the void space left by the coarser grains. The inherent spatial variability

in hydraulic conductivity plays a crucial role in flow rate and total head distribution. Most analytical bounds and close form solutions are based on volume fraction and fail to capture effects associated to the spatial distribution of hydraulic conductivity, such as percolation effects. The hydraulic conductivity decreases with increasing variability (as measured by the coefficient of variation COV in log-normal distributions of hydraulic conductivity with the same mean value). This observation applies to both correlated as well as uncorrelated k-fields. Correlated random fields exhibit lower hydraulic conductivity than uncorrelated fields with otherwise identical statistics, due to the development of high-conductivity percolation paths.

Diffusion in spatially varying media. Numerical for systems with varying coefficient of consolidation show that the dissipation of excess pore pressure is affected by the spatial variability in diffusivity. The time and depth variation of excess pore pressure can be used to infer the spatial variation in the diffusivity using matrix-based inversion techniques. Noise hinders invertibility. The regularized least square solution is generally preferred and minimizes noise effects. The uncertainty in the inverted coefficients of consolidation increases with increasing contrast in diffusivity. Excess pore pressure profiles at small or very large T-values are uninformative.

Terminal density. The new conceptual framework of terminal density is proposed to further advance the understanding of granular materials. This hypothesis presumes the existence of a characteristic density (and associated internal fabric) that supports continuation of the process at constant volume. Many geotechnical process and properties can be conveniently considered under the terminal density framework, such as large-

strain critical state monotonic loading, extreme void ratios e_{max} and e_{min}, oedometric quasi-static loading, and blast densification.

The classical categorization of a "dilative soil" is appropriate for large-strain processes. In fact, large-strain dilative granular materials can experience significant contraction when subjected to cyclic straining at small-to-intermediate strains. Accordingly, a large-strain dilative soil may loose considerable shear strength due to the accumulation of positive excess pore water as a result of repetitive small-to-intermediate undrained shear events.

Blast densification – Unprecedented case history. The extensive laboratory and field site characterization and the close monitoring of four blast coverages in a multi-instrumented test site reveals that the time scale for densification is related to the time scale for excess pore pressure dissipation associated to Stokes re-sedimentation, conduction and diffusion; these processes are affected by the presence of vertical drains and spatial variability in the sediment. Densification is therefore not an "instantaneous" phenomenon.

In the absence of arching in upper layers, surface settlement extends beyond the blasted area by about the blasting depth in each direction. The volumetric strain remains shear strain dependent (terminal density); consequently surface settlement decreases radially from the center of the blasted area. The amount of densification and the amount of water that flows out from the densified site decrease as the number of blasting coverages increases, as the sediment gradually evolves to the terminal density that corresponds to blasting events. The blasting sequence and detonation delays do not seem

to enhance shear induced movements. Simple surface settlement and pore pressure monitoring enhance the understanding of the system and blasting events and provide valuable information for blast design optimization.

7.2 RECOMMENDATIONS AND FUTURE RESEARCH

- *Spatial variability and dynamic effects*. Cyclic changes in total head Dirichlet boundary conditions in spatially varying hydraulic conductivity fields may lead to unexpected emergent phenomena. The reported formation of water films and gaps provides supportive evidence.

- *Site characterization*. Forward and inverse studies in this research hint to the possible development of innovative field characterization approaches, based on extensive instrumentation and concurrent numerical analysis.

- *Time scales*. The definition of the dimensionless time factor needs further analysis in systems with spatially varying diffusivity.

- *Terminal density*. This conceptual framework requires further development and extension to all types of processes in the context of a comprehensive energy formulation.

- *Blast densification*. Blast densification and design can be enhanced by a combination of extensively instrumented field studies and 3D numerical modeling of the process. The relative effects of P-motion blasting and S-motion seismic excitation remain uncertain, as the two events lead to potentially different terminal densities.

APPENDIX A – CONDUCTION MATLAB CODE

Solving Laplace equation Matlab code – Triangular elements.

```
% Finite element program for Laplace's equation with triangular elements.
%
%kode     = flag, 1 for boundary nodes, 0 for internal nodes.
%h        = head in the nodes
%x, y     = coordinates of nodes
%kx, ky   = permeability coefficient in x and y directions
%
% REMEMBER TO CHANGE THE X AND Y SPACING IN THIS FILE
%
clear all
clc
% initialize some variables
%x=zeros(25,1);
%y=x; h=x; kode=x;

Nx=zeros(3,1); NY=Nx; node=Nx;

%FIRST BLOCK. Obtain nodal coordinates
%define # of nodes and elements

nnode=input('how many nodes does your model have? ');
nelem=input('how many elements does your model have? ');

%read coordinates, flag and h values of BC from a file

[x,y,kode,h]=textread('nodescoor.txt','%f %f %f %f');
G=zeros(nnode,nnode);


%SECOND BLOCK. Construc the conductance matrix G
%reading file with the conectivity and the permeability in each element

[inode,jnode,mnode,kx,ky]=textread('ijmtriangles.txt','%d %d %d %f %f');

%building the element conductance and adding this to the global conductance matrix.

for k=1:1:nelem
```

```
    ii=inode(k); jj=jnode(k); mm=mnode(k);kxx=kx(k);kyy=ky(k);
    A=0.5*(x(ii)*y(jj)-x(jj)*y(ii)+x(mm)*y(ii)-x(ii)*y(mm)+x(jj)*y(mm)-x(mm)*y(jj));

    %Nx and Ny are the spatial derivatives of the shape function

    Nx(1)=0.5*(y(jj)-y(mm))/A;
    Nx(2)=0.5*(y(mm)-y(ii))/A;
    Nx(3)=0.5*(y(ii)-y(jj))/A;
    Ny(1)=0.5*(x(mm)-x(jj))/A;
    Ny(2)=0.5*(x(ii)-x(mm))/A;
    Ny(3)=0.5*(x(jj)-x(ii))/A;
    node(1)=ii;
    node(2)=jj;
    node(3)=mm;

    for kk=1:1:3
      L=node(kk);
      G(L,ii)=G(L,ii)+A*(kxx*Nx(1)*Nx(kk)+kyy*Ny(1)*Ny(kk));
      G(L,jj)=G(L,jj)+A*(kxx*Nx(2)*Nx(kk)+kyy*Ny(2)*Ny(kk));
      G(L,mm)=G(L,mm)+A*(kxx*Nx(3)*Nx(kk)+kyy*Ny(3)*Ny(kk));
    end
end

%BLOCK 3. Solving system of equations by iteration.

amax=100;

while amax>0.001
    amax=0;

    for L=1:1:nnode
      oldval=h(L);

      if kode(L)==1
        error=abs(oldval-h(L));
      else
        suma=0;
        for t=1:1:nnode
          if t~=L
            suma=suma+G(L,t)*h(t);
          end
        end
        h(L)=-suma/G(L,L);
        error=abs(oldval-h(L));

      end
```

```
      if error>amax
          amax=error;
      end
   end
end
h
hsummary=horzcat((1:nnode)', h) %summary: nodes' head

xspacing=50
yspacing=50

hnew=reshape(h,xspacing+1,yspacing+1)'

hnew1=flipud(hnew);%Flip matrix in up/down direction, like a mirror
hnew2=fliplr(hnew1); %Flip matrix in left/right direction, like a mirror
             %just to be consistant with the way nodes were generated
hnew=hnew2;
guille=hnew2
surf(guille)
shading interp
[u v]=gradient(guille);
hh=streamslice(-u,-v)
% hold
% quiver(-u,-v)
view(180,-90)
colorbar

%legend()

%calculating Q flow rate per unit deep
q=G*h;
Q=sum (q(1:xspacing+1))
hnew1=flipud(hnew);%Flip matrix in up/down direction, like a mirror
hnew=hnew1;

%computing permeability and saving all data in txt files
permeability=Q/50/(9/50)   % k=Q/Area/i    i=delta H/L
save('h2u.txt','h','-ascii')
save('q2u.txt','q','-ascii')
save('Qu2u.txt','Q','-ascii')
save('matrixh2u.txt','guille','-ascii')
save('keq2u.txt','permeability','-ascii')
```

Auxiliar Matlab code – Generating nodes.

```
% Building coordinates system: nodes and elements

% Define a rectangle, by entering the coordinates of the 4 corners counterclockwise
% starting from the upper-right corner
clc
clear all
sprintf('Define    the    rectangle,    by    entering    \nthe    coordinates    of    4    points
counterclockwise\nstarting from the upper-right corner')
for ii=[1:4]
    sprintf('For point %d:',ii)
    xcorner(ii)=input('x: ');
    ycorner(ii)=input('y: ');
end
sprintf('the coordinates of the rectangule are:')
corner=[[1:ii]' xcorner' ycorner']

%generating the mesh within the rectangle

xspacing=input('x spacing: ');
yspacing=input('y spacing: '); %determiando espaciamiento en x y en y

deltax=(corner(1,2)-corner(2,2))/xspacing;
deltay=(corner(2,3)-corner(3,2))/yspacing; %calculando delta x y deltay

nnode=(xspacing+1)*(yspacing+1) %numeros de nodos

xjoin=[xcorner(1):-deltax:xcorner(2)];
yjoin=[ycorner(1):-deltay:ycorner(4)];

x=repmat(xjoin,1,yspacing+1);

% this is a alternative way to do the same:
% x=xjoin';
% for iii=1:yspacing
%     x=(vertcat(x, xjoin'))
% end

for iii=1:yspacing+1
    yy(((xspacing+1)*iii-xspacing):((xspacing+1)*iii))=yjoin(iii);
end
yy';

join=horzcat((1:nnode)', x',yy') %summary: node xcoordinate ycoordinate
```

```
%Generating conectivity automatically, i.e., creating elements

nelem=xspacing*yspacing*2
elem=zeros(1,3);
for mm=0:yspacing-1
   for m=1:xspacing
      ele(m*2-1,1)=m+mm*(xspacing+1);
      ele(m*2-1,2)=m+mm*(xspacing+1)+(xspacing+2);
      ele(m*2-1,3)=m+mm*(xspacing+1)+(xspacing+1);

      ele(m*2,1)=m+mm*(xspacing+1);
      ele(m*2,2)=m+mm*(xspacing+1)+1;
      ele(m*2,3)=m+mm*(xspacing+1)+(xspacing+2);
   end
   if mm==0
      for k=1:2*xspacing
         elem(k,1)=ele(k,1);
         elem(k,2)=ele(k,2);
         elem(k,3)=ele(k,3);
      end
   else
      elem=vertcat(elem,ele(1:2*xspacing,:));
   end
end
elem

%plotting the nodes of the automatic generated mesh
label=(1:nnode)';
trimesh(elem,x,yy,zeros(size(x))); view(2);
text(x,yy,[num2str(label)]) %this command assigns the values of each node in the figure
hold
plot(x',yy','.b')
xlabel('X coordinates'); ylabel('Y coordinates'); title('Generated mesh')
axis([min(x)-0.5 max(x)+0.5 min(yy)-0.5 max(yy)+0.5])
grid off
text('que picante! funciona!')
```

Auxiliar Matlab code – Generating mesh.

```matlab
% Building coordinates system: nodes and elements
% COPYRIGHT Guillermo Narsilio 2002

% Define a rectangle, by entering the coordinates of the 4 corners counterclockwise
% starting from the upper-right corner
clc
clear all
sprintf('Define    the    rectangle,    by    entering    \nthe    coordinates    of    4    points
counterclockwise\nstarting from the upper-right corner')
for ii=[1:4]
   sprintf('For point %d:',ii)
   xcorner(ii)=input('x: ');
   ycorner(ii)=input('y: ');
end
sprintf('the coordinates of the rectangule are:')
corner=[[1:ii]' xcorner' ycorner']

% Generating the mesh within the rectangle

xspacing=input('x spacing: ');
yspacing=input('y spacing: '); %determiando espaciamiento en x y en y

deltax=(corner(1,2)-corner(2,2))/xspacing;
deltay=(corner(2,3)-corner(3,2))/yspacing; %calculando delta x y deltay

nnode=(xspacing+1)*(yspacing+1) %numeros de nodos

xjoin=[xcorner(1):-deltax:xcorner(2)];
yjoin=[ycorner(1):-deltay:ycorner(4)];

x=repmat(xjoin,1,yspacing+1);

% this is a alternative way to do the same:
% x=xjoin';
% for iii=1:yspacing
%     x=(vertcat(x, xjoin'))
% end

for iii=1:yspacing+1
   yy(((xspacing+1)*iii-xspacing):((xspacing+1)*iii))=yjoin(iii);
end
yy';

join=horzcat((1:nnode)', x',yy') %summary: node xcoordinate ycoordinate
```

%Generating conectivity automatically, i.e., creating elements

```
nelem=xspacing*yspacing*2
elem=zeros(1,3);
for mm=0:yspacing-1
    for m=1:xspacing
        ele(m*2-1,1)=m+mm*(xspacing+1);
        ele(m*2-1,2)=m+mm*(xspacing+1)+(xspacing+2);
        ele(m*2-1,3)=m+mm*(xspacing+1)+(xspacing+1);

        ele(m*2,1)=m+mm*(xspacing+1);
        ele(m*2,2)=m+mm*(xspacing+1)+1;
        ele(m*2,3)=m+mm*(xspacing+1)+(xspacing+2);
    end
    if mm==0
        for k=1:2*xspacing
            elem(k,1)=ele(k,1);
            elem(k,2)=ele(k,2);
            elem(k,3)=ele(k,3);
        end
    else
        elem=vertcat(elem,ele(1:2*xspacing,:));
    end
end
elem
```

% Plotting the nodes of the automatic generated mesh

```
label=(1:nnode)';
trimesh(elem,x,yy,zeros(size(x))); view(2);
text(x,yy,[num2str(label)]) %this command assigns the values of each node in the figure
hold
plot(x',yy','.b')
xlabel('X coordinates'); ylabel('Y coordinates'); title('Generated mesh')
axis([min(x)-0.5 max(x)+0.5 min(yy)-0.5 max(yy)+0.5])
grid off
```

APPENDIX B – DIFFUSION MATLAB CODE

Solving Diffusion equation Matlab code – FTCS (explicit) scheme.

```
%Solving using  EXPLICIT scheme (Cv variable)

clear all
clc

dx=0.25;  %meters
dt=0.05 ; %years
total_thickness=7.5; %meters
N=total_thickness/dx-1;

Cv=[0.5
0.5
0.5
0.5
0.5
0.5
0.5
0.5
0.5
0.5
0.5
0.5
0.5
0.5
0.5
0.5
0.5
0.5
0.5
0.3
0.3
0.3
0.3
0.3
0.3
0.3
0.3
```

```
      0.3
      0.3];
      %creating the Cv media
      for i=1:N+1
        if i==1
          Cvm(i)=Cv(i);
        else
          if i==N+1
            Cvm(i)=Cv(N);
          else
            Cvm(i)=(Cv(i-1)+Cv(i))/2;
          end
        end
      end

      %Internal time scale * 2 (to ensure complete dissipation)
      T=max(total_thickness^2./Cv); %the point is importan to divide number by
number
      T=T/dt;
      r=Cvm*dt/dx^2;

      %Creating LHS matrix to multiply for the next time step.
      beta=r';
      beta(N+1,:)=[];
      gamma=beta;
      delta=r';
      delta(1,:)=[];
      beta(1,:)=[];
      alpha=1-gamma-delta;
      A=diag(beta,-1)+diag(alpha,0)+diag(beta,1);

      %Creating initial conditions, constant rectangular u_o = 1
      u_0=repmat(1,N,1);
      b=u_0;

      %Solving for u at each time step multiplying by matrix A
      for t=2:1:T
        u(:,t)=A*b;
        b=u(:,t);
      end
      %Saving computation adequately with the boundary and initial conditions
      %included.
      u(:,1)=u_0;
      u_boundary=(repmat(0,T,1))';
      u=vertcat(u_boundary,u,u_boundary);
      plot(u,'.-')
```

```
u=u';
save('uexpl3.txt','u','-ascii');
```

Solving Diffusion equation Matlab code – Implicit scheme.

```
%This is a IMPLICIT scheme (Cv variable)
%it is working well.

clear all
clc

dx=0.25;  %meters
dt=0.05;  %years
total_thickness=7.5; %meters
N=total_thickness/dx-1;

Cv=[0.5
0.5
0.5
0.5
0.5
0.5
0.5
0.5
0.5
0.5
0.5
0.5
0.5
0.5
0.5
0.5
0.5
0.5
0.5
0.3
0.3
0.3
0.3
0.3
0.3
0.3
0.3
0.3
0.3
0.3];
```

```
%creating the Cv media
for i=1:N+1
  if i==1
    Cvm(i)=Cv(i);
  else
    if i==N+1
      Cvm(i)=Cv(N);
    else
      Cvm(i)=(Cv(i-1)+Cv(i))/2;
    end
  end
end

%Internal time scale (to ensure complete dissipation)
T=max(total_thickness^2./Cv);   %the point is importan to divide number by
number
T=T/dt;
r=Cvm*dt/dx^2;

%Creating LHS matrix to invert
beta=r';
beta(N+1,:)=[];
gamma=beta;
delta=r';
delta(1,:)=[];
beta(1,:)=[];
alpha=1+gamma+delta;
A=diag(-beta,-1)+diag(alpha,0)+diag(-beta,1);

%Creating the RHS vector to multiply for
u_0=repmat(1,N,1);
b=u_0;

%Solving for u at each time step inverting matrix A
%which is tridiagonal with the \ operator (optimized)
for t=2:1:T
  u(:,t)=A\b;
  b=u(:,t);
end

%Saving the computations properly, including the initial and boundary conditions.
u(:,1)=u_0;
u_boundary=(repmat(0,T,1))';
u=vertcat(u_boundary,u,u_boundary);
%plot(u,'.-')
u=u';
```

```
save('uimpl2.txt','u','-ascii');
```

Solving Diffusion equation Matlab code – Crank-Nicholson scheme.

```
%The Crank Nicholson scheme.

clear all
clc

dx=0.25;  %meters
dt=0.025;  %years
total_thickness=7.5; %meters
N=total_thickness/dx-1;

Cv=[0.5
0.5
0.5
0.5
0.5
0.5
0.5
0.5
0.5
0.5
0.5
0.5
0.5
0.5
0.5
0.5
0.5
0.5
0.5
0.3
0.3
0.3
0.3
0.3
0.3
0.3
0.3
0.3
0.3];
```

```matlab
%creating the Cv media
for i=1:N+1
  if i==1
    Cvm(i)=Cv(i);
  else
    if i==N+1
      Cvm(i)=Cv(N);
    else
      Cvm(i)=(Cv(i-1)+Cv(i))/2;
    end
  end
end


%Internal time scale (to ensure complete dissipation)
T=max(total_thickness^2./Cv);    %the point is importan to divide number by
number
T=T/dt;
r=Cvm*dt/dx^2;

%Creating RHS matrix to multiply the previus time step vector
beta=r'/2;
beta(N+1,:)=[];
gamma=beta;
delta=r'/2;
delta(1,:)=[];
beta(1,:)=[];
alpha=1-gamma-delta;
B=diag(beta,-1)+diag(alpha,0)+diag(beta,1);

%Initial condition
u_0=repmat(1,N,1)

%Creating LHS matrix to invert
beta=r'/2;
beta(N+1,:)=[];
gamma=beta;
delta=r'/2;
delta(1,:)=[];
beta(1,:)=[];
alpha=1+gamma+delta;
A=diag(-beta,-1)+diag(alpha,0)+diag(-beta,1);

b=B*u_0;
```

```
%Solving for u at each time step inverting matrix A
%which is tridiagonal with the \ operator (optimized)
for t=2:1:T
    u(:,t)=A\b;
    b=B*u(:,t);
end

%Saving computation adequately with the boundary and initial conditions
%included.
u(:,1)=u_0;
u_boundary=(repmat(0,T,1))';
u=vertcat(u_boundary,u,u_boundary);
plot(u,'.-')
u=u';
save('ucn3.txt','u','-ascii');
```

REFERENCES

Abbot, M. B. (1960). "One dimensional consolidation of multi-layered soils." *Geotechnique*, 10, 151-165.

Abichou, T., Benson, C. H., and Edil, T. B. (2002). "Micro-structure and hydraulic conductivity of simulated sand-bentonite mixtures." *Clays and Clay Minerals*, 50(2), 537-545.

Al-Khafaji, A. W., and Andersland, O. B. (1992). *Geotechnical Engineering & Soil testing*, Saunders College Publishing.

Al-Qasimi, E. M. A., Charlie, W. A., and Woeller, D. J. (2005). "Canadian Liquefaction Experiment (CANLEX): Blast-induced ground motion and pore pressure experiments." *Geotechnical Testing Journal*, 28(1), 9-21.

Arai, K., Ohta, H., and Kijima, K. (1984). "Estimation of soil parameters based on monitored movement of subsoil under consolidation." *Soils and Foundations*, 24(4), 95-108.

Asaoka, A., and Matsuo, M. (1980). "An inverse problem approach to settlement prediction." *Soils and Foundations*, 20(4), 53-66.

Bal, G., and Chou, T. (2004). "On the reconstruction of diffusions from first-exit time distributions." *Inverse Problems*, 20, 1053-1065.

Bardet, J. P., Idriss, I. M., O'Rourke, T. D., Adachi, N., Hamada, M., and Ishihara, K. (1997). "North America - Japan workshop on the geotechnical aspects of the Kobe, Loma Prieta and Northridge earthquakes." Osaka, Japan.

Baxter, C. D. P. (1999). "An experimental study on the aging of sands," Ph.D. Dissertation, Department of Civil Engineering, Virginia Polytechnic Institute and State University, Blacksburg, Virginia.

Bayoumi, A. (2006). "New laboratory testing for enhanced constitutive modeling," Ph.D. Dissertation, Georgia Institute of Technology, Atlanta, GA.

Berkowitz, B., and Balberg, I. (1993). "Percolation theory and its application to groundwater hydrology." *Water Resour. Res.*, 29(4), 775-794.

Berryman, J. G., and Wang, H. F. (1995). "The elastic coefficients of double-porosity models for fluid transport in jointed rock." *J. Geophys.Res.*, 100, 24611-24627.

Biot, M. A. (1941). "General theory of three dimensional consolidation." *Journal of Applied Physics*, 12, 155-164.

Bishop, A. W., and Henkel, D. J. (1953). "Constant-pressure control for triaxial-compression test." *Geotechnique*, 3(8), 339-344.

Bøe, Ø. (1994). "Analysis of an upscaling method based on conservation of dissipation." *Trans. Porous Media*, 77, 77-86.

Borja, R. I. (1988). "Analysis of consolidation by a quasi-Newton technique." *International Journal for Numerical and Analytical Methods in Geomechanics*, 12(2), 221-222.

Brey, J. J., Prados, A., and Sanchez-Rey, B. (2000). "Thermodynamic description in a simple model for granular compaction." *Physica A: Statistical Mechanics and its Applications*, 275(3-4), 310.

Brown, G. O. "The history of the Darcy-Weisbach equation for pipe flow resistance." *Proceedings of the Environmental and Water Resources History*, 34-43.

Bryan, K., and Caudill, L. F. J. (1996). "An inverse problem in thermal imaging." *SIAM Journal on Applied Mathematics*, 56(3), 715-735.

Burns, S. E., and Mayne, P. W. (1998). "Monotonic and dilatory pore-pressure decay during piezocone tests in clay." *Canadian Geotechnical Journal*, 35(6), 1063-1073.

Byrne, P. M., Puebla, H., Chan, D. H., Soroush, A., Morgenstern, N. R., Cathro, D. C., Gu, W. H., Phillips, R., Robertson, P. K., Hofmann, B. A., Wride, C. E., Sego, D. C., Plewes, H. D., List, B. R., and Tan, S. (2000). "CANLEX full-scale experiment and modelling." *Canadian Geotechnical Journal*, 37(3), 543-562.

Cai, Y.-Q., Liang, X., and Wu, S.-M. (2004). "One-dimensional consolidation of layered soils with impeded boundaries under time-dependent loadings." *Applied Mathematics and Mechanics (English Edition)*, 25(8), 937-944.

Cardwell, W. T., and Parsons, R. L. (1945). "Average permeabilities of heterogeneous oil sands." *Trans. Am. Inst. Min. Metall. Pet. Eng.*, 160, 34-42.

Castro, G. (1969). "Liquefaction of Sands." *Harvard Soil Mechanics Series No. 81, Harvard University, Cambridge MA.*

Charlie, W. A., Rwebyogo, M. F. J., and Doehring, D. O. (1992). "Time-dependent cone penetration resistance due to blasting." *Journal of Geotechnical Engineering*, 118(8), 1200-1215.

Charlie, W. A., Veyera, G. E., and Abt, S. R. (1985). "Predicting Blast Induced Porewater Pressure Increases in Soils." *Int. Journal of Civil Engineering for Practicing and Design Engineers*, 4(3), 311-328.

Chen, A. T. F. (1988). "On seismically induced pore pressure and settlement." Geotechnical Special Publication No. 20, ASCE, New York, NY, USA., 482-492.

Chern, J. C., and Lin, C. C. (1994). "Post-cyclic consolidation behavior of loose sands." Geotech Spec Publ No. 40. (also Proceedings of the Conference on Vertical and Horizontal Deformations of Foundations and Embankments. Part 1 (of 2) 06/16-18/94 College Station, TX, USA), New York, NY. USA, ASCE, 740-747.

Chien, L.-K., Oh, Y.-N., and Chang, C.-H. (2002). "Effects of fines content on liquefaction strength and dynamic settlement of reclaimed soil." *Canadian Geotechnical Journal*, 39(1), 254-265.

Cho, G. C. (2001). "Unsaturated soil stiffness and post-liquefaction shear strength / by," Ph.D. Dissertation, School of Civil and Environmental Engineering, Georgia Institute of Technology, Atlanta.

Cho, G.-C., Dodds, J., and Santamarina, J. C. (2006). "Particle Shape Effects on Packing Density, Stiffness and Strength - Natural and Crushed Sands -." *Journal of Geotechnical and Geoenvironmental Engineering*, Submitted.

Cortellazo, G. (2002). "Comparison between laboratory and in situ values of the coefficient of primary consolidation Cv." *Canadian Geotechnical Journal*, 39, 103-110.

Dafalias, Y. F. (1993). "Overview of constitutive models used in VELACS." *Verification of Numerical Procedures for the analysis of soil liquefaction problems*, 2, 1293-1304.

Dagan, G. (1989). *Flow and transport in porous formations*, Springer-Verlag, Berlin; New York.

Dagan, G., and Lessof, S. C. (2001). "Solute transport in heterogeneous formations of bimodal conductivity distribution 1: Theory." *Water Resource Research*, 37(3), 465-472.

DeGroot, D. J. "Analyzing spatial variability of in situ soil properties, Uncertainty in the geologic environment, from theory to practice." *Uncertainty '96*, Madison, Wisconsin, 210-238.

Dowding, C. H., and Hryciw, R. D. (1986). "A laboratory study of blast densification." *Journal of Geotechnical Engineering*, 112(2), 187-199.

Efendiev, Y., Ginting, V., Hou, T., and Ewing, R. (2006). "Accurate multiscale finite element methods for two-phase flow simulations." *J. Comput. Phys. submitted*.

Elayyan, A., and Isakov, V. (1997). "On the inverse diffusion problem." *SIAM J. Appl. Math.*(57), 1737–48.

El-Kadi, A. I., and Williams, S. A. (2000). "Generating two-dimensional fields of auto-correlated, normally distributed parameters by the matrix decomposition technique." *Ground Water*, 38(4), 530-532.

Erdik, M. (2000). "Report on 1999 Kocaeli and Düzce (Turkey) earthquakes." Bogazici University, Dept. of Earthquake Engineering, 81220 Cengelkoy. Available at http://www.koeri.boun.edu.tr/depremmuh/eqspecials/kocaeli/Kocaelireport.pdf, last accessed 02/10/2006, Istanbul, Turkey.

Fenton, G. A., and Griffiths, D. V. (1996). "Stochastics of free surface flow through stochastic earth dam." *Journal of Geotechnical and Geoenvironmental Engineering*, 122(6), 427-436.

Fernandez, A. L. (2000). "Tomographic imaging the state of stress," Ph.D. Dissertation, School of Civil and Environmental Engineering, Georgia Institute of Technology, Atlanta, GA.

Fiegel, G. L., and Kutter, B. L. (1994). "Liquefaction mechanism for layered soils, Journal of Geotechnical Engineering." *Journal of Geotechnical and Geoenvironmental Engineering*, 120(4), 737-755.

Finno, R. J., and Calvello, M. (2005). "Supported excavations: Observational method and inverse modeling." *Journal of Geotechnical and Geoenvironmental Engineering*, 131(7), 826-836.

Fitts, C. (1991). "Modeling three-dimensional flow about ellipsoidal inhomogeneities with application to flow to a gravel-packed well and flow through lens-shaped inhomogeneities." *Water Resource Research*, 27(5), 815-824.

Fordham, C. J., McRoberts, E. C., Purcell, B., and McLaughlin, P. (1991). "Practical and theoretical problems associated with blast densification of loose sands." *Proceedings of the 44th Canadian Geotechnical Conference of the Canadian Geotechnical Society*, Calgary, Alberta, Canada, X, 92-1 to 92-8.

Frankel, J. I., and Lawless, J. L. (2005). "Numerically stabilizing ill-posed moving surface problems through heat-rate sensors." *Journal of Thermophysics and Heat Transfer*, 19(4), 587-592.

Fredlund, M. D., Stianson, J., and Rykaart, M. "Automatic mesh refinement in the SVFlux and ChemFlux software packages." *UNSAT Asia 2003*.

Gens, A., Ledesma, A., and Alonso, E. E. (1996). "Estimation of parameters in geotechnical backanalysis – II. Application to a tunnel excavation problem." *Computers in Geotechnics*, 18(1), 29-49.

Gioda, G., and Sakurai, S. (1987). "Back Analysis Producers for the Interpretation of Field Measurements in Geomechanics." *Int. J. Numerical and Analytical Methods in Geomechanics*, 11, 555-583.

Gnadhi, S., Dey, A., and Selvam, S. (1999). "Densification of pond ash by blasting." *Journal of Geotechnical and Geoenvironmental engineering*, 125(10), 889-899.

Griffiths, D. V., and Fenton, G. A. (1993). "Seepage beneath water retaining structures founded on spatially random soil." *Geotechnique*, 43(4), 577-587.

Griffiths, D. V., and Fenton, G. A. (2001). "Bearing capacity of spatially random soil: the undrained clay Prandtl problem revisited." *Geotechnique*, 51(4), 351-359.

Hachey, J. E., Plum, R. L., Byrne, J., Kilian, A. P., and Jenkins, D. V. (1994). "Blast densification of a thick, loose debris flow at Mt. St. Helen's, Washington." *Proceedings of Vertical and Horizontal Deformations of Foundations and Embankments, Geotechnical Special publication No. 40*, 1, 502-512.

Hall, C. E. (1962). "Compacting a dam foundation by blasting." *J. Soil Mech. and Found. Div., ASCE*, 88(3), 33-51.

Hanson, K. M. (2000). "Optical tomography reconstruction: inversion based on adjoint differentiation," Duke.

Hào, D. N. (1994). "A non-characteristic Cauchy problem for linear parabolic equations and related inverse problems: I. Solvability." *Inverse Problems*, 10, 295-315.

Harr, M. E. (1987). *Reliability-based design in civil engineering*, Dover Publications, Inc., Mineola, New York.

Head, K. H. (1992). *Manual of soil and laboratory testing: soil classification and compaction tests*, Halsted Press, New York.

Holtz, R. D., and Broms, B. B. "Long-term loading tests as Skå-Edeby." *ASCE Specialty Conference on Performance of Earth and Earth-supported Structures*, Purdue University, 435-464.

Hryciw, R. (1986). "A study of the physical and chemical aspects of blast densification in sands," Ph.D. Dissertation, School of Civil and Environmental Engineering, Northwestern University, Evanston, IL.

Hsu, C.-C., and Vucetic, M. (2004). "Volumetric threshold shear strain for cyclic settlement." *Journal of Geotechnical and Geoenvironmental Engineering*, 130(1), 58-70.

Isakov, V., and Kindermann, S. (2000). "Identification of the diffusion coefficient in a one-dimensional parabolic equation." *Inverse Problems*, 16, 665-680.

Ishihara, K. (1996). *Soil behaviour in earthquake geotechnics*, Clarendon Press; Oxford University Press, Oxford, New York.

Ishihara, K., and Yoshimine, M. (1992). "Evaluation of settlements in sand deposits following liquefaction during earthquakes." *Soils and Foundations*, 32(1), 178-188.

Ivanov, P. L. (1967). "Compaction of noncohesive soils by explosions (translated from Russian 1972)." *Report No. TT 70-57221*, U.S. Department of Commerce, Springfield, Virginia.

Ivanov, P. L. (1983). "Prediction and control techniques to compact loose soils by explosions." *Proc. 8th European Conf. on Soil Mechanics and Foundation Engineering*, Helsinki, Finland, 1.

Iwasaki, T., Tatsuoka, F., and Takagi, Y. (1978). "Shear modulus of sands under cyclic torsional shear loading." *Soils and Foundations*, 18(1), 39-50.

Jefferies, M. G., and Rogers, B. T. (1993). "Discussion of "Time-dependent cone penetration resistance due to blasting" by W. A. Charlie, M. F. J. Rwebyogo, and D. O. Doehring." *Journal of Geotechnical Engineering*, 119(2), 2008-2012.

Jefferies, M. G., and Shuttle, D. A. (2005) "NorSand: features, calibration and use." *Soil constitutive models: evaluation, selection, and calibration - Geotechnical Special Publication; no. 128*, Reston, Va. 204-236.

Jefferies, M. G., and Shuttle, D. A. (2002). "Dilatancy in general Cambridge-type models." *Geotechnique*, 52(9), 625-638.

Jeng, D. S., Rahman, M. S., and Lee, T. L. (1999). "Effects of Inertia Forces on Wave-Induced Seabed Response." *International Journal of Offshore and Polar Engineering*, 9(4), 307-313.

Jones, B. F. (1963a). "The determination of a coefficient in a parabolic differential equation, Part I: uniqueness and existence." *J. Math. Mech.*, 11, 907-918.

Jones, B. F. (1963b). "Various methods for finding unknown coefficients in parabolic differential equations." *Comm. Pure and Appl. Math.*, 16, 33-44.

Kayen, R. E., Barnhardt, W. A., Ashford, S., Rollins, K., Minasian, D. L., and Carkin, B. A. (2005). "High-Resolution Crosshole Radar Tomography: Application to Liquefaction-Induced Changes in Soil on Treasure Island."

Kenney, T., Van Veen, W., Swallow, M., and Sungaila, M. (1992). "Hydraulic conductivity of simulated sand-bentonite mixtures." *Canadian Geotechnical Journal*, 29, 364-374.

Khemissa, M., and Magnan, J.-P. (2000). "Variabilite des resultats d'essais oedometriques sur l'argile molle de Guiche (Variability of the results of oedometer tests on soft Guiche clay)." *Bulletin des Laboratoires des Ponts et Chaussees*(227), 41-50.

Kim, H. (2005). "Spatial variability in soils: stiffness and strength," Ph. D. Dissertation, Georgia Institute of Technology, Atlanta, GA.

Kim, S., and Heydinger, A. G. (2004). "Average degree of consolidation in normally consolidated soil considering the change of coefficient of consolidation with time." *Electronic Journal of Geotechnical Engineering*, 9 E, 6.

King, P. R. (1989). "The use of renormalization for calculating effective permeability." *Transp. Porous Media*, 4, 37-58.

Kokusho, T. (1999). "Water film in liquefied sand and its effect on lateral spread." *Journal of Geotechnical and Geoenvironmental Engineering*, 125(10), 817-826.

Kokusho, T. (2002). "Mechanism for post liquefaction water film generation in layered sand." *Journal of Geotechnical and Geoenvironmental Engineering*, 128(2), 129-137.

Kokusho, T., and Kojima, T. (2002). "Mechanism for post liquefaction water film generation in layered sand." *Journal of Geotechnical and Geoenvironmental Engineering*, 128(2), 129-137.

Koppula, S. D. "Probabilistic consolidation analysis." *Reliability and Risk Analysis in Civil Engineering, Proceedings of ICASP5, the Fifth International Conference on Applications of Statistics and Probability in Soil and Structural Engineering., Vancouver, BC, Can Sponsor: Air Canada; Canadian Geotechnical Soc; Canadian Natl Group of the IABSE; Canadian Pacific Airlines; Canadian Soc for Civil Engineering; et al.*

Kramer, S. L. (1996). *Geotechnical earthquake engineering*, Prentice Hall, Upper Saddle River, N.J.

Krumbein, W. C., and Sloss, L. L. (1963). *Stratigraphy and Sedimentation*, W. H. Freeman and Company, San Francisco.

Kulhawy, F. H., and Mayne, P. W. (1990). "Manual on estimating soil properties for foundation design." Electric Power Research Institute, Palo Alto, Calif.

Kulhawy, F. H., and Phoon, K. K. (1996). "Engineering judgment in the evolution from deterministic to reliability-based foundation design." *Uncertainty in the geologic environment*, Ed. Shackelford, C.D. Nelson, P.P. and Roth, M.J.S., New York, 29-48.

La Fosse, U. (2002). "Improvements by Deep Blasting: Marine Corps Reserve Training Center." *Westover Air Reserve Base*.

Lacasse, S., and Nadim, F. "Uncertainties in characterizing soil properties." *Uncertainty in the geologic environment (GSP 58)*, New York, 49-75.

Lachassagne, P., E. Ledoux, and Marsily, G. d. "Two-dimensional stochastic modeling of flow in non-uniform confined aquifers: Correction of the systematic bias introduced by numerical models when they are used stochastically." *2nd European Conference on the Mathematics of Oil Recovery*, Arles, France, 283–286.

Lambe, T. W., and Whitman, R. V. (1969). *Soil mechanics*, New York, Wiley, 1969.

Landau, L. D., and Lifshiëtìs, E. M. (1960). *Electrodynamics of continuous media*, Pergamon Press, Oxford, New York.

Le Loc'h, G. (1987). "Étude de la composition des perméabilités par des méthodes varationelles," Ph. D., Paris School of Mines, Paris, France.

Lee, I. K., White, W., and Ingles, O. G. (1983). *Geotechnical engineering*, Pitman Publishing, Marsfield, MA.

Lee, J.-S. (2003). "High resolution geophysical techniques for small-scale soil model testing," Ph. D. Dissertation, Georgia Institute of Technology, Atlanta, GA.

Lee, J.-S., and Santamarina, J. C. (2005). "Bender Elements: Performance and Signal Interpretation." *Journal of Geotechnical and Geoenvironmental Engineering*, 131(9), 1063-1070.

Leonards, G. A., and Girault, P. "A study of the one-dimensional consolidation test." *International Conference on Soil Mechanics and Foundation Engineering*, Paris, 116-130.

Liu, A. H., Stewart, J. P., Abrahamson, N. A., and Moriwaki, Y. (2001). "Equivalent number of uniform stress cycles for soil liquefaction analysis." *Journal of Geotechnical and Geoenvironmental Engineering*, 127(12), 1017-1026.

Liu, C., and Ball, W. P. (1999). "Application of Inverse Methods to Contaminant Source Identification from Aquitard Diffusion Profiles at Dover AFB, DE." *Water Resources Research*, 35(7), 1975-1985.

Liu, C., Ball, W. P., and Ellis, J. H. (1998). "An analytical solution to the one-dimensional solute advection-dispersion equation in multi-layer porous media." *Transport in Porous Media*, 30, 25-43.

Lyman, A. K. (1942). "Compaction of cohesionless foundation soils by explosives." *Transactions. ASCE*, 107(Paper No. 2160), 1330-1348.

Lyman, A. K. (1942). "Compaction of cohesionless foundation soils by explosives." *Transactions. ASCE*, 107(Paper No. 2160), 1330-1348.

Makse, H. A., and Kurchan, J. (2002). "Testing the thermodynamic approach to granular matter with a numerical model of a decisive experiment." *Nature*, 415(6872), 614-617.

Massarch, R. K. "Deep compaction of granular soils." *A look back for future geotechnics, chapter 5*, Rotterdam, 181-223.

Matheron, G. (1967). *Eléments Pour une Théorie des Milieux Poreux*, Masson, Paris.

Minaev, O. P. (1993). "Effective compaction of water-saturated soils by blasting." *Osnovaniya, Fundamenty i Mekhanika Gruntov*, 30(2), 17-19.

Mitchell, J. K. (1981). "Soil improvement: State-of-the-art." *Proceedings of Tenth international conference on soil mechanics and foundation engineering (10th ICSMFE)*, Stockholm, Sweden, Vol 4, pp. 509-565.

Mollins, L., Stewart, D., and Cousens, T. (1996). "Predicting the hydraulic conductivity of bentonite-sand mixtures." *Clay Minerals*, 31, 243-252.

Moulton, J. D., Knapek, S., and Dendy, J. E. (1999). "Multilevel upscaling in heterogeneous porous media." Los Alamos National Laboratory, Los Alamos, NM.

Mueth, D. M., Debregeas, G. F., Karczmart, G. S., Eng, P. J., Nagel, S. R., and Jaeger, H. M. (2000). "Signatures of granular microstructure in dense shear flows." *Nature*, 406(6794), 385.

Nagase, H., and Ishihara, K. (1988). "Liquefaction-induced settlements of sand during earthquakes." *Soils and Foundations*, 28(1), 65-76.

Nakata, Y., Hyodo, M., Hyde, A. F. L., and Murata, H. (2001). "Microscopic particle crushingof sand subjected to one-dimensional compression." *Soils and Foundations*, 41(1), 69-82.

Narin van Court, W. A. (1997). "Investigation of the mechanisms and predictive methodologies for explosive compaction," Ph.D. Dissertation, Civil and Environmental Engineering, University of California at Berkley.

Narin van Court, W. A. (2003). "Explosive compaction revisited: New guidance for performing blast densification." *SARA 2003, 12th Panamerican Conference on Soil Mechanics and Geotechnical Engineering and 39th U.S. Rock Mechanics Symposium*, Massachusetts Institute of Technology, Cambridge, MA, USA., 1725-1730.

Narin van Court, W. A., and Mitchell, J. K. (1994). "Soil improvement by blasting." *Journal of Explosive Engineering*, 12(3), 34-41.

Narin van Court, W. A., and Mitchell, J. K. (1998). "Investigation of predictive methodologies for explosive compaction." *Geotechnical Special Publication No. 75*, Seattle, WA, USA, 1, 639-653.

Narsilio, G. A., and Santamarina, J. C. (2004). "Soil classification: physic fundamentals, current practices and recommendations." *Proceedings of the joint XVII Argentinean Congress of Soil Mechanics and Geotechnical Engineering – III Argentinean Congress on Dams and Hydroelectric Use – VIII Symposium of Applied Geology towards Engineering and Environment – Fifth Meeting on Preparation and Use of Thematic Maps, SINERGIA 2004; Also published in the Proceedings of the XXII National Meeting of Soil Mechanics, November 2004, Guadalajara, Mexico. (in Spanish)*, Cordoba, Argentina, 1-18.

NAVFAC. (1986). "Soil Mechanics - Design Manual 7.01." Naval Facilities Engineering Command, Norfolk, VA.

Navy, U. S. (1962). "Design Manual – Soil Mechanics, Foundations and Earth Structures, NAVDOCKS DM-7."

Nielsen, D. R., Biggar, J. W., and Erh, K. T. (1973). "Spatial varibility of field-measured soil-water properties." *Hilgardia, J. Agr. Sci. (Calif. Agr. Experiement Stu.)*, 43, 215-260.

Nishimura, S. I., Shimada, K., and Fujii, H. (2002). "Consolidation inverse analysis considering spatial variability and non-linearity of soil parameters." *Soils and Foundation*, 42(3), 45-61.

Norris, G. M. (1999). "Advances in the effective stress approach to liquefaction behavior." Physics and Mechanics of Soil Liquefaction, P. V. Lade and J. A. Yamamuro, eds., Balkema, Rotterdam, Baltimore, Maryland, 41-52.

Nowak, E. R., Knight, J. B., Ben-Naim, E., Jaeger, H. M., and Nagel, S. R. (1998). "Density fluctuations in vibrated granular materials." *Physical Review E*, 57(2), 1971-1982.

Ortega, A. G. (1996). "Variability of the coefficient of consolidation of the Mexico City clayey sediments on spatial and time scales." *Bulletin of the International Association of Engineering Geology*(54), 125-135.

Özkan, M. Y., Tunçer, M. A., and Yilmaz, Ç. (1996). "An evaluation of Sürgü dam response during 5 May 1986 earthquake." *Soil Dynamics and Earthquake Engineering*, 15, 1-10.

Paice, G. M., Griffiths, D. V., and Fenton, G. A. (1996). "Finite element modeling of settlements on spatially random soil." *Journal of Geotechnical and Geoenvironmental Engineering*, 122(9), 777-789.

Papanicolaou, A., and Diplas, P. "Non-linear settlement of solids due to their self-weight." *International Water Resources Engineering Conference - Proceedings*, 1326-1331.

Phoon, K. K., and Kulhawy, F. H. (1999). "Characterization of geotechnical variability." *Canadian Geotechnical Journal*, 36(4), 612-624.

Poley, A. D. (1988). "Effective permeability and dispersion in locally heterogeneous aquifers." *Water Resource Research*, 24(11), 1921-1926.

Popescu, R., and Prevost, J. H. (1996). "Influence of spatial variability of soil properties on seismically induced soil liquefaction." *Geotechnical Special Publication*(58), 1098-1112.

Popescu, R., Prevost, J. H., and Deodatis, G. (1997). "Influence of spatial variability on soil liquefaction: some design recommendations." *Geotechnique*, 47(5), 1019-1036.

Poulos, H. G. (1980). "A review of the behavior and engineering properties of carbonates soils." *R381*, School of Civil Engineering, University of Sidney, Sydney.

Pradel, D. (1998). "Procedure to evaluate earthquake-induced settlements in dry sandy soils." *Journal of Geotechnical and Geoenvironmental Engineering*, 124(4), 364-368.

Prados, A., Brey, J. J., and Sanchez-Rey, B. (2000). "Hysteresis in vibrated granular media." *Physica A: Statistical Mechanics and its Applications*, 284(1), 277.

Press, W. H. (2002). *Numerical recipes in C++: the art of scientific computing*, Cambridge University Press, Cambridge, UK; New York.

Press, W. H., Teukolsky S. A., Betterling, W. T., and Flannery, B. P. (1992). *Numerical Recipes in FORTRAN. The art of scientific computing.*, Harper & Row, New York.

Pyke, R., Seed, H. B., and Chan, C. K. (1975). "Settlement of sands under multidirectional shaking." *Journal of the Geotechnical Engineering Division*, 101(GT4), 379-398.

Raju, V. R., and Gudehus, G. (1994). "Compaction of loose sand deposits using blasting." *Thirteenth International Conference on Soil Mechanics and Foundation Engineering*, 1145-1150.

Ramm, A. G. (2001). " An inverse problem for the heat equation." *J. Math. Anal. Appl.*, 264, 691-697.

Renard, P., and de Marsily, G. (1997). "Calculating equivalent permeability: a review." *Adv. Water Resour*, 20(5-6), 253-278.

Renard, P., Le Loc'h, G., Ledoux, E., de Marsily, G., and Mackay, R. (2000). "A fast algorithm for the estimation of the equivalent hydraulic conductivity of heterogeneous media." *Water Resources Research*, 36(12), 3567-3580.

Richards, L. A. (1931). "Capillary conduction of liquids in porous media." *Physics*, 1(5), 318-333.

Richart, F. E., Hall, J. R., and Woods, R. D. (1970). *Vibrations of soils and foundations*, Englewood Cliffs, N.J., Prentice-hall [1970].

Robertson, P. K., Wride, C. E., List, B. R., Atukorala, U., Biggar, K. W., Byrne, P. M., Campanella, R. G., Cathro, D. C., Chan, D. H., Czajewski, K., Finn, W. D. L., Gu, W. H., Hammamji, Y., Hofmann, B. A., Howie, J. A., and et, a. (2000). "CANLEX project: summary and conclusions." *Canadian Geotechnical Journal*, 37(3), 563-591.

Rogers, B. T., Graham, C. A., and Jefferies, M. G. (1990). "Compaction of hydraulic fill sand in Molikpaq core." *Prediction and Performance in Geotechnique, 43rd Canadian Geotechnical Conference*, Quebec, Canada.

Rouse, H., and Ince, S. (1957). *History of Hydraulics*, Iowa Inst. of Hydraul. Res., Univ. of Iowa, Iowa City.

Santamarina, J. C., and Cho, G. C. (2001). "Determination of critical state parameters in sandy soils-simple procedure." *Geotechnical Testing Journal*, 24(2), 185-192.

Santamarina, J. C., and Cho, G. C. (2004). "Soil behavior: the role of particle shape." *Advances in Geotechnical Engineering: The Skempton Conference, Proceedings of the Skempton Memorial Conference on Advances in Geotechnical Engineering, held at the Royal Geographical Society*, London, United Kingdom.

Santamarina, J. C., and Fratta, D. (2005). *Discrete Signals and Inverse Problems: an Introduction for Engineers and Scientists*, John Wiley and Sons, Chichester, UK.

Santamarina, J. C., and Lee, J. S. (2006). "Seismic monitoring short-duration events – Liquefaction in 1g models." *Canadian Geotechnical Journal (submitted for publication)*.

Santamarina, J. C., Klein, K. A., and Fam, M. A. (2001). *Soils and waves: [particulate materials behavior, characterization and process monitoring]*, J. Wiley & Sons, Chichester, England; New York.

Savage, S. B. (1994). "The mechanics of rapid granular flows." *Adv. Appl. Mech.*, 24, 289-365.

Schiffman, R. L., and Gibson, R. E. (1964). "Consolidation of Non-homogeneous clay layers." *Proc. ASCE*, 90(SM5), 1-30.

Schofield, A. N., and Wroth, P. (1968). *Critical state soil mechanics*, Mcgraw-hill, London, New York.

Scott, R. F. (1986). "Solidification and consolidation of a liquefied sand column." *Soils and Foundations*, 26(4), 23-31.

Seed, H. B., and Idriss, I. M. (1971). "Simplified procedure for evaluating soil liquefaction potential." *J. Soil Mech. & Found. Div. ASCE*, 97(9), 1249-1273.

Seed, H. B., and Silver, M. L. (1972). "Settlement of dry sands during earthquakes." *J. Soil Mech. & Found. Div. ASCE*, 98(4), 381-397.

Shoji, M., Ohta, H., Arai, K., Matsumoto, T., and Takahashi, T. (1990). "Two-dimensional consolidation back-analysis." *Soils and Foundations*, 30(2), 68-78.

Silver, M. L., and Seed, H. B. (1971). "Volume changes in sands due to cyclic loading." *J. Soil Mech. & Found. Div. ASCE*, 79(9), 1171-1182.

Sivapullaiah, P. V., Sridharan, A., and Stalin, V. K. (2000). "Hydraulic conductivity of bentonite-sand mixtures." *Canadian Geotechnical Journal*, 37(2), 406-413.

Skempton, A. W., and Henkel, D. J. (1953),"The post-glacial clays or the Thames estuary at Tillbury and Shellhaven." *The Third International Conference on Soil Mechanics and Foundation Engineering*, Zurich, 302-208.

Skempton, A. W., and Henkel, D. J. (1957), "Test on London clay from deep boring at Paddington, Victoria and the South Bank." *The Fourth International Conference on Soil Mechanics and Foundation Engineering*, London, 100-106.

Soga, K. (1998). "Soil liquefaction effects observed in the Kobe earthquake of 1995." *Proceedings of the Institution of Civil Engineers, Geotechnical Engineering*, 131(1), 34-51.

Solymar, Z. V. (1984). "Compaction of alluvial sands by deep blasting." *Canadian Geotechnical Journal*, 21, 305-321.

Stewart, J. P., and Whang, D. H. (2003). "Simplified procedure to estimate ground settlement from seismic compression in compacted soils." Proc. 2003 Pacific Conference on Earthquake Engineering, available at http://cee.ea.ucla.edu/faculty/Papers/PCEE_paper_046.pdf , last accessed 02/10/2006, Christchurch, New Zealand, Paper 46 - 8p.

Stewart, J. P., Smith, P. M., Whang, D. H., and Bray, J. D. (2004a). "Seismic compression of two compacted earth fills shaken by the 1994 Northridge earthquake." *Journal of Geotechnical and Geoenvironmental Engineering*, 130(5), 461.

Stewart, J. P., Whang, D. H., Moyneur, M., and Duku, P. (2004b). *Seismic compression of as-compacted fill soils with variable levels of fines content and fines plasticity,"* CUREE Publication No. EDA-05, Consortium of Universities for Research in Earthquake Engineering, Richmond, CA.

Stokoe, K. H., Lee, J. N.-K., and Lee, S. H.-H. (1991). "Characterization of soil in calibration chambers with seismic waves." *Proc. Symp. Calibration Chamber Testing 2*, Postdam, NY, 363-376.

Sutera, S. P. (1993). "The history of Poiseuille's law." *Annual Review of Fluid Mechanics*, 25, 1-19.

Tanaka, M., Guzik, A., Matsumoto, T., and Bialecki, R. A. (2005). "An inverse estimation of multi-dimensional load distributions in thermoelasticity problems via dual reciprocity BEM." *Computational Mechanics*, 37(1), 86-95.

Tatsuoka, F., Sasaki, T., and Yamada, S. "Settlement in saturated sand induced by cyclic undrained simple shear." *Eighth World Conference on Earthquake Engineering*, San Francisco, 95-102.

Terzaghi, K., Peck, R. B., and Mesri, G. (1996). *Soil Mechanics in Engineering Practice*, John Wiley and Sons, New York.

Terzagui, K., and Peck, R. B. (1967). *Soil Mechanics in engineering practice*, John Wiley and Sons, New York.

Thomas, J. W. (1995). *Numerical partial differential equations*, Springer, New York.

Tokimatsu, K., and Seed, H. B. (1987). "Evaluation of settlements in sands due to earthquake shaking." *Journal of Geotechnical Engineering*, 113(8), 861-878.

Tonon, F., Bernardini, A., and Mammino, A. (2000). "Reliability analysis of rock mass response by means of random set theory." *Reliability Eng. and System Safety*, 70(3), 263-282.

U.S. Department of the Interior, U. S. G. S. (2005). "Earthquake Hazard Program." Last date accessed: August 13, 2005. http://earthquake.usgs.gov/hazmaps/interactive/

Valdes, J. R. (2002). "Fines migration and formation damage - microscale studies," Ph.D. Dissertation, Georgia Institute of Technology, Atlanta, GA.

van Hecke, M. (2005). "Granular Matter: A tale of tails." *Nature*, 435(23), 1041-1042.

van Impe, W. F. (1989). *Soil improvement techniques and their evolution*, Brookfield publishers, Rotterdam.

Vanmarcke, E. H. (1977). "Probabilistic modeling of soil profiles." *Journal of Geotechnical Engineering*, 103(GT11), 1227-1246.

Vincens, E., Labbe, P., and Cambou, B. (2003). "Simplified estimation of seismically induced settlements." *International Journal for Numerical and Analytical Methods in Geomechanics*, 27(8), 669.

Wallace, G. B., and Otto, W. C. (1964). "Differential settlement at Selfridge Air Force Base." *Journal of the Soil Mechanics and Foundations Division*, 90(SM5), 197-220.

Warren, J., and Price, H. (1961). "Flow in heterogeneous porous media." *Society of Petroleum Engineers Journal*, 1, 153-169.

Wen, X.-H., and Gómez-Hernández, J. J. (1996). "Upscaling hydraulic conductivities in heterogeneous media: an overview." *J. Hydrol.*, 183(1-2), ix–xxxii.

Whitman, R. L., Lambe, P. C., and Akiyama, J. (1982). "Consolidation during dynamics test on a centrifuge." *Preprint82-063, ASCE, New York, N.Y.*

Wild, P. A. (1961). "Tower foundations compacted with explosives." *Electr. World*(66), 36-38.

Yamamuro, J. A., Covert, K. M., and Lade, P. V. (1999). "Static and cyclic liquefaction of silty sands." Physics and Mechanics of Soil Liquefaction, P. V. Lade and J. A. Yamamuro, eds., Balkema, Rotterdam, Baltimore, Maryland, 55-65.

Yang, H., Xie, X., Zhang, J., and Xie, K. (2004). "Spatial probability characteristic of one-dimensional consolidation for double-layered soil." *Hejiang Daxue Xuebao (Gongxue Ban)/Journal of Zhejiang University (Engineering Science)*, 38(9), 1166-1169.

Yin, H.-M. "Recent and new results o determination of unknown coefficients in parabolic partial differential equations with over-specified conditions." *Inverse problems in diffusion processes: proceedings of the GAMM-SIAM Symposium*, Philadelphia Regensburg, Germany, 181-198.

Yoon, S. S. (2005). "Array-based measurements of surface wave dispersion and attenuation using frequency-wavenumber analysis," Ph.D. Dissertation, School of Civil and Environmental Engineering, Georgia Institute of Technology, Atlanta, GA.

Youd, T. L. (1973). "Factors controlling maximum and minimum densities of sands." *Evaluation of relative density and its Role in geotechnical projects involving cohesionless soils*, ASTM SPT 523, 98-112.

Youd, T. L. (1984). "Recurrence of liquefaction at the same site." Proceedings of the Eigth World Conference on Earthquake Engineering, Volume III, San Francisco, CA., 231-238.

Youd, T. L., Idriss, I. M., Andrus, R. D., Arango, I., Castro, G., Christian, J. T., Dobry, R., Finn, W. D. L., Harder Jr, L. F., Hynes, M. E., Ishihara, K., Koester, J., Liao, S. S. C., Marcuson III, W. F., Martin, G. R., Mitchell, J. K., Moriwaki, Y., Power, M. S., Robertson, P. K., Seed, R. B., and Stokoe, K. H. (2001). "Liquefaction resistance of soils: Summary report from the 1996 NCEER and 1998 NCEER/NSF Workshops on evaluation of liquefaction resistance of soils." *Journal of Geotechnical and Geoenvironmental Engineering*, 817-833.

Young, R. N., Alonso, E., and Tabba, M. M. (1977). "Application of risk analysis to the prediction of slope stability." *Canadian Geotechnical Journal*, 14(4), 540-553.

Zeitoun, D. G., and Baker, R. (1992). "A stochastic approach for settlement predictions of shallow foundations." *Geotechnique*, 42(4), 617-629.

Zhang, L., Yu, X., and Hu, T. (1998). "Optimization of compaction zoning in loess embankments." *Canadian Geotechnical Journal*, 35(4), 611-621.

Zhang, Z. F., Ward, A. L., and Keller, J. "Determining the Hydraulic Conductivity of Sediments Containing Gravel." *The ASA-CSSA-SSSA International Annual Meetings*, Salt Lake City.

VITA

Guillermo Andres Narsilio was born on November 2nd, 1977 in Cordoba, Argentina. He received his Diploma in Civil Engineering from Universidad Nacional de Cordoba, Argentina in March 2001 with Summa cum Laude distinction. Mr. Narsilio remained at his University for teaching and for consulting. In January 2002, he started his graduate school in the United States at the Georgia Institute of Technology and received his Master of Science in Civil Engineering in December 2003 and his Master of Science in Mathematics in February 2006. He became a Ph.D. in May 2006 from the Georgia Institute of Technology. Dr. Narsilio has recently accepted a Research Fellow position at the University of Melbourne, Australia.